Dust evolution in photon-dominated regions

Thiébaut-Antoine Schirmer

université
PARIS-SACLAY

Dust evolution in photon-dominated regions

Thèse de doctorat de l'université Paris-Saclay

École doctorale n° 127, Astronomie et astrophysique d'Ile-de-France (AAIF)
Spécialité de doctorat: astronomie et astrophysique
Unité de recherche: Université Paris-Saclay, CNRS, Institut d'astrophysique spatiale, 91405, Orsay, France
Référent: Faculté des sciences d'Orsay

Thèse présentée et soutenue à Orsay, le 1er Octobre 2020, par

Thiébaut-Antoine SCHIRMER

Composition du jury:

Jacques LE BOURLOT Professeur, Université Paris Diderot	Président
Maarten BAES Professeur, Ghent University	Rapporteur et Examinateur
Olivier BERNÉ Chargé de recherche (HDR), Université Paul Sabatier	Rapporteur et Examinateur
Karine DEMYK Directrice de recherche, Université Paul Sabatier	Examinatrice
Philippe LAUDET Docteur-Ingénieur, Centre national d'études spatiales	Examinateur
Jérome PETY Directeur de recherche, Université Grenoble Alpes	Examinateur
Alain ABERGEL Professeur, Université Paris-Saclay (IAS)	Directeur de thèse
Laurent VERSTRAETE Professeur, Université Paris-Saclay (IAS)	Co-directeur de thèse

Thèse de doctorat

NNT: 2020UPASP094

Dust Evolution in Photon-dominated regions

Thiébaut Schirmer

DUST EVOLUTION IN PHOTON-DOMINATED REGIONS

THIÉBAUT SCHIRMER

ABSTRACT

Micro-physical processes on interstellar dust surfaces are tightly connected to dust properties (i.e. dust composition, size, and shape) and play a key role in numerous phenomena in the interstellar medium (ISM). The large disparity in physical conditions (i.e. density and gas temperature) in the ISM triggers an evolution of dust properties. The analysis of how dust evolves with the physical conditions is a stepping stone towards a more thorough understanding of interstellar dust. As physical conditions vary widely and are spatially resolved in nearby photon-dominated regions (PDRs), they are the ideal place to study dust evolution as a function of physical conditions. In this thesis, I focus on how does interstellar dust evolves with physical conditions in nearby PDRs. To this end, I modelled dust emission and scattering using the THEMIS interstellar dust model together with the 3D radiative transfer code SOC. I used *Spitzer* and *Herschel* observations to confront the results of my modelling in order to constrain the dust properties. I found that nano-grains are strongly depleted in the outer irradiated part of the Horsehead and that grains coagulate together to form aggregates in the inner dense part of the Horsehead. I proposed a scenario where in the outer part of the Horsehead nebula, all the nano-grain have not yet had time to re-form completely through photo-fragmentation of aggregates and the smallest of the nano-grain that are sensitive to the radiation field are photo-destroyed. In the inner part of the Horsehead nebula, grains most likely consist of multi-compositional mantled aggregates, as would expected in high density regions.

RÉSUMÉ

Les processus microphysiques à la surface des poussières interstellaires sont étroitement liés à leurs propriétés (i.e. la taille et la forme des poussières) et jouent un rôle clé dans de nombreux phénomènes du milieu interstellaire (MIS). La grande disparité des conditions physiques (i.e. la densité et la température du gaz) dans le MIS déclenche une évolution des propriétés des poussières. L'analyse de l'évolution de la poussière en fonction des conditions physiques est un tremplin vers une compréhension plus approfondie de la poussière interstellaire. Étant donné que les conditions physiques varient considérablement et sont spatialement résolues dans les régions photon-dominées (PDRs) proches, elles constituent le lieu idéal pour étudier l'évolution de la poussière en fonction des conditions physiques. Dans cette thèse, je me concentre sur la façon dont la poussière interstellaire évolue en fonction des conditions physiques dans les PDRs proches. À cette fin, j'ai modélisé l'émission et la diffusion de la poussière en utilisant le modèle de poussière interstellaire THEMIS ainsi que le code de transfert radiatif 3D SOC. J'ai utilisé les observations *Spitzer* et *Herschel* pour confronter les résultats de ma modélisation afin de contraindre les propriétés de la poussière. J'ai constaté que les nano-grains sont fortement déplétés dans la partie irradiée de la tête de cheval et que les grains coagulent pour former des agrégats dans la partie dense de la tête de cheval. J'ai proposé un scénario dans lequel, dans la partie irradiée de la nébuleuse de la tête de cheval, tous les nano-grains n'ont pas encore eu le temps de se reformer par la photofragmentation des agrégats et les plus petits des nano-grains sensibles au champ de rayonnement sont détruits par le rayonnement. Dans la partie intérieure de la nébuleuse de la Tête de cheval, les grains sont constitués d'agrégats, comme attendu dans les régions à haute densité.

SYNTHÈSE EN FRANÇAIS

Bien que l'on puisse penser que l'espace entre les étoiles est vide, c'est loin d'être le cas. En effet, cet espace appelé milieu interstellaire (MIS) est composé de gaz et de poussières. C'est dans le milieu interstellaire, où gaz et poussières se rassemblent sous l'influence de la force gravitationnelle pour former des nuages denses, que les étoiles prennent vie. Par conséquent, il est important de comprendre les différents phénomènes qui se déroulent dans le MIS afin de comprendre l'évolution de notre Galaxie et par conséquent, de l'Univers.

Bien qu'elles ne représentent que 1 % de la masse totale du milieu interstellaire, les poussières interstellaires jouent un rôle essentiel au sein de ce même milieu car impliquées dans différents processus physiques et chimiques qui se produisent sur leurs surfaces. Ces processus peuvent chauffer le gaz, comme l'effet photoélectrique, ou alors le refroidir suite à des collisions entre les molécules du gaz et les grains de poussière. En agissant comme un catalyseur, permettant aux atomes et aux molécules de réagir à sa surface, la poussière est aussi fortement impliquée dans la chimie du milieu interstellaire. La poussière joue également un rôle dans la redistribution du rayonnement stellaire UV-visible en rayonnement IR-millimétrique, un processus qui dépend de la masse, du volume et également de la composition des grains de poussière. L'efficacité de ces processus dépend fortement des propriétés de la poussière telles que la taille des grains, composition et la forme. Il est donc important de contraindre les propriétés de la poussière afin de comprendre les différents phénomènes qui se déroulent dans le milieu interstellaire. Cependant, la grande disparité des conditions physiques (densité et irradiation) dans le milieu interstellaire entraîne une évolution des propriétés de la poussière, telle que la masse, le volume, la forme ainsi que la composition.

Au cours de ma thèse, j'ai donc essayé de comprendre comment la poussière interstellaire évolue en fonction des conditions physiques. À cette fin, j'ai étudié l'évolution de la poussière dans les régions photon-dominées, où les conditions physiques varient considérablement et peuvent être résolues spatialement. Ces régions sont donc un endroit unique pour étudier la façon dont la poussière évolue avec les conditions physiques locales.

La première partie de ma thèse se concentre sur les différents outils utilisés pour mener à bien ce projet. Pour modéliser les grains de poussière, j'ai utilisé le modèle THEMIS, qui propose un scénario d'évolution des grains du milieu diffus vers le milieu dense. Du fait qu'une région photon-dominée est une région dense, la façon dont se propage les photons en son sein est compliquée et nécessite donc une approche détaillée quant au transfert du rayonnement dans la matière, c'est ce qu'on appelle le transfert radiatif. J'ai donc utilisé un code de transfert radiatif appelé SOC, qui m'a permis de modéliser avec précision l'émission et la diffusion observées dans les régions photon-dominées en utilisant le modèle THEMIS. Étant donné que le transfert radiatif n'est pas intuitif, j'ai étudié l'influence de la modification des propriétés des grains sur leurs émission, avec et sans transfert radiatif, pour dissocier des effets uniquement liés au transfert radiatif.

La deuxième partie de ma thèse concerne l'application de ces outils à un cas concret, la nébuleuse de la tête de cheval. J'ai utilisé les observations des télescopes spatiaux Spitzer et Herschel pour confronter les résultats de ma modélisation afin de contraindre les propriétés de la poussière. J'ai constaté que les nano-grains sont fortement déplétés dans la partie irradiée de la tête de cheval et que les grains coagulent pour former des agrégats dans la partie dense de la tête de cheval. J'ai proposé un scénario dans lequel tous les nano-grains n'ont pas encore eu le temps de se reformer par la photo-fragmentation des agrégats dans la partie

irradiée et que les plus petits des nano-grains sensibles au champ de rayonnement sont détruits par le rayonnement. Dans la partie dense de la nébuleuse de la Tête de cheval, les grains sont constitués d'agrégats, comme attendu dans les régions à haute densité. En conclusion, j'ai montré qu'il n'est pas possible de reproduire les observations dans la tête de cheval en utilisant des grains de poussière provenant du milieu interstellaire diffus. Il est nécessaire de faire évoluer les grains en modifiant leurs propriétés pour comprendre les observations dans les régions photon-dominées.

ACKNOWLEDGMENTS

À ma famille, mes amis et mes collègues.

CONTENTS

LIST OF FIGURES

LIST OF TABLES

Part I

GENERAL INTRODUCTION AND PHD OBJECTIVES

GENERAL INTRODUCTION AND PHD OBJECTIVES

En vérité, le chemin importe peu, la volonté d'arriver suffit à tout.

Albert Camus - *Le Mythe de Sisyphe*

The celestial vault has historically been a source of great fascination for human kind. As the evolution of astronomy over time could be, at the very least, a thesis subject, I chose to develop only three aspects that are of special interest to me.

Around the 4th century BC, the mathematician and astronomer Philolaos claimed that the world is made of *harmony and numbers*, in proportions that correspond to the three basic tones in music (i.e. the octave (2:1), fifth (3:2), and fourth (4:3)). Based on his own perception of the world, he introduced the notion of *musica universalis* (also called, *music of the spheres* or *harmony of the spheres*) that was later described in *La République*, by Plato. Thence, from the observed harmony in the celestial vault, which implies an organised world, the notion of *Cosmos* emerged for the first time:

'À ce qu'assurent les doctes pythagoriciens, Calliclès, le ciel, la Terre, les Dieux, les hommes, forment ensemble une communauté, ils sont liés par l'amitié, l'amour de l'ordre, le respect et la tempérance, le sens de la Justice. C'est pourquoi le tout du monde les Sages l'appellent Cosmos, ou ordre du monde, et non pas désordre ou dérèglement.'

Plato, *Gorgias*, 507 e - 508 a

In an entirely different domain, a masterpiece of Celtic art, the Brno pitcher (see Fig. 1, left panel), was discovered in May 1941. Albeit the magnificent bronze ornaments on this pitcher suggested they were only there for decoration, the french archeologist and historian, Venceslas Kruta, went further in 2007. Using reconstruction of the starry sky of Brno at the summer and winter solstices, in the year that the creation of the pitcher was made, he found complete agreement between the constellations and the ornaments (see Fig. 1, right panel). This highlights the deep knowledge of the sky that the Celts had at that time (4th and 3rd century BC), as well as their fascination for the starry vault.

In 1584, at the instigation of Tycho Brahe, one of the most important observatories (see Fig. 2, left panel) in Europe was built on the small Swedish island of Ven (which was Danish at this time). As refracting telescopes were built only 20 years after the creation of this observatory, all the measurements were made with instruments such as sextants and quadrants (see Fig. 2, right panel), with the naked eye. We can see the precision with which these instruments have been built, which enabled the astronomers of the time to establish a catalogue of 1000 stars with an accuracy of the order of one arc minute. It was the most precise and complete catalogue of stars at the time. Later, Johannes Kepler used this catalog and most especially the measurements that were made of the planets, to establish his laws of planetary motions, the well-known *Kepler laws*.

Nowadays, our fascination for the sky is, fortunately, still intact. While lying on the ground and looking at the stars, more and more details will appear, as our eyes adapt to this peaceful obscurity. With some luck, mostly due to the geographic position, a broad white band that slices through the sky, pops out at our eyes ... This is our Galaxy, the Milky way. Albeit it contains a large number of stars, it is possible to distinguish many dark places. Although one

might think that the space between the stars is empty, it is far from being so. Indeed, this space is composed of gas and dust, known as the interstellar medium (ISM). It is in the ISM, where gas and dust gather to form dense clouds, where the stars are brought to life. As a consequence, it is important to understand the different phenomena that take place in the ISM in order to understand the evolution of our Galaxy and, as a result, of the Universe.

Despite representing only 1 % of the ISM total mass, interstellar dust plays an essential role within the ISM through different microphysical processes that occur on dust surfaces that can heat the gas, such as the photoelectric effect, or cool the gas through gas-grain collisions. By acting as a catalyst, allowing atoms and molecules to react on its surface, dust is strongly involved in the chemistry of the ISM. Dust also plays a role in the redistribution of UV-visible stellar radiation into IR-millimeter radiation, a process that depends on the dust mass, the volume of dust grains and also upon their composition. The efficiency of these processes strongly depends upon the dust properties such as the grain size, composition and shape. It is therefore important to be able to constrain dust properties in order to understand the different phenomena that take place in the ISM. However, the wide disparity in the physical conditions (density and irradiation) throughout the ISM triggers an evolution of the dust properties.

During my PhD, I have therefore tried to understand how does interstellar dust evolves with physical conditions. To this end, I studied dust evolution in nearby photon-dominated regions, where the physical conditions vary widely and can be spatially resolved. These regions are therefore a unique place to study how dust evolves with the local physical conditions.

In chapter ii, I describe the structure of the interstellar medium. I will particularly depict interstellar dust, from its signatures in the Universe, by way of evidence for its evolution within different environments, to the mechanisms that lead it to radiate. I will also present photon-dominated regions, that are at the heart of my work to study how does dust evolves with physical conditions.

In order to study dust evolution in photon-dominated regions, we need observations. I will therefore present, in chapter iii, the different space observatories that provide us with these observations, and detail the observations of the Horsehead Nebula that I used in this work.

These observations require models and tools in order to interpret the dust emission and scattering in such regions. Consequently, I introduce the interstellar dust model I used in this study, THEMIS, in chapter iv. I also describe the local dust emission modelling tool, DustEM, and the two radiative transfer codes that I used, DustPDR and SOC.

In chapter v, I present a detailed analysis of the dust emission and scattering properties resulting from the calculations that I performed and then, the evidence for dust evolution in the Horsehead that I have highlighted. I will also discuss the implications of these results for the physics and chemistry of this region. This thesis ends with a concluded chapter vi.

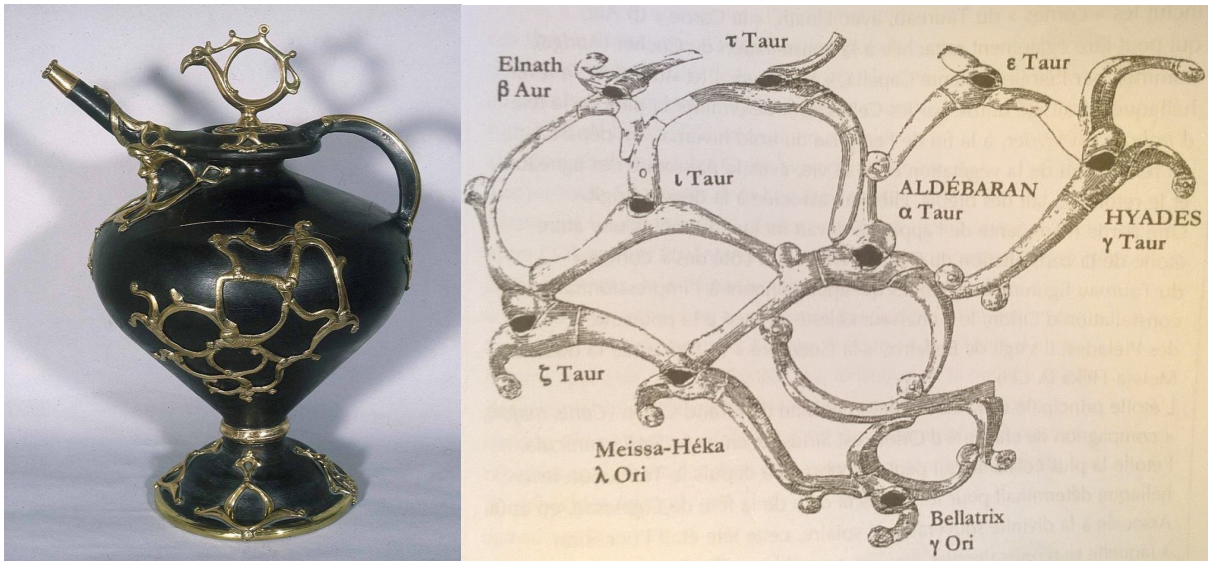

Figure 1: Left: The Brno pitcher. Right: Representation of the ornaments of the Brno pitcher with the associated stars. Credits: Venceslas Kruta.

Figure 2: Left: *Stjerneborg*, the buried Danish astronomical observatory created at the initiative of Tycho Brahe, on the small Swedish Island of Ven. Right: A quadrant in the Tycho Brahe Museum on the Ven Island. Credits: Thiébaut Schirmer.

Part II

ASTROPHYSICAL CONTEXT

1 THE INTERSTELLAR MEDIUM

Aujourd'hui s'appelle Aujourd'hui, et demain Peut-être.
Johann Wolfgang von Goethe - *Les maximes et réflexions*

Contents

A large amount of the observable matter (~ 99%) in our Galaxy is found within stars[1] although they occupy a very small volume. The 1% of mass left fills up the space between stars, known as the interstellar medium (ISM). It is composed by mass of 1% dust and 99% gas (70% hydrogen and 30% helium that is, 90% hydrogen and 10% helium by number of atoms), whose intrinsic properties make it possible to distinguish several structures. Since hydrogen is the largely dominant element in the interstellar medium (see Fig. 3), it is customary to characterize the density of such media by the number[2] of protons per unit volume, n_H.

Dust grains, with diameters ranging from nanometers to micrometers, are mixed with the interstellar gas. They are mostly formed in the cold atmospheres of evolved stars, in novae, and supernovae. Although dust represents only about one hundredth of the mass of the ISM, it plays an important role in the physics and chemistry of the interstellar medium through the extinction and emission of radiation, through the chemical reactions that take place on the surface of these grains, and in the gas heating. We describe dust in more details in Sect. 2.

In this section, we first describe the different phases that composed the ISM and their evolution over time. Then, we present the different sources of energy of the ISM. To finish, we introduce the different heating and cooling mechanisms of the ISM.

1.1 A STRUCTURED ENVIRONMENT

Astrophysics is a science which is primarily based on the observation and classification of astronomical objects. The multi-wavelength observations of galaxies and especially of our Galaxy, the Milky Way, shows a wide heterogeneous distribution of stellar and interstellar matter.

1 The velocity field of the Galaxy shows that another mass component is needed so far of unknown origin. This mass component which does not shine is called dark matter (also missing mass) and represents represents 4 times the stellar mass (8×10^{11} $M_\odot$).

2 $n_H = n(H) + n(H^+) + 2\,n(H_2)$.

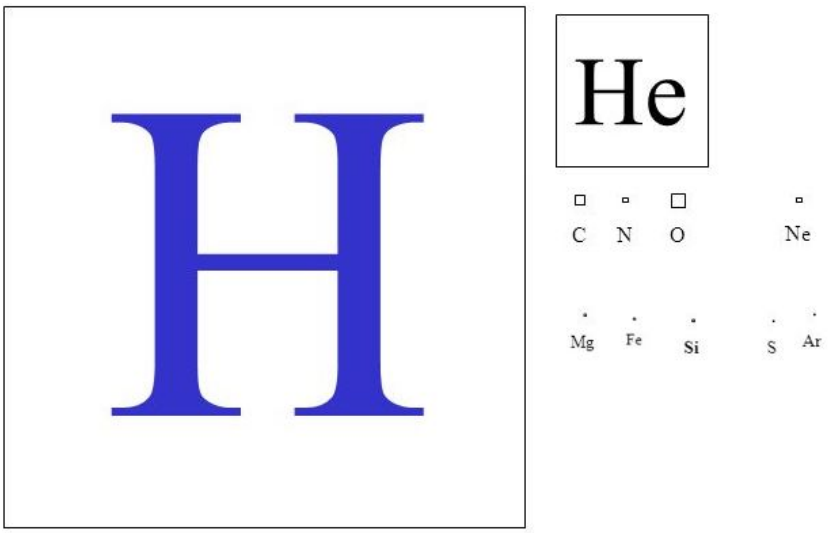

Figure 3: *The astronomer's periodic table* where the relative cosmic abundance are represented by the area of the boxes. Image created by Benjamin McCall.

McKee and Ostriker, 1977 proposed a classification of the ISM based on the hydrogen state (ionised, atomic, and molecular). Later, as the density and temperature are the two main variables that control the gas state equation, the community decided to use these two physical parameters to discriminate the different regions of the ISM (e.g. Ferrière, 2001; Draine, 2011). However, this classification suffers from some limitations because there are regions where the physical conditions are such that they cannot be fitted into the usual classification. Nevertheless, this classification remains an efficient tool to characterise the ISM in a faithful and simple way, albeit not adapted to PDRs. However, Snow and McCall, 2006 proposed a classification based on the state of the hydrogen and carbon in the gas, which follows variations in the UV radiation field. This classification is therefore appropriate for the study of PDRs, where the UV radiation field decreases progressively from the illuminated edge to the densest regions (see Sect. 3). We present here these two classifications schemes.

1.1.1 *Classification based on the gas state*

In the usual classification of the ISM, five phases are defined (e.g. Ferrière, 2001; Draine, 2011), based on the physical conditions (see Table 1 for a summary), described as follows:

- the *hot ionised medium* (HIM) represents an important part of the volume of our Galaxy but a small part of its mass. It fills a spherical structure on a very large scale that encompasses the disc of the galaxy, called the galactic halo. Its particularly low density allows the energetic radiation and shock waves produced by the supernovae to propagate there, heating the gas to the highest temperatures attained in the ISM. The gas in this region is therefore mostly ionised. The HIM is thought to be the result of the so-called galactic fountain where the ram pressure of supernovae sends gas out of the galactic plane. In the course of its long cooling this gas get denser and falls back on the galactic plane in the form of high-velocity or intermediate-velocity clouds, hence the fountain name (e.g. Miville-Deschênes et al., 2005; Marchal et al., 2019).
- the *warm neutral medium* (WNM) where photons above 13.6 eV are mostly suppressed. Therefore, hydrogen is found in this neutral form in this medium, which has temperatures of a few thousand K and densities between 0.1 and 1 cm^{-3}. It is important to note

Table 1: Summary of the physical conditions in the five phases of the ISM described in Sect. 1.1.1. All the values are taken from Draine, 2011.

Phase	T_{gas} [K]	n_H [cm^{-3}]	Volume [%]	M [$10^9 M_\odot$]	tracers
HIM	$\geqslant 10^{5.5}$	~ 0.004	50%	0.02	UV, x ray, radio synchrotron
WNM	~ 5000	0.6	30%	2	HI 21 cm emission
CNM	~ 100	30	4%	3	HI 21 cm absorption
WIM	$\sim 10^4$	$0.2 - 10^4$	20%	2	H_α, UV, x ray, radio synchrotron
Molecular	$\sim 10 - 20$	$10^2 - 10^6$	1%	2.3	CO 2.6-mm, dust far-IR emission

that the heating of such regions cannot be ensured by the photoionisation of the atoms because the electrons do not have time to heat the gas as they recombine quickly. Thus, it is the photoelectric effect on dust grains that is responsible for the heating of these regions;

- the *cold neutral medium* (CNM) is organised in the form of interconnected filaments and clouds, is less dense than the molecular phase and the hydrogen is therefore in atomic form;

- the *warm ionised medium* (WIM) where photons can have energies above 13.6 eV leading to the photoionisation of hydrogen atoms. The gas is thus almost fully ionised and reaches temperatures around 10^4 K. In the photoionisation process, energetic electrons (with a few tens of eV in kinetic energy) are injected into the gas releasing their energy via inelastic collisions with gas species. A detailed review of this phase can be found in Haffner et al., 2009;

- the *molecular medium* is essentially in the form of molecular clouds that occupy the galactic disc plane. In such regions, the temperature is about only 10 K and varies only slightly while the density covers a wide range ($n_H \sim 10^2 - 10^6$ cm^{-3}). This reflects that the denser parts of the molecular clouds are not in pressure equilibrium with the surrounding neutral medium. These regions undergo a phase of gravitational collapse, the first phase of star formation. In addition, these regions are sufficiently cold to allow ice mantles to form on dust grains (H_2O, CO_2, CO, ...);

1.1.2 *Classification based on the hydrogen and carbon states*

The classification proposed by Snow and McCall, 2006 consists of four different regions, based on the hydrogen and carbon states, described as follows:

- the *diffuse atomic gas* corresponds to the region where the UV radiation field is high enough to efficiently dissociates all molecules and especially the molecular hydrogen. There, the molecular hydrogen abundance is less than 10%;

- the *diffuse molecular gas* corresponds to the region where the UV radiation field is high enough to ionise carbon atoms but low enough to prevent the molecular hydrogen photodissociation. There, the molecular hydrogen abundance is greater than 10% and the abundance of ionised carbon atoms is greater than 50%;

- the *translucent gas* corresponds to the region where the UV radiation field is low enough to prevent the ionisation of carbon atoms but still high enough to dissociate CO molecules. There, the abundance of ionised carbon is less than 50% and the abundance of CO is greater than 90%;
- the *dense molecular gas* corresponds to the region where the UV radiation field is low enough to prevent the photodissociation of CO molecules. There, the CO abundance is greater than 90%.

As the radiation field decreases progressively in PDRs, due to both dust extinction and H_2 self-shielding, this classification is therefore well adapted to PDRs as the hydrogen and carbon states are driven by UV radiation.

1.2 AN EVOLVING ENVIRONMENT

Although it may appear static, the interstellar medium is constantly evolving. Indeed, interstellar matter is dynamically evolving at all scales, from the molecular scale to large structures, resulting in physical and chemical transformations.

Interstellar matter can be transported through different processes. For instance, at the scale of giant molecular clouds (around a 100 pc across), the energy injected by stellar winds and shock waves maintains turbulent and often supersonic flows, that help to shape these clouds on a wide range of spatial scales, giving them a fractal structure. The differential rotation of the Galaxy also sets these clouds in rotation on large scales, then the injected energy cascades on smaller scales.

Many motions of interstellar matter revolve around the formation, life, and death of stars. This is called the cycle of galactic matter. Star formation takes place within molecular clouds, as soon as the mass of a condensate of matter exceeds a certain critical mass beyond which gravitational collapse is possible. The core contracts and the temperature rises until, if the initial mass of the condensation is sufficient, the fusion temperature of the hydrogen is reached. In this case, the nuclear fusion reactions with hydrogen are initiated, the excess energy thus produced allows the object to radiate without drawing on its gravitational potential energy and therefore, stop the gravitational collapse: a star is born. If it is massive enough ($1 - 10$ $M_\odot$), it will radiate mostly in the UV range: such stars belong to the O and B types. In molecular clouds, the strong UV radiation field of OB stars generates photon-dominated regions (PDR) where the gas is strongly heated and dissociated.

The life of a star is long, from a few tens of millions for the most massive stars to more than the age of the Universe for the least massive ones, and consists of several successive phases. It is possible to determine these different phases from the knowledge of the initial mass of the condensate. The ejected matter from stars in stellar winds and during the terminal phases of their evolution (supernovae or planetary nebulae) mixes with the surrounding matter and therefore feeds diffuse and dense media. It is this same matter that will be one day form other condensates.

Nuclear fusion reactions that take place in stars consume hydrogen nuclei to form helium nuclei and then carbon and oxygen nuclei if the initial mass of the condensation is large enough. Subsequently, other nuclear reactions allow the synthesis of the other elements of the periodic table classification: it is through this cycle that the interstellar matter is enriched (see Fig. 4).

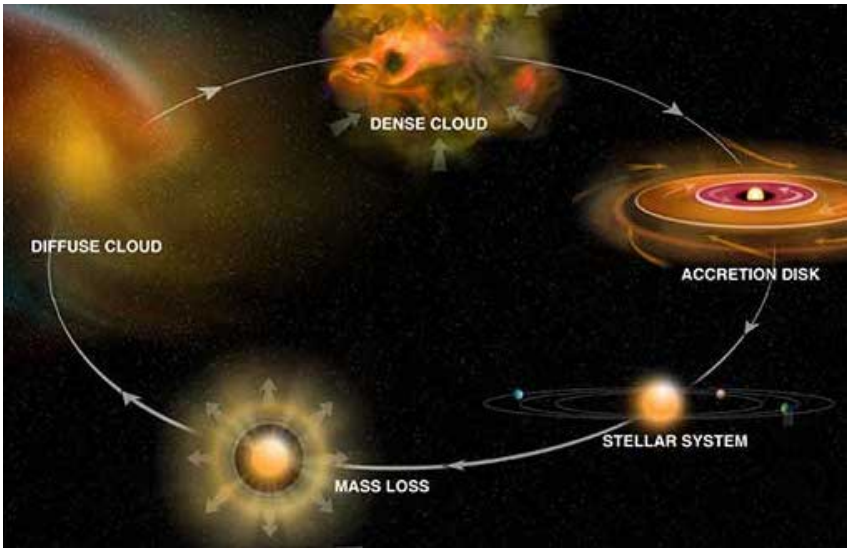

Figure 4: Interstellar matter cycle. Credit: Bill Saxton, NRAO/AUI/NSF.

1.3 RADIATIVE ENERGY SOURCES IN THE ISM

The interstellar medium is irradiated by the interstellar radiation field (ISRF, see Fig. 5) produced by all of the stars and molecular clouds of the galaxy. Some features stand out from this spectrum:

- the thermal emission at $\lambda \sim 10^3$ μm which corresponds to the photons of the *cosmic microwave background* (CMB), that were emitted at the recombination era. Due to the expansion of the Universe, they have been redshifted to the microwave spectral range. The CMB is well reproduced by a black-body law at 2.7 K;
- the dust continuum emission from IR to submm wavelengths;
- the aromatic bands between 3 and 20 μm, due to the aromatic structures in nano-grains ($a < 1$ nm);
- the emission at visible wavelengths originating from low-mass and intermediate-mass stars;
- the UV emission from massive hot stars.

The latter photon population plays a major role in the physics and chemistry of irradiated regions. This UV photon flux is often characterised by a single parameter G_0, the so-called Habbing unit (Habing, 1968) defined as follows:

$$G_0 = \frac{1}{1.6 \times 10^{-3}\,(\mathrm{erg\,s^{-1}\,cm^{-2}})} \int_{6\,\mathrm{eV}}^{13.6\,\mathrm{eV}} I_\nu \, d\nu, \tag{1}$$

where I_ν is the specific intensity, expressed in $\mathrm{erg\,cm^{-2}\,s^{-1}\,Hz^{-1}}$.

Another energy source that can be an important heating process in the dense ISM, such as the molecular regions of PDRs, is due to the cosmic rays. They are nuclei of atoms (usually protons) circulating in the Galaxy at relativistic energies of up to 10^{20} eV.

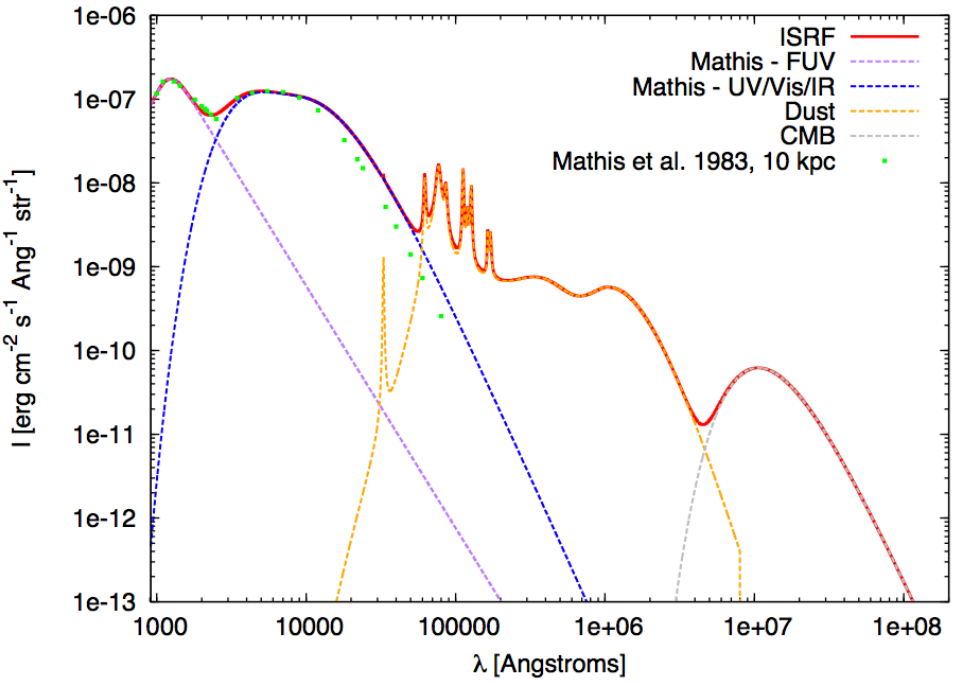

Figure 5: The interstellar radiation field for $G_0 = 1$.

1.4 GAS HEATING AND COOLING PROCESSES IN THE ISM

1.4.1 *Gas heating*

There are different ways to heat the gas in the ISM, through photons and cosmic rays, chemical reactions, dust grains, and also dynamical processes.

Radiation or cosmic rays can eject electrons from species, called *photoelectrons*. As these photoelectrons have low energies, they cannot excite or ionise other species in the ISM. We can therefore consider that all of the energy of these photoelectrons is used to heat the gas via thermalisation with electrons. It has been shown that the photoelectric efficiency is largest for the smallest grains of nanometric size (Bakes and Tielens, 1994). This is an important result that should be emphasized because these same nano-grains are likely to evolve in PDRs (see Sect. 10) and therefore, affect the heating through the photoelectric effect (see Sect. 10.3.2.2).

In the ISM, numerous chemical reactions occur. Some of these are exothermic and therefore, can heat the gas. For instance, the H_2 formation on dust grains (see Sect. 2.5) is highly exothermic and can be a major source of heating in PDRs (see Sect. 3). This is also an important result that should be emphasized for the following. Indeed, H_2 is formed on dust surfaces and because most of the dust surface is contains in nano-grains that are likely to evolve in PDRs (see Sect. 10), this therefore affects the H_2 formation and the gas heating through this mechanism.

Finally, gas-grain coupling can also heat the gas, especially in dense regions where dust grains are hotter than the gas because of the IR radiation field that can penetrates there because of the low dust extinction in the IR.

1.4.2 *Gas cooling*

The interstellar gas can cool through radiation of species excited by collisions and inverse mechanisms of some heating processes.

Inelastic collisions between gas species (H, H2, electrons) and atoms or molecules which become excited can therefore, cool the gas through long wavelength emission lines. As the temperature increases, higher energy levels can be reached by collisions with electrons and consequently lead to gas cooling. Note that the excitation of the $n = 2$ level of the atomic hydrogen which deexcite by emitting in the Lyman α line is a very efficient cooling mechanism (Le Bourlot, Forêts, and Flower, 1999). In dense regions, the rotational lines of CO dominate the gas cooling.

The inverse mechanisms of the heating processes described above are also an important source of gas cooling. Indeed, both electron recombination with charged grains and gas-grain coupling between hot gas and cold grains result in a decrease of the gas temperature.

2 DUST IN THE UNIVERSE

What is success?
To laugh often and much;
to win the respect of intelligent people and the affection of children;
to earn the appreciation of honest critics and endure the betrayal of false friends;
to appreciate the beauty;
to find the best in others;
to leave the world a bit better, whether by a healthy child, a garden patch
Or a redeemed social condition;
to know even one life has breathed easier because you have lived.
This is to have succeeded.

Ralph Waldo Emerson

Contents

2.1 DUST SIGNATURES

2.1.1 *Extinction and polarisation*

2.1.1.1 *Quantifying dust extinction*

When photons emerging from a star travel through a cloud that contains both dust and gas, they can be absorbed and scattered by dust grains, this is what is called *dust extinction*. As we will see in Sect. 7.1, if we consider an incident radiation field $I_\lambda(z=0) = I_{\lambda,0}$, that enters in a cloud, the radiation field leaving this cloud (with the hypothesis that there are no sources of energy in the cloud) can be expressed as:

$$I_\lambda = I_{\lambda,0} \exp(-\tau_\lambda), \tag{2}$$

where $\tau_\lambda = \tau_{\lambda,\text{abs}} + \tau_{\lambda,\text{sca}}$ is the optical depth of the cloud.

Besides, dust extinction can be quantified by the following parameter, simply called the *extinction*:

$$A_\lambda = -2.5 \log\left(\frac{I_\lambda}{I_{\lambda,0}}\right). \tag{3}$$

Using Eq. (2) in the previous equation, we can therefore simplify A_λ as:

$$A_\lambda = 1.086 \times \tau_\lambda. \tag{4}$$

However, neither $I_{\lambda,0}$ nor τ_λ can be directly measured. Therefore, the numerical value of A_λ cannot be determined from Eq. (3) or Eq. (4), which is why the *color excess* was introduced. The *color excess* is the difference between optical depths at two different wavelengths. Let us consider the following two fluxes:

- $F_{\lambda,\text{ext}}$, which is the flux received by an observer, emitted by a star at a distance D_1, that has been reddened because of dust extinction in a cloud with an optical depth τ_λ;
- $F_{\lambda,\text{w/o ext}}$, which is the flux received by an observer, emitted by a star (of the same spectral type) at a distance D_2, without being reddened;

As the flux received from a star with a luminosity $L_{\lambda,\star}$ at a distance D, and the associated magnitude, are expressed as:

$$F_{\lambda,\text{obs}} = \frac{L_{\lambda,\star}}{4\pi D^2} \exp(-\tau_\lambda) \quad \text{and} \quad m_{\lambda,\text{obs}} = 2.5\,(\log(L_{\lambda,\star}) - \tau_\lambda + 2\log(D) + \text{constant}), \tag{5}$$

this implies:

$$F_{\lambda,\text{ext}} = \frac{L_{\lambda,\star}}{4\pi D_1^2} \exp(-\tau_\lambda) \qquad \text{and} \qquad F_{\lambda,\text{w/o ext}} = \frac{L_{\lambda,\star}}{4\pi D_2^2}, \tag{6}$$

and therefore:

$$\Delta m_\lambda = m_{\lambda,\text{ext}} - m_{\lambda,\text{w/o ext}} = 2.5 \times \left(-\tau_\lambda - 2\log\left(\frac{D_1}{D_2}\right)\right). \tag{7}$$

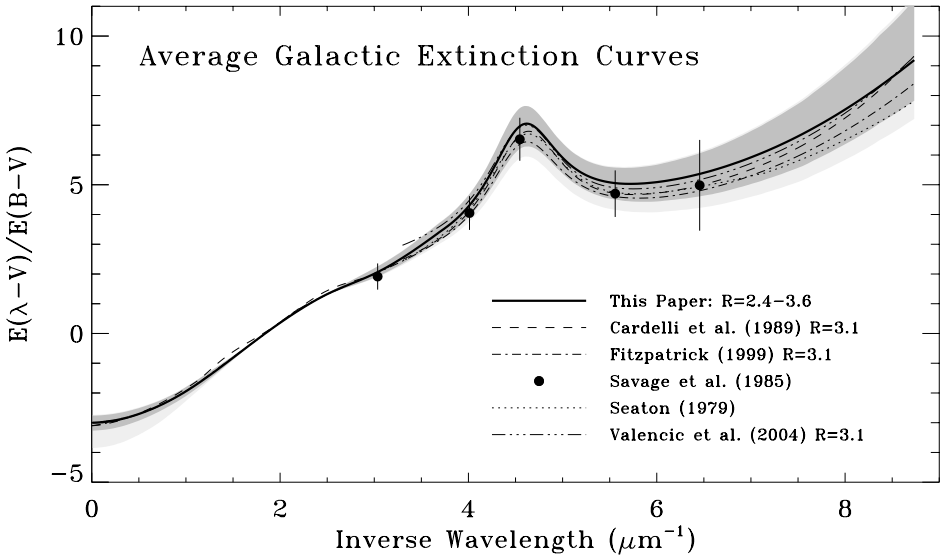

Figure 6: Extinction curves for $2.4 < R_V < 3.6$ (Fitzpatrick and Massa, 2007).

The color excess is thus defined as:

$$E(\lambda, \lambda') = \Delta m_\lambda - \Delta m_{\lambda'} = 2.5\,(\tau_{\lambda'} - \tau_\lambda)\,. \tag{8}$$

The standard color excess generally used is the color excess between the B band ($\lambda = 0.44$ μm) and the V band ($\lambda = 0.55$ μm), noted $E(B, V) = E(B-V) = E_{B-V}$.

Thence, it is possible to define the standard interstellar extinction that is used in many studies (see Fig. 6), defined as:

$$\mathrm{Ext}(\lambda) = \frac{E(\lambda, V)}{E_{B-V}} = \frac{A_\lambda - A_V}{A_B - A_V} = \frac{\tau_\lambda - \tau_V}{\tau_B - \tau_V}. \tag{9}$$

It is therefore possible to compare variation of extinction with the wavelength even if stars are not of the same type, because of the E_{B-V} normalisation. Finally, Cardelli, Clayton, and Mathis, 1989 introduced R_V, a parameter which characterises the extinction law and defined as:

$$R_V = \frac{A_V}{E_{B-V}}. \tag{10}$$

Extinction curves (see Eq. (9)) for different values of R_V (see Eq. (10)) are shown in Fig. 6.

2.1.1.2 *Spectroscopic features*

THE UV BUMP AT 217.5 NM In 1965, a strong extinction at ~ 217 nm (see Fig. 8) was discovered (Stecher, 1965) and labeled as the well-known *UV extinction bump* (Stecher and Donn, 1965). Albeit both its width and intensity vary with the environment, which could be due to dust evolution (see Sect. 2.2 and Sect. 10), its position barely varies (Fitzpatrick and

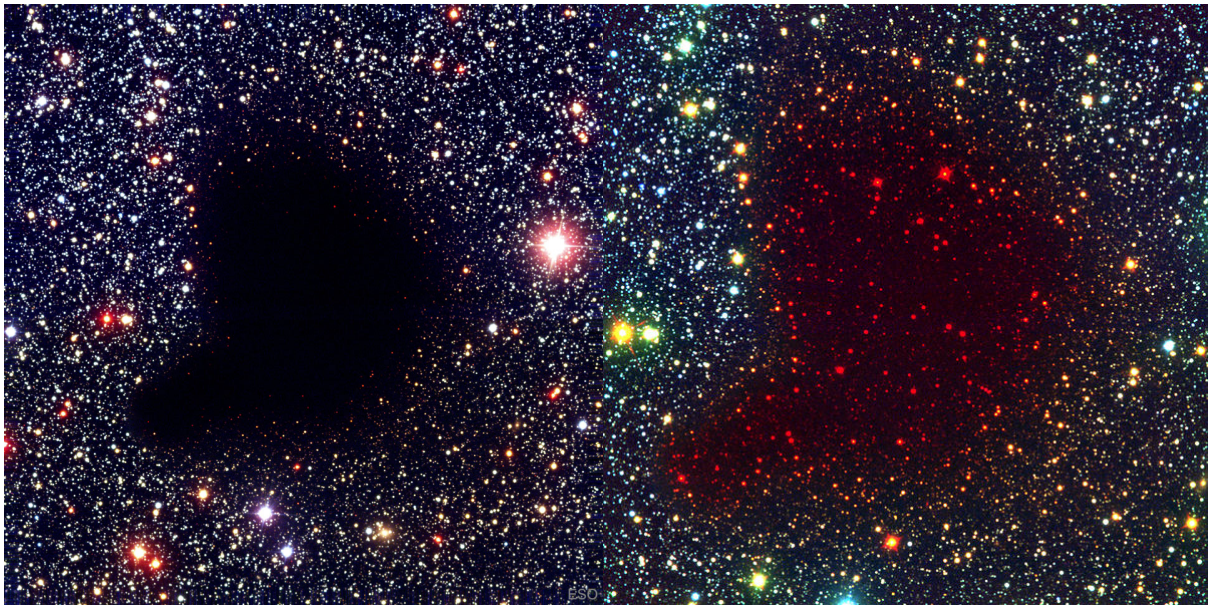

Figure 7: Left: The dark molecular cloud Barnard 68 observed in the visible. Credits: FORS Team, 8.2-meter VLT Antu, ESO. Right: Barnard 68 seen in the visible at 0.44 μm (blue), in the near-IR at 0.768 μm (green) and 2.2 μm (red). Credits: ESO.

Massa, 1986). Even after more than fifty years of studies, the origin of this bump is still unclear, although different materials have been proposed to explain this feature, all without satisfactory success:

- graphite (e.g. Stecher and Donn, 1965; Draine and Lee, 1984);
- polycyclic aromatic hydrocarbons[1] (PAHs) (e.g. Joblin, Leger, and Martin, 1992; Duley and Seahra, 1998; Li and Greenberg, 2002a; Steglich et al., 2011);
- hydrogenated amorphous carbon (e.g. Hecht, 1986; Jones, 1990; Sorrell, 1990; Mennella et al., 1996; Jones, 2016; Gavilan et al., 2017);
- quenched carbonaceous composite (e.g. Sakata et al., 1995);
- coals (e.g. Papoular et al., 1995);
- silicate grains (e.g. Steel and Duley, 1987).

Draine, 1989 gave an overview on the interpretation of this UV bump. As the albedo at these wavelengths is relatively low, the UV bump is therefore mostly due to absorption. This suggests that the UV bump is due to nanometric particles that can absorb at these wavelengths.

SILICATE ABSORPTION FEATURES The silicate absorption features are dominated by two strong absorption bands at 9.7 μm and 18 μm (see Fig. 9, left panel), that are both observed in the diffuse ISM (e.g. Whittet et al., 1997; Chiar et al., 2000, 2006; Fogerty et al., 2016) and in molecular clouds (e.g. Breemen et al., 2011). These two absorption bands are assigned to the Si-O stretch and O-Si-O bending modes, respectively.

As these absorption bands are broad and featureless, this strongly suggests that the silicates are amorphous in the ISM. This is reinforced by observations in the OMC-1 Orion dense

1 In chemistry, PAHs are molecules composed of aromatic cycles (C_6).

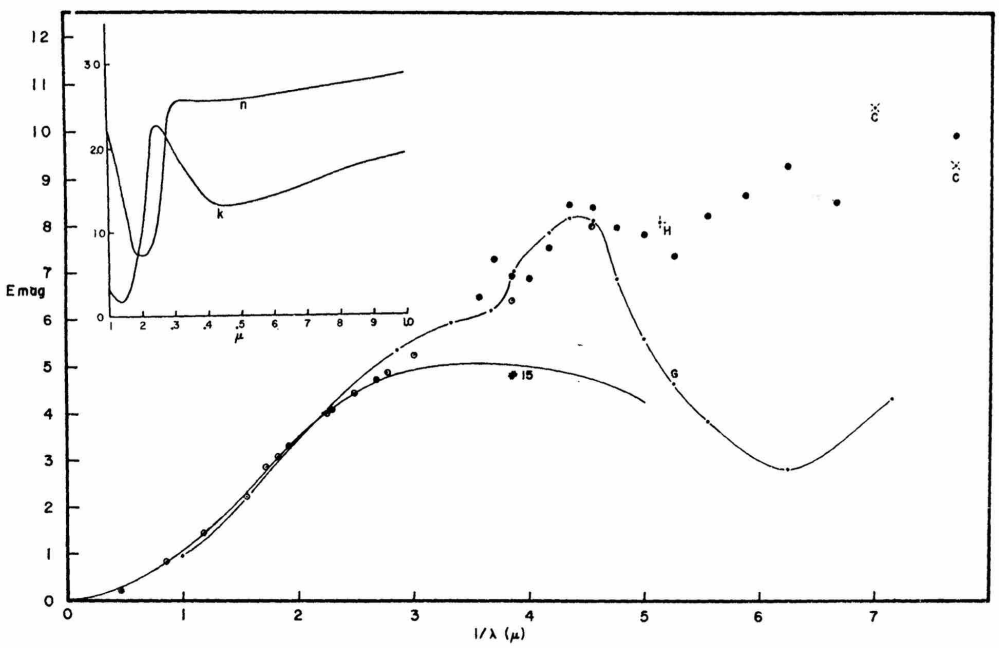

Figure 8: Mean observed interstellar extinction (filled circles) from Stecher, 1965. The solid line corresponds to the theoretical prediction using graphite grains (Stecher and Donn, 1965).

molecular cloud which show that the 9.7 μm band is polarised (see Fig. 9, right panel) and without any sub-features (Dyck et al., 1973), as is the 18 μm band (Aitken et al., 1996; Smith et al., 2000), which therefore supports amorphous silicates. However, observations of oxygen-rich cool giants (e.g. Gilman, 1969; Waters et al., 1996; Li and Draine, 2001b; Kemper, Vriend, and Tielens, 2004; Wright, Do Duy, and Lawson, 2016) showed that silicate grains that are forming in the atmospheres of such giants are composed of both amorphous and crystalline silicates. This suggests that:

- energetic processes such as shocks or grain-grain collisions, bring disorder to the crystalline structure of these silicates and therefore, turn them into amorphous silicates;
- only a small fraction of dust grains are created in the atmosphere of oxygen-rich cool giants. The majority of the dust being created from condensation in the ISM (Draine, 1990).

ALIPHATIC HYDROCARBON ABSORPTION FEATURES The discovery of the 3.4 μm extinction feature (see Fig. 10) was made in 1979 through observations towards the Galactic Center (Willner et al., 1979; Wickramasinghe and Allen, 1980). Thence, this feature has been observed in various environments:

- in galaxies (e.g. Butchart et al., 1986; Adamson, Whittet, and Duley, 1990; Sandford et al., 1991; Pendleton et al., 1994; Imanishi and Dudley, 2000; Yamagishi et al., 2012)
- in planetary nebulae around evolved stars (e.g. Muizon, D'Hendecourt, and Geballe, 1990; Geballe et al., 1992; Hrivnak, Geballe, and Kwok, 2007);
- in protoplanetary disks (e.g. Brooke, Tokunaga, and Strom, 1993; Meeus et al., 2001; Acke and Ancker, 2004; Habart, Natta, and Krügel, 2004; Acke et al., 2010; Maaskant et al., 2014; Seok and Li, 2017; Boutéraon et al., 2019).

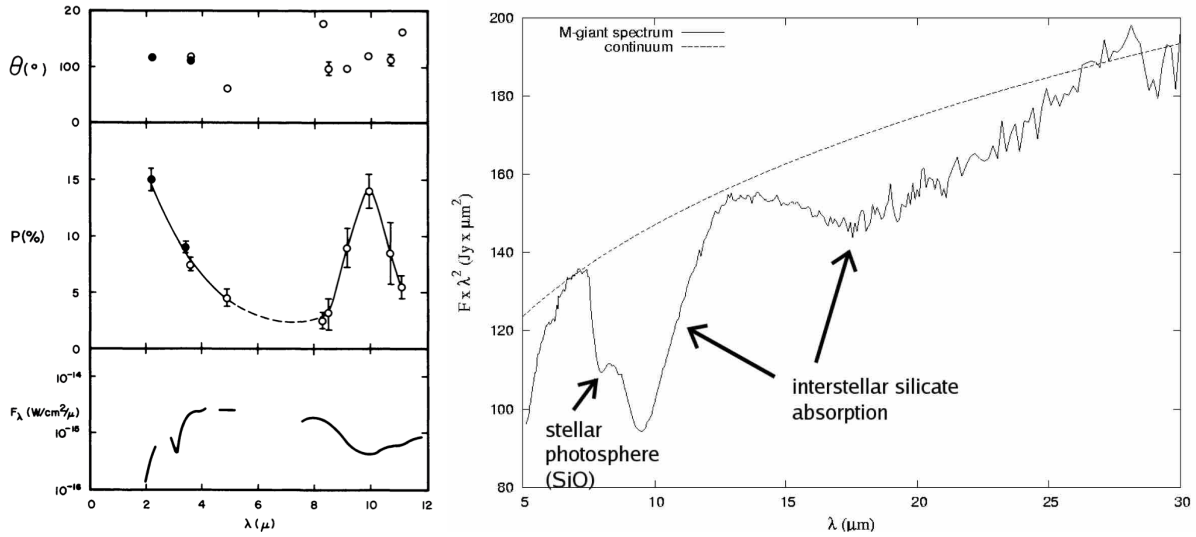

Figure 9: Left: Observed polarisation parameters as a function of the wavelength (Dyck et al., 1973). These observations were made towards the Orion nebula at the Kitt Peak National Observatory. Right: Spectrum of a giant obtained with *Spitzer*. The extinction along the line of sight towards this star is $A_V \sim 10$ (Breemen et al., 2011).

This feature is associated to the C-H stretching mode in saturated aliphatic hydrocarbons, albeit that there is no consensus about the material that contains such aliphatic hydrocarbons. It should be noted that this feature is composed of three sub-features at 3.385 μm, 3.420 μm, and 3.485 μm which are associated with the symmetric and asymmetric C-H stretches in CH_3 and CH_2 (Greenberg et al., 1995).

Polarisation observations towards the Galactic Center of this 3.4 μm absorption band (Adamson et al., 1999), revealed that this feature is barely polarised. Adamson et al., 1999 proposed that the aliphatic-rich carbonaceous component is not around silicate grains as mantles, as suggested by core-mantle models (Desert, Boulanger, and Puget, 1990; Jones, 1990; Jones et al., 2013, 2017) albeit that this was not in contradiction with a potential aromatic-rich carbonaceous mantle around silicate grains (Li and Greenberg, 2002b). However, the lack of spectropolarimetric observations at this time did not allow this statement to be confirmed. Later, observations towards the Galactic Center done by Chiar and Tielens, 2006 showed that the 3.4 μm absorption band is still essentially unpolarised but more importantly, that the 9.7 μm silicate absorption band is polarised. As a consequence, carbonaceous material around silicate grains can indeed not be aliphatic-rich. It was therefore proposed (Jones et al., 2013) that the amorphous silicate component is separated from a carbonaceous grain component that is aliphatic-rich and at the origin of the 3.4 μm absorption band (Jones, 2012a,c).

AROMATIC HYDROCARBON ABSORPTION FEATURES Two weak absorptions features at 3.3 μm and 6.2 μm (see Fig. 11), associated with aromatic hydrocarbons (Schutte et al., 1998; Chiar et al., 2000), have been observed in various environments:

- towards the galactic center for the 3.3 μm feature (Chiar et al., 2000) and the 6.2 μm feature (Schutte et al., 1998; Chiar et al., 2000);
- towards molecular clouds for the 3.3 μm feature (Sellgren et al., 1995; Brooke, Sellgren, and Geballe, 1999).

The absorption feature strengths were predicted in Li and Draine, 2001a and were consistent with the previous observations. It must also be noted that three other absorption features

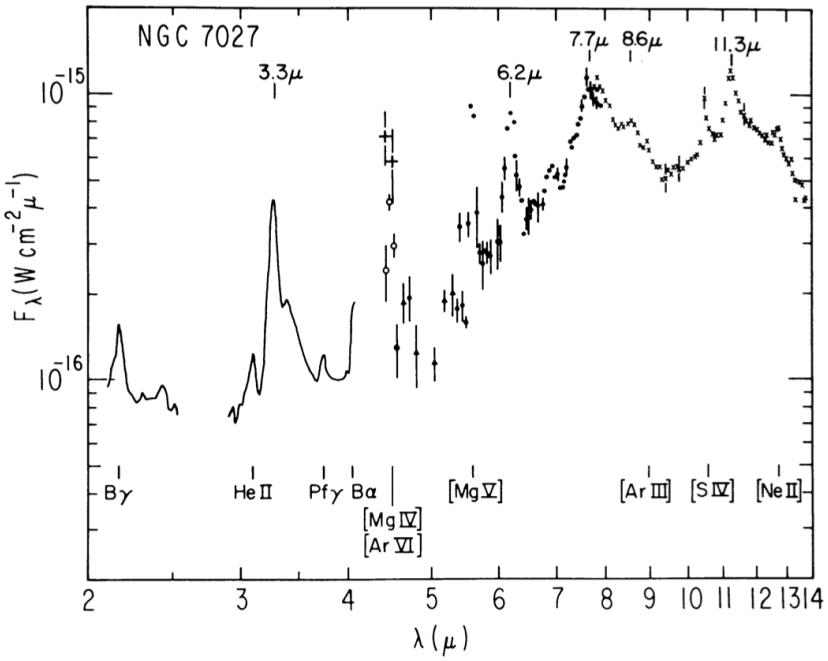

Figure 10: Spectrum of NGC 7027 from 2 to 13 μm (Willner et al., 1979). The unidentified features are marked.

at 7.7, 8.6, and 11.3 μm are also associated with the aromatic hydrocarbons but are difficult to observe in absorption because of the strong 9.7 μm silicate absorption feature.

ICE ABSORPTION FEATURES In dense and cold regions of the ISM ($n_H > 10^3$ H cm^{-3}), molecules are expected to condense onto the surface of dust grains to form ice mantles. The detection of numerous ice absorption bands such as those of H_2O, CO, CO_2, CH_3OH, NH_3, CH_4, H_2CO, and OCN^- (Ehrenfreund and Charnley, 2000), reinforced this scenario. These ices are observed in molecular clouds, in protoplanetary disk, towards the center of the Galactic Center and around evolved stars (see Boogert, Gerakines, and Whittet, 2015, and references therein)

DIFFUSE INTERSTELLAR BANDS (DIBS) In 1922, two absorption bands at 578 nm and 579.7 nm were discovered (Heger, 1922), that were significantly broader than the usual atomic interstellar absorption lines. Later, Merrill, 1934 clearly stated that these bands were unidentified. It was the beginning of one of the greatest mysteries in astrophysics, the *Diffuse interstellar bands* (DIBs). Some of these DIBs are shown in Fig. 12 (Jenniskens and Desert, 1994). So far, about 400 DIBs have been discovered (e.g. Hobbs et al., 2009) from the near-IR to the near-UV. Many efforts have been made to understand the origin of these DIBs. Among the possibilities, PAHs were proposed to explain part of these DIBs (e.g. Salama and Allamandola, 1992; Snow and Destree, 2011), as well as C_{60}^+ (e.g. Foing and Ehrenfreund, 1994; Campbell et al., 2015), C_7^- (e.g. Tulej et al., 1998), and small carbon chain molecules (e.g. Danks and Lambert, 1976; Smith, Snow, and York, 1977). It must also be noted that it has not yet been shown that these bands are polarised (e.g. Martin and Angel, 1974, 1975; Adamson and Whittet, 1992, 1995; Somerville, 1996).

It was recently established that the depletion of materials which produce DIBs is correlated with the dust extinction in dense cores (Fan et al., 2017; Elyajouri and Lallement, 2019). This could be explained by dust evolution from diffuse to dense regions.

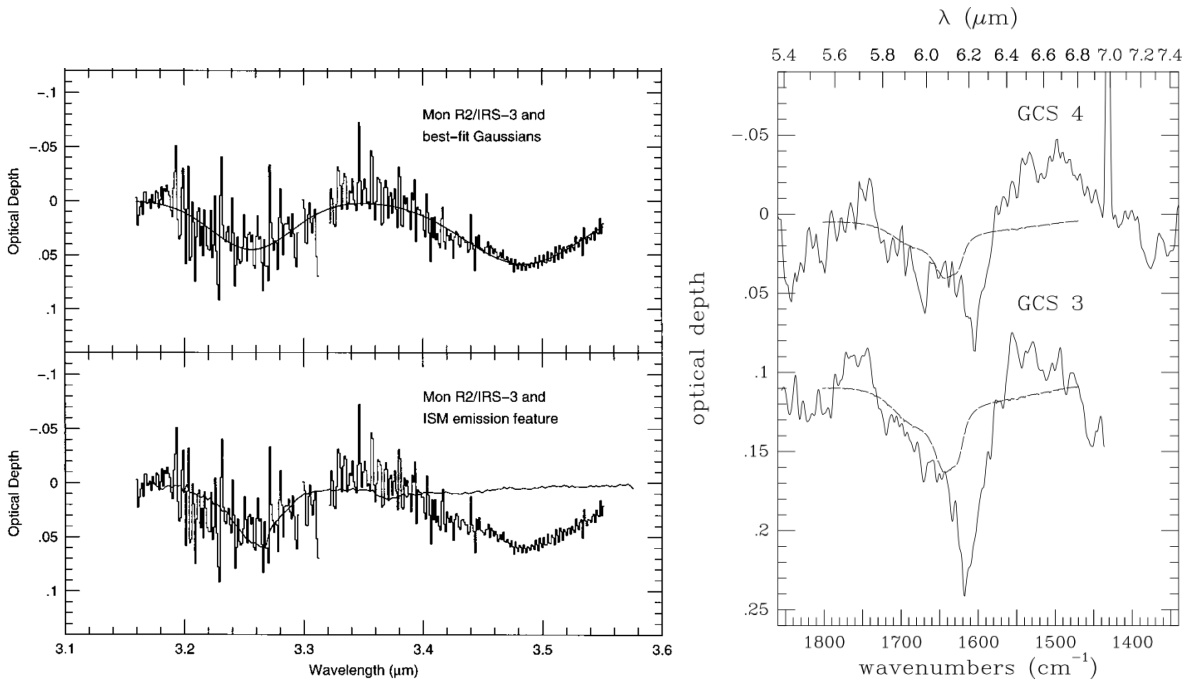

Figure 11: Top left: Optical depth between 3.16 and 3.55 μm along the line of sight towards Mon R2/IRS 3, compared to the sum of two Gaussians (solid curves), centered at 3.256 μm and 3.484 μm. Bottom left: Same but compare to the profile of the aromatic interstellar emission feature (solive curve) in IRAS 21282+5050 (Nagata et al., 1988). Figures from Sellgren et al., 1995. Right: The 6.2 μm absorption feature towards GCS 3 and GCS 4. The dashed curves indicate the expected contribution of the OH bending mode of solid H_2O expected to be present for sources which show the 3 μm absorption band. Arbitrary offsets are used. Figure from Schutte et al., 1998.

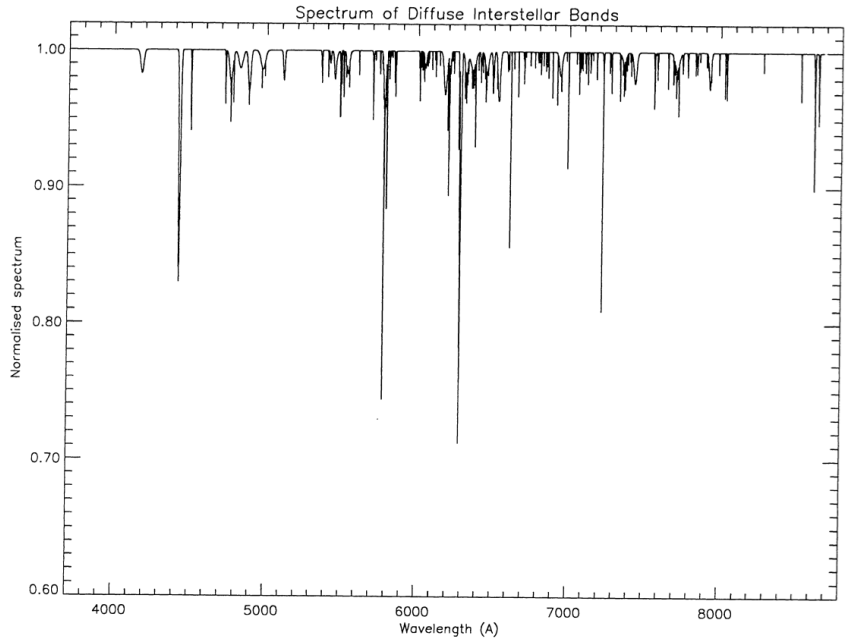

Figure 12: DIB spectrum from 400 μm to 800 μm (Jenniskens and Desert, 1994).

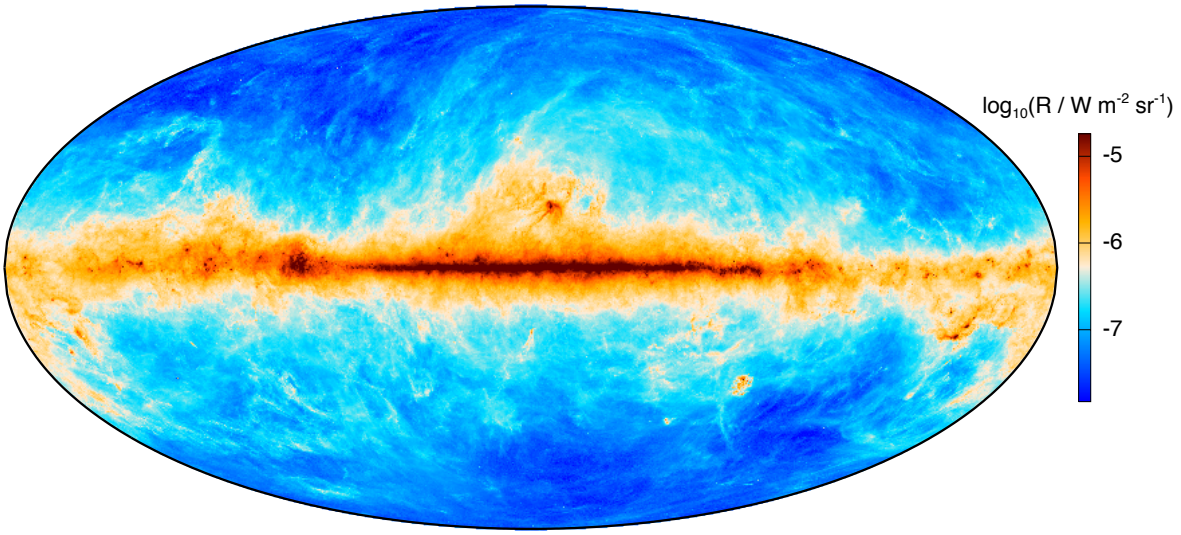

Figure 13: All-sky map of dust radiance at 5′ resolution (Planck Collaboration et al., 2014).

2.1.2 *Emission*

EMISSION FROM LARGE GRAINS THAT ARE IN THERMAL EQUILIBRIUM As we will see in Sect. 2.4.3, large grains that are in thermal equilibrium emit as a modified blackbody. Fig. 13 shows the all-sky map of dust radiance (Planck Collaboration et al., 2014). The large dynamics range in intensity is due to variations in column density and also to variations in local conditions (illumination, dust evolution). The origin of this emission is most likely due to both amorphous silicate and carbonaceous grains but their relative contributions are still much debated.

AROMATIC EMISSION In the near- and mid-IR, several features (3.3, 6.2, 7.7, 8.6, 11.3, and 12.7 μm, see Fig. 14) were observed for the first time in the spectrum of planetary nebulae (Gillett, Forrest, and Merrill, 1973). At this time, there were no satisfactory explanations for the origin of these bands hence they were called *unidentified infrared* (UIR) bands. Later, these bands were associated to aromatic-rich hydrocarbons (Duley and Williams, 1981) and most particularly, to PAHs (Leger and Puget, 1984; Allamandola, Tielens, and Barker, 1985). As these bands originate from stochastically heated small aromatic-rich hydrocarbons, they are called *Aromatic Infrared Bands* (AIBs) (Allamandola, Tielens, and Barker, 1989). These bands have been observed in numerous environments:

- planetary nebulae (e.g. Peeters et al., 2002)
- reflection nebulae (e.g. Moutou et al., 1999; Peeters et al., 2002)
- HII regions (e.g. Hony et al., 2001; Peeters et al., 2002)
- circumstellar envelopes (e.g. Peeters et al., 2002; Geers et al., 2006)
- external galaxies (e.g. Genzel et al., 1998; Peeters et al., 2002; Regan et al., 2004; Brandl et al., 2006; Armus et al., 2007; Smith et al., 2007)
- protoplanetary disks (e.g. Acke and Ancker, 2004; Boutéraon et al., 2019)

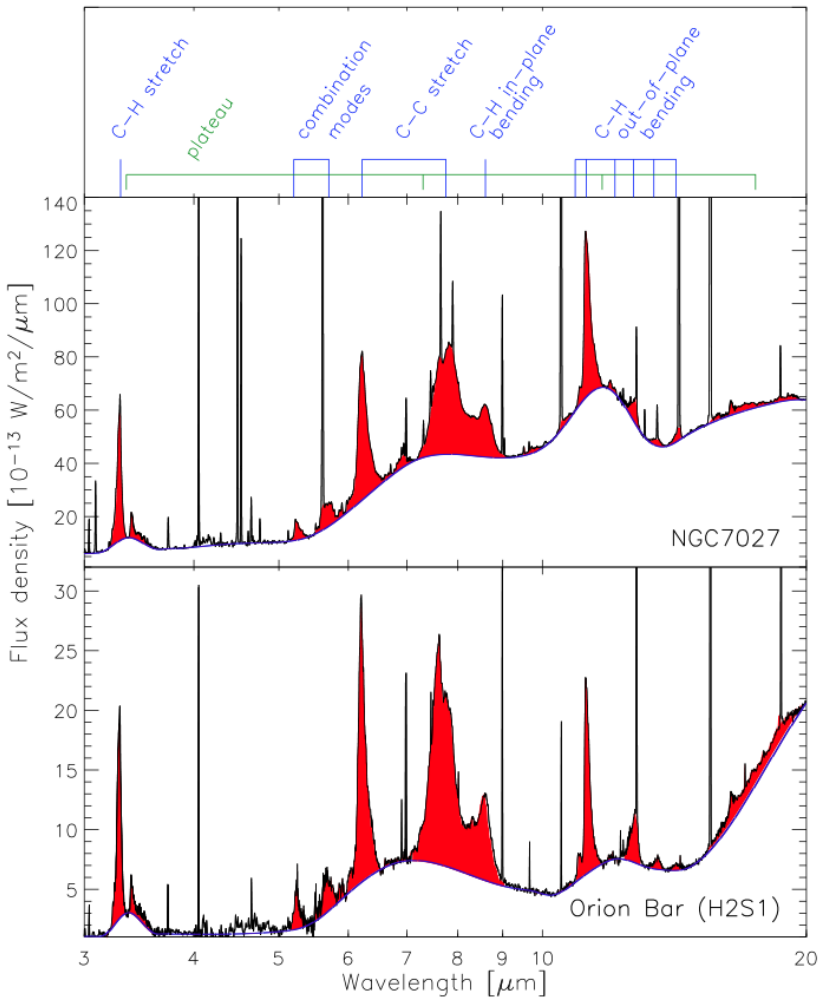

Figure 14: Top: Mid-infrared spectra of NGC 7027. Bottom: Mid-infrared spectra of the photon-dissociation region in the Orion Bar. The vibrational modes of PAHs associated with the different AIBs are showed on the top of the figure. Figure from Tielens, 2008 and Peeters et al., 2002.

- photon-dominated regions (e.g. Verstraete et al., 1996; Burton et al., 2000; Verstraete et al., 2001; Abergel et al., 2002; Compiègne et al., 2007) and more references in Sect. 2.2.

Tielens, 2008 gave a detailed review of AIBs. As we will see in Sect. 2.2, these bands are very useful to probe PDRs.

ALIPHATIC EMISSION The emission of aliphatic-rich hydrocarbons is dominated by a strong emission band at 3.4 μm, itself composed of sub-structures at 3.4, 3.46, 3.51, and 3.56 μm (Muizon, D'Hendecourt, and Geballe, 1990). These signatures are associated with aliphatic-rich carbonaceous hydrocarbons (Duley and Williams, 1983). Two features at 6.9 and 7.3 μm are also associated with this component (Kwok, Volk, and Hrivnak, 1999).

It is interesting to note that the band ratio between the aromatic emission at 3.3 μm and the aliphatic emission at 3.4 μm can be used to study the aromatic to aliphatic dust ratio in different environments such as protoplanetary disks (e.g. Boutéraon et al., 2019) and in PDRs (e.g. Chiar et al., 2013).

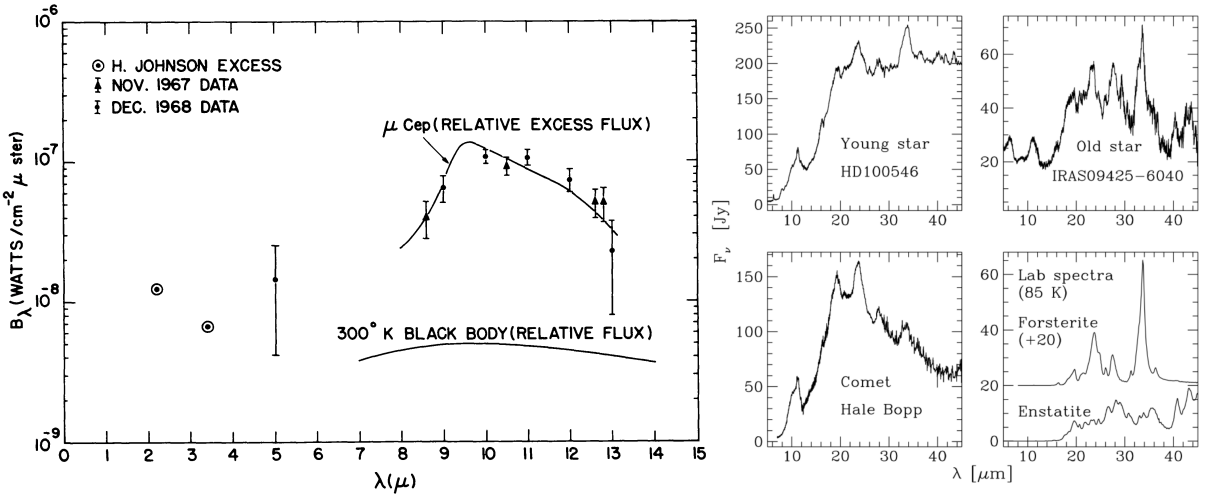

Figure 15: Left: Dust emission observed from Trapezium region as a function of wavelength (Stein and Gillett, 1969). Right: IR emission spectra around stars and of the Hale-Bopp comet, where crystalline features of silicates can be found (Molster and Kemper, 2005).

SILICATE EMISSION Silicate emission is dominated by the two strong bands at 9.7 μm (see Fig. 15, left panel) and 18 μm, associated with amorphous silicates. However, observations of oxygen-rich cool giants (e.g. Kemper, Vriend, and Tielens, 2004; Molster and Kemper, 2005; Wright, Do Duy, and Lawson, 2016) showed that silicate grains that are forming in the atmosphere of such stars are composed of two populations, amorphous and crystalline silicates. The signatures of crystalline silicates around stars can be found in Fig. 15 (right panel) (Molster and Kemper, 2005). As discussed previously, because silicates are found in their amorphous form in the ISM, there are processes that transform them from their crystalline to their amorphous form in the ISM (Demyk et al., 2001).

EXTENDED RED EMISSION (ERE) Discovered in 1980 in the Red Rectangle (Schmidt, Cohen, and Margon, 1980), the *extended red emission* is a broad emission band that covers part of the visible and near-IR (from 540 μm to 900 μm, see Fig. 16). This emission has been observed in various environment such as the diffuse ISM (Witt et al., 2008), HII regions (Darbon et al., 2000), reflection nebula (Witt and Boroson, 1990), and planetary nebula (Furton and Witt, 1990). The ERE is generally attributed to dust heated photoluminescence (Witt et al., 2006) but could also be due to both photoluminescence and thermal emission (Duley, 2009). With the aim of understanding the origin of the *extended red emission*, different materials have been proposed:

- hydrogenated amorphous carbons (HACs) (e.g. Duley, 1985; Witt and Schild, 1988; Witt and Boroson, 1990);
- polycyclic aromatic hydrocarbons (PAHs) (e.g. D'Hendecourt et al., 1986; Vijh, Witt, and Gordon, 2005; Berné et al., 2008);
- laboratory-synthesized quenched carbonaceous composite (QCC) (e.g. Sakata et al., 1992);
- C_{60} (e.g. Webster, 1993);
- coal (Papoular et al., 1996);
- carbon nanoparticles (e.g. Seahra and Duley, 1999);

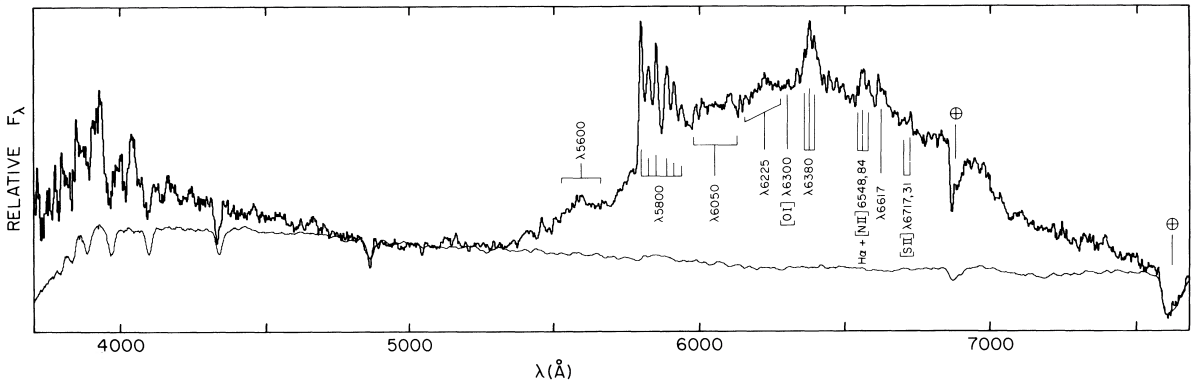

Figure 16: Spectra of HD 44179 and its associated nebulosity (Schmidt, Cohen, and Margon, 1980).

- crystalline silicon nanoparticles (e.g. Ledoux et al., 1998; Witt, Gordon, and Furton, 1998);
- nanodiamonds (e.g. Chang, Cuppen, and Herbst, 2006)

Whereas, due to their high photoluminescence efficiency, PAHs were a good candidate to explain the ERE, observations show that the ERE and the PAH emission were not spatially correlated (Perrin and Sivan, 1992; Kerr et al., 1999; Darbon et al., 2000) which diminished the PAHs ability to explain the ERE. This was also reinforced by the observation that there is no PAH emission in the Bubble Nebula albeit ERE is observed (Sivan and Perrin, 1993).

2.2 EVIDENCE FOR DUST EVOLUTION IN THE UNIVERSE

Some of the first evidence for dust evolution was shown by Fitzpatrick and Massa, 1986 through the variation in the 217.5 nm interstellar bump (see Fig. 17) from diffuse ($R_V = 3.1$) to denser regions (up to $R_V \sim 5.5$). Similarly, other studies (e.g. Cardelli, Clayton, and Mathis, 1989; Cardelli and Clayton, 1991; Campeggio et al., 2007) found the same variations, which were for the first time explained by Kim, Martin, and Hendry, 1994 as due to a decrease in the carbonaceous nano-grain abundance (relative to the gas) together with an increase in larger grain abundance.

It is also possible to follow dust evolution from its emission in the mid-IR (from stochastically heated nano-grains) and in the far-IR (where large grains in thermal equilibrium emit). This has led to a wealth of studies (e.g. Boulanger et al., 1990; Laureijs, Clark, and Prusti, 1991; Abergel et al., 1994; Bernard et al., 1999; Stepnik et al., 2003; Flagey et al., 2009, ...) revealing that nano-grains disappear in dense regions as they coagulate onto larger grains. Dust evolution is also highlighted by variations in its far-IR opacity as a function of the local environment (e.g. Juvela et al., 2011; Planck Collaboration et al., 2011a; Martin et al., 2012; Roy et al., 2013; Ysard et al., 2013; Juvela et al., 2015; Köhler, Ysard, and Jones, 2015, ...), which has been explained with dust coagulation and the accretion of ice mantles. This scenario is supported by numerical simulations of dust evolution in dense regions (e.g. Ossenkopf and Henning, 1994; Ormel et al., 2011; Köhler, Ysard, and Jones, 2015).

Photon-dominated regions (PDRs) (Hollenbach and Tielens, 1997, 1999) correspond to the interface between HII regions and molecular clouds that are irradiated by energetic stars that are located close by. In these regions, the physical conditions vary widely, and hence PDRs are a unique place to study how do dust, gas, and local physical conditions evolve with depth, we will talk in more details about such regions in Sect. 3.

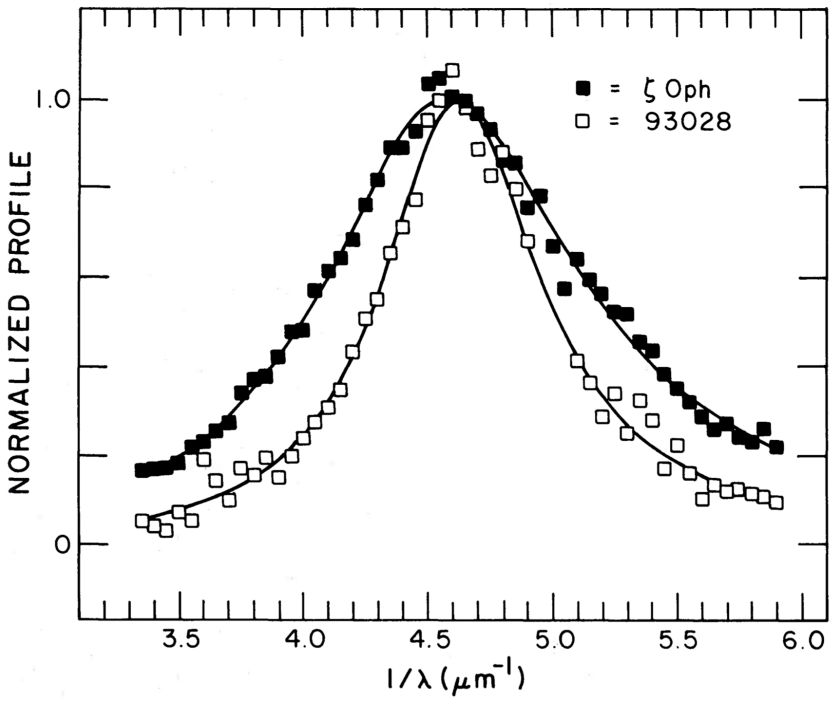

Figure 17: Normalised extinction profiles for the broadest and narrowest bumps in the extinction profiles sample of (Fitzpatrick and Massa, 1986).

We describe here non-exhaustively, the evidence for dust evolution in different environments, such as PDRs (see Sect. 2.2.1), galaxies (see Sect. 2.2.2), dark clouds (see Sect. 2.2.3), and other environments like supernova remnants and star forming regions (see Sect. 2.2.4).

2.2.1 *Dust evolution in PDRs*

The mid-IR spectrum of PDRs presents a wealth of emission features overlying the continuum emission (e.g. the Orion Bar spectrum shown in the bottom panel of Fig. 14) which has been extensively analysed in several PDRs using the *Infrared Space Observatory* (ISO) and *Spitzer* data. Strong variations in the spectra have been found across PDRs and between PDRs.

Based on ISO spectroscopy with the SWS spectrograph of the Orion bar, Peeters et al., 2002 showed that the variation in the features in the $6-9$ μm spectral range (emission bands at 6.0, 6.2, 6.6, 7.0, 7.7, 8.3, and 8.6 μm) are linked with variations in the local physical conditions but also with both formation and evolution processes associated with PAHs. Using mid-IR spectra of NGC 7023 obtained with both *ISO* and *Spitzer*, Peeters et al., 2004 showed that observed spectroscopic variations in the $15-21$ μm spectral range could be due to variations in PAHs abundance.

Rapacioli et al., 2006 theoretically studied mechanisms that lead to the formation and destruction of coronene clusters, under interstellar conditions and especially in PDRs. They found that almost all the collisions lead to cluster growth and that they are thermally photoevaporated much faster than they are reformed, hence it is difficult for coronene clusters to exist in such regions. These mechanisms of grain destruction are very important to understand how dust evolves in such regions.

From imaging and spectroscopic observations with ISOCAM ($5-16$ μm) Abergel et al., 2002 showed that at the illuminated edge of Orion B, there is a systematic decrease in the intensity of the aromatic features (especially at 7.7 μm) relative to the continuum inside the

shielded molecular regions compared to the photo-dissociated and photo-ionised regions. In parallel, Rapacioli, Joblin, and Boissel, 2005 have decomposed ISOCAM spectroscopic observations of NGC 7023 and ρ Oph-SR3 into different spectral components, including cationic PAHs, neutral PAHs and carbonaceous nano-grains. This approach was extended using $5-35$ μm *Spitzer* observations of other PDRs (Ced 201, NGC 7023 East and North-West, ρ Ophiuchi West filament) by Berné et al., 2007. These studies conclude that variations in the mid-IR spectra can be explained by the photodestruction of nano-grains into free PAHs.

Benefiting from the wide range of spatially resolved objects observed with *ISO* and *Spitzer*, including PDRs, Magellanic H II regions, and galaxies of various types, Galliano et al., 2008 found that albeit the 6.2, 7.7, and 8.6 μm emission bands are correlated, the ratio between those bands and the 11.3 μm emission band can vary up to an order of magnitude. They proposed that these variations are due to variation in the relative abundance of ionised PAHs, due to the photoprocessing induced by the intense UV radiations at the irradiated part of the Orion bar.

With the arrival of *Herschel* observing in the far-IR, it was possible to study the emission of large grains in thermal equilibrium together with the emission of stochastically heated nano-grains already observed with *ISO* and *Spitzer*. In the East region of the PDR NGC 7023 and combining *Herschel* and *Spitzer* data, Abergel et al., 2010 have shown that the emission of stochastically heated nano-grains is overestimated by a factor ~ 2, which suggests an overestimation of the nano-grain abundance with respect to the large grain abundance. This could be due to the photodestruction of nano-grains by intense UV photons in the irradiated part of the PDR. This was later reinforced by a multi-PDR study done by Pilleri et al., 2012. They indeed found using the fitting tool PAHTAT applied to Spitzer spectra of NGC 2023, NGC 7023 and ρ Oph, that the nano-grain abundance decreases with an increase in the local UV radiation field, which strongly suggests that nano-grains are photodestroyed by UV photons. A similar result was found in Andrews et al., 2015 as they showed, based on mid-IR spectra with *Spitzer* of NGC 7023, NGC 2023, and NGC 1333, that the PAHs abundance decreases with an increase in the UV radiation field, which they interpret in terms of PAHs photodestruction by UV photons.

arab_evolution_2012_paper showed that a decrease in the PAH abundance together with an increase in the larger grain emissivity, fits well the Spitzer and Herschel observations of the Orion bar. This can be explained as PAHs are photodestroyed and/or they coagulate onto the surface of larger grains hence increasing their emissivity.

Evidence for grain coagulation in PDRs were later highlighted in other studies. For instance, a multiwavelength study of IC 434 (Ochsendorf and Tielens, 2015) exhibited a bimodal dust grain distribution in this region, which they interpreted as grain coagulation into large porous grains or fluffly aggregates. Also, mid-IR photometry with SOFIA of the Orion Bar and the Orion HII region (Salgado et al., 2016) required coagulated grains to explain the decrease by a factor 5 to 10 of the UV and infrared dust opacities from the diffuse ISM to these PDRs.

Evidence of dust evolution has also been shown in IC 63 by Van De Putte et al., 2019 based on extinction mapping from the UV to the near-IR (that is, from 275 nm to 1.6 μm).

2.2.2 *Dust evolution in galaxies*

Based on TIMMI2 observations in the N-Band (813 μm) on the ESO 3.6 m telescope, Martín-Hernández et al., 2006 studied three starburst galaxies (NGC 3256, the dwarf galaxy II ZW 40, and the WR galaxy He 2-10). They found a dependence between the PAH emission and the hardness of the radiation field. When the [S IV]/[Ne II] ratio, that is proportional to the hardness of the radiation field, is smaller than 0.35, PAH emission is observed whereas it is

not observed when the [S IV]/[Ne II] ratio is larger than 0.35. Albeit the simplest explanation would be that PAHs are efficiently photodestroyed by UV photons, they also proposed that these UV photons can be absorbed by dust grains before reaching PAHs and therefore, cause a low PAH emission. More recently, Relaño et al., 2018 used IR and submm observations (*Spitzer* and *Herschel*) of the whole disc of M33 and found that the nano-grains abundance increases with a decrease of the large grains abundance at high values of H_α. As H_α emission is proportional to the UV radiation field, it would mean that UV photons efficiently erode large grains into nano-grains.

Bernard et al., 2008 used *Spitzer* and *IRAS* observations of the Large Magellanic Cloud (LMC) and found that the 70 μm emission increases from the Milky Way, to the LMC and then, to the Small Magellanic Cloud (SMC). As dust emission at 70 μm is dominated by large grains, they proposed that there are more nano-grains in the Milky Way than in both the LMC and the SMC. They argued that large grains are likely to be eroded in the diffuse ISM as they are not shielded from UV photons, as they could be in high density regions such as the LMC and the SMC. This scenario is reinforced by Chastenet et al., 2019 as they found, based on *Spitzer* and *Herschel* observations, that the PAH abundance is larger in the diffuse ISM than in both the LMC and the SMC, which could be due to efficient PAH production by fragmentation of large grains and/or growth of PAHs in the molecular gas.

Another study of the gas-to-dust ratio in the LMC and the SMC (Roman-Duval et al., 2014), based on *Herschel*, HI 21 cm, CO, and H_α observations, showed that the slope of the dust-to-gas ratio in the LMC and the SMC is lower by a factor ~ 2 than in the diffuse ISM. They stated that it could be due to the coagulation of dust grains and/or the accretion of gas-phase metals onto dust grains.

2.2.3 *Dust evolution in dark clouds*

Based on infrared and optical photometry, as well as on measurements of the wavelength dependence of polarisation in the ρ Oph cloud, Carrasco, Strom, and Strom, 1973 found that grains are larger in the higher density regions of this cloud. They argued that this increase in dust size probably results from depletion of heavy elements from the gas on the grain surface. Later, this scenario was reinforced as Jura, 1980 found that the opacity in the visible towards ρ Oph is lower than the opacity in the diffuse ISM, which he interpreted in terms of grain coagulation. Later, Cardelli, Clayton, and Mathis, 1989 observed in ρ Oph and Nu Ori that the extinction per H nucleus integrated over the UV to the near-IR spectral range (0.125 μm to 3.4 μm) is lower than in the diffuse ISM. They claimed that grains are larger in dense clouds, because of grain coagulation instead of accretion of mantles.

Using *IRAS* observations of molecular clouds in the Chameleon, Taurus, and Ursa Majors complexes, Boulanger et al., 1990 showed that the 12 μm emission band from stochastically heated nano-grains does not follow the spatial distribution of the 100 μm emission from larger grains. They showed that the strong variations in the ratio between the emission in these two bands cannot be explained by variation in the UV radiation field. To explain such variations, they argued that these are due to variations in the ratio between the abundance of nano-grains that are stochastically heated and the abundance of large grains. They proposed a scenario where nano-grains condensed on the surface of large grains, before being photo-processed into aromatic-rich grains. This scenario was reinforced as Laureijs, Clark, and Prusti, 1991 showed, based on *IRAS* observations of dark clouds containing L134, L183, and L1780, that the 100 μm emission band was detected in some regions where the 60 μm emission band was not detected. They proposed that a thin mantle can condensate on dust grains in the transition layer between low density regions and high density regions.

Benifiting from *Spitzer* data, Flagey et al., 2009 observed the Taurus complex and found that the FIR dust opacity is larger by a factor ~ 2 than the average value for the diffuse ISM. Moreover, they found that the IR emission varies throughout the filamentary structure in this complex. They argued that these variations could be explained by both variation in the radiation field and abundances of PAHs and nano-grains. Later, a filament of the Taurus complex (L1506) was observed with *Herschel* (Ysard et al., 2013). The authors had to increase the grain opacity to simultaneously fit both the near-IR extinction and the *Herschel* emission. They stated that this could be explained by the coagulation of dust grains to form fluffy aggregates, which makes sense because of the high density ($n_H > 10^3$ H cm^{-3}) in such starless dense regions.

Grain growth was also invoked in other dark clouds to explain the *Spitzer* observations. Indeed, variations in the mid-IR extinction law (3.6 to 24 μm) obtained with *Spitzer* in three dark clouds (Ophiuchus, Perseus, and Serpens), were explained in terms of grain growth (Chapman et al., 2009). Later, the Coalsack nebula, a starless dense cloud, was observed with *Spitzer* at five different positions in order to cover the disparity in physical conditions in this dark cloud (Wang et al., 2013). They showed that the color-excess decreases from diffuse to dense regions of this nebula, which they explained in terms of dust growth from diffuse to dense regions. This was reinforced as Köhler et al., 2012 who showed that the coagulation of small grains ($a = 3.5$ nm) onto the surface of grain aggregates (that are composed of four large grains with $a = 60$ nm), can explain both the increase in the far-IR dust opacity and the decrease in dust grain temperature, from diffuse to dense regions.

Formation of ice around grains was also considered in dense cloud. Indeed, based on *Spitzer* observations of stars behind dark clouds, McClure, 2009 showed that the variation in the shape of the extinction curves could be due to coagulation of ice-mantled grains, rather than ice-mantled grains alone. This scenario was reinforced as Köhler, Ysard, and Jones, 2015 studied the influence of using grain aggregates (with or without an ice mantle) in dense regions instead of using diffuse ISM-like grains. They showed that using aggregates instead of diffuse ISM-like dust, implies an increase in the far-IR opacity by a factor of 3, up to 7 if using aggregates with an ice mantle. They conclude that dust evolution through coagulation and accretion can explain the observed variations in the dust emission, from the diffuse ISM to denser regions.

2.2.4 *Dust evolution in other environments*

Spitzer observations of both Puppis A, a supernova remnant, and its neighboring molecular cloud, showed that almost all the PAHs, as well as 25% of the carbonaceous and silicate dust mass, have been destroyed due to the shock wave (Arendt et al., 2010). This phenomenon has also been observed with IR spectro-imagery observations of SN 1006, another supernova remnant. Indeed, a large decrease in the IR emission after the shock wave has passed strongly suggests large grain destruction through sputtering (Winkler et al., 2013).

Evidence for dust evolution in star forming regions have also been found. Flaherty et al., 2007 used *Spitzer* observations to determine IR extinction laws towards five star forming regions (Orion A cloud, NGC 2069/71, NGC 2024/23, Serpens, and Ophiuchus). They found that the extinction laws were similar but different from those towards the diffuse ISM. They argued that it could be due to an evolution of dust properties from the diffuse ISM to dense regions of the ISM. This was later reinforced as spectroscopic observations from the mid-IR to the far-IR towards a star forming region, revealed that the mid-IR to far-IR extinction law flattens with an increase of the mass surface density (Lim, Carey, and Tan, 2015). They stated

that this may highlight that grains are growing from diffuse to dense regions and that ice mantle can form around these grains.

2.2.5 *Summary*

From all the above evidence it is clear that dust evolves, primarily as a result of fragmentation and growth processes [2]. Because of the larger number of events, dust evolution is more efficient (faster) in star forming regions where strong density and radiation fields prevail. In such regions and in order to identify the true dust evolution signatures, the radiative transfer problem must be treated accurately using a 3D matter distribution. This program has guided this PhD project and is discussed in the Chapter v.

2.3 DUST OPTICAL PROPERTIES

In astrophysics, the bulk of the information that we gather stems from light. Since interstellar dust interacts efficiently with light, it is essential to describe how these dust grains interact with radiation.

2.3.1 *Dust absorption and scattering efficiencies*

The Maxwell electromagnetic equations describe how matter interacts with an electromagnetic field. Within the framework of Mie's theory, it is possible to find a solution to these equations, for an electromagnetic wave interacting with a spherical particle.

When a spherical particle interacts with an oscillating electric field $E(r,t) = E_0(r)e^{-i\omega t}$, the response of the particle can be characterized by a complex dielectric function:

$$\epsilon(\omega) = \epsilon_1(\omega) + i\epsilon_2(\omega), \tag{11}$$

where $\omega = 2\pi c/\lambda$ is the angular frequency. The complex dielectric function is related to the complex refractive index $m(\omega) = n + ik$ by $m^2 = \epsilon$. Whereas k can be inferred from absorption measurements of the material through the parameter $\alpha = 2\pi k/\lambda$, the corresponding n is usually calculated using the Kramers-Kronig relation:

$$n(\omega) = \frac{1}{\pi} P \int_{-\infty}^{+\infty} \frac{k(\omega')}{\omega' - \omega} d\omega', \tag{12}$$

where P is the principal value of the integral.

Knowing the refractive index, is it possible to compute the absorption and scattering efficiencies, using codes such as BHMIE (Bohren and Huffman, 2004) or based on the discrete dipole approximation (DDA) for non-spherical particles (Draine, 1988; Draine and Flatau, 1994) but the latter computations are time consuming. However, at long wavelengths one can use an analytical expression to calculate the absorption and scattering efficiencies in the Rayleigh approximation (i.e. $x = 2\pi a/\lambda << 1$):

$$Q_{abs} = 4\,x\,\mathrm{Im}\left(\frac{m^2-1}{m^2+2}\right), \tag{13}$$

2 Other dust transformations also occur meanwhile such as aliphatic to aromatic transition in carbon grains or cristalline to amorphous transition in silicate grains.

$$Q_{sca} = \frac{8}{3} x^4 \left| \frac{m^2 - 1}{m^2 + 2} \right|^2 . \tag{14}$$

If $(m^2 - 1)/(m^2 + 2)$ varies little with the wavelength, Eq. (13) and Eq. (14) can be simplified as follows:

$$Q_{abs} \propto x \qquad \text{and} \qquad Q_{sca} \propto x^4. \tag{15}$$

2.3.2 *Dust anisotropy factor*

2.3.2.1 *Definition*

Based on observations across the Milky Way, obtained to verify the existence of diffuse interstellar radiation, Henyey and Greenstein, 1941 introduced a function that allows us to determine, from one parameter $-1 < g < +1$ (that will be later called the *anisotropy factor*), the probability $p(\theta)$ that a photon is scattered by an angle[3] θ. This function is defined as follows:

$$p(\theta) = \frac{1}{4\pi} \frac{1 - g^2}{(1 + g^2 - 2\, g\, \cos(\theta))^{3/2}}. \tag{16}$$

This function is normalized, so that the integral over 4π steradians is unity:

$$\int_\Omega p(\theta)\, d\Omega = \int_{\Phi=0}^{2\pi} \left(\int_{\theta=0}^{\pi} p(\theta)\, \sin(\theta)\, d\theta \right) d\Phi = 1. \tag{17}$$

Eq. (16) can also be written as a function of $\mu = \cos(\theta)$:

$$p(\mu) = \frac{1}{2} \frac{1 - g^2}{(1 + g^2 - 2\, g\, \mu)^{3/2}}. \tag{18}$$

The probability of forward scattering (i.e. $\theta = 0$, $\mu = 1$) is $p(\mu = 1) = (1 - g^2)/2(1 - g)^3$ whereas the probability for backward scattering (i.e. $\theta = \pi$, $\mu = -1$) is $p(\mu = -1) = (1 - g^2)/2(1 + g)^3$. Thence, we can define the following ratio:

$$\frac{p(\mu = 1)}{p(\mu = -1)} = \left(\frac{1 + g}{1 - g} \right)^3, \tag{19}$$

which is larger than the unity in the case of a forward scattering and smaller than the unity in the case of a backward scattering. If this ratio is equal to the unity, the scattering is therefore isotropic. Thus:

- if $g > 0$: forward scattering;
- if $g < 0$: backward scattering;
- if $g = 0$: isotropic scattering.

Whilst $p(\theta)$ is simple, it is a widely used approximation because it has a simple development in Legendre polynomials which allows analytical calculations impossible to do otherwise.

3 The angle θ is formed by the trajectory of the incident photon and the trajectory of the scattered photon.

Figure 18: Left: The reflection nebula IC2118, also known as the *witch nebula*. Credit: NASA/STScI Digitized Sky Survey/Noel Carboni. Right: The reflection nebula NGC 1999 observed with the Hubble's Wide Field Planetary Camera 2 (WFPC2). Credits: NASA and The Hubble Heritage Team (STScI).

2.3.2.2 *Application to 1D parallel plane geometry*

It is useful, while studying the interactions between dust and photons in a 1D plane-parallel geometry (see Sect. 7.2), to introduce the backward scattering cross section $\sigma_{\nu,b}$ defined as follows:

$$\sigma_{\nu,b} = \sigma_\nu \int_{\frac{\pi}{2}}^{\pi} p(\theta) \sin(\theta) d\theta, \tag{20}$$

where σ_ν is the scattering cross section (see Eq. (60)), and $p(\theta)$ the probability that a photon is scattered towards a direction determined by the angle θ (see Eq. (16)).

Using the commonly accepted value of the anisotropy factor for the diffuse ISM, that is $g = 0.6$ (Witt, Friedmann, and Sasseen, 1997; Schiminovich et al., 2001), the result of the previous equation indicates that 88 % of photons are forward scattered and 12 % that are back scattered.

2.4 GRAIN TEMPERATURES

In the ISM, interactions between dust grains and photons or through collisions with gas species lead to an increase in the temperature of the grains. In irradiated regions such as PDRs, dust heating is dominated by the absorption of photons and that due to collisions is negligible in comparison.

The irradiation of a grain leads to the elevation of an electron into an excited electronic state. Thence, different scenarios (see Fig. 19) are possible:

- where the energy of the photon is large enough, the dust grain can fragment or loose an energetic electron that can heat the gas (photoelectric effect);

- the grain can radiatively decay by electronic transitions whose energy is at most that of the absorbed photon. This process is called *fluorescence*;
- alternatively, the energy absorbed by the grain can decay, via non-radiative transitions, to the vibrational levels of underlying electronic states, a process called *internal conversion*.

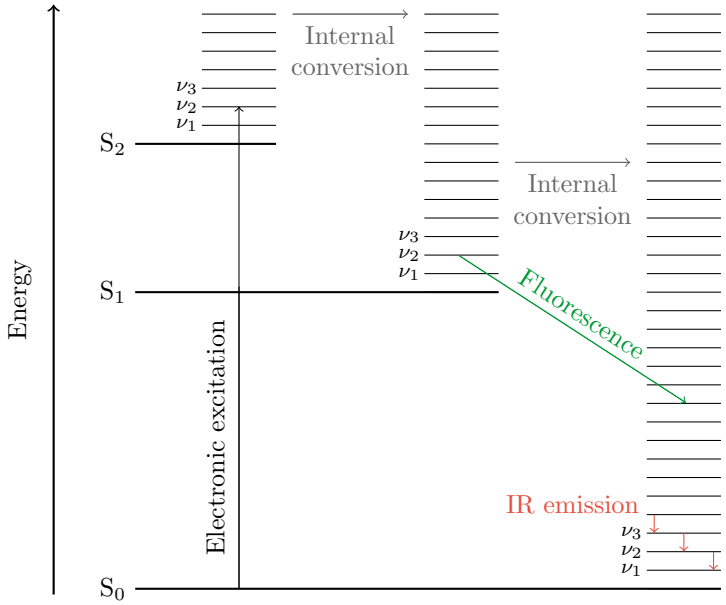

Figure 19: Representation of the main electronic mechanisms (excitation, internal conversion, fluorescence, IR emission) in a particle.

2.4.1 *Dust heating and cooling rates*

Assuming that the internal conversion is the dominant mechanism among these three processes, the heating rate of a dust grain, $P_{abs}(a)$, by the absorption of radiation can be written as follows:

$$P_{abs}(a) = \left(\frac{dE}{dt}(a)\right)_{abs} = \int_0^{+\infty} J_\nu \, \pi a^2 \, Q_{abs}(a, \nu) \, d\nu, \tag{21}$$

where J_ν is the intensity of the radiation absorbed by a grain with a radius a and $Q_{abs}(a, \nu)$, the absorption efficiency of this grain.

The internal conversion is followed by an energy cascade that ends up with vibrational (and rotational) excitation of the electronic ground state which leads to emission from active vibrational modes, as observed (IR bands between 3 and 20 µm). The radiative cooling associated with the infrared emission of a grain with radius a, can be expressed as follows:

$$P_{em}(a, T_d) = \left(\frac{dE}{dt}(a, T_d)\right)_{em} = \int_0^{+\infty} 4\pi \, B_\nu \, (T_d) \, \pi a^2 \, Q_{abs}(a, \nu) \, d\nu, \tag{22}$$

where $B_\nu \, (T_d)$ is the blackbody radiation intensity for a dust grain with a temperature T_d.

2.4.2 *Equilibrium temperature and stochastically heated grains*

From the above, it is possible to define the equilibrium temperature, T_{eq}, which corresponds to the dust temperature at which the cooling of the grain is equal to the heating. We find this temperature by solving the following equation:

$$P_{em}(a, T_{eq}) = P_{abs}(a). \tag{23}$$

Fig. 20 shows the radiative cooling rate, P_{em}, as a function of the grain temperature and the radiative heating rate, P_{abs}, which does not depend on the dust grain temperature. These rates, as well as quantities that will be defined later, are obtained for a-C:H/a-C grains (see Sect. 6). We also show in this figure, the equilibrium temperature, T_{eq}, as a function of the grain radius, a, obtained numerically by solving Eq. (23). Note that the larger a grain, the smaller its equilibrium temperature. This is expected as the number of internal modes increases with the dust size hence the absorbed energy will be spread over more modes. A larger grain will therefore not heat up as much as a smaller grain would, for a given absorbed energy.

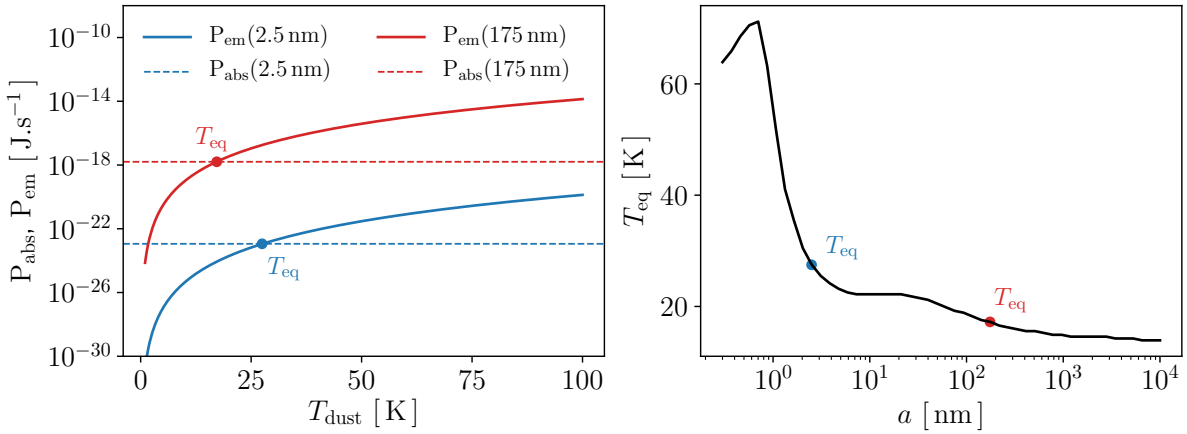

Figure 20: Left: Radiative cooling rate, P_{em}, as a function of the grain temperature for a radius of a = 2.5 nm (blue line) and 175 nm (red line). Radiative heating rate, P_{abs}, is shown in horizontal dashed line for a = 2.5 nm (blue dashed line) and 175 nm (red dashed line). These rates are obtained for a-C:H/a-C grains (see Sect. 6) and for a standard ISRF with G_0 =1. Right: Equilibrium temperature, T_{eq}, as a function of the grain size.

The relation between the internal energy of a grain and its temperature is given by its heat capacity. When a grain reaches its equilibrium temperature, it is possible to determine its internal energy, E_{int}, defined as follows:

$$E_{int}\left(a, T_{eq}(a)\right) = \int_0^{T_{eq}(a)} C\left(a, T\right)\, dT, \tag{24}$$

where $C\left(a, T\right)$ is the heat capacity of a grain with a radius a at temperature T and $T_{eq}(a)$, the equilibrium temperature of a grain with a radius a (see Fig. 20, right panel).

Fig. 21 shows the heat capacity for a grain size varying from a = 0.3 nm to a = 10^3 nm, as well as the internal energy as a function of the grain size. One can see that for a given temperature, the heat capacity increases with the dust size, meaning that a larger grain will store more thermal energy than a smaller grain that is at the same temperature. Also, regardless of

the grain size, the heat capacity increases with the temperature, meaning that the warmer a grain, the larger its thermal energy. The internal energy has been computed with the equilibrium temperatures showed in Fig. 20. It is interesting to compare the internal energy to the mean energy per absorbed photon, $\langle h\nu \rangle_{abs}$. From there, we can define two cases:

- $E_{int} > \langle h\nu \rangle_{abs}$: The internal energy is larger than the mean energy per absorbed photon hence the absorption of a photon by the grain causes a small increase in its temperature. Therefore, these grains are in thermal equilibrium and their temperature is equal to the equilibrium temperature, T_{eq};
- $E_{int} < \langle h\nu \rangle_{abs}$: The internal energy is smaller than the mean energy per absorbed photon hence the absorption of a photon by the dust grain causes a large increase in its temperature. Between the absorption of two photons, the grain cools down and so its temperature is strongly fluctuating above and below its equilibrium temperature. These grains are not in thermal equilibrium and it is therefore not possible to define their temperature by an equilibrium temperature. For these grains, it is more convenient to study their temperature distribution function dP/dT, where $P(T)$ is the probability that a dust grain has a temperature less or equal to T.

Using diffuse ISM-like grains and a standard ISRF with $G_0 = 1$, we have $\langle h\nu \rangle_{abs} \sim 6.4 \times 10^{-12}$ erg, based on the discussion above, it is possible to define a dust size limit, a_{lim}, above which grains are in thermal equilibrium. We show this limit in Fig. 21 (right plot), which corresponds to $a_{lim} \sim 8$ nm. In Sect. 6.2.2.3, we study the influence of the radiation field on this dust size limit using a different criterion that requires first to define the average temperature of a grain, T_{mean}, calculated with the temperature distribution function dP/dT.

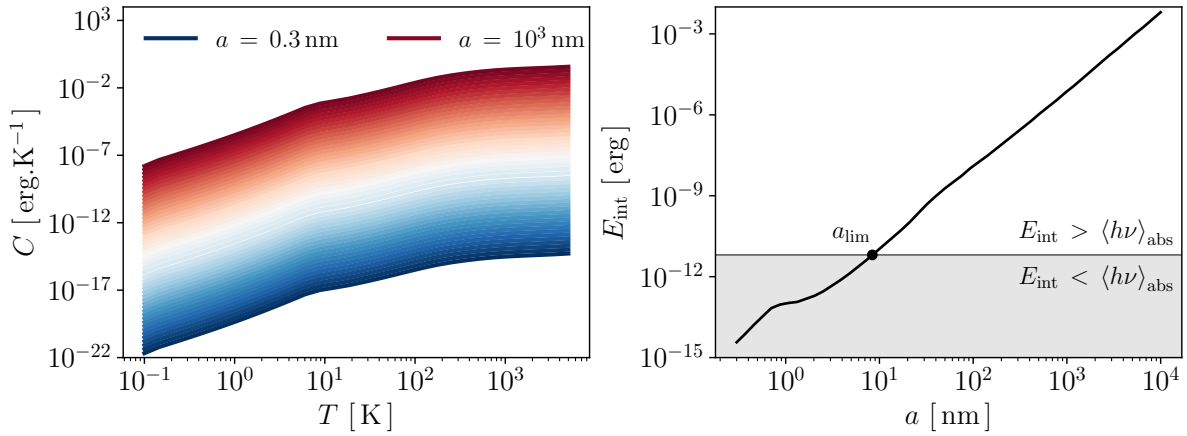

Figure 21: Left: Heat capacities (see Jones et al., 2013) as a function of temperature for a varying from 0.3 nm (blue line) to 10^3 nm (red line) for a-C:H/a-C grains. Right: Internal energy of a-C:H/a-C grains as a function of dust size. The darker grey part delimited by the horizontal line corresponds to grain sizes for which the internal energy is lower than the mean energy per absorbed photons for a standard ISRF with $G_0 = 1$.

2.4.3 *Dust emission and temperature distribution function*

There are different methods to compute the temperature distribution function, whether it is from Monte Carlo simulations of $T(t)$ (e.g. Draine and Anderson, 1985) or through the discretized steady stade disribution function (e.g. Desert, Boulanger, and Shore, 1986; Draine and

Li, 2001). For instance, DustEM (see Sect. 6) computes the temperature distribution function using this second method, described in Desert, Boulanger, and Shore, 1986.

Fig. 22 shows the temperature distribution function, computed with DustEM, for different dust sizes. Note that the larger the grain, the narrower the temperature distribution function, which means that the grain tends towards a single temperature. From the temperature distribution function of a grain with a given size a, it is possible to define its emissivity:

$$I_\nu(a) = \pi a^2 Q_{em}(a, \nu) \int_0^\infty B_\nu(T) \left(\frac{dP}{dT}(a)\right) dT, \tag{25}$$

where $Q_{em}(a, \nu) = Q_{abs}(a, \nu)$, from Kirchhoff laws. Fig. 22 also shows the dust SED (Spectral Energy Distribution) for different grain sizes, obtained with Eq. (25). For grains that are in thermal equilibrium, the temperature distribution function can be approximated by $\delta(T - T_{eq})$. Hence for these grains, Eq. (25) can be simplified as follows:

$$I_\nu(a) = \pi a^2 Q_{abs}(a, \nu) \int_0^\infty B_\nu(T)\, \delta(T - T_{eq})\, dT = \pi a^2 Q_{abs}(a, \nu)\, B_\nu(T_{eq}). \tag{26}$$

Based on Eq. (26), grains that are in thermal equilibrium emit as a modified blackbody at a temperature T_{eq}. This is indeed apparent in Fig. 22 as the shape of the spectrum for large grains is typical of a modified blackbody. For smaller grains that are not in thermal equilibrium and stochastically heated, we can see that they are responsible for the emission in the near and mid-IR, comprising the dust continuum and aromatic features due to vibrational modes of aromatic structures.

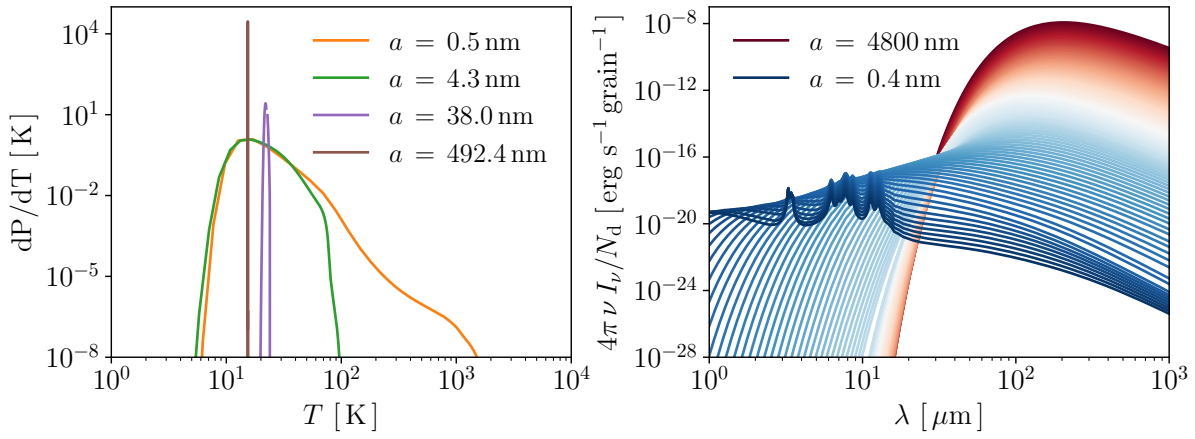

Figure 22: Left: Temperature distribution function dP/dT, computed with DustEM, for a-C grains with different sizes (a = 0.5 nm in orange, 4.3 nm in green, 38 nm in purple, brown in 492.4 nm) for a standard ISRF with $G_0 = 1$. Right: Spectral energy distribution (see Eq. (25)) for a-C grains with a that varies from 0.4 nm (blue line) to 4800 nm (red line) for a standard ISRF with $G_0 = 1$.

$$I_\nu = N_H \int_{a_{min}}^{a_{max}} \frac{dn}{da} I_\nu(a)\, da = N_H \int_{a_{min}}^{a_{max}} \frac{dn}{da} \pi a^2 Q_{abs}(a, \nu) \int_0^\infty B_\nu(T) \left(\frac{dP}{dT}(a)\right) dT \tag{27}$$

From this, it is possible to compute the total emission of a dust model. Based on the THEMIS dust model for the diffuse ISM (see Sect. 6.2), with the size distributions defined in Fig. 45, it is possible to compute the total dust spectrum using Eq. (27), implemented in DustEM. This spectrum is also shown in Fig. 45 and will be discussed later.

2.5 DUST-ASSISTED CHEMISTRY

In the ISM, chemical reactions do not only occur through direct collisions between atoms and molecules but also at the surface of dust grains. In particular, molecular hydrogen cannot form through direct collision because it has no dipole moment to radiate the energy in excess of the bound state. However, as it is the most abundant molecule in the Universe, there must be a viable and efficient scenario for H_2 formation, where a third particle takes this excess energy. It was therefore proposed (Gould and Salpeter, 1963; Hollenbach and Salpeter, 1971) that this third particle is a dust grain, that allows atoms and molecules to react on its surface. Furthermore, the H_2 formation is efficient between 11 and 19 K (e.g. Chang, Cuppen, and Herbst, 2006) because:

- below 11 K, hydrogen atoms are fixed onto the dust surface and cannot migrate hence react together;
- above 19 K, hydrogen atoms are evaporated from the dust surface hence cannot react onto dust surface.

However, this very limited range of dust temperature is unlikely to be consistent with the observations (e.g. Cazaux and Tielens, 2004; Habart et al., 2004, 2011). Two other mechanisms of H_2 were therefore proposed (e.g. Le Bourlot et al., 2012, and reference therein), known as the *Langmuir-Hinshelwood* reaction and the *Eley-Rideal* reaction.

Bron, 2014 showed later that the H_2 formation through the Langmuir-Hinshelwood mechanism on stochastically-heated grain appears to efficiently form molecular hydrogen in the warm outer region of PDRs. A complementary study (Jones and Habart, 2015) showed that the UV photolysis of a-C(:H) grains leads to the release of molecular hydrogen and can therefore be a viable route to efficiently form H_2 in the warm outer region of PDRs (that is, the illuminated edge of the PDR that is mostly atomic). It must be noted that as H_2 is formed on dust surface and because most of the dust surface is contains in small grains that are likely to evolve in PDRs (see Sect. 10), this therefore affects the H_2 formation (see Sect. **??**).

Besides, the molecular hydrogen is not the only molecule that can form on the surface of grains. In dense clouds, the low temperature reached by dust grains prevents freshly formed molecules (mainly H_2O, CO, and CO_2) from being instantaneously evaporated. As a consequence, ice mantles composed of these molecules can form around grains. For further details, Gibb et al., 2004 give an overview of ices in the ISM.

2.6 DUST MODELS

Interstellar dust grains absorb UV photons emitted by stars and subsequently emit in the infrared. The analysis of this emission gives information about the dust properties (size, composition, and shape), the dust mass along the line of sight and the intensity of the radiation emitted by the star that heats the dust grains. However, these properties are not inferred directly from the emission spectrum. Indeed, one has to specify dust properties and the associated optical properties and then, one can constrain the dust model by computing quantities[4] to be compared with the observations.

Following the discovery of the interstellar reddening (Schalén, 1929; Trumpler, 1930) and based on the Mie's theory, it was proposed by Schoenberg and Jung, 1934 that this phenomenon could be due to a distribution of water ice, silicate or metal particles, that absorb

4 Dust extinction, scattering, emission, and polarisation.

and scatter starlight. Later, Hulst, 1943 and Oort and Hulst, 1946 introduced the first dust model, known as the *dirty-ice* model, which consists of atoms (H, O, C, and N) that gather to form frozen saturated molecules. Kamijo, 1963 showed theoretically that silicate material (SiO_2) formed in the atmosphere of cool stars, could allow atoms to condensate onto its surface to form *dirty ice*. However, albeit this model reproduced well the reddening, it was not able to explain the relatively high degree of polarisation in the extinction (Hall, 1949; Hiltner, 1949). As graphite dust properties are isotropic, this implies that they can polarise stellar radiation much more than the *dirty ice*. Therefore, dust composed of graphite that condenses in the atmosphere of carbon stars was considered to explain such polarisation observations (Cayrel and Schatzman, 1954; Hoyle and Wickramasinghe, 1962). Furthermore, graphite was at this time the most likely choice to explain a strong extinction at ~ 217 nm that was discovered by Stecher, 1965 and later labeled as the well-known *UV extinction bump* (Stecher and Donn, 1965).

Theoretically predicted by Kamijo, 1963, observations of oxygen-rich cool giants (Gilman, 1969) showed that grains forming in the atmosphere of such giants are mainly silicates (Al_2SiO_4 and Mg_2SiO_4). This led Hoyle and Wickramasinghe, 1969 to propose that interstellar dust was composed of both graphite and silicate grains that are formed in the atmosphere of oxygen-rich giant stars. The presence of silicate in dust grains was later reinforced because silicates were observed in different regions in emission (Knacke et al., 1969; Stein and Gillett, 1969; Woolf and Ney, 1969; Maas, Ney, and Woolf, 1970) and in absorption (Hackwell, Gehrz, and Woolf, 1970; Gillett and Forrest, 1973). These studies led to dust models that are composed of both graphite and silicate, that are still commonly used nowadays. Among these models emerged the well-known *MRN dust model* (Mathis, Rumpl, and Nordsieck, 1977), based upon these studies and composed of graphite and olivine-type silicate. This model was later improved by Draine and Lee, 1984 by tuning the optical properties of bare silicate and graphite particles in order to fit observations, resulting in the well-known *astronomical* graphite and silicate. This model was later improved by adding for instance, amorphous carbon and PAHs (e.g. Desert, Boulanger, and Puget, 1990; Sorrell, 1990; Rowan-Robinson, 1992; Siebenmorgen and Kruegel, 1992; Dwek, 1997; Draine and Li, 2001; Li and Draine, 2001a; Li and Greenberg, 2002a; Draine and Li, 2007; Siebenmorgen, Voshchinnikov, and Bagnulo, 2014). It is clear that this model is built on the assumption that the different dust populations (silicate, graphite, and PAHs for instance) are distinct and therefore not mixed. Despite fitting well to the observations, graphite is unlikely to be abundant in the ISM. Consequently, other models that follow the same approach but with amorphous carbon instead of graphite, were built (Zubko, Dwek, and Arendt, 2004; Compiègne et al., 2011; Galliano et al., 2011). As an alternative to these MRN-based models, another approach was considered in parallel with all these developments.

Even if the *dirty ice* model was not extensively used in the 70's, studies were undertaken in order to explain the 3.1 μm feature of H_2O that is supposed to originate from *dirty ice*. However, this feature was not found (Danielson, Woolf, and Gaustad, 1965; Knacke, Cudaback, and Gaustad, 1969). Driven by the desire to understand why this feature was not observed, Greenberg, 1973 predicted, based on laboratory experiments, that complex organic molecules may form as mantles around silicates. However, gas and dust are mixed together in the ISM which strongly suggests that dust is mixed into inhomogeneous assemblages such as graphite and silicate core ice-mantled grains (Wickramasinghe, 1963). Based on these studies, the *core-mantle* models were born (e.g. Greenberg, 1982; Duley, Jones, and Williams, 1989; Desert, Boulanger, and Puget, 1990; Jones, 1990; Greenberg and Li, 1999; Jones et al., 2013, 2017).

During the almost sixty years of development briefly presented above, many different interstellar dust models have been proposed. They can be divided into these three broad categories:

- *silicate-graphite models*, that are composed of silicate and graphite (Mathis, Rumpl, and Nordsieck, 1977; Draine and Lee, 1984; Kim, Martin, and Hendry, 1994) and the expansion of this model, using PAH (e.g. Siebenmorgen and Kruegel, 1992; Weingartner and Draine, 2001a; Li and Greenberg, 2002a);
- *composite models*, that are composed of grain aggregates of carbon and silicate (e.g. Mathis and Whiffen, 1989; Mathis, 1996; Zubko, Dwek, and Arendt, 2004);
- *core-mantle models*, that are composed of a core of silicate or aliphatic carbon, both surrounded by an aromatic carbon mantle (e.g. Desert, Boulanger, and Puget, 1990; Jones, 1990; Jones et al., 2013, 2017).

During my PhD, I used THEMIS (e.g. Jones et al., 2013, 2017) which is extensively described in Sect. 6.2. The advantage of such a core-mantle model is the natural description of dust evolution through carbonaceous mantle composition and size (Jones, Duley, and Williams, 1987; Duley, Jones, and Williams, 1989; Jones, 1990; Li and Greenberg, 1997; Cecchi-Pestellini et al., 2010; Zonca et al., 2010; Cecchi-Pestellini, Viti, and Williams, 2014; Cecchi-Pestellini et al., 2014; Köhler, Jones, and Ysard, 2014; Ysard et al., 2015, 2016), throughout different environments. As the physical conditions (UV radiation field and density) vary widely in PDRs (see Sect. 3), THEMIS is perfectly suitable to study dust evolution in such regions.

3 PHOTON-DOMINATED REGIONS

Every day, once a day, give yourself a present.
FBI Special Agent Dale Cooper - *Twin Peaks*

Contents

In star forming regions, the UV radiation field of massive stars profoundly affects the parent cloud, heating and dissociating the surrounding molecular gas. Transition regions from hot, ionized gas to cold, neutral molecular gas thus appear (see Fig. 23) called *photodissociation* or *photon-dominated regions* (PDRs, Hollenbach and Tielens, 1999; Le Petit et al., 2006). PDRs are thus intimately linked to star formation and their bright emission is commonly used to trace and characterize this process in the Universe.

PDRs are bright and their physical conditions are observed to vary widely: these regions are therefore unique laboratories to study processes affecting the gas and the dust and ultimately the formation of stars. In this section, I present the basic aspects of PDRs and focus on the processes related to dust grains.

3.1 GENERAL VIEW

Broadly speaking, a PDR delineates the border of a molecular cloud as it is exposed to the UV radiation field from a nearby massive star. Observations of their emission (see Fig. 23) show that PDRs can be divided into two broad parts. In the first one, closer to the exciting star, most of the incident radiative energy is deposited: this results in a warm ($T > 100$ K), dissociated gas with, in front, a thin layer of ionized gas[1]. In the second part, further from the exciting star, the gas is cooler and molecular. For further reference in this manuscript, we therefore divide a PDR into

- the outer part, composed of atomic gas where processes related to the illuminating radiation field are dominant (ionization, dissociation, fragmentation of grains) and,
- the inner part, composed of dense, molecular gas where recombination or association processes dominate due to collisions (e.g., H_2 formation or grain growth).

Such a structure is set primarily by the attenuation of the incident radiation field (in particular its UV part). Indeed, on their way inside the cloud, photons undergo extinction by dust grains or trigger resonant absorption in H_2 molecules (the self-shielding process, Hollenbach

1 Interstellar matter is highly opaque to photons of energy above 13.6 eV thus containing the ionized gas in small volumes. The mass budget of PDRs is therefore dominated by the neutral gas on which we focus here.

and Tielens, 1999). Attenuation along the light rays is then estimated from the column density N_H. Assuming a standard extinction law, N_H can be expressed in terms of optical opacity, A_V[2].

The resulting stratification of composition and temperature can be seen in the PDR model results of Fig. 23 where the outer (inner) part corresponds to $A_V \leqslant 0.1$ ($A_V > 0.1$) respectively. These curves result from the competition between photon-related processes (e.g. dissociation, dust photoelectric heating of the gas) and collision-driven ones (H2 formation and gas cooling). The structure of a PDR is therefore set by the ratio G_0/n_H between the intensity of the UV radiation field (for photon-related processes) and the gas density n_H (for collisional processes).

In PDR modeling, some important simplifying assumptions are made. First, the geometry of the irradiated region is taken to be that of a parallel, semi-infinite slab. Second the PDR is assumed to have a constant gas density (isochoric model) or a constant gas pressure (isobaric model): in the second case the density profile $n_H(z)$ (z being the depth inside the PDR) will vary, reflecting temperature changes. The temperature is an important quantity that controls the gas composition (atomic or molecular) and the emission of the PDR: it is set by the thermal balance, i.e., the equilibrium between gas heating and cooling processes (see Fig. 24 and Fig. 25). In neutral gas, the heating is dominated by the photoelectric effect of dust grains[3]. The gas cooling is ensured by inelastic collisions between abundant species (H, H_2, He, and electrons) and atoms or molecules: brought to an excited level these latter species decay spontaneously by IR emission that efficiently escapes the PDR and carries away the excitation energy which is thus lost from the gas. In neutral gas the cooling is due to fine-structure lines of [C^+] at 158 μm, [O] at 63 and 145 μm and rotational lines of H_2 and CO (see Fig. 23).

3.2 GAS-GRAIN INTERACTIONS

In PDRs, dust grains are central to several processes drawing energy from the radiation field to heat and transform the gas. Dust is also essential to trigger the chemistry. All these processes linking the dust and the gas are called gas-grain interactions.

Due to their continuous extinction from the UV to the near-IR (see Fig. 65), dust grains efficiently absorb and scatter the incident radiation field thus controlling the radiative transfer or the way light penetrates and heats the PDR. About 97% of the energy absorbed by dust is converted to IR emission and the remaining energy fraction (3%) leads to gas heating via the photoelectric effect (e.g. Habart et al., 2001). In this process, a dust grain absorbs a UV photon of energy 6 to 13.6 eV and releases an electron with a kinetic energy of 1 to 2 eV that will heat the gas upon thermalisation. It must be noted that the photoelectric efficiency has been shown to be largest for the smallest grains of nanometric size (Bakes and Tielens, 1994).

Another important dust-aided process is that of H_2 formation. Indeed, to overcome the exchange energy between protons spin, H_2 formation requires a third partner that is very rare at interstellar densities. It has therefore been proposed (Gould and Salpeter, 1963), that H_2 forms by catalytic reactions at the surface of dust grains. This process is also dominated by the contribution of nano-grains ($a \leqslant 10$ nm) because they have a large surface-to-volume ratio.

Gas-grain interactions are therefore key processes in PDRs mostly involving nano-grains (less than 10 nm in size). On the other hand, it is known (see Sect. 2.2) that dust evolves in the ISM leading in particular to a changing abundance of nano-grains that can be destroyed or

2 The column density N_H is related to A_V by $N_H/E(B-V) = 5.8 \times 10^{21}$ atoms cm^{-2} mag^{-1}, with the adopted following convention $A_V/E(B-V) = 3.1$. Then, $A_V = 1$ corresponds to $N_H \simeq 1.87 \times 10^{21}$ atoms cm^{-2}.

3 In dense gas ($n_H \geqslant 10^4$ cm^{-3}), gas heating by collisional deexcitation of UV pumped H_2 is also important.

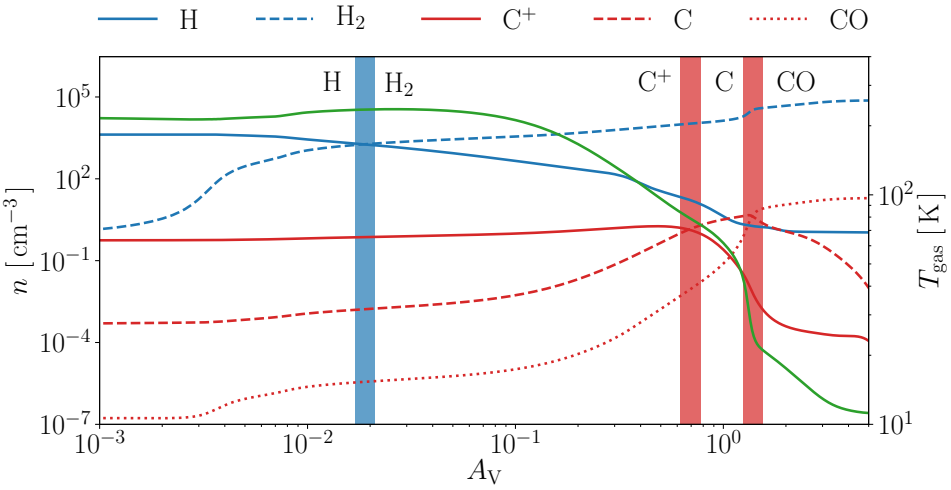

Figure 23: Density profiles across a PDR for H (blue solid line), H_2 (blue dashed line), C^+ (red line), C (red dashed line), and CO (red dotted line). The vertical blue stripe corresponds to the $H \rightarrow H_2$ transition. The first (from the left) vertical red stripe corresponds to the $C^+ \rightarrow C$ transition and the second one, to the $C \rightarrow CO$ transition. The gas temperature is shown by the green line. All quantities were computed using the Meudon PDR Code (Le Petit et al., 2006) using a standard ISRF with $G_0 = 10^2$ (from the left) and an isobaric model with $P = 10^6$ cm^{-3} K. These conditions correspond to those the Horsehead Nebula encounter (see Sect. 5.2).

reformed from larger grain mantles, under the action of UV light (see Sect. 10). Studying the abundance profile of nano-grains in PDRs is therefore of primary importance to understand these regions.

3.3 PDR EMISSION

The emission spectrum of PDRs occurs mostly in the IR to mm wavelength range and is dominated by the continuum contribution of dust. Bright narrow lines from gas cooling species are superimposed on this continuum. Most of these emission components can be used, more or less directly (transfer or opacity effects) to constrain the physical conditions of the PDR, namely, the local density n_H and the intensity of the local UV field G_0.

In the warm, atomic, outer part of the PDR, the ratio of the O lines at 63 and 145 µm constrains n_H while the intensity of the C^+ line at 158 µm provides information on the temperature. In the molecular, inner part of the PDR, the H_2 and CO rotational lines are powerful tools to extract (with radiative transfer models) both n_H and T.

The dust emission also carries a wealth of information, first of all on the dust properties itself (size distribution, grain composition and structure, etc...) but also on the physical conditions of the PDR. If the small to large grain ratio is known, the incident UV factor can be found as well as the mass along the line of sight (Compiègne et al., 2011). In practice, PDRs are dense environments where scattering must be taken into account: dust models must therefore be used within radiative transfer codes in order to provide realistic predictions of the PDR dust emission. This PhD project follows along these lines, focusing on extracting the evolving properties of dust grains across PDRs of known or at least well constrained density profile and incident radiation field.

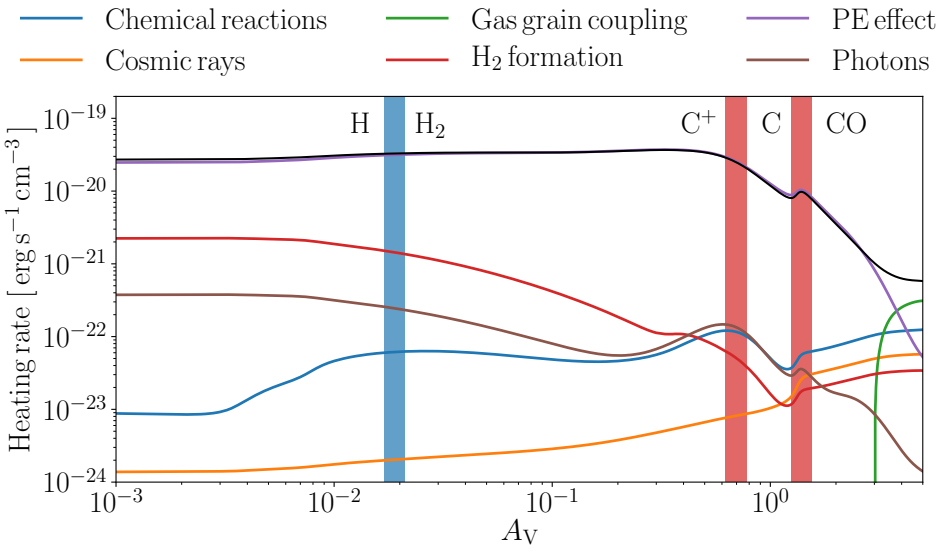

Figure 24: Heating rates profiles across the PDR for chemical reactions (blue line), gas-grain coupling (green line), photoelectric effect (purple line), cosmic rays (orange line), H_2 formation (red line), and photons (brown line). The total heating rate is shown by the black line. The vertical blue stripe corresponds to the $H \rightarrow H_2$ transition. The first (from the left) vertical red stripe corresponds to the $C^+ \rightarrow C$ transition and the second one, to the $C \rightarrow CO$ transition. These heating rates were computed using the Meudon PDR Code (Le Petit et al., 2006) using a standard ISRF with $G_0 = 10^2$ (from the left) and an isobaric model with $P = 10^6$ cm^{-3} K. These conditions correspond to those the Horsehead encounter (see Sect. 5.2).

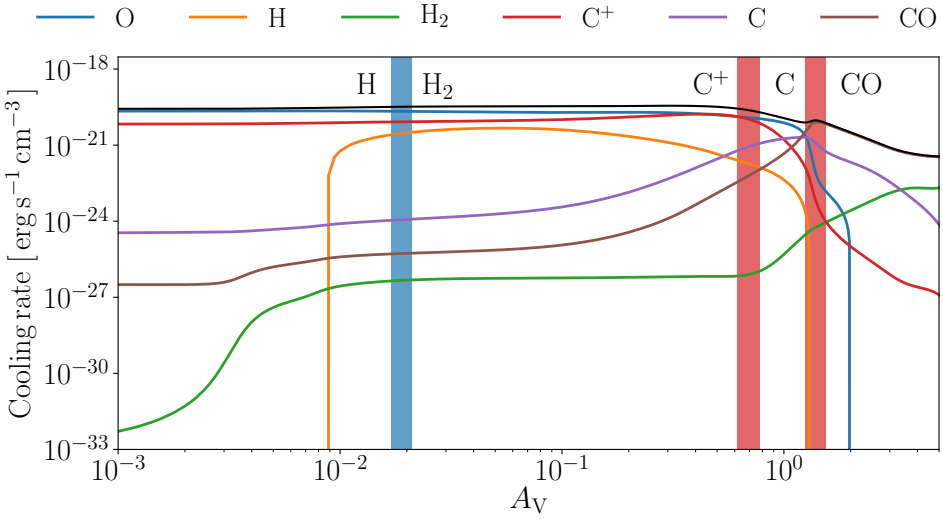

Figure 25: Cooling rates profiles across the PDR for O (blue line), H (orange line), H_2 (green line), C^+ (red line), C (purple line), and CO (brown line). The total cooling rate is shown by the black line. The vertical blue stripe corresponds to the $H \rightarrow H_2$ transition. The first (from the left) vertical red stripe corresponds to the $C^+ \rightarrow C$ transition and the second one, to the $C \rightarrow CO$ transition. These heating rates were computed using the Meudon PDR Code (Le Petit et al., 2006) using a standard ISRF with $G_0 = 10^2$ (from the left) and an isobaric model with $P = 10^6$ cm^{-3} K. These conditions correspond to those the Horsehead encounter (see Sect. 5.2).

Part III

OBSERVATIONS AND DATA PROCESSING

4 SPACE OBSERVATORIES

A la question toujours posée "Pourquoi écrivez-vous ?", la réponse du Poète sera toujours la plus brève "Pour mieux vivre".

Saint-John Perse - *Vivre & Mieux*

Contents

4.1 SPITZER AND HERSCHEL

The *Spitzer Space Telescope* (SST) (Werner et al., 2004) was launched on August 25, 2003. It was conceived to observe from the mid-IR to far-IR, from 3.6 to 160 μm, with a 85 cm primary mirror and three observing instruments:

- The *Infrared Array Camera* (IRAC) that observed in four photometric bands centered on 3.6, 4.5, 5.8, and 8 μm;
- The *Multiband Imaging Photometer for Spitzer* (MIPS) that observed in three photometric bands centered on 24, 70, and 160 μm;
- The *Infrared Spectrograph* (IRS), a spectrometer at low spectral resolution ($R = \lambda/\Delta\lambda \sim 60-120$) between 5.2 and 38 μm, and high spectral resolution ($R = \lambda/\Delta\lambda \sim 600$) between 9.9 and 37.2 μm.

The *Herschel* space telescope was launched in May 14, 2009 to observe in the far-IR, from 70 to 500 μm, with a primary mirror of 3.5 m and three observing instruments:

- the *Photodetector Array Camera and Spectrometer* (PACS) that observed in three photometric bands centered on 70, 100, and 160 μm. Spectroscopic observations were possible between 51 and 105 μm and between 102 and 220 μm with a spectral resolution of $R = \lambda/\Delta\lambda \sim 1000-4000$;
- the *Spectral and Photometric Imaging Receiver* (SPIRE) that observed in three photometric bands centered on 250, 350, and 500 μm. Spectroscopic observations were made between 194 and 313 μm and between 303 and 671 μm;
- the *Heterodyne Instrument for the Far-Infrared* (HIFI), composed of four spectrometers, that generated spectra covering a wavelength range from 157 to 625 μm.

During my PhD, I used photometric observations from *Spitzer*/IRAC (3.6, 4.5, 5.8, and 8 μm), *Spitzer*/MIPS (24 μm), *Herschel*/PACS (70 and 160 μm), and *Herschel*/SPIRE (250, 350, and 500 μm). The associated photometric bands are described in Sect. 4.2 and the *Point Spread Functions* (PSFs) in Sect. 4.3.

4.2 PHOTOMETRIC BANDS

Photoconductors such as the detectors used by IRAC and MIPS, count the number of received photons regardless of their energy. The number of electrons generated from the absorption of a photon is quantified by the quantum efficiency $R(\nu)$, expressed in electrons per photon, which depends on the frequency of the incident photon.

In order to express the number of electrons generated by a detector that receives an incident flux F_ν, we first define the number of photons dN_{ph} crossing the detector surface element dA, during a time interval dt, with frequencies in $[\nu, \nu + d\nu]$:

$$dN_{ph} = \frac{F_\nu}{h\nu}\, dt\, dA\, d\nu, \tag{28}$$

and therefore, the number of photons per unit time and per detector surface area, from an incident flux F_ν is:

$$\frac{dN_{ph}}{dt\, dA} = \frac{F_\nu}{h\nu}\, d\nu. \tag{29}$$

Thence, the number of electrons, per unit time and per detector surface area, generated by dN_{ph} photons received by the detector is:

$$\frac{dN_e}{dt\, dA} = \int_{\nu_{min}}^{\nu_{max}} \frac{F_\nu}{h\nu}\, R(\nu)\, d\nu, \tag{30}$$

where $R(\nu)$ is the quantum efficiency and ν_{min} (ν_{max}) is the minimum (maximum) frequency of the photometric band.

Each instrument has a specific flux convention F_ν^{conv}, such that the flux in the band $F_{\nu_0}^{band}$ is the interpolated value of the observed spectrum at the wavelength where the photometric band is centered: $F_{\nu_0}^{band} = F_\nu^{conv}(\nu_0)$. Therefore, regardless of the spectrum shape and whatever the flux convention:

$$F_{\nu_0}^{band} = F_{\nu_0}^{conv}(\nu_0) \times \frac{dN_e}{dN_e^{conv}} = \frac{\displaystyle\int_{\nu_{min}}^{\nu_{max}} F_\nu\, R(\nu)\, \left(\frac{\nu_0}{\nu}\right)\, d\nu}{\displaystyle\int_{\nu_{min}}^{\nu_{max}} R(\nu)\, \frac{F_\nu^{conv}(\nu)}{F_\nu^{conv}(\nu_0)}\, \left(\frac{\nu_0}{\nu}\right)\, d\nu}. \tag{31}$$

If the usual convention is chosen, $F_\nu^{conv} \propto \nu^{-\alpha}$, then Eq. 31 become:

$$F_{\nu_0}^{band} = \frac{\displaystyle\int_{\nu_{min}}^{\nu_{max}} F_\nu\, R(\nu)\, \left(\frac{\nu_0}{\nu}\right)\, d\nu}{\displaystyle\int_{\nu_{min}}^{\nu_{max}} R(\nu)\, \left(\frac{\nu_0}{\nu}\right)^{\alpha+1}\, d\nu}. \tag{32}$$

Following the conventions from the IRAC and MIPS documentation, the fluxes $F_{\nu_0}^{IRAC}$ in the four bands of IRAC (3.6, 4.5, 5.8, and 8 μm), and the flux $F_{\nu_0}^{MIPS}$ in the MIPS band (24 μm), are written as follows:

$$F_{\nu_0}^{IRAC} = \frac{\displaystyle\int_{\nu_{min}}^{\nu_{max}} F_\nu\, R(\nu)\, \left(\frac{\nu_0}{\nu}\right)\, d\nu}{\displaystyle\int_{\nu_{min}}^{\nu_{max}} R(\nu)\, \left(\frac{\nu_0}{\nu}\right)^2\, d\nu} \quad \text{and} \quad F_{\nu_0}^{MIPS} = \frac{\displaystyle\int_{\nu_{min}}^{\nu_{max}} F_\nu\, R(\nu)\, d\nu}{\displaystyle\int_{\nu_{min}}^{\nu_{max}} R(\nu)\, \left(\frac{\nu_0}{\nu}\right)^2\, d\nu}. \tag{33}$$

Bolometers such as those used in the PACS and SPIRE instruments integrate the absorbed power whatever the photon number count is. The power received per detector surface element dA and per unit frequency is:

$$\frac{dE}{dt\, dA\, d\nu} = F_\nu. \tag{34}$$

With $R(\nu)$, the spectral response of one band of the instrument, the flux in this band is defined as:

$$F_{\nu_0}^{\text{band}} = \frac{\displaystyle\int_{\nu_{\min}}^{\nu_{\max}} F_\nu\, R(\nu)\, d\nu}{\displaystyle\int_{\nu_{\min}}^{\nu_{\max}} R(\nu)\, \frac{F_\nu^{\text{conv}}(\nu)}{F_\nu^{\text{conv}}(\nu_0)}\, d\nu}. \tag{35}$$

Following the conventions from the PACS and SPIRE documentation, the fluxes $F_{\nu_0}^{\text{PACS}}$ in the two bands of PACS (70 and 160 µm) and the fluxes $F_{\nu_0}^{\text{SPIRE}}$ in the three SPIRE band (250, 350, and 500 µm), are written as follows:

$$F_{\nu_0}^{\text{PACS}} = \frac{\displaystyle\int_{\nu_{\min}}^{\nu_{\max}} F_\nu\, R(\nu)\, d\nu}{\displaystyle\int_{\nu_{\min}}^{\nu_{\max}} R(\nu)\, \left(\frac{\nu_0}{\nu}\right) d\nu} \quad \text{and} \quad F_{\nu_0}^{\text{SPIRE}} = \frac{\displaystyle\int_{\nu_{\min}}^{\nu_{\max}} F_\nu\, R(\nu)\, \left(\frac{\nu_0}{\nu}\right)^2 d\nu}{\displaystyle\int_{\nu_{\min}}^{\nu_{\max}} R(\nu)\, \left(\frac{\nu_0}{\nu}\right)^3 d\nu}. \tag{36}$$

The calibration uncertainty in the IRAC bands (3.6, 4.5, 5.8, and 8 µm) is 2 % (Reach et al., 2005), 4 % in MIPS (24 µm) (Engelbracht et al., 2007), 5 % in PACS (70 µm) (Gordon et al., 2007), 12 % in PACS (160 µm) (Stansberry et al., 2007), and 15 % in the three SPIRE bands (250, 350, and 500 µm) (Swinyard et al., 2010). We considered all these errors to be independent of the wavelength and also independant of one another to first order. Fig. 26 shows these ten photometric bands.

4.3 POINT SPREAD FUNCTIONS

A *Point Spread Function* (PSF) corresponds to the actual image of a point source as seen by an instrument. In an ideal case, this point source would be seen as a point in the image taken by the instrument. However, the instrumental image of a point source is spatially spread due to diffraction. This phenomenon is quantified by the PSF and must be carefully taken into account when comparing model results such as dust emission and scattering, to the observations. The PSFs for each of the ten instruments are shown from Fig. 27 (IRAC, 3.6 µm) to Fig. 36 (SPIRE, 500 µm).

In practice and for an extended object, the simulated intensity $I_\nu(x,y)$, is the result of the convolution between the model intensity[1] $I_{\nu,\text{nc}}(x,y)$, and the PSF, $f(x,y)$:

$$I_\nu(x,y) = (I_{\nu,\text{nc}} * f)\,(x,y). \tag{37}$$

1 The subscript *'nc'* is for *'non convolved'*.

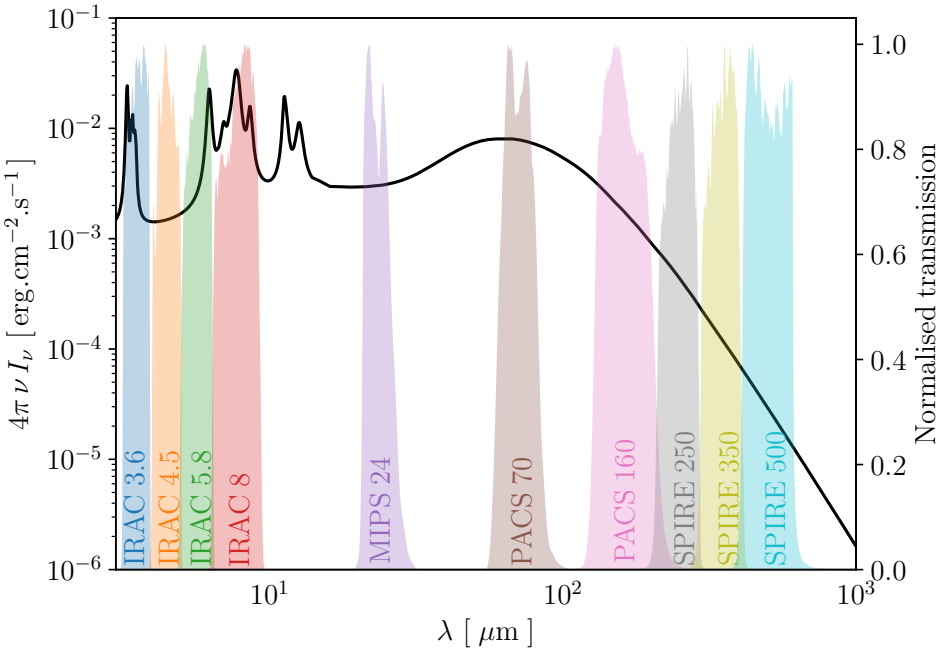

Figure 26: In colors, the ten photometric bands used in this study (3.6, 4.5, 5.8, 8, 24, 70, 160, 250, 350, and 500 µm). The black line shows a dust spectrum computed with DustEM using diffuse ISM-like dust, for a standard ISRF with $G_0 = 1$ and $N_H = 10^{20}$ H cm^{-2}.

I present how I computed the dust model intensity (emission and scattering) $I_\nu(i_y, i_z)$ (see Fig. 62) in Sect. 9.1. In order to compare to the observed intensity, I convolved $I_{\nu,nc}(i_y, i_z)$ with the appropriate PSFs, as follows:

$$I_\nu(i_y, i_z) = \sum_{j_y=-N_y/2}^{N_y/2} \left(\sum_{j_z=-N_z/2}^{N_z/2} I_{\nu,nc}(j_y, j_z)\, f(i_y - j_y, i_z - j_z) \right), \tag{38}$$

where N_y and N_z are the number of pixels along the y-axis and z-axis, respectively (see Fig. 56).

A photon-dominated region is a particular region where the intensity distribution along the axis perpendicular (that is, the y-axis) to the star-PDR axis (that is, the z-axis), has an extremely smooth gradient (see Fig. 62), such as an edge-on galaxy (Bocchio et al., 2016). Consequently, we can consider that $I_{\nu,nc}(i_y, i_z) = I_{\nu,nc}(i_z)$ and Eq. 38 can therefore be simplified to:

$$I_\nu(i_y, i_z) = \sum_{j_z=-N_z/2}^{N_z/2} I_{\nu,nc}(j_z) \left(\sum_{j_y=-N_y/2}^{N_y/2} f(i_y - j_y, i_z - j_z) \right). \tag{39}$$

Thence, following Bocchio et al., 2016, we can introduce the notion of a linear PSF or *line spread function* (LSF), that we note $f_{linear}(i_z)$, and define as:

$$f_{linear}(i_z) = \sum_{i_y=-\infty}^{+\infty} f(i_y, i_z). \tag{40}$$

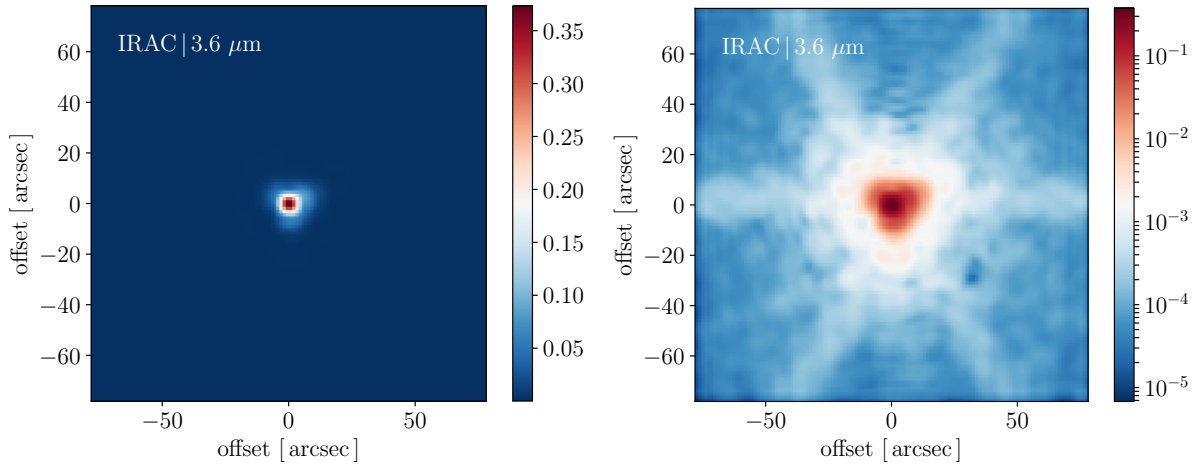

Figure 27: Left: IRAC PSF at 3.6 μm on a linear scale for a pixel size of 1.22″. Right: Same on a logarithmic scale.

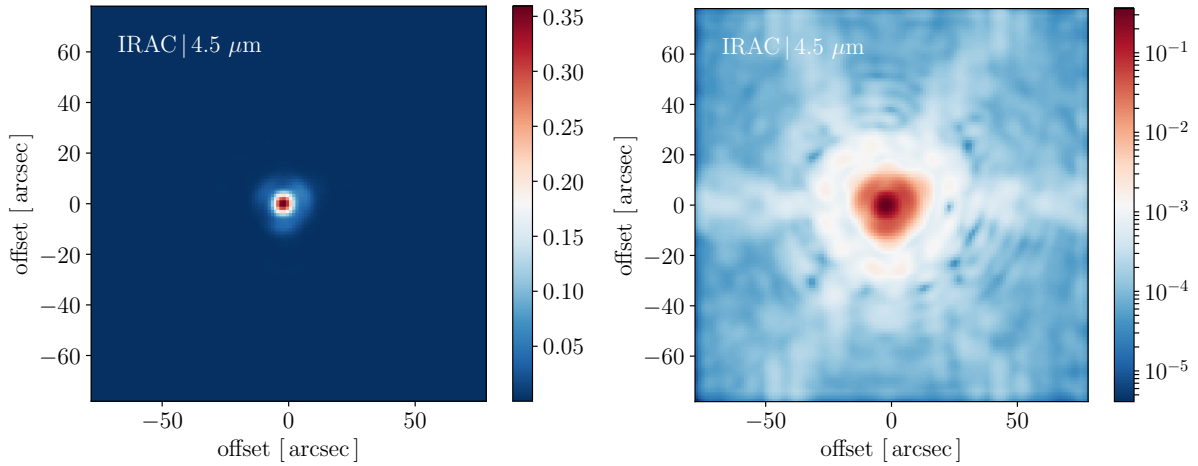

Figure 28: Left: IRAC PSF at 4.5 μm on a linear scale for a pixel size of 1.22″. Right: Same on a logarithmic scale.

Using the *line spread function*, Eq. (39) can therefore be simplified to:

$$I_\nu(i_y, i_z) = I_\nu(i_z) = \sum_{j_z=-N_z/2}^{N_z/2} I_{\nu,\mathrm{nc}}(j_z)\, f_{\mathrm{linear}}(i_z - j_z). \tag{41}$$

Fig. 37 shows the *line spread function* of the ten photometric bands.

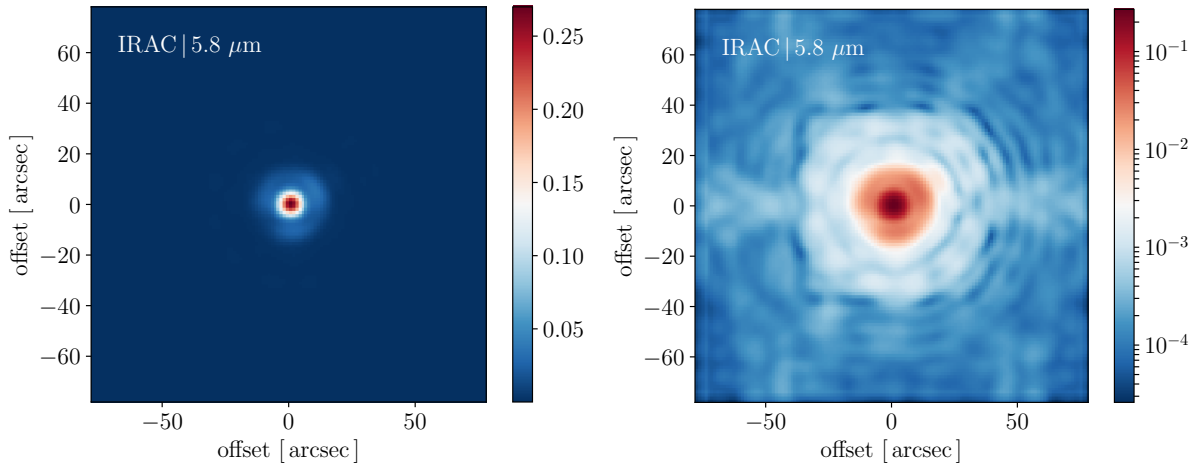

Figure 29: Left: IRAC PSF at 5.8 μm on a linear scale for a pixel size of 1.22″. Right: Same on a logarithmic scale.

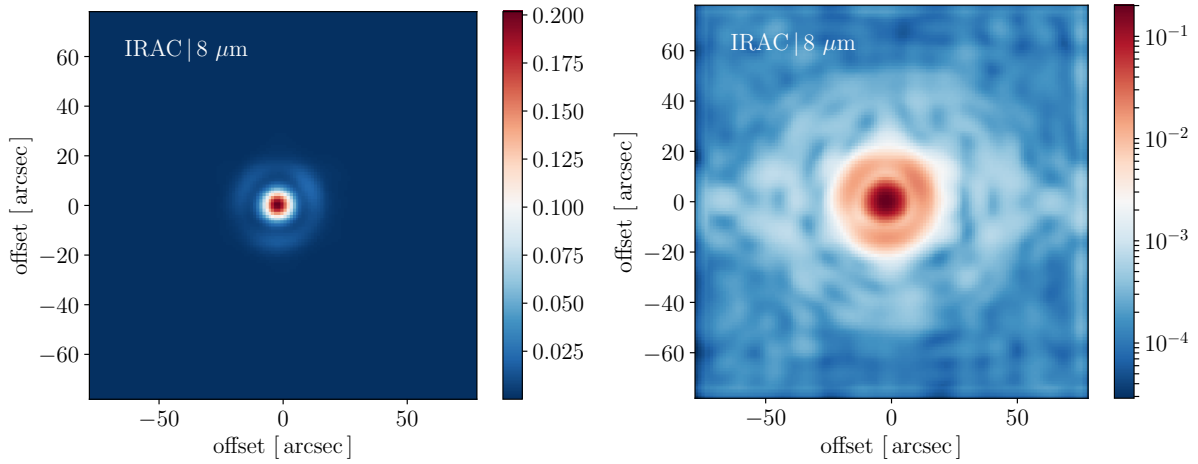

Figure 30: Left: IRAC PSF at 8 μm on a linear scale for a pixel size of 1.22″. Right: Same on a logarithmic scale.

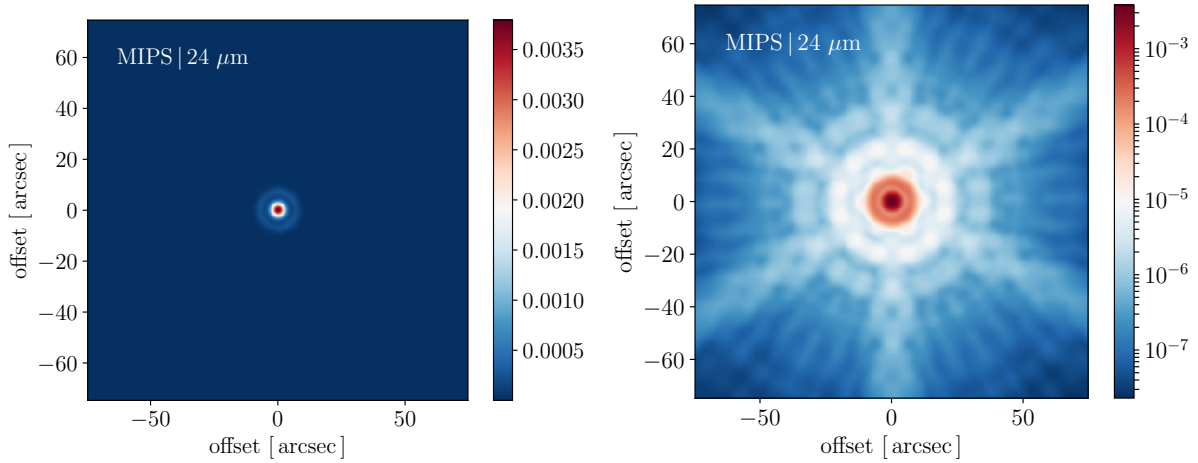

Figure 31: Left: MIPS PSF at 24 μm on a linear scale for a pixel size of 0.5″. Right: Same on a logarithmic scale.

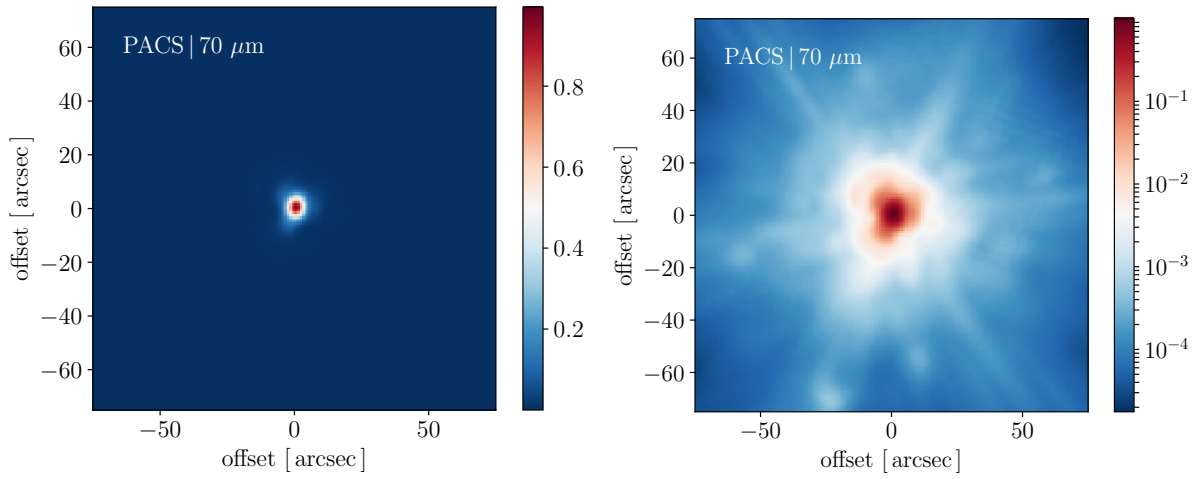

Figure 32: Left: PACS PSF at 70 μm on a linear scale for a pixel size of 1″. Right: Same on a logarithmic scale.

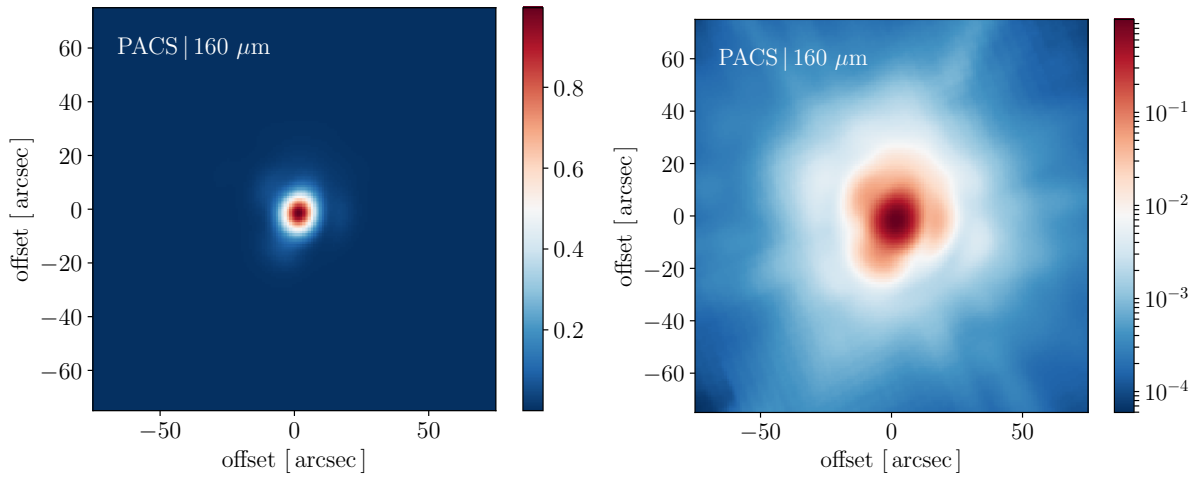

Figure 33: Left: PACS PSF at 160 μm on a linear scale for a pixel size of 1″. Right: Same on a logarithmic scale.

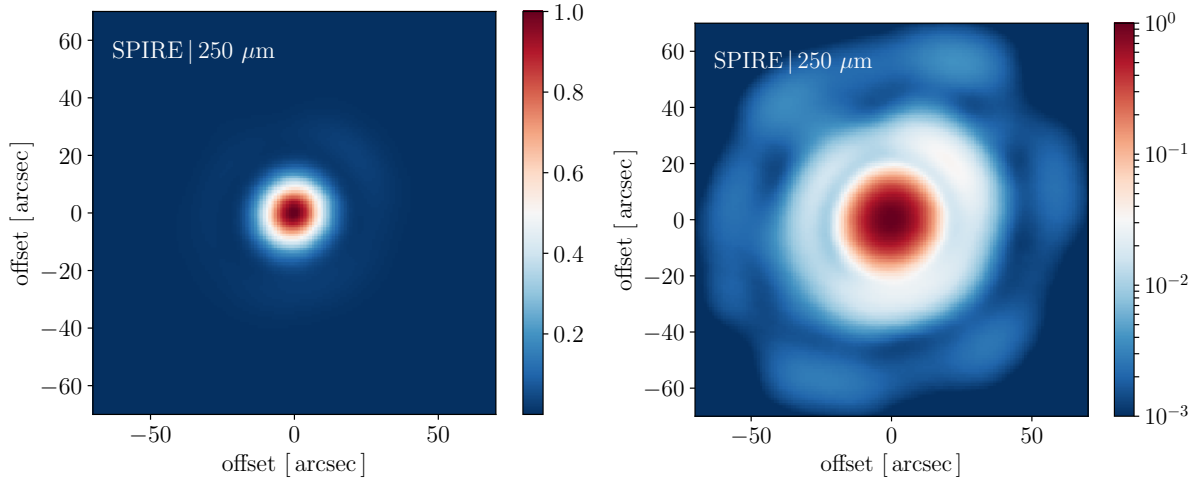

Figure 34: Left: SPIRE PSF at 250 μm on a linear scale for a pixel size of 1″. Right: Same on a logarithmic scale.

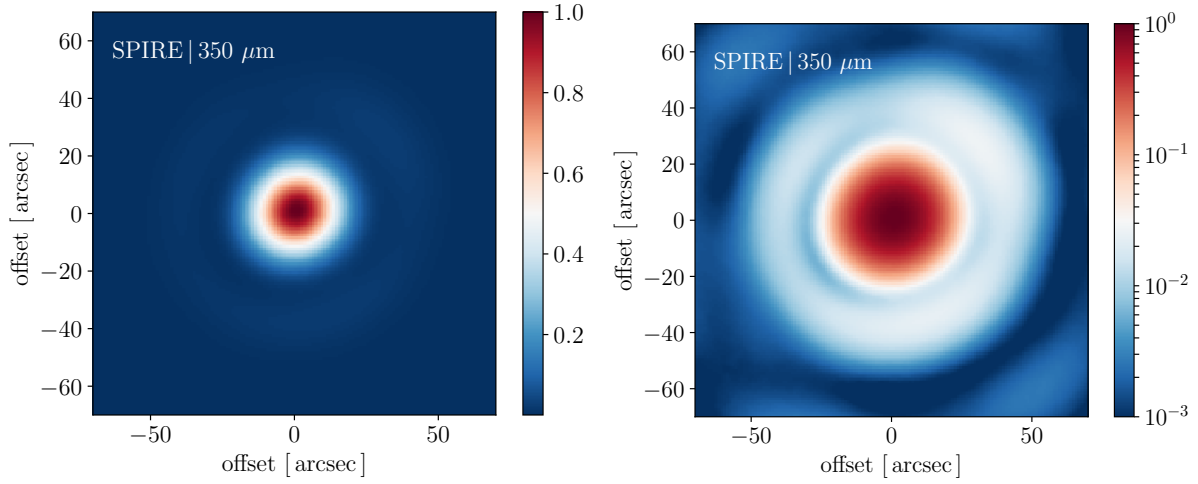

Figure 35: Left: SPIRE PSF at 350 μm on a linear scale for a pixel size of 1″. Right: Same on a logarithmic scale.

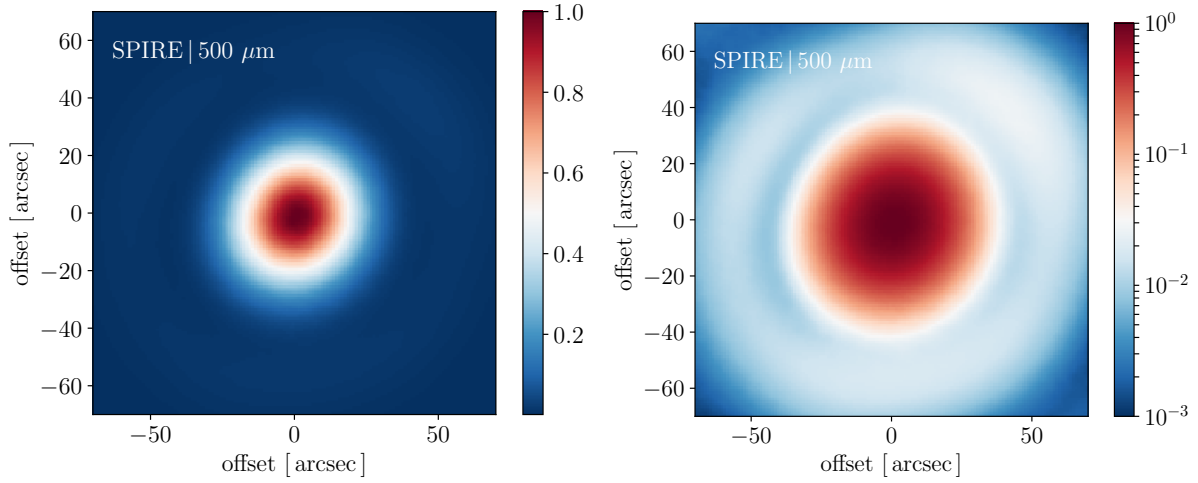

Figure 36: Left: SPIRE PSF at 500 μm on a linear scale for a pixel size of 1″. Right: Same on a logarithmic scale.

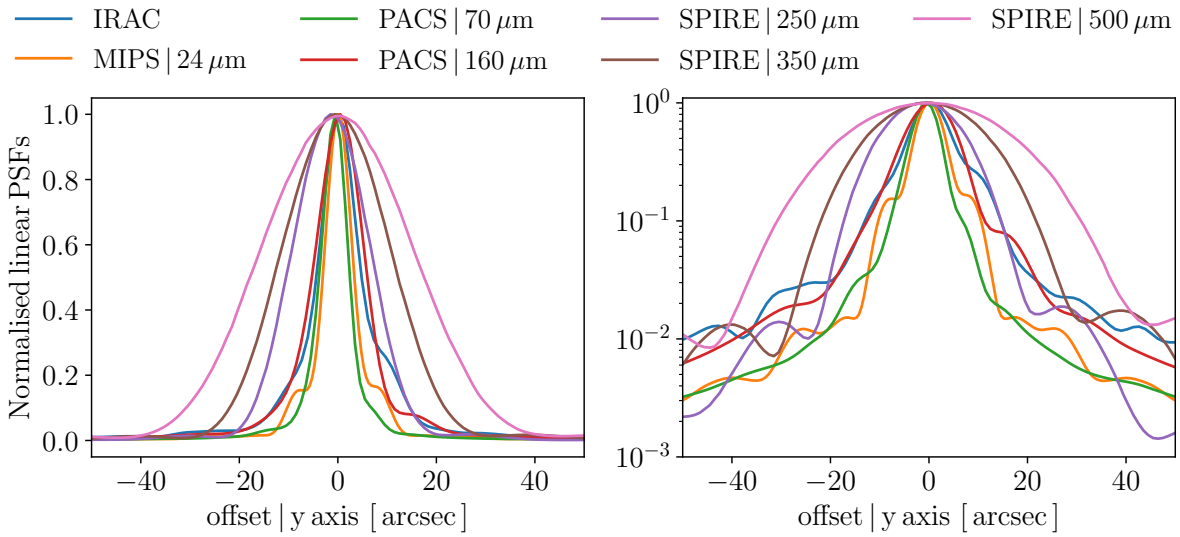

Figure 37: Left: Normalised linear PSFs on a linear scale for IRAC (blue line), MIPS 24 μm (orange line), PACS 70 μm (green line), PACS 160 μm (red line), SPIRE 250 μm (purple line), SPIRE 350 μm (brown line), and SPIRE 500 μm (pink line). Right: Same on a logarithmic scale.

5 THE HORSEHEAD NEBULA

Ah, to softly slip behind the scene
One clear and snow-draped, silent winter night,
To pierce the density which seems to screen,
Obstruct the splendor of that cosmic light,
To pass beyond that dark and mystic cloud
Which looms like portal in a garden wall,
The ancient loveliness within to shroud,
How it one's fancy does inspire, enthrall.
In that great starlit garden of the sky,
Where light eternal dwells in calm repose,
Who knows what beauty there might greet the eye,
What undreamed truth a brief glimpse there disclose
As strange as thought, to thought there is no space,
At will, one's thoughts the universe may embrace.

Lisa Odland - *The Horse-Head Nebula*

Contents

Figure 38: Deep exposure of the Orion B molecular cloud. Credit: Rogelio Bernal Andreo (Deep Sky Colors).

5.1 PRESENTATION OF THE HORSEHEAD

The Horsehead, located in the Orion B molecular could (see Fig. 38), is an archetypal PDR situated at ~ 400 pc (Anthony-Twarog, 1982) that is illuminated by the binary star σ-Orionis

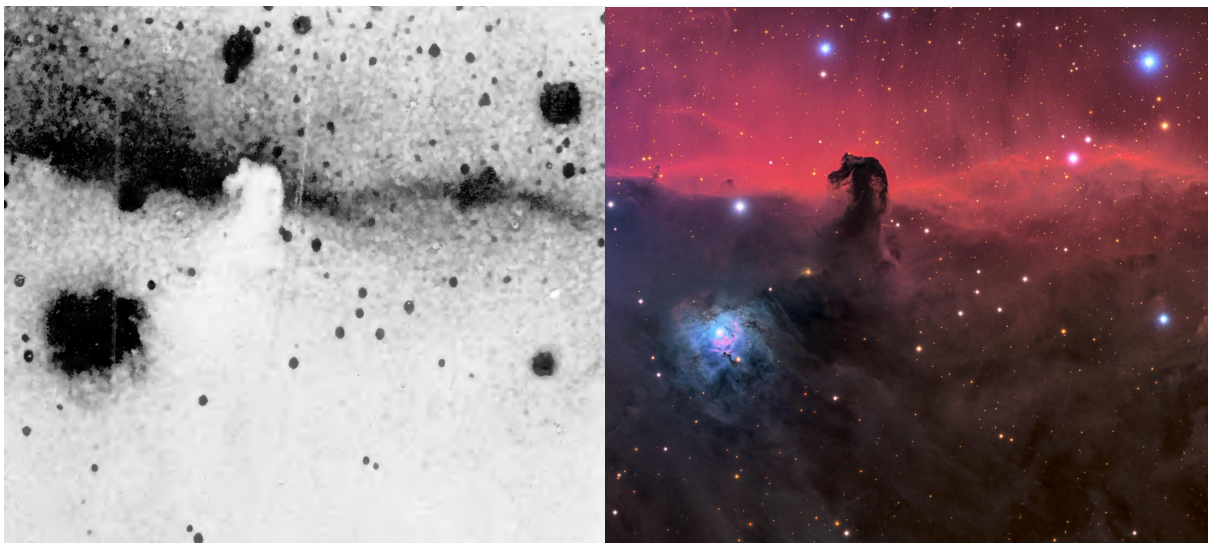

Figure 39: Left: The Horsehead as seen on a plate in Barnard, 1913. Right: The Horsehead seen one century later. Credits: Cosmic Speck Photography.

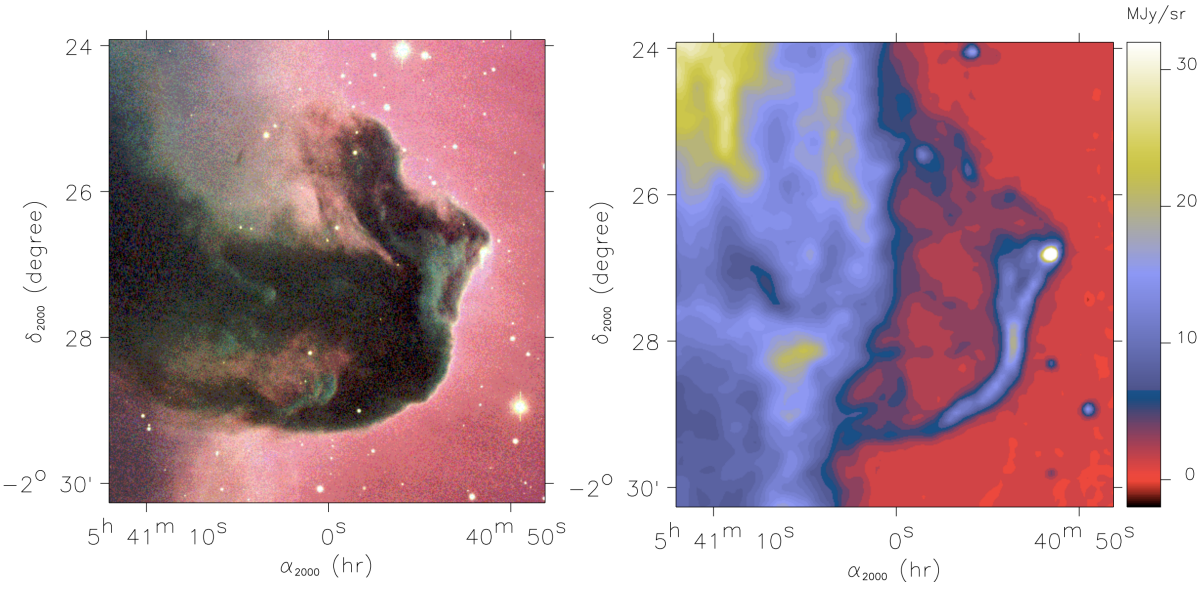

Figure 40: Left: Composite colour image of the Horsehead nebula with the VLT (ESO). Right: ISOCAM map of the Horsehead nebula in the LW2 filter ($5 - 8.5$ μm) (Abergel et al., 2003).

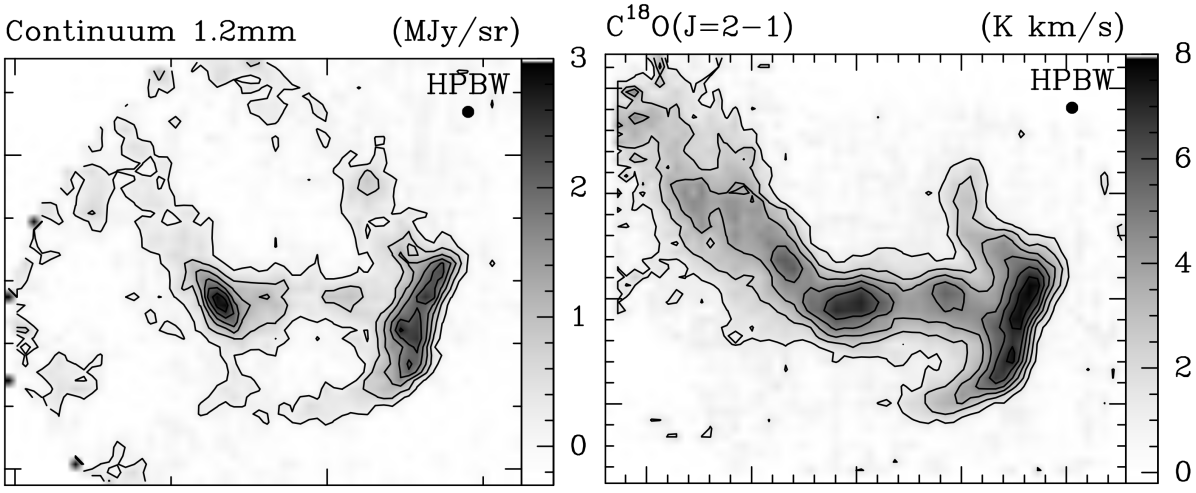

Figure 41: Left: Continuum emission at 1.2 mm observed by MAMBO2 (Hily-Blant et al., 2005). Right: Integrated emission map of $C^{18}O$ $(2-1)$ (Hily-Blant et al., 2005).

which is an O9.5V binary system (Warren and Hesser, 1977) with an effective temperature of $T_{eff} \sim 34600$ K (Schaerer and Koter, 1997) located at a projected distance $d_{edge} \sim 3.5$ pc from the Horsehead edge. Observations of the Horsehead have been made in the visible (e.g. Boer, 1983; Neckel and Sarcander, 1985) and at millimeter wavelengths for ^{12}CO and ^{13}CO (e.g. Milman et al., 1973), ^{12}CO (e.g. Stark and Bally, 1982), NH_3 (e.g. Sandell et al., 1986), CS (e.g. Lada, Bally, and Stark, 1991), C^+ (e.g. Zhou et al., 1993) and ^{13}CO (e.g. Kramer, Stutzki, and Winnewisser, 1996).

Later, mid-IR observations (Abergel et al., 2003, see Fig. 40, right panel) with ISOCAM highlighted that the Horsehead is likely to be seen edge-on and therefore offers us a unique opportunity to study dust, gas and the evolution of the local physical conditions with depth into the Horsehead. This has led to many studies at millimeter wavelengths for CO (Pound, Reipurth, and Bally, 2003), $C^{18}O$ (Hily-Blant et al., 2005, see Fig. 41), CS, $C^{34}S$ and HCS^+ (Goicoechea et al., 2006), CI and CO (Philipp et al., 2006), DCO^+ (Pety et al., 2007), HCO and $H^{13}CO^+$ (Gerin et al., 2009), $H^{13}CO^+$, DCO^+, and HCO^+ (Goicoechea et al., 2009), H_2CO (Guzmán et al., 2011), CF^+ (Guzmán et al., 2012), l-C_3H^+ (Pety et al., 2012), CH_3CN, HC_3N, and C_3N (Gratier et al., 2013), H_2CO and CH_3OH (Guzmán et al., 2013), NH_3 (Ohashi, Kitamura, and Akashi, 2013), and HCOOH, CH_2CO, CH_3CHO and CH_3CCH (Le Gal et al., 2017).

Teyssier et al., 2004 found that although carbonaceous nano-grains are expected to be photodestroyed by the intense UV field at the edge of the Horsehead, they do still exist there. The authors suggest that the photoerosion of carbonaceous nano-grains into small hydrocarbons is more efficient than the photo-destruction of small hydrocarbons at the Horsehead edge. This scenario is reinforced by observations by Pety et al., 2005, who found hydrocarbons such as CCH, c-C_3H_2, and C_4H in the UV-irradiated outer part of the Horsehead. This is supported by laboratory experiments on thermal processed and UV-irradiated dust analogues (see Smith, 1984; Zubko, Dwek, and Arendt, 2004; Alata et al., 2014, 2015; Duley et al., 2015). Based on Spitzer observations, Compiègne et al., 2007 proposed a scenario where PAHs survive in HII regions, and Compiègne et al., 2008 reported that spectral variations in the mid-IR cannot be explained by radiative transfer effects alone and therefore are a consequence of the dust evolution across the Horsehead.

5.2 ON THE DENSITY PROFILE OF THE HORSEHEAD

Performing radiative transfer calculations requires information on the density profile across the Horsehead. We used the density profile that was established by Habart et al., 2005 by combining different observations. They first observed the H2 1-0 S(1) fluorescent emission line with the SOFI instrument at the NTT, as this line is very sensitive to both the radiation field and the gas density. This observation was then combined with previous observations of H_α and dust mid-IR emission to constrain the density profile at the edge of the Horsehead. Finally, they also used CO millimeter observations from the IRAM 30 m telescope (Abergel et al., 2003; Teyssier et al., 2004) and the Plateau de Bure Interferometer (Pety et al., 2005), as well as 1.2 mm dust continuum emission obtained with MAMBO at the IRAM 30 m telescope (Teyssier et al., 2004) in order to constrain the density profile in the inner part. All these observations were interpreted with the Meudon PDR code (Le Petit et al., 2006).

This density profile (see Fig. 42, upper panel) was also used in Compiègne et al., 2008 and Arab et al., 2012 and is defined as follows :

$$n_H(z) = \begin{cases} n_0 \times \left(\frac{z}{z_0}\right)^\gamma & \text{if } z < z_0 \\ n_0 & \text{if } z > z_0, \end{cases} \tag{42}$$

where

$$n_0 = 2 \times 10^5 \,\mathrm{H\,cm^{-3}} \; ; \; z_0 = 0.06\,\mathrm{pc} \; ; \; \gamma = 2.5 \; ; \; z = d_\star - d_{edge}, \tag{43}$$

with z the position from the edge of the Horsehead, γ the power-law exponent of the gas density profile and z_0 the depth beyond which the constant density n_0 is reached.

The authors also estimated the length of the Horsehead along the line of sight, l_{PDR}. They found that this parameter is constrained to be between 0.1 pc and 0.5 pc. We assumed that the density profile is independent of the position along the line of sight (see Fig. 42, bottom panel).

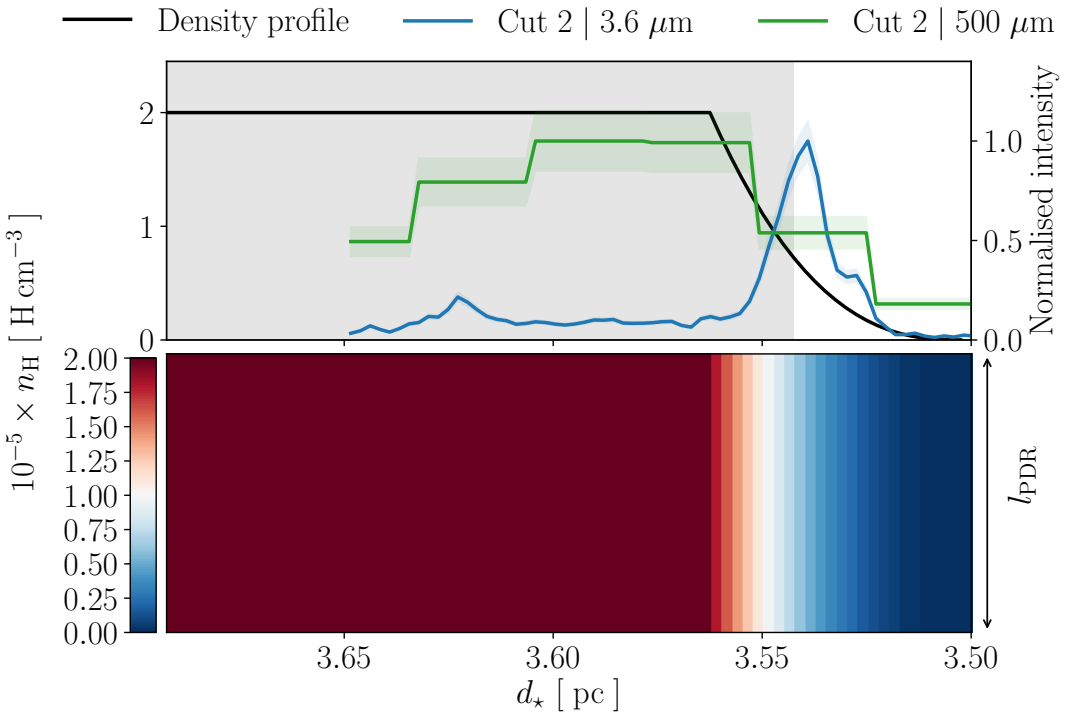

Figure 42: Top: Assumed density profile across the Horsehead (black line, see Sect. 5.2). Normalised dust-observed emission (blue line) in IRAC (3.6 μm, see Fig. 63). Normalised dust observed emission (green line) in SPIRE (500 μm). The grey part corresponds to the inner part of the Horsehead, defined in Sect. 9.3.2.1. Bottom: Density profile in 2D-space defined by the distance to the star, $d_\star$, and the length of the Horsehead along the line of sight, l_{PDR}. Figure from Schirmer et al., 2020, see Sect. 10.

Part IV

MODELS AND TOOLS

During this PhD, I have used different models and tools to compute the dust emission in photon-dominated regions. This requires a dust model and the appropriate tools to model the local emission of the dust populations in this dust model. As photon-dominated regions are optically thick, it was therefore necessary to study how photons interact with the matter and hence to perform radiative transfer.

I first present DustEM in Sect. 6.1, which computes dust emission for a given dust model. Then I introduce THEMIS in Sect. 6.2, the interstellar dust model I used all along this work. Finally, in Sect. 7, I describe some basics about radiative transfer, as well as the radiative transfer code I used in the first part of my PhD, DustPDR, and the second one I used afterwards, SOC.

6 THEMIS AND DUSTEM

Si beaucoup de beauté est ici, c'est que partout il y a beaucoup de beauté.
Rainer Maria Rilke - *Lettres à un jeune poète*

Contents

6.1 MODELLING LOCAL DUST EMISSION WITH DUSTEM

DustEM[1] (Compiègne et al., 2011) is a modelling tool that computes the extinction, emission, and polarisation of interstellar dust grains heated by photons. The computations were done locally, that is, without radiative transfer and assuming an optically thin medium.

To this end, several physical quantities are required in order to use DustEM:

- the absorption and scattering efficiency, $Q_{abs}(a, \nu)$, $Q_{sca}(a, \nu)$ respectively, as well as the anisotropy factor, $g(a, \nu)$;
- the specific heat capacity, $C(a, T)$;
- the intensity of the incident radiation field, I_ν.

Together with these quantities, one must also define the grain properties in a file, GRAIN.DAT, in which the following parameters must be provided, for each dust component:

- the grain type (a-C, a-C:H/a-C or a-Sil/a-C for instance);
- the number of dust sizes;
- the dust mass to gas ratio, M_d/M_H, as well as its specific mass density ρ, expressed in $g.cm^{-3}$;

1 DustEM is available here : http://www.ias.u-psud.fr/DUSTEM

- the grain minimum and maximum size, a_{min} and a_{max} respectively;
- the shape of the size distribution, which is a function that describes, for a given dust type, the distribution of the dust mass as a function of size:
  - plaw: power-law size distribution (see Eq. (44));
  - ed: applies an exponential decay to the power-law size distribution (see Eq. (44));
  - logn: log-normal size distribution (see Eq. (45));
- parameters that define the power-law size distribution with an exponential cut-off (α, a_t, a_c, see Eq. (44)) and/or the log-normal size distribution (a_0, σ, see Eq. (45)).

As written above, the dust size distribution is defined through the keywords that refer either to a power-law size distribution with an exponential cut-off or a log-normal size distribution, defined respectively as follows:

$$\frac{dn}{da} \propto \begin{cases} a^{\alpha} & \text{if} \quad a < a_t, \\ a^{\alpha} \times \exp\left(-\left(\frac{a-a_t}{a_c}\right)^3\right) & \text{if} \quad a \geqslant a_t, \end{cases} \tag{44}$$

$$\frac{dn}{da} \propto \frac{1}{a} \times \exp\left(-\left(\frac{\log(a/a_0)}{2\sigma}\right)^2\right). \tag{45}$$

Based on these input parameters, the temperature distribution function dP/dT (see Sect. 2.4) is determined by iteratively solving Eq. (25) in Desert, Boulanger, and Shore, 1986 in the approximation where the grain cooling is fully continuous. Afterwards, using the optical properties together with the temperature distribution function, Eq. (27) is calculated for each dust type to provides the total SED.

6.2 THEMIS

Here I decribe, the interstellar dust model that I used throughout this work, THEMIS[2] (The Heterogeneous dust Evolution Model for Interstellar Solids, see Jones et al., 2013, 2017). First, the philosophy of THEMIS is presented; second, THEMIS for the diffuse ISM is described; finally, THEMIS for starless dense regions is depicted.

6.2.1 *Philosophy of THEMIS*

Developped at the IAS, THEMIS is the first dust model that provides a description of grain properties that reflects evolutionary processes. Specifically, the optical properties of grains are described as a function of their structure (core-mantle) and composition (the C-to-H ratio in carbonaceous grains). Indeed, in the ISM, dust evolution is mostly driven by UV photons and collisions between grains or with gas species. The efficiency of these processes, set by the UV flux G_0 and the density n_H, determines the structure and composition of the dust.

THEMIS is based on two main dust materials:

2 THEMIS is available here : https://www.ias.u-psud.fr/themis/

- amorphous olivine-type and pyroxene-type silicates with iron and iron sulphide nano-inclusions a-$Sil_{Fe,FeS}$;
- amorphous hydrocarbons solids a-C(:H) materials, which encompasses a-C:H materials, that are H-rich and aliphatic-rich and a-C materials that are H-poor and aromatic-rich. This component is introduced in 3 papers:
  - in Jones, 2012a, the link between the composition, the chemical bonds, and the vibrational modes of a-C(:H) grains is established;
  - in Jones, 2012b, the optical properties that cover the electromagnetic range from the far-UV to the cm, are presented;
  - in Jones, 2012c, the size dependance and the evolution of the a-C(:H) optical properties in response to the local radiation field variations is depicted.

The other major aspect of THEMIS is the Core-Mantle description of dust grains. For the purpose of understanding this depiction and especially in the context of PDRs, it is important to understand the influence of UV irradiation which chiefly affects the carbonaceous dust population. As represented in Fig. 43, UV photons can photo-destroy C-H bonds and therefore, engender the creation of C=C bonds. Thus, the irradiation of a-C(:H) materials leads to their progressive aromatisation[3]. As the typical penetration depth of a UV photon in a-C(:H) material is about 20 nm (see Fig. 15, Jones, 2012b), carbonaceous grains that are smaller than 20 nm are entirely photo-darkened and hence aromatic-rich, these are a-C grains.

Regarding larger carbonaceous grains, they are composed of an aliphatic-rich a-C:H core surrounded by an H-poor/aromatic-rich a-C mantle assumed to be 20 nm thick, which prevents the photo-processing of the core and hence allows it to remain aliphatic-rich. These are the large a-C:H/a-C grains.

However, one must emphasize that this description is built upon the assumption that these grains had time to be photo-darkened. In other words, the typical timescale associated with the photo-darkening of a dust grain is assumed to be smaller than the typical time the grain has been in existence (i.e. the age of the universe as a first approximation). An analytical expression of the photo-darkening timescale, $\tau_{pd}(a)$, is derived from the photo-darkening rate, $\Lambda_{pd}(a)$, in Jones et al., 2014 and defined as follows:

$$\tau_{pd} = \Lambda_{pd}^{-1} = \frac{1}{\sigma_{CH}\, F_{EUV}\, Q_{abs}(a)\, \epsilon(a)}, \tag{46}$$

where $F_{EUV} \simeq 3 \times 10^7$ photons $s^{-1}\,cm^{-2}$ is the EUV[4] photon flux in the local ISM, $\sigma_{CH} \simeq 10^{-19}$ cm^2 is the CH bond photo-dissociation cross-section, $Q_{abs}(a)$ is the dust absorption efficiency which depends almost solely on the radius in the EUV range and $\epsilon(a)$, is a size-dependent photo-darkening efficiency, defined as follows:

$$\epsilon(a) = \left(\frac{2}{a[nm]}\right) \text{ for } a > 2\,nm \quad \text{else} \quad \epsilon(a) = 1. \tag{47}$$

Fig. 44 shows the photo-darkening timescale, τ_{pd}, as a function of the grain size. The photo-darkening timescale takes values around 10^5 years, a value comparable to the time between

3 The aromatisation refers to the process that transforms an aliphatic-rich carbonaceous material to an aromatic-rich material. In that case we will speak of photo-darkening as an aromatic rich material appears dark compared to an aliphatic rich material.

4 Extreme ultraviolet photons with energies from 10 eV up to 124 eV (corresponding to 124 nm to 10 nm respectively).

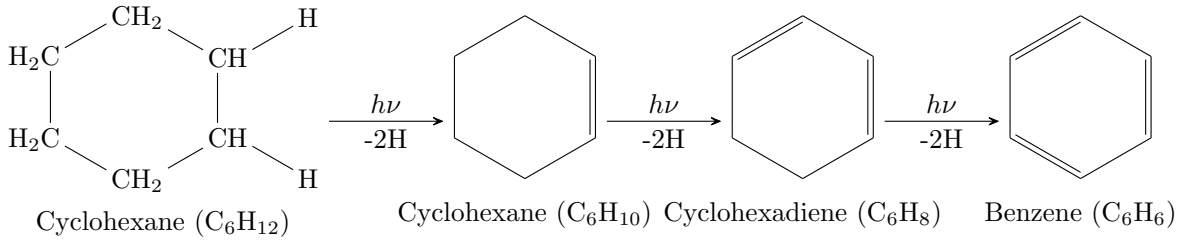

Figure 43: Representation of a chemical road that an aliphatic-rich carbonaceous material (cyclohexane), under irradiation, follows to become aromatic-rich (benzene). Photo-dissociation of C-H bonds leads to the creation of C=C bonds.

grain-grain collisions (Stepnik et al., 2003) but shorter than the dynamical timescale 10^7 years (Draine, 2011), describing the evolution of a molecular cloud. Therefore, carbonaceous grains that are smaller than 20 nm have time to be fully photo-darkened as do the 20 nm mantles of larger grains.

Thus, this view provides us with a continuous description of carbonaceous grains from the smallest that contain aromatic cycles and are stochatiscally heated to the largest that are in thermal equilibrium.

In addition, dust observations[5] (e.g. Planck Collaboration et al., 2011a,b) in the far-IR and sub-mm of the diffuse ISM are well fitted with a modified blackbody ($\beta \sim 1.8$) and a single temperature ($T_{dust} \sim 18\,K$ in the diffuse ISM). Therefore the emission in the far-IR can be represented by a single dust population. In THEMIS, it is assumed that this dust population is composed of silicate, surrounded by a mantle of carbonaceous material. Furthermore, modelling work done by Li and Greenberg, 2002b showed that the 3.4 μm C-H feature is expected to be polarised. However, using spectro-polarimetric observations along lines of sight oriented towards the Galactic center, Chiar and Tielens, 2006 found that the 3.4 μm C-H feature is essentially unpolarised, which strongly suggests that the carbonaceous material surrounding the silicate core, is H-poor and aromatic-rich (e.g. Jones, 2012a,c). It is therefore assumed in THEMIS that the carbonaceous mantle around a-Sil grains is aromatic-rich. This mantle is therefore smaller than 20 nm because conversely, it will not be entirely photo-darkened hence aromatic-rich (Jones, 2012b). Based on this 20 nm upper limit, and derived from the quantity of carbon that is left after determining what is in the gas and in the carbonaceous grains, an a-C mantle of 5 nm arround the a-Sil core is thus assumed. These grains are called a-Sil/a-C. A representation of these two dust populations can be found in Fig. 44 (left panel).

6.2.2 *THEMIS model for the diffuse ISM*

6.2.2.1 *Size distribution*

The THEMIS model for the diffuse ISM is composed of three dust populations that are build upon the two materials of carbon (a-C(:H)) and silicate (a-Sil), that were described in the previous section. These three dust populations are defined as follows:

- a-C(:H) dust population whose size distribution follows a power-law with an exponential cut-off. As this population is essentially composed of a-C grains (i.e. grains that are smaller than 20 nm), we will refer to it as a-C grains, although some a-C:H/a-C core/mantle grains are included.

5 Observations made with Planck, Herschel and IRAS

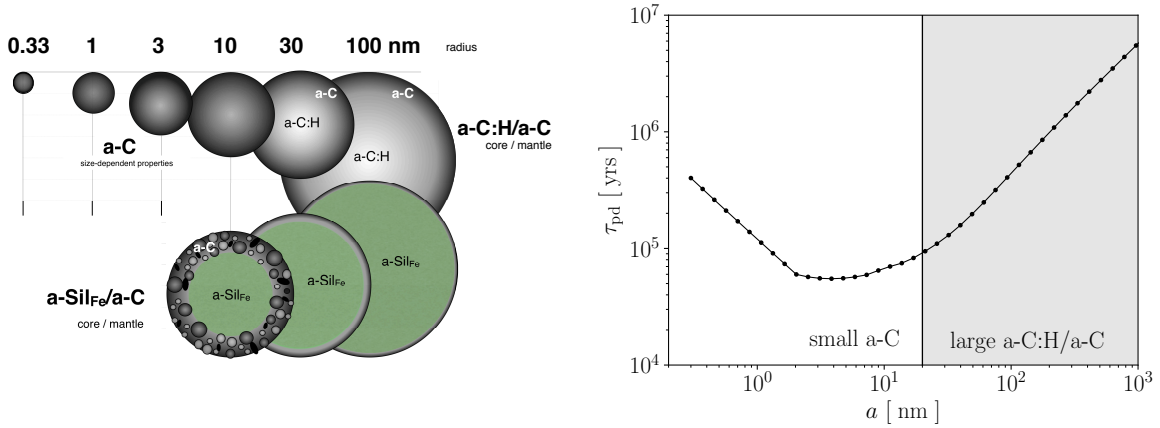

Figure 44: Left: Representation of THEMIS for the diffuse ISM. Black (light grey) parts refers to aromatic-rich (aliphatic-rich) material. Green parts refers to the silicate material. (Jones et al., 2013). Right: Photo-darkening timescale for the carbonaceous material, as a function of the grain size (see Eq. (46)). The darker grey part delimited by the vertical black line at 20 nm corresponds to the large core-mantle grains.

- a-C(:H) dust population whose size distribution follows a log-normal law. As this population is essentially composed of a-C:H/a-C core-mantle grains (i.e. grains that are larger than 20 nm), we will refer to it as a-C:H/a-C grains, although a few a-C are included.
- a-Sil/a-C dust population whose size distribution follows a log-normal law.

The size distribution of these three populations are shown in Fig. 45 and the associated parameters are detailed in Table. 2. As these grains are composed of either an a-C:H core or a silicate core a-Sil surrounded in both cases by an aromatic carbonaceous mantle a-C, we will refer to THEMIS for the diffuse ISM as Core-Mantle grains (CM) or diffuse ISM-like dust.

Fig. 45 also shows the spectra associated to these three dust populations, obtained with DustEM and considering a standard ISRF with $G_0 = 1$ and $N_H = 10^{20}$ H.cm^{-2}. It can be seen that dust emission in the near and mid-IR is entirely coming from a-C grains while dust emission in the far-IR is mainly coming from a-Sil/a-C grains. The aromatic bands in the near and mid-IR come from a-C grains, which make sense as most of the aromatic structures are contained in this population.

6.2.2.2 *Optical properties*

Optical properties are essential for understanding how a grain will interact with a photon (see Sect. 2.4). Based on laboratory experiments (Jones, 2012b), optical properties for THEMIS have been derived, following the formalism described in Sect. 2.3.

Fig. 46 shows the absorption efficiency, the scattering efficiency and the anisotropy factor for both the a-C:H/a-C and a-Sil/a-C populations, as a function of grain size. Regarding the dust absorption efficiency, it can be seen that regardless of the grain size and the composition (both a-C:H/a-C and a-Sil/a-C), Q_{abs} decreases with λ. This is hardly surprising since this result is known, the higher the energy of the incident photon is, the more likely it is to be absorbed by the grain. One may also note the presence of the aromatic bands for the smallest a-C:H/a-C grains, that are solely a-C grains given that they are smaller than 20 nm. The behaviour of the dust scattering efficiency is basically similar to the dust absorption efficiency, the higher the energy of the incident photon, the more likely it is to be scattered by the grain. One can also see that in the IR/submm, the absorption efficiencies decrease with λ (see Fig. 46,

Table 2: Size distribution parameters for each dust population. p-law is a power-law with an exponential tail and log-n is a log-normal distribution.

Name	size	α	a_{min}	a_{max}	a_c	a_t	a_0
			[nm]	[nm]	[nm]	[nm]	[nm]
Core Mantle grains (CM) - Diffuse ISM-like dust							
a-C	p-law	5	0.4	4900	10	50	-
a-C:H/a-C	log-n	-	0.5	4900	-	-	7
a-Sil/a-C	log-n	-	1	4900	-	-	8
Aggregated Mantle Mantle grains (AMM)							
AMM	log-n	-	47.9	700	-	-	479
Aggregated Mantle Mantle Ice grains (AMMI)							
AMMI	log-n	-	91.2	700	-	-	610

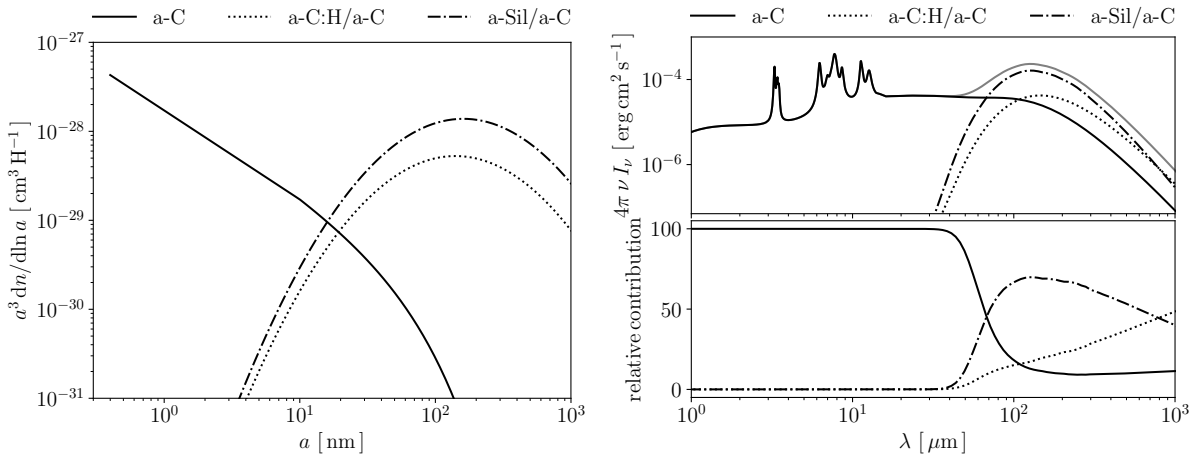

Figure 45: Left: Dust size distributions for a-C (black line), a-C:H/a-C (dotted line) and a-Sil/a-C (dotted dashed line). Top right: spectra for a-C (black line), a-C:H/a-C (dotted line) and a-Sil/a-C (dotted dashed line), computed with DustEM, using the standard ISRF with $G_0 = 1$ and $N_H = 10^{20}$ H.cm^{-2}. Bottom right: Relative contribution to the total spectrum for each dust component.

upper panels) and the scattering efficiencies decrease with λ^4 (see Fig. 46, middle panels). This behaviour is well known and described in the context of the Rayleigh approximation (see Sect. 2.3.1).

Finally, whether it is for a-C:H/a-C or a-Sil/a-C grains, the anisotropy factor for small grains is close to zero regardless of the wavelength. Photon scattering (see Sect. 2.3) by small grains is therefore isotropic. Regarding larger grains, the anisotropy factor is non-null in the UV, visible and near-IR, meaning that photon scattering at these wavelenghts is non-isotropic and oriented in the same direction as the incident photons.

6.2.2.3 *Stochastically heated grains vs. grains in thermal equilibrium*

The larger the grain, the higher the heat capacity hence large grains are at thermal equilibrium while small grains are stochastically heated (see Sect. 2.4). We represent the temperature distribution function dP/dT for different sizes of a-C grains with a standard ISRF and $G_0 = 1$ in Fig. 22. We note that the larger the grain is, the narrower the distribution is, until reaching a Dirac, which means that large grains are single temperature.

Here we investigate the size above which we can consider that grain is in thermal equilibrium. With this aim, we compare two temperatures:

- T_{eq} the equilibrium temperature of a dust grain, obtained through a thermal balance of the dust heating and cooling processes (see Sect. 2.4);
- T_{mean} the average temperature of a dust grain, obtained with the temperature distribution function dP/dT (see Fig. 22).

Albeit T_{mean} is physically relevant regardless of the dust size, this is not the case for T_{eq} as it has a physical meaning only for grains that are in thermal equilibrium. For grains that are in thermal equilibrium, $T_{mean} \sim T_{eq}$. We therefore consider that above a difference of 1 K between those two temperatures, grains are not in thermal equilibrium. In Fig. 47, T_{mean}, T_{eq} as well as the absolute difference between these temperatures are shown as a function of the dust size. Above $a = 7$ nm, ΔT_{a-C} and $\Delta T_{a-Sil/a-C}$ are below 1 K hence all dust grains that are larger than 7 nm are in thermal equilibrium.

6.2.2.4 *Influence of the radiation field on dust emission*

Here we study the influence of the radiation field, through the parameter G_0, on dust emission. Fig. 48 shows the dust size limit a_{lim} beyond which dust grains are in thermal equilibrium (following the criterion that was described in the previous section), as a function of G_0. We note that the larger G_0, the smaller the dust size limit. For a given dust size, the absorption of a photon by a grain leads to an increase in its temperature, then it cools by emitting infrared photons. If the radiation field is strong enough (i.e. if G_0 is large enough), some grains do not have time to cool significantly before the absorption of the next photon hence they are in thermal equilibrium. Therefore, an increase in G_0 results in smaller grains being in thermal equilibrium, which explains the decrease in a_{lim} with an increase in G_0.

Fig. 48 shows the dust spectra for G_0 varying from 1 to 10^5. We note that the emission in the near and mid-IR coming from a-C grains scales linearly with G_0. Regarding the emission from larger grains in thermal equilibrium, it is also scaling linearly with Go but shifts towards longer wavelengths hence larger grains are warmer.

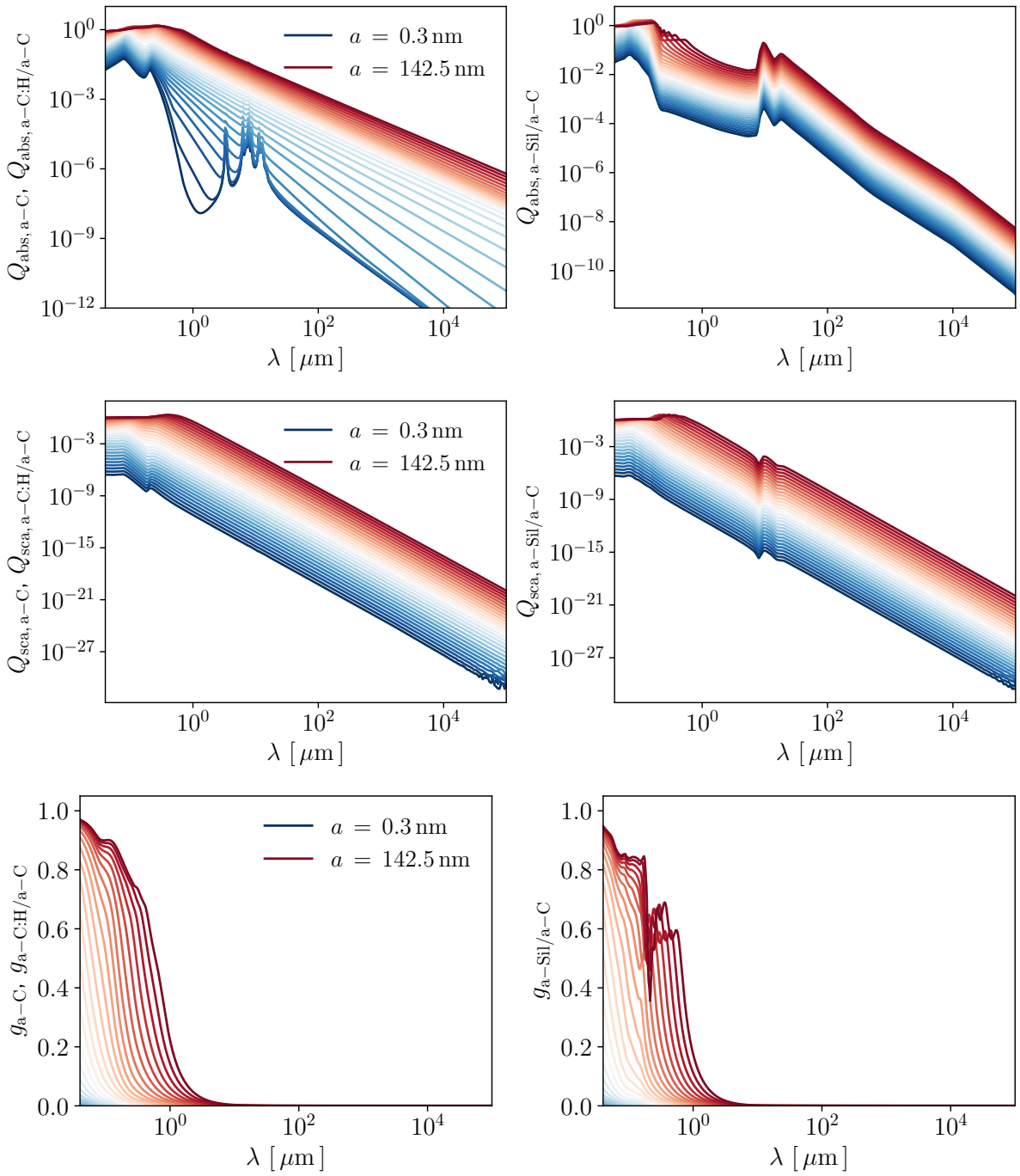

Figure 46: Top: Dust absorption efficiency for a-C:H/a-C (left) and a-Sil/a-C (right) with dust sizes varying from 0.3 nm (blue) to 142.5 nm (red). Middle: Dust scattering efficiency for a-C:H/a-C (left) and a-Sil/a-C (right). Bottom: Anisotropy factor for a-C:H/a-C (left) and a-Sil/a-C (right).

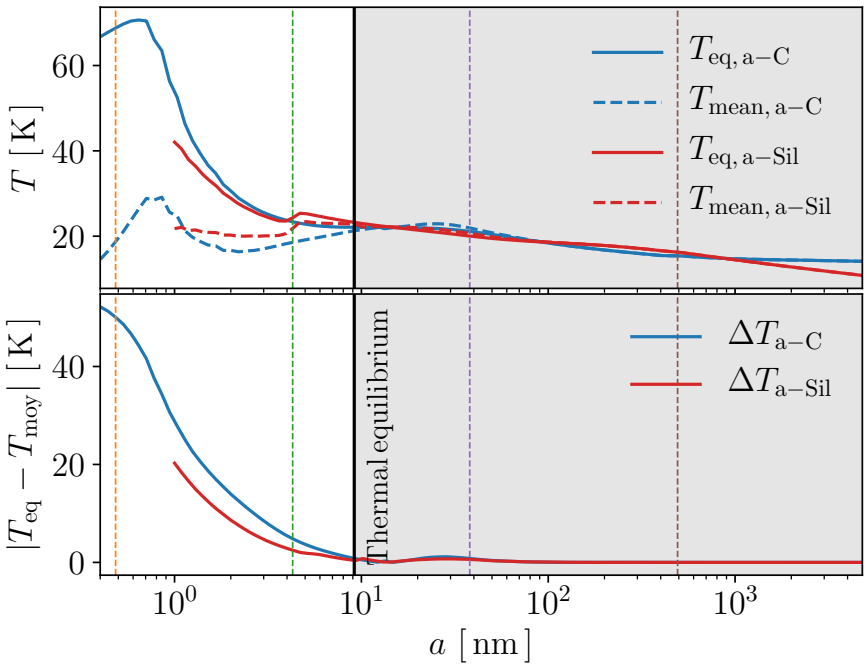

Figure 47: Top: T_{eq} (solid lines) and T_{mean} (dashed lines) for a-C grains (in blue) and a-Sil/a-C grains (in red) as a function of the dust radius. Bottom: Absolute difference between T_{eq} and T_{mean} for a-C grains in blue and a-Sil/a-C grains in red. The darker grey part delimited by the vertical black line corresponds to the sizes for which grains are in thermal equilibrium (i.e. $\Delta T \leqslant 1$). The vertical orange, green, purple and brown dashed lines corresponds to the sizes associated with the temperature distribution functions in Fig. 22.

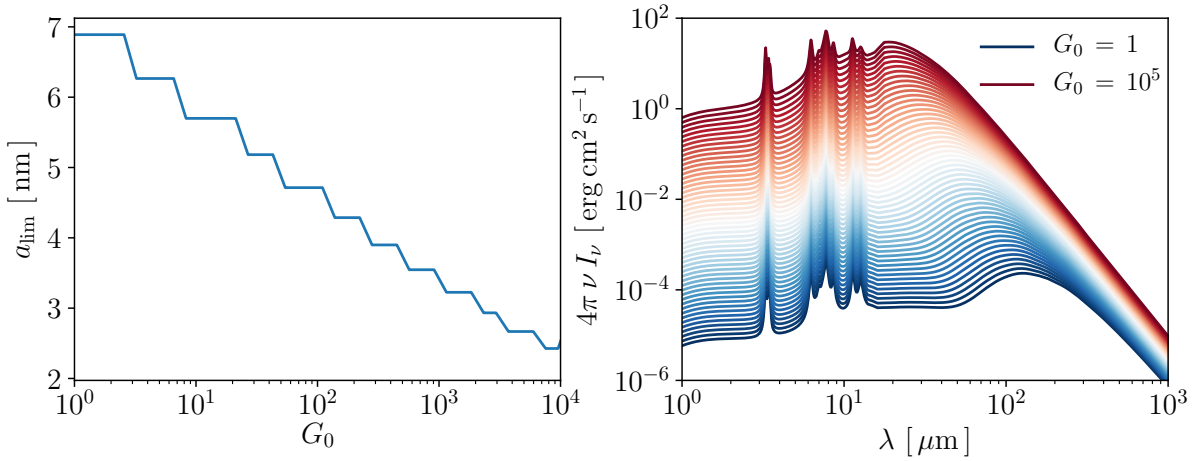

Figure 48: Left: Dust size limit a_{lim} above which dust grains are in thermal equilibrium, as a function of G_0. Right: Dust spectra for G_0 varying from 1 (Blue line) to 10^5 (red line), computed with DustEM using dust size distributions showed in Fig. 45.

6.2.2.5 *Influence of the dust size distribution on dust emission*

Modelling dust emission in PDRs with the aim of fitting the observations necessarily involves modifying the dust properties for the diffuse ISM through their size distributions. As we will see in Sect. v, dust emission is affected by both radiative transfer effects and variations of dust properties. Therefore, in order to disentangle the radiative transfer effects on dust emission, from those of variations in dust properties, we study the influence of such variations without radiative transfer with DustEM.

We modified the dust size distribution of the a-C grains through the three following parameters:

- The a-C abundance, i.e. the a-C mass to gas ratio, M_{a-C}/M_H, which we varied from 0.01 $\times 10^{-2}$ to 0.20 $\times 10^{-2}$ in steps of 0.01 $\times 10^{-2}$;
- The a-C minimum size, $a_{min,a-C}$, which we varied from 0.4 nm to 0.9 nm in steps of 0.02 nm;
- The slope of the a-C power-law size distribution, α, which we varied from -7 to -4 in steps of 0.1;

The dust size distributions described above, as well as the associated spectra computed with DustEM using a standard ISRF with $G_0 = 1$, are shown in Fig. 49.

A decrease in M_{a-C}/M_H or an increase in $a_{min,a-C}$ or α, leads to a decrease in the mass of the smallest a-C grains and therefore, a decrease in the near-IR emission. As the total dust mass is fixed, an increase in $a_{min,a-C}$ or α leads to a redistribution of the dust mass from the smallest to the largest a-C grains hence an increase in the mid-IR emission. In the far-IR, dust emission is unaffected by variations in M_{a-C}/M_H, $a_{min,a-C}$ and α as a-C grains are barely responsible for any dust emission at these long wavelengths. However, the dust emission in the far-IR slightly increases with an increase in α as the mass of the largest a-C increases significantly, unlike an increase in $a_{min,a-C}$.

6.2.3 *From diffuse to dense regions*

As the density increases, larger grains will evolve through processes such as carbon accretion and coagulation then coagulate together and therefore, change dust optical properties (e.g. Köhler, Ysard, and Jones, 2015).

As described in Jones et al., 2014, large grains can form a second mantle either through accretion of C and H atoms, available in the gas phase or through coagulation of a-C grains on the grain surface. As accretion occurs in dense regions ($A_V > 1$), the re-hydrogenation process is sufficiently efficient to leave the mantle H-rich and/or, the UV radiation field attenuated sufficiently to prevent mantle photo-processing. Photo-processing is efficient in regions where the UV radiation field is only weakly attenuated (Alata et al., 2014). The influence of this mantle formation around large grains on their optical properties is described in Köhler, Ysard, and Jones, 2015. These grains are called Core-Mantle-Mantle grains (CMM).

In denser regions, large grains coagulate together to form grain aggregates. As the coagulation timescale of a-C grains on large grains is shorter than that of large grain coagulating together (e.g. Köhler et al., 2012), we can assume that all the a-C grains are incorporated in the large grains thus in coagulated grains. As described in Köhler, Ysard, and Jones, 2015, we assumed that coagulated grains are composed of one large grain with an aliphatic amorphous carbon core and three large grains with an amorphous silicate core of olivine and pyroxene

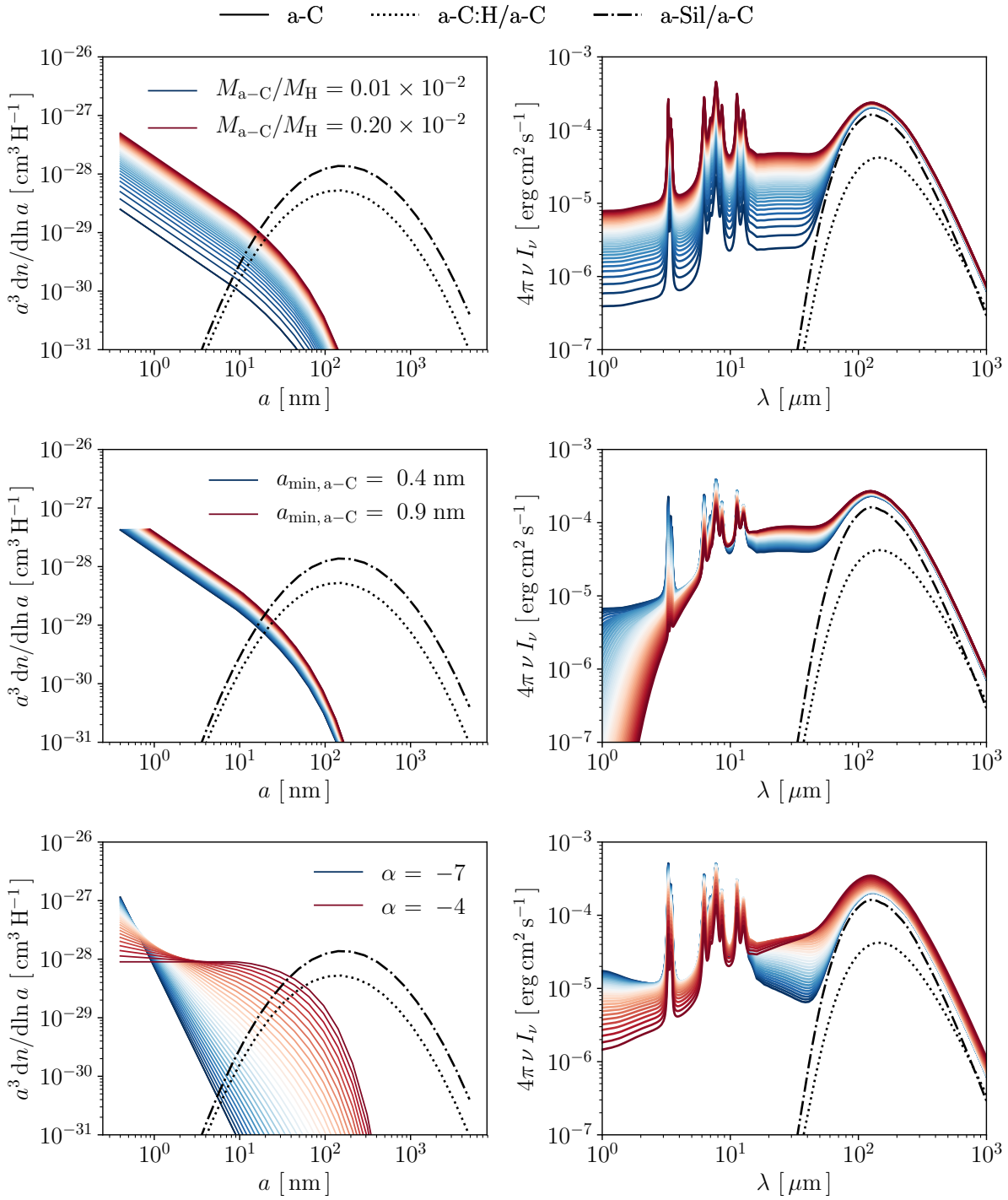

Figure 49: Left: Dust size distributions of a-C grains for M_{a-C}/M_H varying from 0.01 $\times$ 10^{-2} (blue line) to 0.20 $\times$ 10^{-2} (red line) (top), $a_{min,a-C}$ varying from 0.4 nm (blue line) to 0.9 nm (red line) (middle), α varying from -7 (blue line) to -4 (red line) (bottom). Dust size distributions for a-C:H/a-C grains and a-Sil/a-C grains are shown in dotted and dotted dashed lines respectively. Right: Spectra associated with these dust size distributions. Note that the lines in colours represent the total spectra and not only the a-C grains spectra.

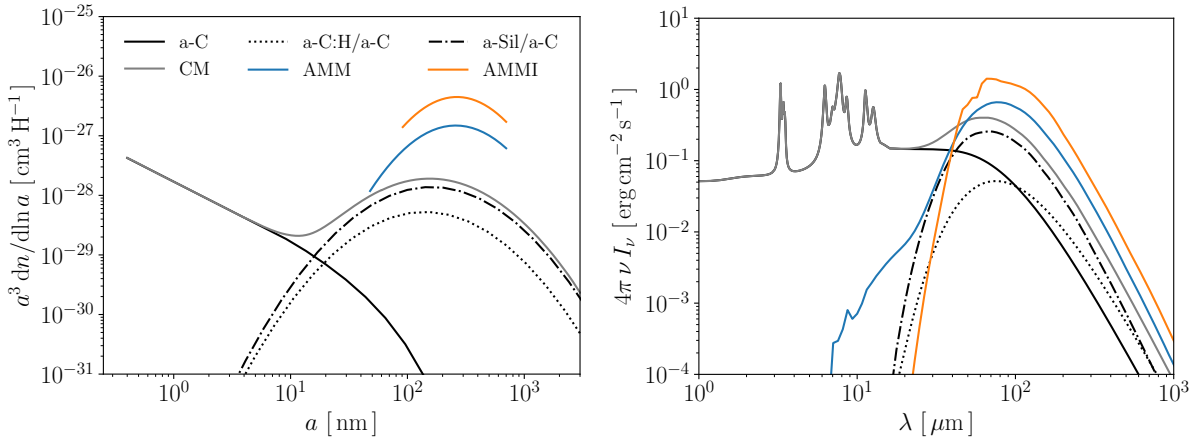

Figure 50: Left: Size distributions of the dust mixtures from THEMIS (parameters are listed in Table. 2) for CM-grains, i.e. diffuse ISM-like dust (grey line), AMM (blue line) and AMMI (orange line), i.e. grain aggregates typical of starless dense clouds. Black line, dotted-line and dash-dot line correspond to a-C, a-C:H/a-C and a-Sil/a-C respectively, which are the sub-components of the CM-grains. Right: Associated spectra, computed with DustEM with a radiation field corresponding to a star at 34 600 K with $G_0 = 100$ and $N_H = 10^{20}$ H cm^2.

type with Fe/FeS inclusions. These aggregates of CMM are called Aggregate-Mantle-Mantle grains (AMM). Above a given threshold into cloud extinction ($A_V \sim 1.5$), a mantle of water-ice forms around coagulated grains, these grains are called Aggregate-Mantle-Mantle-Ice grains (AMMI).

In the following, we use several dust mixtures (see Fig. 51) that are labelled in Table 2, as in Köhler, Ysard, and Jones, 2015 and Jones et al., 2017. The size distributions of these dust mixtures as well as their associated spectra computed with DustEM, can be found in Fig. 50 where it can be seen that grain aggregates (AMM and AMMI) are more emissive than CM grains.

6.2.4 *A brief history of THEMIS*

Behind the development of THEMIS are many hidden studies that have been undertaken by the core team. Here we summarise the papers that compose the backbone of THEMIS.

THEMIS came to light, partly motivated by the fact that the wide disparity of physical conditions in the ISM triggers an evolution of dust grains, such as their composition, size, and shape. Indeed, dust irradiation by UV photons leads to the destruction of C-H bonds in a-C(:H) grains, and therefore to their progressive aromatisation (see Fig. 43). It was therefore necessary to define a framework in which to study the consequences of the (de)-hydrogenation of a-C(:H) grains on their emission. This was based on the formalism of eRCN[6] models for H-rich a-C(:H) grains (Phillips, 1979; Döhler, Dandoloff, and Bilz, 1980; Thorpe, 1983; Jones, 1990) and DG[7] models for H-poor a-C(:H) grains (Tamor and Wu, 1990). These studies lead to the three founding papers of THEMIS (Jones, 2012a,b,c) that were later used to create THEMIS (Jones et al., 2013). Eversince, further studies have improved upon this dust model.

Bocchio et al., 2012, 2013 found that small a-C(:H) grains (with $N_C < 1000$ or $a < 3$ nm) are efficiently destroyed in hot gas (10^4-10^8 K), due to UV photons heating and collisions with electrons, and that therefore they cannot be abundant in such regions. They also studied in

6 extended Random Covalent Network
7 Defective Graphite

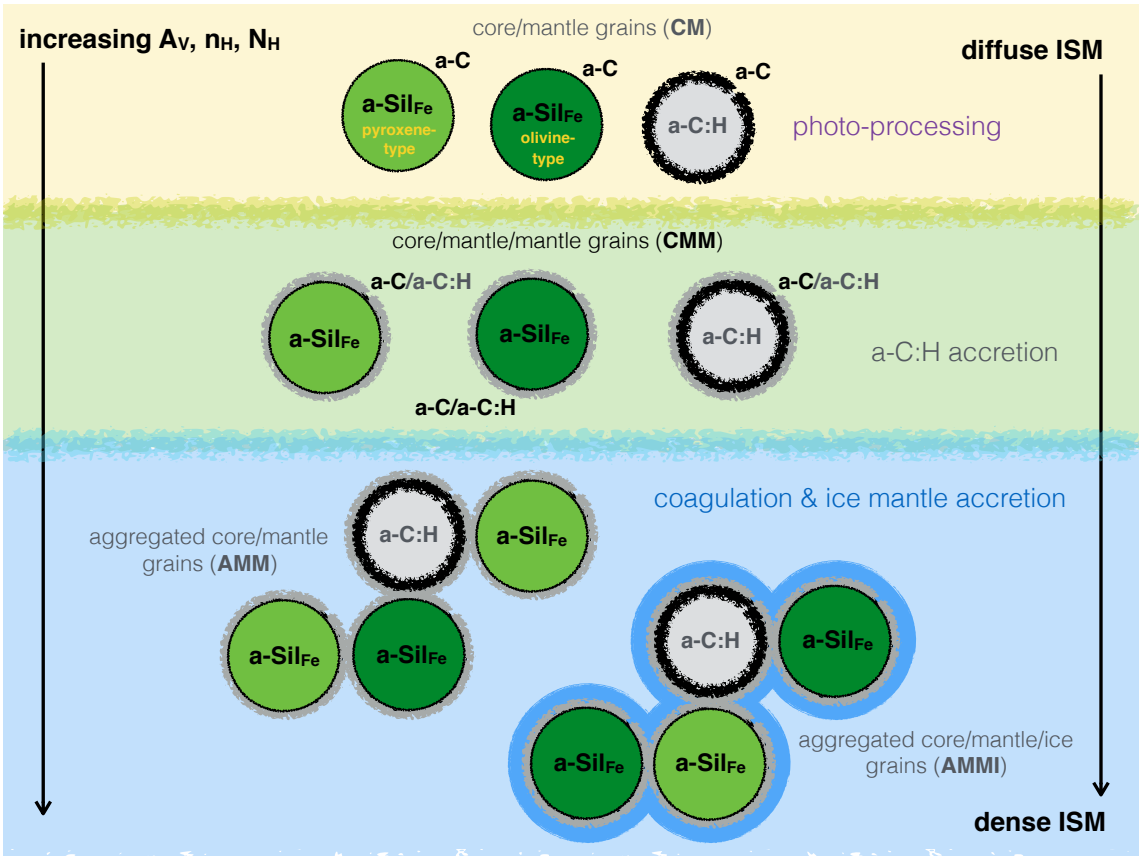

Figure 51: Schematic view of the dust evolution from the diffuse ISM to denser regions, mainly through photo-processing, accretion and coagulation (Jones et al., 2017).

Bocchio, Jones, and Slavin, 2014, dust destruction in shock waves (50-200 km s^{-1}) and showed that a-C(:H) grains are efficiently destroyed in these regions. As observations were pointing towards larger abundances of a-C(:H) grains in the ISM, which was not in agreement with this large a-C(:H) grain destruction efficiency, they proposed that dust grains must reform in the dense regions of the ISM.

As discussed in the introduction of this thesis, the observed far-IR dust opacity increases from diffuse to dense regions of the ISM. Köhler et al., 2012 showed that the coagulation of small grains ($a = 3.5$ nm) onto the surface of grain aggregates (that are composed of four large grains with $a = 60$ nm), can explain both the increase in the far-IR dust opacity and the decrease in dust grain temperature, from diffuse to dense regions. This study showed that aggregates, which will later be at the origin of the so-called AMM and AMMI used in this thesis, is required to understand the observations from dense regions of the ISM. Using the radiative transfer code CRT (the previous version of SOC) together with DustEM, Köhler, Ysard, and Jones, 2015 studied the influence of using grain aggregates (with or without an ice mantle) in dense regions instead of using diffuse ISM-like grains. They showed that using aggregates instead of diffuse ISM-like dust, implies an increase in the far-IR opacity by a factor of 3, up to 7 if using aggregates with an ice mantle. They showed that dust evolution through coagulation and accretion can explain the observed variations of the dust emission, from the diffuse ISM to denser regions.

Regarding the silicate component, Köhler, Jones, and Ysard, 2014 showed that using amorphous olivine-type and pyroxene-type silicates better matches the interstellar silicate absorption band profiles, than the astronomical silicates of Draine and Li, 2007. The silicates of Köhler, Jones, and Ysard, 2014 were therefore used in THEMIS after this study.

The H_2 formation process was also studied in the framework of THEMIS and in the case of low to moderate ratiation field intensities ($1 \leqslant G_0 \leqslant 10^2$). Hydrogen molecules are released from a-C(:H) grains through UV photolysis. This new road for H_2 formation was studied in Jones and Habart, 2015 and seems to be a viable route to form H_2 in regions where the radiation field is moderate.

Later, Ysard et al., 2015 added constraints on the aromatic-rich carbonaceous mantle around both carbonaceous and silicate grains, using Planck observations of the diffuse ISM. They also showed that dust properties must evolve as variations of the radiation field alone cannot explain the observed variation of the dust emission within the ISM.

In dense interstellar clouds, dust scattering of the incident interstellar radiation can be observed in the near-IR and mid-IR. This phenomenon was labelled as *Cloudshine* for the near-IR (Foster and Goodman, 2006) and *Coreshine* for the mid-IR (Pagani et al., 2010). Later, (Lefèvre et al., 2014) showed that these observations can be explained in terms of grain growth. Within the THEMIS framework, Jones et al., 2016; Ysard et al., 2016 showed that these observations can be well explained with a combination of an aliphatic-rich silicate mantle around CM grains and coagulation of these grains into aggregates (AMM, AMMI).

Similar to the first paper that describes THEMIS (Jones et al., 2013), a second general paper about THEMIS presents the updated version of THEMIS (Jones et al., 2017), taking into account the studies described above.

Then, as dust grains evolve from diffuse to dense regions, Ysard et al., 2018 studied the variation in optical properties of both the large grains in THEMIS ($a > 50$ nm) and the grain aggregates, as a function of their size, composition, and structure. They found that the optical properties are highly dependant on grain properties and therefore, that it is required to consider the detailed grain structure in order to understand how dust evolves with physical conditions such as the radiation field and the local density.

For seven years, THEMIS has been used by many researchers around the world. An exhaustive list of about 40 papers where THEMIS is used, can be found here.

7 RADIATIVE TRANSFER TOOLS

Ceux qui rêvent éveillés ont conscience de mille choses qui échappent à ceux qui ne rêvent qu'endormis.

Edgar Allan Poe - *Eleonora*

Contents

In astrophysics, most of the information comes through light. However, photons strongly interact with dust and gas species. It is therefore important to understand how light travels throughout the matter, from the stellar inferno to the deepest part of the human eye. This domain is known as radiative transfer.

7.1 ABOUT RADIATIVE TRANSFER

An important quantity in radiative transfer is the specific intensity, I_ν, which is why we define it first. We consider photons crossing, during a time interval dt, the surface element $d\Sigma$ centered in M and whose normal vector is $\mathbf{n}$ (see Fig. 52). The total energy of photons, with frequencies in $[\nu, \nu + d\nu]$ and whose directions are inside the solid angle $d\Omega$ around the direction[1] $\mathbf{k}$, is proportional to dt, the frequency internal $d\nu$, the surface element $d\Sigma$, and to the solid angle $d\Omega$. This energy can therefore be written as follows:

$$dE_\nu(l) = I_\nu(l) d\Sigma d\Omega dt d\nu, \tag{48}$$

1 In that case, it is assumed that $\mathbf{k}$ is perpendicular to the surface element $d\Sigma$ hence $\mathbf{k} = \mathbf{n}$.

where $I_\nu(l)$ is the specific intensity. More generally, when $\theta = (\mathbf{n}, \mathbf{k})$ is introduced, Eq. 48 become

$$dE_\nu(l) = I_\nu(l)\cos(\theta)d\Sigma d\Omega dt d\nu. \tag{49}$$

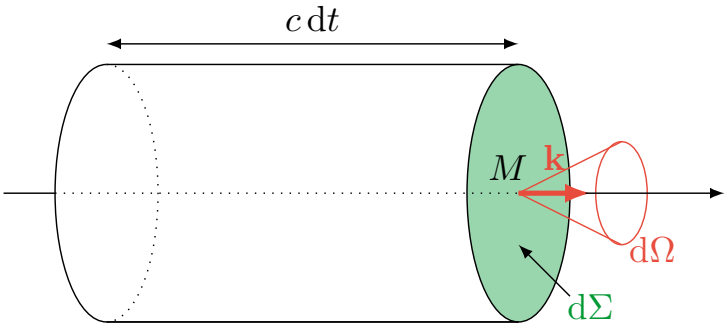

Figure 52: Definition of the notation that is used to describe the specific intensity I_ν. The latter is expressed across an elementary surface $d\Sigma$ (in green), in a direction $\mathbf{k}$ (in red) inside a solid angle element $d\Omega$.

The Universe is far from being empty hence the specific intensity varies under the influence of absorption, emission, and scattering. We therefore need to study the spatial variations of the specific intensity throughout the matter.

In Sect. 7.1.1 we describe how the specific intensity varies under the influence of the absorption and emission. In Sect. 7.1.2 we describe how the specific intensity varies under the influence of the absorption, emission, and scattering.

7.1.1 *Radiative transfer without scattering*

In order to define the radiative transfer equation, with or without scattering, the general idea is to consider an elementary volume and to perform an energy balance inside this volume. We therefore consider an elementary cylinder oriented in the direction $\mathbf{k}$, with a surface $d\Sigma$ centered in M with a height $dl = c\,dt$, where l is the position along this axis defined by M and $\mathbf{k}$ (see Fig. 53).

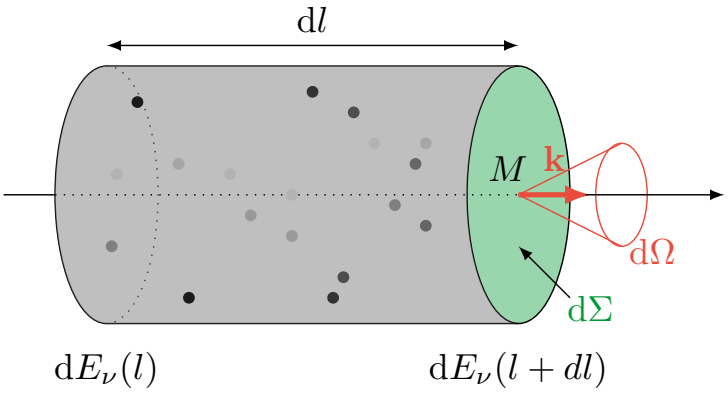

Figure 53: Definition of the notation that is used to express the variation of energy $d^2E_\nu(l)$, between l and $l+dl$, across a cylinder oriented in the direction $\mathbf{k}$, with a surface $d\Sigma$ centered in M with a height dl, where l is the position along this axis defined by M and $\mathbf{k}$. In this case, only absorption and dust emission are taken into account. The black/grey dots correspond to the particles. As the particles are located at different depths inside the cylinder, the intensity that we receive is different from one particle to another, hence the different shades of grey.

We first define the quantity that contributes to a decrease in energy inside this elementary cylinder and then, the quantity that contributes to an increase in energy. Thence, we perform the energy balance to establish the radiative transfer equation without scattering.

7.1.1.1 *Dust absorption and emission from a theoretical vantage point*

DUST ABSORPTION The (negative) variation of energy $d^2E_{\nu,abs}$ of $dE_\nu(l)$ between l and $l+dl$, because of the processus of absorption, can be expressed as follows:

$$d^2E_{\nu,abs} = -\kappa_\nu \, dl \, dE_\nu < 0, \tag{50}$$

where

$$\kappa_\nu = \int_{a_{min}}^{a_{max}} Q_{abs}(a,\nu)\,\pi a^2 \, dn(a), \tag{51}$$

with $n(a)$ the number of particles[2] with a radius a per unit of volume, a_{min} and a_{min} are the minimum and maximum radii of the particles size distribution, and Q_{abs} the absorption efficiency of the particle (see Sect. 2.3).

From this quantity κ_ν stems an important notion in astrophysics, the optical depth τ_ν that is defined as follows:

$$d\tau_\nu = \kappa_\nu dl. \tag{52}$$

This quantity is dimensionless. We talk about an optically thin medium when $\tau_\nu << 1$ and an optically thick medium when $\tau_\nu >> 1$.

2 We assume here and all along this work that particles are spherical.

DUST EMISSION The presence of radiative sources in the considered cylinder contributes to variations in $dE_\nu(l)$. The (positive) variation of energy $d^2E_{\nu,em}$ of $dE_\nu(l)$ between l and $l + dl$ can be expressed as follows:

$$d^2E_{\nu,em} = \epsilon_\nu dV d\Omega dt d\nu > 0, \tag{53}$$

where ϵ_ν is the emissivity and $dV = d\Sigma dl$ is the volume of the elementary cylinder. This is the power emitted per unit volume, per unit solid angle, and per frequency interval towards the direction $\mathbf{k}$. It is expressed in $W\,m^{-3}\,Hz^{-1}\,sr^{-1}$.

7.1.1.2 *Generation of the radiative transfer equation without scattering*

In the case where only the processes of absorption and emission occur and using the quantities defined above, the energetic balance is written as follows:

$$dE_\nu(l + dl) - dE_\nu(l) = d^2E_\nu(l) = d^2E_{\nu,abs} + d^2E_{\nu,em}. \tag{54}$$

As $dl << 1$, we can approximate $dE_\nu(l + dl)$ with its first order Taylor expansion $dE_\nu(l + dl) = dE_\nu(l)/dl + dE_\nu(l)$. Thus, Eq. (54) can therefore be simplified as follows:

$$\frac{dE_\nu(l)}{dl} = d^2E_{\nu,abs} + d^2E_{\nu,em}. \tag{55}$$

Using Eq. (48), Eq. (50), and Eq. (53) inside Eq. (55), the radiative transfer equation without scattering can be written as follows:

$$\frac{dI_\nu(l)}{dl} = -\kappa_\nu(l)I_\nu(l) + \epsilon_\nu(l), \tag{56}$$

and if $\kappa_\nu \neq 0$, in terms of optical depth (see Eq. (52)):

$$\frac{dI_\nu(\tau)}{d\tau_\nu} = -I_\nu(\tau) + S_\nu(\tau), \tag{57}$$

where $S_\nu(\tau) = \epsilon_\nu(\tau)/\kappa_\nu(\tau)$ is the source function. With $I_\nu(\tau_\nu = 0) = I_{0,\nu}$, the solution of this first-order differential equation can be written:

$$I_\nu(\tau) = I_{0,\nu}\, e^{-\tau_\nu(l)} + \int_0^{\tau_\nu(l)} S_\nu\left(\tau'_\nu\right) \exp\left(-\left(\tau_\nu(l) - \tau'_\nu\right)\right) d\tau'_\nu. \tag{58}$$

In a purely absorbing medium (that is, $S_\nu = 0$), the previous equation can be simplified to yield the well-known Beer-Lambert law.

7.1.2 *Radiative transfer with scattering*

In the previous section, we described radiative transfer with only absorption and emission. However, if we want to perform radiative transfer in the ISM accurately, it is necessary to take into account scattering. The major difficulty with scattering is that all the regions are connected. Moreover, conversely to absorption (emission) that only contributes to a negative

(positive) variation of $dE_\nu(l)$, scattering has two contributions to variations of $dE_\nu(l)$: a positive contribution $d^2E^+_{\nu,sca}$, and a negative contribution $d^2E^-_{\nu,sca}$ (see Fig. 54).

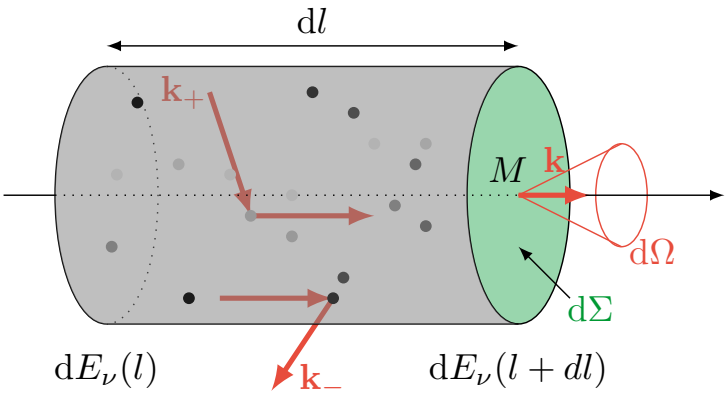

Figure 54: Definition of the notation used to express the variation of energy $d^2E_\nu(l)$, between l and $l + dl$, across a cylinder oriented in the direction $\mathbf{k}$, with a surface $d\Sigma$ centered in M with a length dl, where l is the position along this axis defined by M and $\mathbf{k}$. In this case, dust absorption, emission and scattering, are taken into account. The black/grey dots correspond to the particles. As the particles are located at different depth inside the cylinder, the intensity received is different from one particle to another, hence the different shades of black.

When a photon with a incident direction $\mathbf{k}$ is scattered by a particle in a direction $\mathbf{k}'_-$ (negative contribution to $dE_\nu(l)$), we can express the energy $d^2E^-_{\nu,sca}$ associated with this negative contribution, as follows:

$$d^2E^-_{\nu,sca} = -\sigma_\nu dl dE_\nu = -\sigma_\nu I_\nu dV d\Omega dt d\nu < 0, \tag{59}$$

where

$$\sigma_\nu = \int_{a_{min}}^{a_{max}} Q_{sca}(a, \nu)\, \pi a^2\, dn(a), \tag{60}$$

with $n(a)$ the number of particles with a radius a per unit of volume, a_{min} and a_{max} are the minimum and maximum radii of the particles size distribution, and Q_{sca} the scattering efficiency of the particle (see Sect. 2.3). Note that σ_ν has the same dimension as κ_ν (see Eq. (51)), i.e. inverse length.

In order to express the positive contribution of scattering to $dE_\nu(l)$, it is necessary to first define the differential scattering cross-section $\tilde{s}_{\nu,sca}(\mathbf{k} \to \mathbf{k}')$, which characterizes the scattering efficiency of an incident photon with a direction $\mathbf{k}$ (inside the solid angle $d\Omega$) towards a direction $\mathbf{k}'$ (inside the solid angle $d\Omega'$). The differential scattering cross-section $\tilde{s}_{\nu,sca}(\mathbf{k} \to \mathbf{k}')$ is related to the differential scattering coefficient $\tilde{\sigma}_\nu(\mathbf{k} \to \mathbf{k}')$ through the relation $\tilde{\sigma}_\nu(\mathbf{k} \to \mathbf{k}') = n\, \tilde{s}_{\nu,sca}(\mathbf{k} \to \mathbf{k}')$, where n is the number of particles per unit volume. With this definition, $\tilde{\sigma}_\nu(\mathbf{k} \to \mathbf{k}')$ is linked to σ_ν by the following relation:

$$\sigma_\nu = \int \frac{\tilde{\sigma}_\nu(\mathbf{k} \to \mathbf{k}')}{4\pi} d\Omega'. \tag{61}$$

Note that if the scattering isotropic $\tilde{\sigma}_\nu(\mathbf{k} \rightarrow \mathbf{k}')$ does not depend on the direction, $\sigma_\nu = \tilde{\sigma}_\nu(\mathbf{k} \rightarrow \mathbf{k}')$.

Thence, it is possible to express the energy $d^2E^+_{\nu,sca}$ associated with the positive variation of $dE_\nu(l)$, as follows:

$$d^2E^+_{\nu,sca}(\mathbf{k}) = \left(\frac{1}{4\pi}\int_{\Omega'} \tilde{\sigma}_\nu(\mathbf{k'} \rightarrow \mathbf{k})\, I_\nu(\mathbf{k'})\, d\Omega'\right) dV d\Omega dt d\nu > 0. \tag{62}$$

As the positive and negative contributions of the scattering to $dE_\nu(l)$ are now defined, it is possible to establish the radiative transfer equation with scattering, from the quantities defined above, and the energetic balance defined as follows:

$$dE_\nu(l+dl) - dE_\nu(l) = d^2E_\nu(l) = d^2E_{\nu,abs} + d^2E_{\nu,em} + d^2E^-_{\nu,sca} + d^2E^+_{\nu,sca}. \tag{63}$$

As $dl << 1$, we can approximate $dE_\nu(l+dl)$ with its first order Taylor expansion $dE_\nu(l+dl) = dE_\nu(l)/dl + dE_\nu(l)$ and using Eq. (48), Eq. (50), Eq. (53), Eq. (59), and Eq. (62) inside Eq. (63), the radiative transfer equation with scattering is therefore defined as follows:

$$\frac{dI_\nu(l)}{dl} = -(\kappa_\nu(l) + \sigma_\nu(l))\, I_\nu(l) + \epsilon_\nu(l) + \frac{1}{4\pi}\int_{\Omega'} \tilde{\sigma}_\nu(\mathbf{k'} \rightarrow \mathbf{k})\, I_\nu(\mathbf{k'})\, d\Omega'. \tag{64}$$

This equation clearly highlights the further challenge imposed by scattering in radiative transfer as even if the emissivity, as well as the absorption and scattering coefficients do not depend on the radiation field, we need to resolve this integro-differential equation.

7.2 DUSTPDR, A 1D RADIATIVE TRANSFER CODE

DustPDR is a 1D radiative transfer code that has been developed at the IAS and used in previous studies (e.g Compiègne et al., 2008; Arab et al., 2012). During the first part of my PhD and before using a more sophisticated radiative transfer code (that is, SOC, see Sect. 7.3), I used DustPDR, which is described here.

7.2.1 *Presentation of DustPDR*

DustPDR is built upon the semi-infinite plane-parallel approximation, which is valid if the star is far from the cloud. The latter is defined as an infinite slab that receives radiation orthogonally. Hence, radiative transfer is only considered along the star-cloud axis (i.e. along the z-axis in Fig. 55).

In order to perform radiative transfer along the PDR, several quantities that define the radiation field and the PDR are required:

- the radiation field at the edge of the PDR, $I_{\nu,0}$;
- the density profile along the PDR, $n_H(z)$;
- the width of one cell, Δ;
- the dust-to-gas ratio for each dust population along the PDR, $\left(M_{dust,j}/M_H\right)(z)$ where j refers to the dust population (e.g. a-C, a-C:H/a-C, a-Sil/a-C, ...).

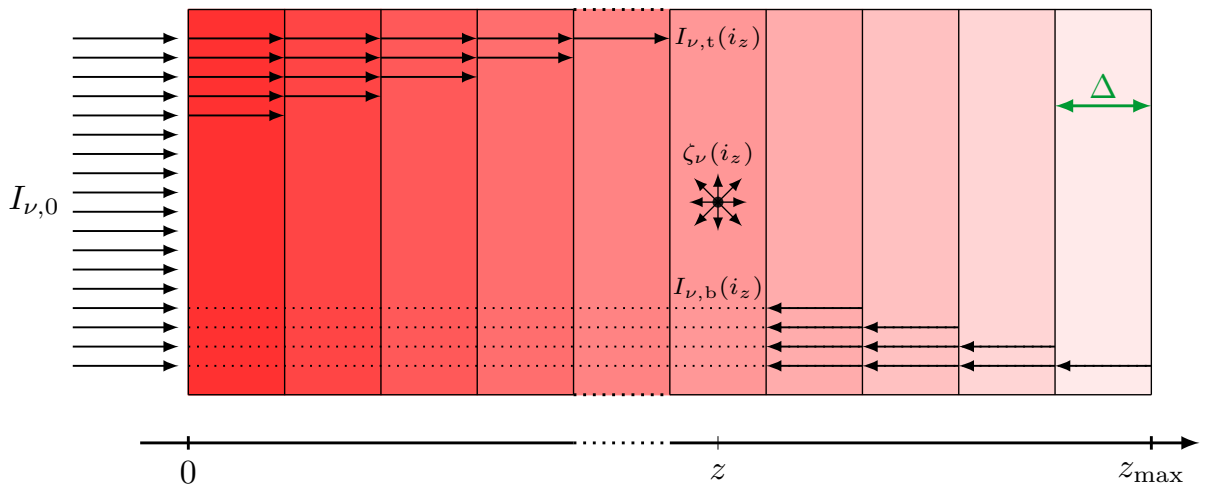

Figure 55: Schematic illustration of a PDR illuminated by a radiation field (from the left) described by its specific intensity $I_{\nu,0}$. The quantities $I_{\nu,t}(i_z)$, $I_{\nu,b}(i_z)$, and $\zeta_\nu(i_z)$ correspond to the transmitted intensity, back-scattered intensity, and the dust emission per proton, respectively. The width of a cell Δ, is represented in green. The red shades correspond to the dust temperature, that is decreasing from the illuminated edge of the PDR to the denser part.

As DustPDR is linked with DustEM in order to compute the dust emission, the dust properties are therefore provided through DustEM. From there, radiative transfer is performed and provides us with the specific intensity along the PDR, $I_\nu(z)$, that is defined as:

$$I_\nu(i_z) = I_{\nu,t}(i_z) + I_{\nu,b}(i_z) + I_{\nu,IR}(i_z). \tag{65}$$

As described theoretically in the previous section, there are three contributions (see Eq. (65)) to this intensity:

- $I_{\nu,t}(z)$, the transmitted intensity from the star that is attenuated by both dust absorption and dust scattering (back-scattering contributes negatively to this transmitted intensity and forward-scattering contributes positively to this transmitted intensity), between $z = 0$ and z;
- $I_{\nu,IR}(z)$, the intensity (essentially in IR) emerging from the dust that has been heated;
- $I_{\nu,b}(z)$, the back-scattered intensity by parts of the clouds that are located between z and z_{max}.

In the following section, we describe these three different intensities by bridging the analytical equations described in Sect. 7.1 and their numerical expressions in the context of DustPDR. Although the treatment of the dust absorption and emission with this geometry is not difficult, the treatment of scattering is still complicated, hence we will also describe the assumptions that are made.

7.2.2 *Dust emission and absorption from a numerical vantage point*

We here present how dust emission and absorption are treated in DustPDR. In an environment where only absorption exists (i.e. $S_\nu(\tau) = 0$), Eq. (57) can be simplified, and the solution of this equation is:

$$I_{\nu,t}(z) = I_{\nu,0} \exp\left(-\tau_\nu(z)\right). \tag{66}$$

This is an analytical expression that needs to be adapted numerically. By defining i_z, the index of a cell located at position z, the previous equation can be numerically written:

$$I_{\nu,t}(i_z) = I_{\nu,0} \exp\left(-\tau_\nu(i_z)\right). \tag{67}$$

In Sect. 7.1, τ_ν was described by taking into account only the absorption (see Eq. (51) and Eq. (52)). As seen in Sect. 7.1.2, photons that are back-scattered contribute negatively to variations of I_ν. We can therefore define an effective κ_ν, defined as $\kappa_\nu^{\text{eff}} = \kappa_\nu + \sigma_{\nu,b}$, where $\sigma_{\nu,b}$ is the backward scattering cross section (see Sect. 2.3.2.2). Thence, we can express numerically τ_ν as:

$$\tau_\nu(i_z) = \sum_{i=0}^{i_z} \kappa_\nu^{\text{eff}}(i)\,\Delta = \sum_{i=0}^{i_z} \left(\kappa_\nu(i) + \sigma_{\nu,b}(i)\right)\Delta. \tag{68}$$

In an environment with only emission (i.e. $\kappa_\nu(\tau) = 0$), Eq. (56) can be simplified, and the solution of this equation is:

$$I_{\nu,\text{IR}}(z) = \int_0^{z_{\max}} \epsilon_\nu(z') \exp\left(-\left(\tau_\nu(z) - \tau_\nu(z')\right)\right) dz'. \tag{69}$$

In DustPDR, it is assumed that dust IR emission is not absorbed within the cloud hence $\tau_\nu << 1$. This implies that $\exp\left(-\left(\tau_\nu(z) - \tau_\nu(z')\right)\right) \simeq 1$ and Eq. (69) can therefore be simplified as follows:

$$I_{\nu,\text{IR}}(z) = \int_0^{z_{\max}} \epsilon_\nu(z') dz', \tag{70}$$

and numerically:

$$I_{\nu,\text{IR}}(i_z) = \sum_{i=0}^{i_{\max}} \epsilon_\nu(i)\Delta, \tag{71}$$

with $\epsilon_\nu(i_z) = n_H(i_z)\zeta_\nu(i_z)/4\pi\nu$ where ζ_ν is the dust emission per proton, computed by DustEM and expressed in $\mathrm{W\,m^{-2}}$.

7.2.3 *Dust scattering from a numerical vantage point*

Back-scattered photons from cells that are located deeper into the PDR, i.e. beyond the position z, contribute positively to the total intensity $I_\nu(z)$ that is emerging from the cell located at the position z. The elementary back-scattering intensity $dI_{\nu,t}(z')$, emerging from a cell located at the position $z' > z$, is attenuated by dust extinction. We can therefore define the back-scattered intensity as follows:

$$I_{\nu,b}(z) = \int_z^{z_{max}} dI_{\nu,b}(z') \exp\left(-\tau_\nu(z' \rightarrow z_{max})\right), \tag{72}$$

where

$$\tau_\nu(z \rightarrow z_{max}) = \int_z^{z_{max}} \kappa_\nu^{eff}(z) dz = \int_z^{z_{max}} \left(\kappa_\nu(z) + \sigma_{\nu,b}(z)\right) dz. \tag{73}$$

The elementary back-scattering intensity $dI_{\nu,t}(z')$ can be expressed as the difference between the transmitted intensity and the same intensity with a dilution factor that corresponds to what has been back-scattered along an elementary back-scattered depth, $d\tau_{\nu,b} << 1$. Thus:

$$dI_{\nu,b}(z) = I_{\nu,t}(z)\left(1 - \exp\left(d\tau_{\nu,b}(z)\right)\right) \simeq I_{\nu,t}(z)\, d\tau_{\nu,b}(z). \tag{74}$$

By integrating the previous equation between z and z_{max}, the back-scattered intensity can be expressed as follows:

$$I_{\nu,b}(z) = \int_z^{z_{max}} I_{\nu,t}(z') \exp\left(-\tau_\nu(z' \rightarrow z_{max})\right)\, d\tau_{\nu,b}(z'), \tag{75}$$

and numerically written:

$$I_{\nu,b}(i_z) = \sum_{i=i_z}^{i_{z_{max}}} I_{\nu,t}(i) \exp\left(-\tau_\nu(i \rightarrow i_{z_{max}})\right)\, \Delta\tau_{\nu,b}(i), \tag{76}$$

where

$$\Delta\tau_{\nu,b}(i) = \sigma_{\nu,b}(i)\, \Delta. \tag{77}$$

This description of the scattering in DustPDR is built upon the assumption that a photon can be back-scattered once, which is not strictly true. In practice, a photon can be back-scattered an infinite number of times. However, among the 12 % of photons that are back-scattered (see Sect. 2.3.2.2), only 12 % of these photons will be back-scattered a second time (that is, only 1 % of the initial number of photons). Considering that a photon is back-scattered only once is therefore a reasonable assumption.

Thence, using the expressions of the transmitted intensity (see Eq. (67)), the intensity emerging from dust (see Eq. (71)), and the back-scattered intensity (see Eq. (76)), the total intensity (see Eq. (65)) is defined as follows:

$$I_\nu(i_z) = I_{\nu,0} \exp\left(-\tau_\nu(i_z)\right) + \sum_{i=0}^{i_{z_{max}}} \epsilon_\nu(i_z)\Delta + \sum_{i=i_z}^{i_{z_{max}}} I_{\nu,t}(i) \exp\left(-\tau_\nu(i \rightarrow i_{z_{max}})\right)\, \Delta\tau_{\nu,b}(i). \tag{78}$$

7.2.4 *Dust self-absorption along the line of sight*

Radiative transfer is performed along the star-PDR axis (i.e. the z-axis). However, the intensity $I_{\nu,\,obs}$ received by the observer is attenuated by dust self-absorption in the PDR along the line of sight (i.e. the observer-PDR axis). We therefore need to take this effect into account, which is not negligible in the near-IR (see Sect. 9.4).

To this end, we introduce l_{PDR}, the length of the PDR along the line of sight. Thence, the intensity received by the observer is defined as follows:

$$I_{\nu,\,obs}(i_z) = I_\nu(i_z) \times \int_0^{l_{PDR}} \frac{\exp(-\tau_\nu(l, i_z))}{l_{PDR}} dl, \tag{79}$$

where $I_\nu(i_z)$ is the total intensity emerging from the cell located at the position i_z (see Eq. 78), and $\tau_\nu(l, i_z)$ the optical depth inside the cell located at the position i_z, defined as:

$$\tau_\nu(l, i_z) = \int_0^{l_{PDR}} \kappa_\nu(l, i_z) dl. \tag{80}$$

The dust opacity κ_ν (see Eq. (51)) depends on the dust properties ($Q_{abs}(a, \nu)$), size (a), and density (n). These three quantities are fixed for a given cell, $\kappa_\nu(l, i_z) = \kappa_\nu(i_z)$ and we can therefore simplify Eq. (80) to:

$$\tau_\nu(l, i_z) = \kappa_\nu(i_z)\, l_{PDR}. \tag{81}$$

Thence, Eq. (82) becomes

$$I_{\nu,\,obs}(i_z) = I_\nu(i_z)\, \exp(-\kappa_\nu(i_z)\, l_{PDR}). \tag{82}$$

The major drawback of DustPDR, which is a consequence of the 1D plane parallel approximation, is that the total intensity only takes into account photons that are emitted by dust and not those that are scattered by dust towards the observer. As scattering is not negligible in the near-IR, we therefore need to use a radiative transfer code that takes into account the contribution of scattered photons to the total intensity received by the observer.

7.3 TOWARDS A 3D MONTE-CARLO RADIATIVE TRANSFER CODE : SOC

In the second part of my PhD, I used the 3D radiative transfer code SOC (Scattering with OpenCL), which is described here. We first present an overview of this code, followed by a presentation of the Monte Carlo approach upon which this code is constructed. Finally, we describe the input files that are required to use this code, as well as the output files that it provides us with.

7.3.1 *Presentation of SOC*

SOC (Juvela, 2019) is a 3D Monte Carlo radiative transfer code, parallelised using OpenCL libraries which computes dust emission and scattering. SOC was benchmarked with other radiative transfer codes in Gordon et al., 2017 and used in Juvela et al., 2018a,b, 2019. In SOC, clouds can be defined on regular Cartesian grids or octree grids.

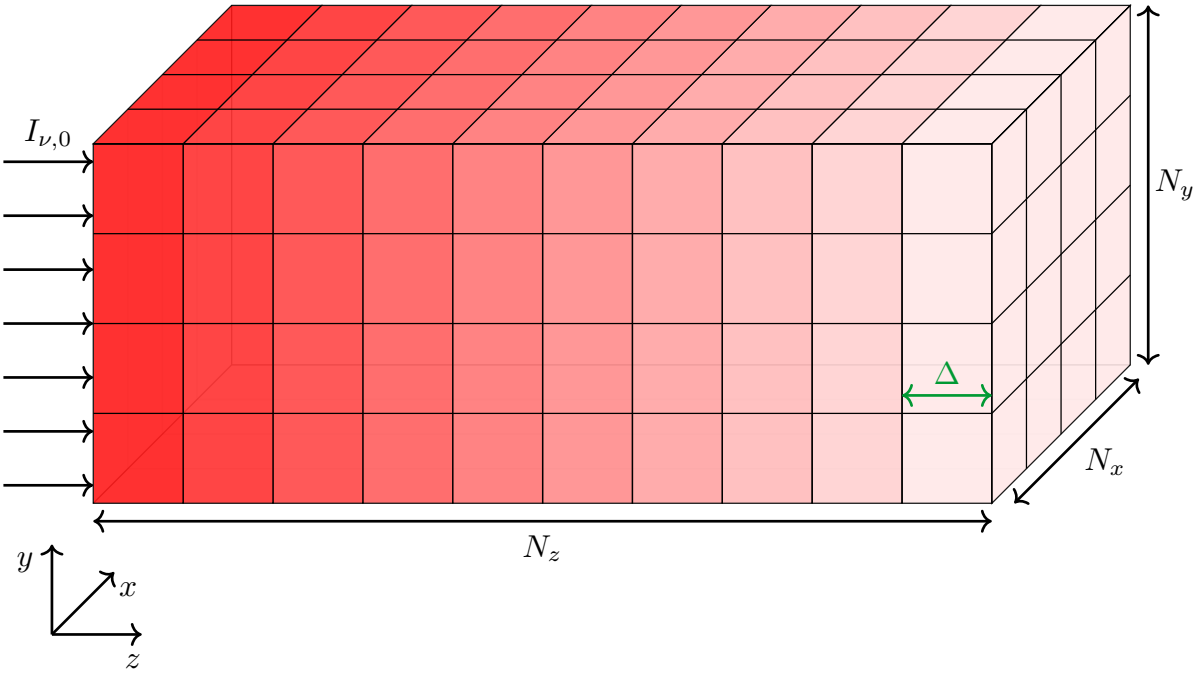

Figure 56: Schematic illustration of a PDR illuminated by a radiation field (from the left) described by its specific intensity $I_{\nu,0}$, modeled in 3D with SOC. The red shades correspond to the dust temperature, that is decreasing from the illuminated edge of the PDR to the denser part. N_x, N_y, and N_z correspond to the number of cells along the x, y, and z axis, respectively. Each cell is a cube with a size Δ (that is, $\Delta_x = \Delta_y = \Delta_z = \Delta$).

7.3.2 *Monte-Carlo*

SOC uses the Monte-Carlo method, that is based on random draw. The idea is to simply follow the trajectory of the photons, using probability to determine how far a photon travels before interacting, then whether this interaction is scattering or absorption, and finally, if it is scattering, the direction of the photon. The benifit of this approach is its simple description and implementation in codes. However, in order to get a significant statistic (that is, to reduce the noise), the number of photons that have to be followed in a simulation needs to be large enough (see Sect. **??**).

7.3.2.1 *Scattering from the probability point of view*

Here we describe how scattering is treated from the probability point of view. With this aim, we define the albedo that quantifies the contribution of scattering to the extinction:

$$\omega_\nu = \frac{\sigma_\nu}{\kappa_\nu + \sigma_\nu} < 1. \tag{83}$$

We first introduce the notion of *Mean free path*, that is required to define quantities such as the average number of times a photon is scattered before being absorbed, as well as the average distance beyond which a photon can propagate before being absorbed. These notions are useful to understand the basics of Monte-Carlo simulations for radiative transfer.

MEAN FREE PATH It can be seen that if $\omega_\nu = 0$, photons are always absorbed by dust and if $\omega_\nu = 1$, photons are always scattered by dust. Thence, the probability that a photon is scattered is ω_ν and the probability that a photon is absorbed is $\eta = 1 - \omega_\nu$.

We now define the probability[3] $P_{ni}(\tau_\nu)$ that a photon will not interact with a dust grain after a given optical depth τ_ν. We can then consider a number of photons N_0, with frequencies between ν and $\nu + d\nu$, that propagate across a uniform environment containing dust. The number of photons that are left at the optical depth τ_ν is provided by the Beer-Lambert law (see Eq. (58), with $S_\nu = 0$) and defined as: $N(\tau_\nu) = N_0 \exp(-\tau_\nu)$ where $\tau_\nu = (\kappa_\nu + \sigma_\nu)\, l$. The probability that interaction takes place before τ_ν is therefore:

$$P_{ni}(\tau_\nu) = \exp(-\tau_\nu). \tag{84}$$

From there, we can also define the probability $P_i(\tau_\nu)$ that a photon will interact with a dust grain after a given optical depth τ_ν:

$$P_i(\tau_\nu) = 1 - P_{ni}(\tau_\nu) = 1 - \exp(-\tau_\nu). \tag{85}$$

Then, the probability $dP_i(\tau_\nu)$ that a photon will interact between τ_ν and $\tau_\nu + d\tau_\nu$ can be written:

$$dP_i(\tau_\nu) = P_i(\tau_\nu) \times P_{ni}(d\tau_\nu) = \exp(-\tau_\nu)(1 - \exp(-d\tau_\nu)). \tag{86}$$

As $d\tau_\nu << 1$, we can approximate $\exp(-d\tau_\nu)$ with its first order Taylor expansion $\exp(-d\tau_\nu) = 1 - d\tau_\nu$. We can therefore simplify Eq. (86) as follows:

$$dP_i = \exp(-\tau_\nu) d\tau_\nu. \tag{87}$$

Finally, the average distance $\langle l \rangle$ beyond which a photon will interact with a grain (that is, the *mean free path*), is:

$$\langle l \rangle = \int_0^{+\infty} l \, dP_i = \int_0^{+\infty} \frac{\tau_\nu}{\kappa_\nu + \sigma_\nu} \exp(-\tau_\nu) d\tau_\nu = \frac{1}{\kappa_\nu + \sigma_\nu} \tag{88}$$

It is clear from this that the larger κ_ν and/or σ_ν are, the lower the *mean free path* is. This makes sense as an increase in both κ_ν and σ_ν entails an increase in the probability that a photon will be absorbed or scattered by a dust grain.

NUMBER OF SCATTERINGS BEFORE ABSORPTION AND THE ASSOCIATED LENGTH In order to define the average number of times a photon is scattered before being absorbed, we first introduce the probability $p(N)$ that a photon is scattered exactly N times before being absorbed. As these events (scattering and absorption) are independent, this probability corresponds to the multiplication of the probability that a photon is scattered N times (that is, $(\omega_\nu)^N$) by the probability that a photon is absorbed only one time (that is, $\eta = 1 - \omega_\nu$). The probability $p(N)$ that a photon is scattered exactly N times before being absorbed can therefore be written:

$$p(N) = (\omega_\nu)^N (1 - \omega_\nu). \tag{89}$$

3 The subscrit 'ni' is for 'non-interaction'.

Hence, as successive scattering of a photon is comparable to a random walk with independant successive steps, the average distance where a photon is absorbed, compared to its initial position, is:

$$\langle N_\nu \rangle = \sum_0^{+\infty} N\, p(N) = (1-\omega_\nu) \sum_{N=0}^{+\infty} N\, (\omega_\nu)^N \frac{\omega_\nu}{1-\omega_\nu}. \tag{90}$$

To simplify this equation, it is possible to use a power series expansion as $\omega_\nu < 1$:

$$g(\omega_\nu) = \sum_{N=0}^{+\infty} (\omega_\nu)^N = \frac{1}{1-\omega_\nu} \quad \text{thus} \quad g'(\omega_\nu) = \sum_{N=0}^{+\infty} N(\omega_\nu)^{N-1} = \frac{\omega_\nu}{1-\omega_\nu}, \tag{91}$$

and Eq. (90) can therefore be simplified to:

$$\langle N_\nu \rangle = (1-\omega_\nu)\omega_\nu\, g'(\omega_\nu) = \frac{\omega_\nu}{1-\omega_\nu}. \tag{92}$$

We note that when $\omega_\nu \to 0$, $\langle N_\nu \rangle \to 0$, expected because such value of ω_ν entails that there are no scattering at all but only absorption. A photon is therefore directly absorbed by a dust grain and never scattered. In contrast, if $\omega_\nu \to 1$, $\langle N_\nu \rangle \to +\infty$, again as expected because such value of ω_ν implies that there are no absorption but only scattering. A photon will consequently always be scattered and never absorbed by a dust grain. In this case ($\omega_\nu \to 1$), it is possible to simplify Eq. (92) as follows:

$$\langle N_\nu \rangle \simeq \frac{1}{1-\omega_\nu} = \frac{\kappa_\nu + \sigma_\nu}{\kappa_\nu}. \tag{93}$$

Thence, the average distance at which a photon is absorbed, compared to its initial position, is:

$$l_m = \sqrt{\langle N_\nu \rangle} \times \langle l \rangle = \sqrt{\frac{\omega_\nu}{1-\omega_\nu}} \times \frac{1}{(\kappa_\nu + \sigma_\nu)}, \tag{94}$$

and if $\omega_\nu \to 1$:

$$l_m \simeq \sqrt{\frac{\kappa_\nu + \sigma_\nu}{\kappa_\nu}} \times \frac{1}{(\kappa_\nu + \sigma_\nu)} = \frac{1}{\sqrt{\kappa_\nu} \times \sqrt{\kappa_\nu + \sigma_\nu}} = \frac{1}{\kappa'_\nu}, \tag{95}$$

where $\kappa'_\nu = \sqrt{\kappa_\nu} \times \sqrt{\kappa_\nu + \sigma_\nu}$, which is the geometric mean of κ_ν and $\kappa_\nu + \sigma_\nu$.

As $\kappa'_\nu > \kappa_\nu$, Eq. (95) reveals the increase in the distance travelled by a photon before being absorbed, a direct consequence of multiple scattering.

7.3.2.2 *Application to Monte-Carlo simulations*

A JOURNEY OF A PHOTON As seen in the previous section, the optical depth through which the photon travels until its next scattering follows an exponential law whose probability density function is

$$f(\tau_\nu) = \exp(-\tau_\nu). \tag{96}$$

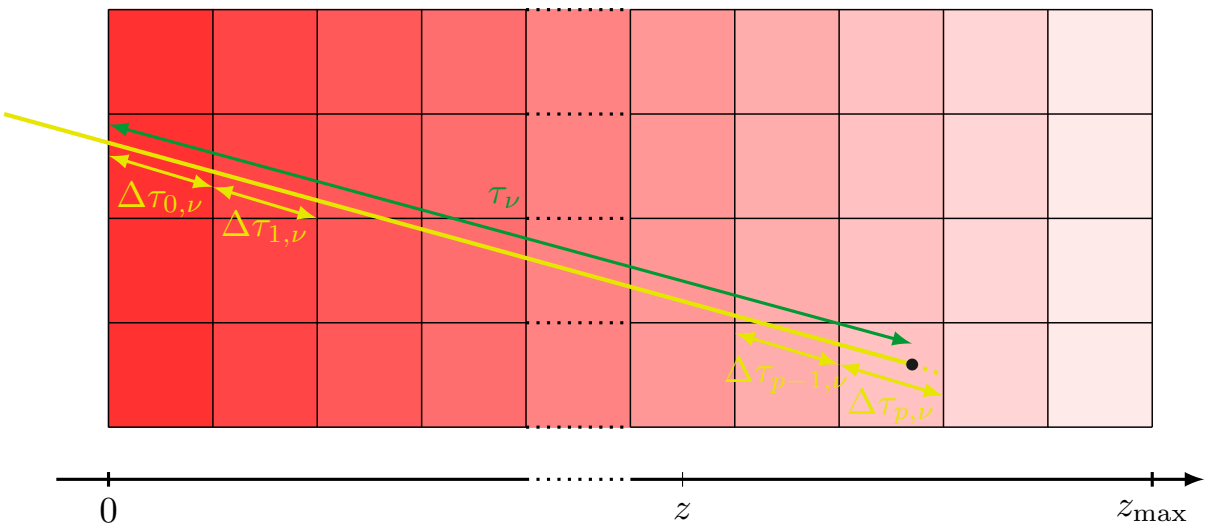

Figure 57: Schematic illustration of a photon that propagates (yellow line) throughout a PDR until an interaction with a grain (black dot). The red shades correspond to the dust temperature, decreasing from the illuminated edge of the PDR to the denser part. For the sake of simplicity, we represent this PDR in 2D, although Monte-Carlo simulations are described by a 3D geometry in Sect. 7.3.2.2.

It is therefore possible to define a random optical depth which follows this probability density function. For this, we can draw a random number x uniformly distributed in $[0, 1[$ and we obtain the random optical depth as follows:

$$\tau_\nu = -\ln(1 - x_\nu). \tag{97}$$

Thence we follow the propagation of a photon cell by cell in order to determine in which cell this photon will interact with a dust grain. From a mathematical point of view, we search for the cell index p in which an interaction between a photon and a grain occurs, in such a way that

$$\sum_{i=0}^{p-1} \Delta\tau_{i,\nu} < \tau_\nu < \sum_{i=0}^{p} \Delta\tau_{i,\nu}, \tag{98}$$

where $\Delta\tau_{i,\nu}$ is the optical depth through which a photon passes in the i-th cell (see Fig. 57). Sometimes, based on the trajectory of the incident photon, the random optical depth takes a photon outside of the cloud. In that case, either another photon is created and we follow it, or the previous photon is forced to stay inside the cloud based on boundary conditions.

Knowing the cell in which an interaction takes place, there are two possible scenarios:

- the incident photon is absorbed by a grain and heats it accordingly. Then, the dust grain cool down by emitting IR photons, without any preferred direction (isotropic radiation);
- the incident photon is scattered in a randomly drawn direction, taking into account the non-isotropic behaviour of the scattering, quantified by the Henyey-Greenstein phase function (see Sect. 2.3.2).

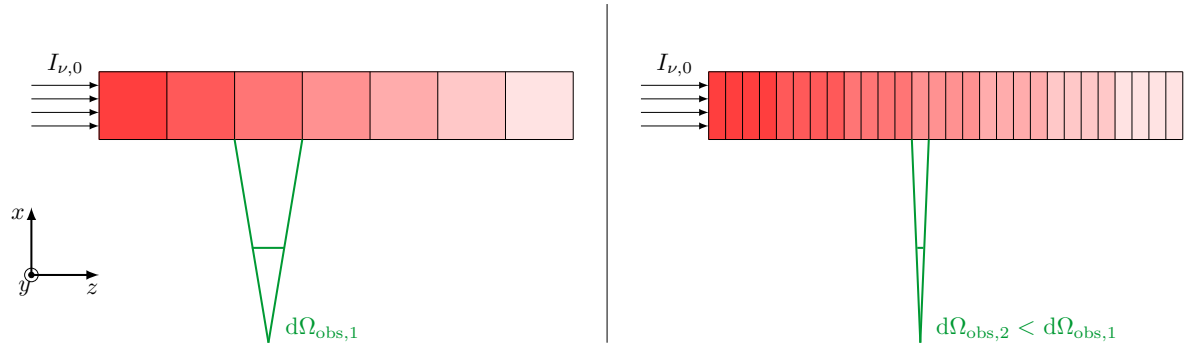

Figure 58: Schematic illustration of the influence of increasing the observer size in order to increase the number of photons received by the observer. The red shades correspond to the dust temperature, that is decreasing from the illuminated edge of the PDR to the denser part. For the sake of simplicity, we represent this PDR in 2D, although Monte-Carlo simulations are described in a 3D geometry in Sect. 7.3.2.2.

FOLLOWING MULTIPLE PHOTONS: PHOTON PACKAGES As all the stars in the ISM emit a huge number of photons, it would be convenient to follow all of these photons in a Monte-Carlo simulation. However, this would be too time consuming. Thus, these photons are gathered into photon packages based on the assumption that photons in the same package follow the same trajectory and undergo the same treatment (absorption or scattering). In order to get significant statistics, it is necessary to run Monte-Carlo simulations with enough photon packages hence to perform a convergence study to find a satisfactory number of photon packages (that is, high enough to get a low signal-to-noise ratio, and low enough to get a reasonable computation time). We will talk about such convergence study in more details in Sect. **??**.

7.3.2.3 *Treatment of photons received by the observer*

With radiative transfer, photons that are scattered towards the observer and those that are emitted by dust grains towards the observer, are gathered. However, the probability that a photon package is scattered or emitted towards the observer is proportional to $d\Omega_{obs}/4\pi$, where $d\Omega_{obs}$ is the solid angle inside which photons that are received are observed by the observer. In practice, $d\Omega_{obs} << 1$ hence most of the photons that emerge from the PDR will not be observed and consequently, the signal-to-noise ratio will be low.

Different methods exist to bypass this problem and one of these is called the *peeling* method. It consists of removing part of the radiation from the photon package as it passes through the cloud, and extracting from it what the observer sees. It is also possible to artificially increase the observer size (that is, increase $d\Omega_{obs}$) in order to increase the probability of receiving photons emerging from the PDR. However, this method entails a decrease in the spatial resolution seen by the observer (see Fig. 58).

7.3.3 *Input and output files*

Albeit exhaustive information regarding the input and output files is available on SOC website, I describe the basics of SOC, as well as the keywords that I used extensively.

Following the example of many radiative transfer codes, it is necessary to provide the information below to use SOC:

- the cloud description is provided through the value of the density of hydrogen atoms per cm^3 (thus express in $H.cm^{-3}$) in each cell. It is possible to use a hierarchical grid but I did not have to use such grid as the computation time was satisfactory given the grid I chose;
- the dust description is provided through dust optical properties ($g(a, \nu)$, $Q_{sca}(a, \nu)$, $Q_{abs}(a, \nu)$), for each dust type (e.g. a-C, a-C:H/a-C, a-Sil/a-C, ...);
- the radiation field of an extended source is described by its intensity in $W\,m^{-2}\,Hz^{-1}\,sr^{-1}$ and for a point source, described by its luminosity in $erg\,s^{-1}\,Hz^{-1}$. Note that it is possible to add as many sources as needed. If the source is an isotropic background (typically the interstellar radiation field), there is obviously no need to describe the position of the source. However, for both extended and point sources, it is necessary to specify their positions, relative to the cloud. Moreover, for extended sources, one needs to give a value for the *opening angle*, which is the angular diameter of the source as seen from the cloud. We will discuss this parameter in more detail in Sect. **??**;
- the dust-to-gas ratio for each dust population in each cell of the cloud, $\left(M_{dust,j}/M_H\right)(x, y, z)$ where j refers to a particular dust component (e.g. a-C, a-C:H/a-C, a-Sil/a-C, ...);
- general information provided in a file (ini-file) where SOC extracts paths regarding the other input files and parameters such as:
  - the number of photon packages per frequency, emitted by the isotropic background source (called *bgpackets* in the ini-file);
  - the number of photon packages per frequency, emitted by dust grains inside the cloud (called *cellpackets* in the ini-file);
  - the position of the point source (x, y, z, see Fig. 56) as well as the location of the file that contains its luminosity;
  - the position of the extended source (x, y, z, see Fig. 56) as well as both the location of the file that contains its intensity and the *opening angle*;
  - the direction towards the observer that is used to define the 2D dust emission map;
  - the number of iterations. Zero iterations means that dust emission is not taken into account in the simulation. One iteration entails that dust emission is taken into account upon the assumption that dust is only heated by the radiation of the source that has been attenuated by dust extinction. Two iterations implies that dust emission is taking into account upon the assumption that dust is heated by radiation of the source that has been attenuated by dust extinction but also by dust emission from the previous iteration, albeit this contribution is often negligible. This number can be larger than two;
  - the method used for the simulation of the point source. Depending on this choice, photon packages are sent from the source either in the 2π solid angle that contains the cloud or only towards the visible surface element of the cloud.

We would like to emphasize that these files and parameters are only a part of the options available in SOC. We only described those that were used in this study. SOC provides us with the following files:

- a binary file that contains the 2D dust emission map (depending on the position of the observer, that is defined in the ini-file) for each frequency. In other words, if the observer

is located on the x-axis, the 2D dust emission map is an array with dimensions (N_ν, N_y, N_z) where N_ν is the number of frequencies, N_y and N_z are the number of cells along the y-axis and the z-axis (see Fig. 56), respectively;

- a binary file that contains the 2D scattered map. As for the 2D dust emission map, it depends on the position of the observer. In addition to the three dimensions in the 2D dust emission map, it is possible to get the scattered emission map for different angles. In other words, if the observer is located on the x-axis, the 2D scattered map is an array with dimensions ((N_ν, N_{dir}, N_y, N_z)), where N_{dir} is the number of directions in the orthogonal plan defined by the y-axis and the z-axis;

Part V

DUST MODELLING ACROSS PDRS

8 FROM 1D TO 3D RADIATIVE TRANSFER CODE

If somebody tells you there is a rule, break it. That's the only thing to move things forward.

Hans Zimmer

Contents

DustPDR is a 1D radiative transfer code while SOC is a 3D radiative transfer code, and so here we present here the differences between them and the consequences for the computation of dust emission in the Horsehead Nebula.

8.1 PHYSICAL CONDITIONS AND DESCRIPTION OF THE SIMULATIONS

In order to compare dust emission computed with both DustPDR and SOC, it is necessary to perform simulations under the same physical conditions (that is, the density profile and the radiation field) and to make sure that the numerical convergence (that is, the number of photon packages and the number of iterations in the case where we take dust emission into account in the dust heating) as well as the spatial convergence (that is, the choice of the spatial grid), have been reached.

We chose the density profile that is used to study the Horsehead as well as the radiation field that is illuminating it, both are described in Sect. 5.2.

Regarding the spatial grid, we chose the same number of bins along the z-axis, $N_z = 77$, with the same sizes, $\Delta = 0.0025$ pc. As SOC is a 3D radiative transfer code, it is also required to specify the number of bins along the x-axis and the y-axis. For the y-axis, we chose $N_y = 7$, that is a relatively low number but large enough to avoid side effects. As for the x-axis, we chose $N_x = 40$ which implies $l_{PDR} = 0.10$ pc.

Concerning the numerical convergence, we took a number of photon packages that is large enough to reach it.

The spectra at each position along the z-axis were extracted and integrated in the ten photometric bands (see Sect. 4.2) and convolved with the appropriate PSFs (see Sect. 4.3).

Fig. 59 shows the dust emission profiles (that is, the specific intensity along the z-axis) in the ten photometric bands, for four different cases:

- using SOC with zero iteration (blue lines), meaning that dust emission is not used in the simulation to heat dust, only the attenuated radiation field emerging from the illuminating star is used;
- using SOC with one iteration (red lines), meaning that dust emission is used in the simulation to heat dust grains, in addition to the attenuated radiation field emerging from the illuminating star;

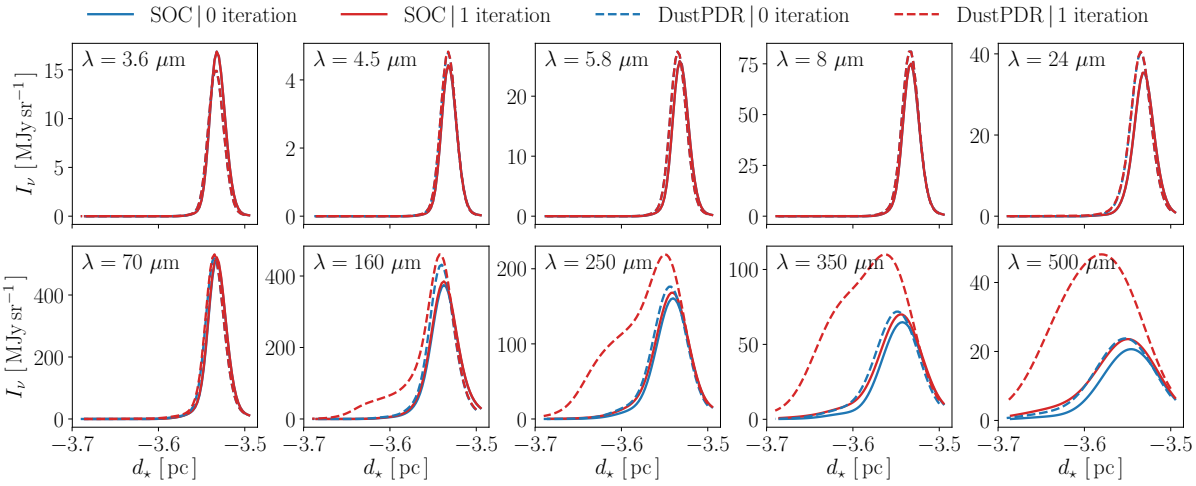

Figure 59: Modelled dust emission profiles across the Horsehead. Each of the ten figures corresponds to the dust emission profile across the Horsehead in the ten following photometric bands: 3.6 µm, 4.5 µm, 5.8 µm, 8 µm, 24 µm, 70 µm, 160 µm, 250 µm, 350 µm, 500 µm. Blue lines refer to the dust emission profiles modelled using SOC with zero iteration (without taking into account the dust emission in the radiative transfer) and red lines with one iteration (taking into account the dust emission in the radiative transfer). Blue dashed lines refer to the dust emission profiles modelled using DustPDR with zero iteration and red dashed lines with one iteration.

- using DustPDR with zero iteration (blue dashed lines);
- using DustPDR with one iteration (red dashed lines).

We chose to compare DustPDR and SOC with zero and one iteration because it allows us to disentangle the differences that are due to the scattering only and those that are due to the scattering and dust emission. Indeed, with zero iteration, dust emission is computed but not added to the radiation field that is used to compute dust emission, although it is taken into account with one iteration.

8.2 COMPARISON BETWEEN DUST EMISSION PROFILES FROM 1D TO 3D

We first present the cross-comparison between SOC and DustPDR obtained with zero iteration and then, with one iteration.

8.2.1 *Comparison with o iteration : influence of the scattering*

In the near- and mid-IR, the difference between the dust emission profiles computed with SOC and DustPDR is relatively small and less than 5 %. As stochastically heated grains mostly emit at these wavelengths, the difference between SOC and DustPDR is solely due to the treatment of these grains that are not in thermal equilibrium.

In the far-IR, the dust emission profiles computed with DustPDR are slightly higher than those computed with SOC. The treatment of the large grains is the same regardless of the code used hence the differences are due to radiative transfer effects. DustPDR is built on the assumption that 88% of the scattered photons are forward scattered and 12% are back scattered, regardless of the dust type. In SOC, the treatment of the scattering is more thorough.

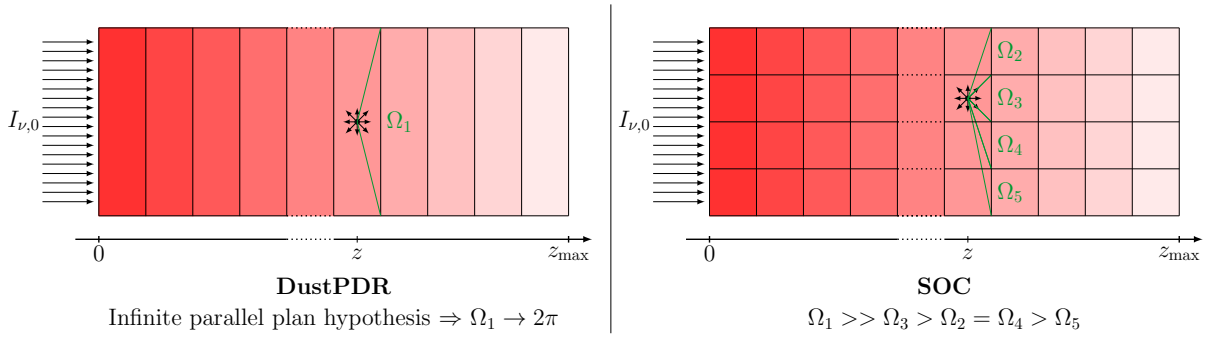

Figure 60: Schematic illustration of the influence of the geometry used in DustPDR (left) and SOC (right) on dust emission. For the sake of simplicity, the cloud representation in SOC is shown here in 2D.

Indeed, scattering is treated separately for each dust type and size using the anisotropy coefficient. In practice, there are less photons that are forward scattered with SOC than with DustPDR. As a consequence, there are slightly more photons in the denser part of the PDR to heat large grains with DustPDR than with SOC. Therefore, the intensity in the far-IR is a little higher with DustPDR than with SOC.

8.2.2 *Comparison with 1 iteration : influence of dust emission*

In the DustPDR framework, when dust emission is included[1] in the radiation field that is heating dust grains, it is assumed that one cell receive 50% of the dust emission emitted in each of the other cells. This is a straightforward consequence of the 1D geometry used in DustPDR. In other words, it means that one cell receives photons from other cells within a solid angle of 2π (see Fig. 60).

In SOC, one cell only receives photons within the solid angle from which the latter is seen by an other cell, which is lower than 2π and decreases for cells further away from the considered cell.

The main consequence is that the IR dust emission in one cell is strongly overestimated in the DustPDR framework, which has consequences in regions where the infrared energy is not negligible compared to the UV/visible energy, typically in the denser part of the PDRs where the UV radiation field has been absorbed.

Indeed, Fig. 61 (left panel) shows the radiation field received with DustPDR at two different positions in the Horsehead (at $i_z = 15$, where the maximum of emission in the near-IR is and at $i_z = 23$, where the maximum of emission in the far-IR is (see Fig. 59)). We see that the UV radiation field is strongly damped when moving deeper in the PDR (from $i_z = 15$ to $i_z = 23$), contrary to the IR radiation field, which is expected because dust extinction is very efficient at UV-Visible wavelengths but not at IR wavelengths. Moreover, we can see that the received IR power (see Fig. 61, top right panel) barely varies with depth inside the Horsehead, which is a consequence of the low extinction by dust in the IR. This means that, to first order, we can approximate the IR radiation field in one cell by the sum of all the dust IR contributions from the other cells. Conversely, the UV-Visible radiation field is strongly diminished and dust heating is dominated by dust IR emission (see Fig. 61, (bottom right panel)) beyond a given depth into the Horsehead, typically where the maximum of the far-IR emission occurs.

We can indeed see this effect in Fig. 59. In the near and mid-infrared, there is no difference between zero and one iteration, whether using DustPDR or SOC because as the stochastically

1 That is, with at least one iteration.

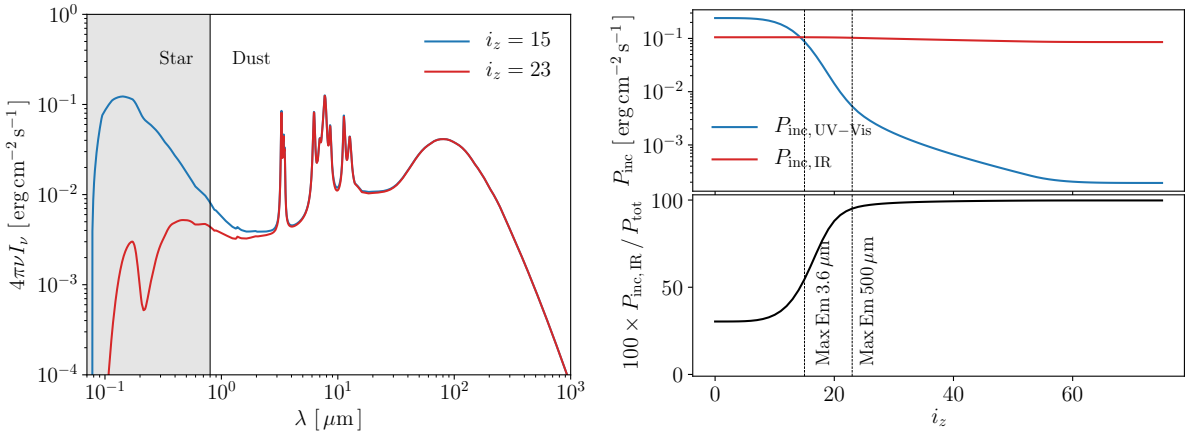

Figure 61: Left: Radiation field received in the DustPDR framework, by a cell located at the position $i_z = 15$ (blue line) and $i_z = 23$ (red line). The darker grey part corresponds to the radiation that is mostly coming from the illuminated star and the white part, from the heated dust. Top right: Received IR (0.8 to 500 µm) power as a function of the depth in the Horsehead (red line) and received UV-Visible (0.04 to 0.8 µm) power as a function of the depth in the Horsehead (blue line). Bottom right: Contribution of the received IR power to the total received power as a function of the depth in the Horsehead. The two vertical dashed lines correspond to the position of the maximum emission (see Fig. 59) in the near-IR (at 3.6 µm) and in the far-IR (at 500 µm).

heated grains emits at the edge of the PDR where the heating by IR dust photons is negligible in comparison to heating by UV photons from the illuminating star. Thus, even if there is more IR energy when dust IR emission is included, it is the heating by UV photons that dominates dust heating. In the far-infrared, dust emission is larger with DustPDR than with SOC because the maximum emission is located in the denser part of the PDR where the UV radiation field is lower hence dust heating by IR dust photons is no longer negligible in comparison with heating by UV photons. Thus, in the DustPDR case, there is more IR energy from dust that is received in one cell than in SOC hence dust heating by dust IR photons is higher in the DustPDR framework.

8.3 CONSEQUENCES

To summarise, results obtain with DustPDR will always leads to an overestimation of the IR emission received by dust grains in the far infrared, compared to those obtain with SOC. Large grains in the DustPDR frawework are therefore hotter than those in SOC. In the following and during all of the study, radiative transfer is performed with SOC.

9 DUST EMISSION AND SCATTERING MODELLING

La poésie de la terre ne meurt jamais.

John Keats - *Poésie & Terre*

Contents

9.1 ON THE CREATION OF THE DUST EMISSION AND SCATTERING PROFILES

From the description of the PDR (density profile and illuminating source) to the comparison between the dust modelled and the dust observed emission profiles, there are different steps that are described here. Unless otherwise stated, the results presented below are obtained with diffuse ISM-like dust (that is, CM grains with $M_{a-C}/M_H = 0.17 \times 10^{-2}$, $\alpha = -5$, and $a_{\min,a-C} = 0.4$ nm, see Fig. 45) and $l_{PDR} = 0.10$ pc. The density profile used is the one of the Horsehead hence $n_0 = 2 \times 10^5$ H cm^{-3}, $z_0 = 0.06$ pc, and $\gamma = 4$ (see Fig. 42). The radiation field illuminating the Horsehead edge (that is, $i_z = 0$) corresponds to a blackbody at 34 600 K with G_0 =100. Here are the procedural steps:

- run SOC to compute radiative transfer that provides us with dust emitted and scattered spectra for each value of i_y and i_z (see Fig. 56 for the notation);
- integrate these spectra over the ten photometric bands (3.6, 4.5, 5.8, 8, 24, 70, 160, 250, 350, and 500 µm) (see Sect. 4.2), which provides us with the intensity in each of these ten photometric bands for each value of i_y and i_z.

  Fig. 62 shows the dust emission intensity in each of the ten photometric bands as a function of both i_y and i_z. Note that the longer the wavelength, the deeper the position of the dust maximum emission, which indicates that radiative transfer effects induce a stratification of the emission;
- extract the emission and scattering profiles for $i_y = 3$ (which corresponds to the middle of the y-axis, in order to avoid possible side effets);

- convolve these emission and scattering profiles in the ten photometric bands with the linear PSFs (see Sect. 4.3).

  Fig. 63 shows the dust emission profiles in the ten photometric bands, both convolved and not convolved with the PSFs. Note that the effects of convolution are not significant in the near-IR because the width of the PSF at these wavelengths is smaller than the width of the emission profile. These effects are significant in the far-IR because the PSFs are larger at these wavelengths;

From now on, the procedure described above is applied to compute the dust emission and scattering profiles, used in the following sections.

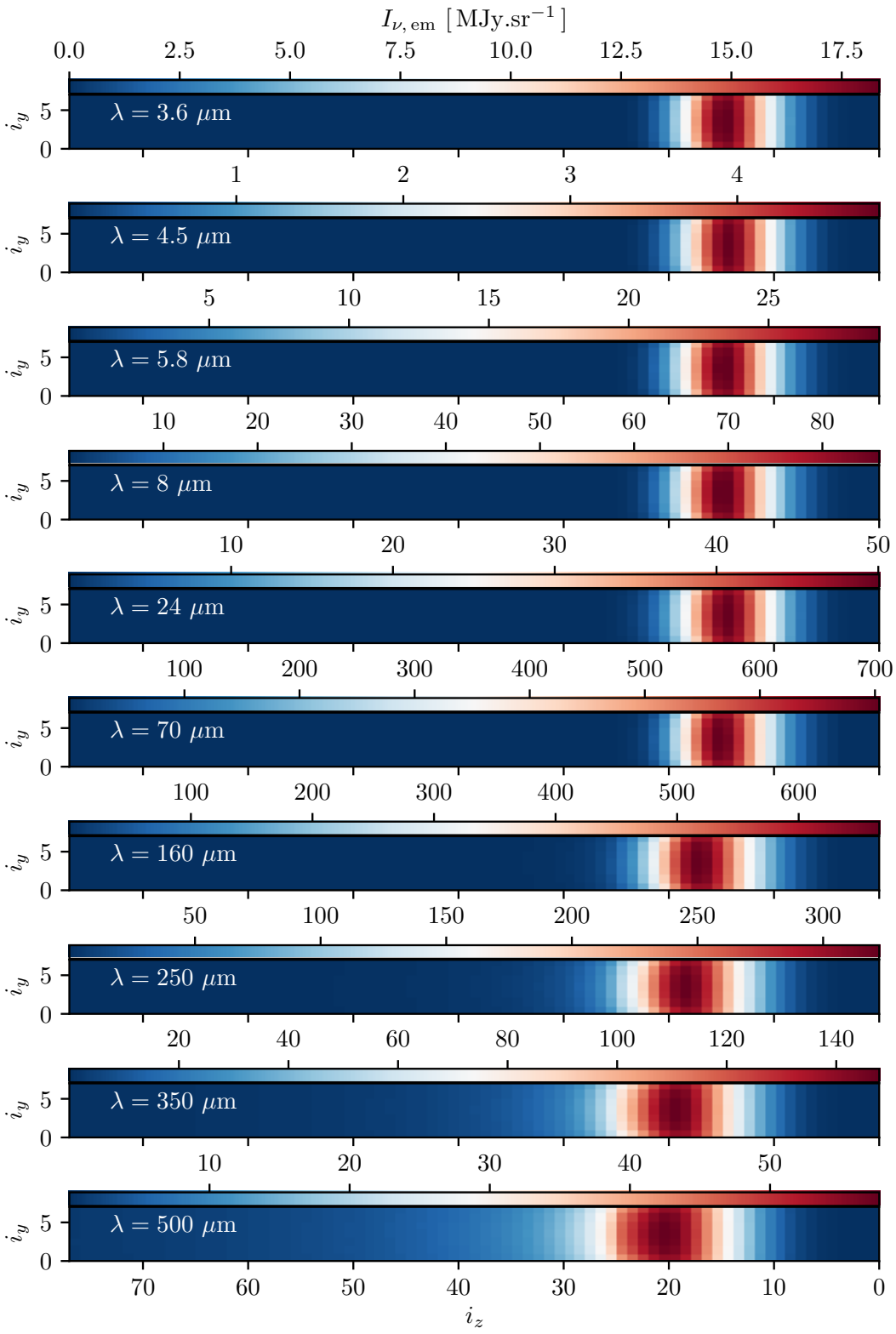

Figure 62: Dust emission profiles across the Horsehead in the ten photometric bands (3.6, 4.5, 5.8, 8, 24, 70, 160, 250, 350, and 500 µm). These profiles are not convolved with the PSFs. The i_y and i_z indexes are described in Fig. 56. This modelling was done using diffuse ISM-like dust and the density profile that describes the Horsehead (see beginning of Sect. 9.1 for more details). The illuminating star is on the right.

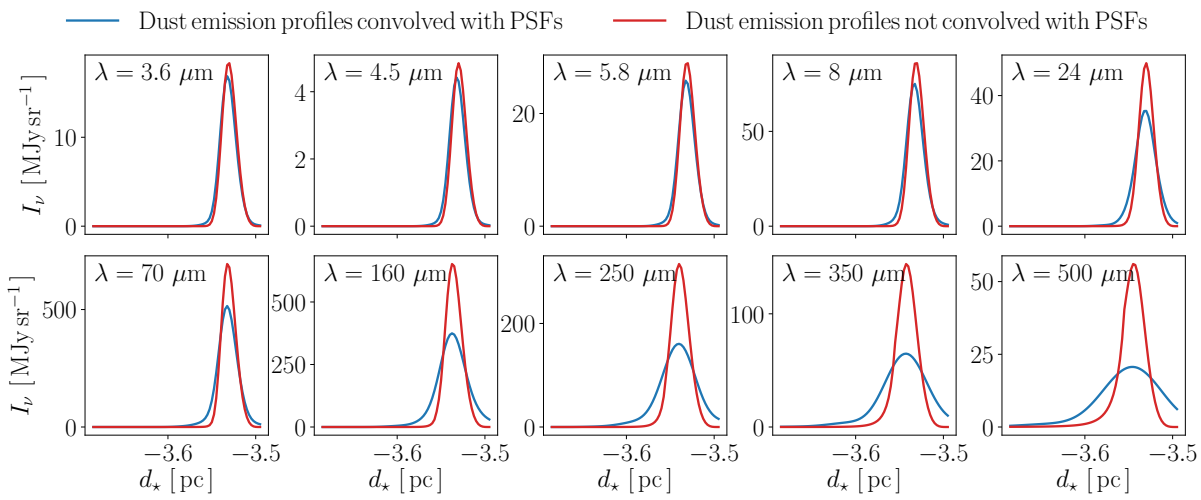

Figure 63: Dust emission profiles across the Horsehead in the ten photometric bands (3.6, 4.5, 5.8, 8, 24, 70, 160, 250, 350, and 500 μm) for $i_y = 3$ see Fig. 62. Profiles that are convolved with the PSFs are in blue and those that are not convolved with the PSFs are in red. This modelling was done using diffuse ISM-like dust and the density profile that describes the Horsehead (see beginning of Sect. 9.1 for more details).

9.2 INFLUENCE OF DUST PROPERTIES ON DUST EXTINCTION

With the aim of understanding the influence of variations in dust properties on dust scattering and emission, it is first important to describe the influence of variations in dust properties on the dust absorption and scattering cross sections.

The dust absorption cross section per unit gas mass, $\tilde{\kappa}_\lambda$, and the dust scattering cross section per unit gas mass, $\tilde{\sigma}_\lambda$, both expressed in cm^2 g^{-1}, are defined as:

$$\tilde{\sigma}_{abs,\lambda} = \frac{1}{M_H}\int_{a_{min}}^{a_{max}} Q_{abs}(a,\lambda)\,\pi a^2\,dn(a) \quad \text{and} \quad \tilde{\sigma}_{sca,\lambda} = \frac{1}{M_H}\int_{a_{min}}^{a_{max}} Q_{sca}(a,\lambda)\,\pi a^2\,dn(a) \quad (99)$$

where Q_{abs} and Q_{sca} are the absorption and scattering efficiencies, respectively (see Fig. 46, upper and bottom panels), $dn(a)$ is the number of grains of radius between a and $a + da$, and M_H is the gas mass equal to M_i/Y_i with M_i the total mass and Y_i the mass fraction of grains of type i (that is, a-C, a-C:H/a-C, or a-Sil/a-C).

Fig. 64 shows the dust absorption and scattering cross sections per unit gas mass for diffuse ISM-like dust. We see that a-C grains dominate the absorption in the UV while other grain types dominate the absorption in the visible-IR. In fact because of the steep power law size distribution of a-C grains (see Sect. 6), this absorption is dominated by the smallest a-C grains of radii $\leqslant 2$ nm.

Fig. 65 shows the behaviour of the absorption of a-C grains with variations in the a-C mass fraction M_{a-C}/M_H (upper left panels), the minimum size $a_{min,a-C}$ (middle left panels), and the α power law exponent of the a-C grain size distribution (lower left panels). It is clear that the corresponding UV absorption is sensitive to changes in M_{a-C}/M_H and α while little affected by variations in $a_{min,a-C}$. As for scattering, it is dominated by the contribution of a-Sil/a-C and a-C:H/a-C grains (see Fig. 65, right panels). However, we can see that a large increase in α leads to a non-negligible contribution of a-C grains to the scattering.

Fig. 65 show the behaviour of the absorption (left panels) and scattering (right panels) cross sections with variations in the a-C grain mass fraction M_{a-C}/M_H (upper panels), the mini-

mum size $a_{\mathrm{min,\,a-C}}$ (middle panels), and the α power law exponent of the a-C grains size distribution (lower panels). The UV absorption is mainly due a-C grains, and appears very sensitive to changes of M_{a-C}/M_H and α while little affected by variations of $a_{\mathrm{min,\,a-C}}$. By contrast scattering is dominated by the contribution of a-Sil/a-C and a-C:H/a-C grains (see Fig. 65, right panels). However, we can see that a large increase in α can lead to a non-negligible contribution of a-C grains to the scattering. To summarise:

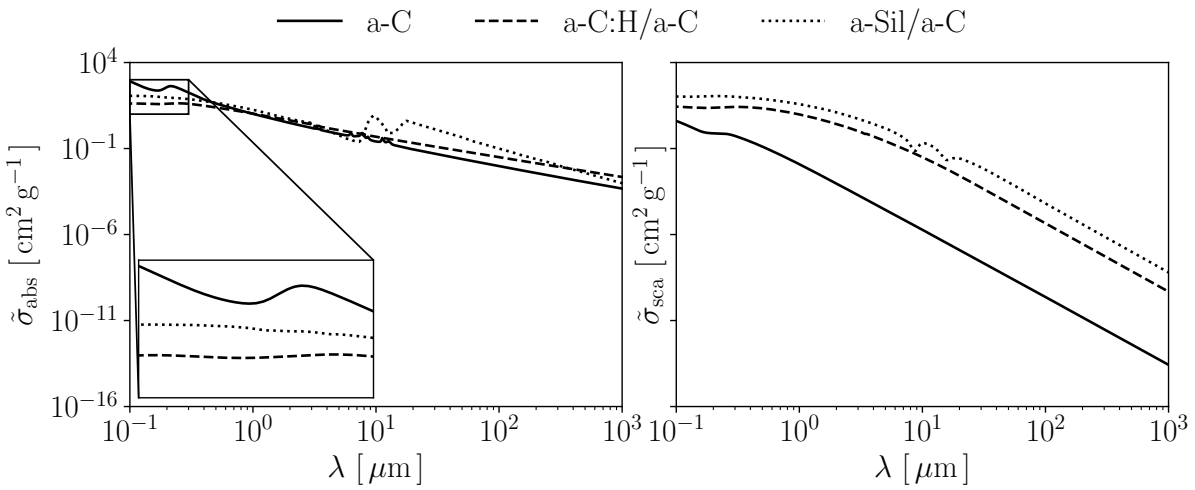

Figure 64: Absorption cross section per unit gas mass, using diffuse ISM-like dust, for a-C grains (black line), a-C:H/a-C grains (black dashed line), and a-Sil/a-C grains (black dotted line). Top right: Same for scattering cross section per unit gas mass.

- a decrease in M_{a-C}/M_H implies a decrease in the dust mass of a-C grains (see Sect. 6.2.2.5 and Fig. 49, upper left panel) hence a decrease in the a-C dust extinction. As the UV dust extinction is dominated by a-C grains, a decrease in M_{a-C}/M_H entails a decrease in the UV total dust extinction. Moreover, small a-C grains do not dominate dust scattering hence even if a decreases in M_{a-C}/M_H entails a decrease of the a-C dust scattering, the total dust scattering is unaffected by variations in M_{a-C}/M_H.
- an increase in $a_{\mathrm{min,\,a-C}}$ implies a moderate redistribution of the a-C dust mass from small a-C grains towards large a-C grains (see Sect. 6.2.2.5 and Fig. 49, middle left panel). As small a-C grains dominates the dust extinction in the UV, an increase in $a_{\mathrm{min,\,a-C}}$ entails therefore a slight decrease in the UV dust extinction. Moreover, as large a-C grains can contribute to the scattering, an increase in $a_{\mathrm{min,\,a-C}}$ implies a slight increase in the a-C dust scattering, but negligible to affect the total dust scattering.
- an increase in α implies a larger redistribution of the a-C dust mass from small a-C grains towards large a-C grains (see Sect. 6.2.2.5 and Fig. 49, bottom left panel). As small a-C grains dominate the dust extinction in the UV, an increase in α therefore entails a large decrease in the UV dust extinction. Moreover, as the a-C dust mass redistribution towards large grains is important, an increase in α leads to a huge increase in the a-C dust scattering, which is no longer negligible compared to a-C:H/a-C and a-Sil/a-C scattering for high values of α. Therefore, an increase in α leads to an increase in the total dust scattering.

Now that the influence of variations in the dust properties on both dust extinction and scattering cross sections have been described, we will present the consequences of such variations on the dust emission and scattering across the Horsehead.

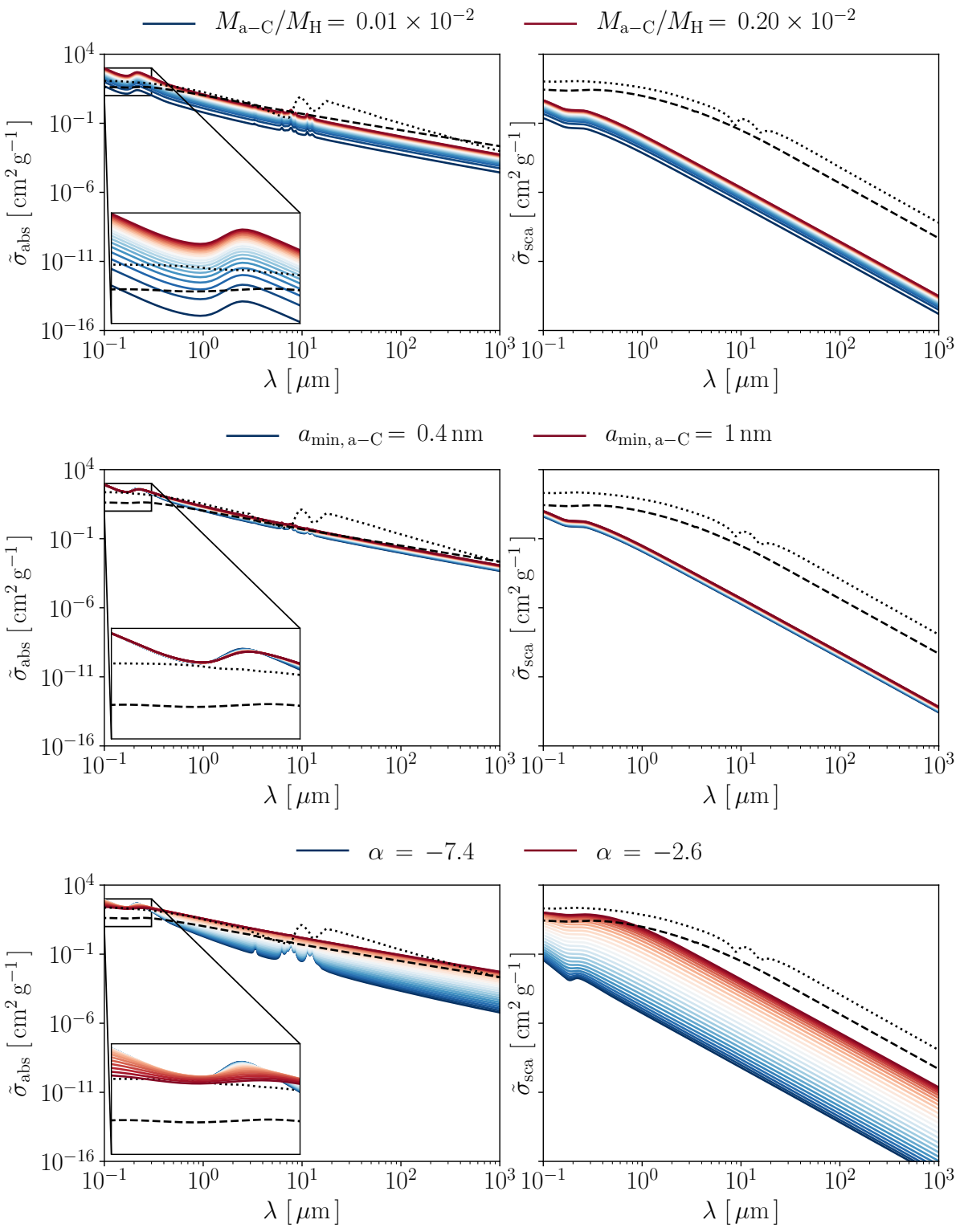

Figure 65: Top left: Absorption cross section per unit gas mass for a-C grains (black line), a-C:H/a-C grains (black dashed line), and a-Sil/a-C grains (black dotted line). Top right: Same for scattering cross section per unit gas mass. Middle left: Absorption cross section per unit gas mass for a-C grains with $a_{\mathrm{min,\,a-C}}$ that varies from 0.4 nm (blue line) to 1 nm (red line) in steps of 0.02 nm, a-C:H/a-C grains (black dashed line), and a-Sil/a-C grains (black dotted line). Middle right: Same for scattering cross section per unit gas mass. Bottom left: Absorption cross section per unit gas mass for a-C grains with α that varies from -7.4 (blue line) to -2.6 nm (red line) in steps of 0.2, a-C:H/a-C grains (black dashed line), and a-Sil/a-C grains (black dotted line). Bottom right: Same for scattering cross section per unit gas mass.

9.3 INFLUENCE OF DUST PROPERTIES ON DUST EMISSION AND SCATTERING IN PDRS

Variations in the dust properties will change the dust absorption and scattering cross sections (see Sect. 9.2), and therefore the dust emission spectrum (see Sect. 6.2.2.5 and Fig. 49, right panels). Up to now we have presented computations done in the optically thin case although the medium in PDRs is generally optically thick. With the aim of conducting a systematic study of dust properties in PDRs by comparison with the observed dust emission and dust scattering, we need to understand the influence of radiative transfer in order to disentangle its effects from variations in the dust properties.

To this end, I performed radiative transfer modelling across the Horsehead for different dust properties. In the following, the density profile used is the one already defined for the Horsehead with $n_0 = 2 \times 10^5$ H cm^{-3}, $z_0 = 0.06$ pc, and $\gamma = 4$. The radiation field illuminating the Horsehead from the right side corresponds to a blackbody at 34 600 K with G_0 =100. Also, spectra are shown for two positions in the Horsehead, which will be referred to in the following at the positions:

- $i_z = 23$, that corresponds to the position of maximum dust emission in the far-IR at 500 µm (see Fig 66, first vertical black line from the left). This position is located in the inner part of the Horsehead, where the UV radiation field is low (G_0 attenuated by a factor $\sim$ 100 at least) and the density is high ($n_H > 10^3$ H cm^{-3});
- $i_z = 15$, that corresponds to the position of maximum dust emission in the near-IR at 3.6 µm (see Fig 66, second vertical black line from the left). This position is located in the outer part of the Horsehead, where the UV radiation field is high ($G_0 \sim 100$) and the density is low ($n_H \sim 10 - 100$ H cm^{-3}).

Then, to study the influence of dust properties on dust emission and scattering, the following grids were explored:

- M_{a-C}/M_H varying from 0.01×10^{-2} to 0.20×10^{-2} in steps of 0.01×10^{-2}. The dust emission and scattering spectra are shown in Fig. 67 (top panels) and the associated dust emission profiles are shown in Fig. 68 (top panel);
- $a_{min,a-C}$ varying from 0.4 nm to 1 nm in steps of 0.02 nm. The dust emission and scattering spectra are shown in Fig. 67 (middle panels) and the associated dust emission profiles are shown in Fig. 68 (middle panel);
- α varying from -7 to -2.6 in steps of 0.1. The dust emission and scattering spectra are shown in Fig. 67 (bottom panels) and the associated dust emission profiles are shown in Fig. 68 (bottom panel);

9.3.1 *Dust emission*

Large grains (a-C:H/a-C and a-Sil/a-C) are warmer at $i_z = 15$ (see Fig. 68, right panels) than at $i_z = 23$ (left panels) as we see that the maximum intensity associated with their emission (that is the modified blackbody bump in the far-IR) shifts towards longer wavelengths. The nano-grains (a-C) are also warmer at $i_z = 15$ than at $i_z = 23$ (left panels) because their emission, which is proportional to G_0, decreases from $i_z = 15$ to $i_z = 23$. This effect is due to the damping of the radiation field with increasing depth into the Horsehead, because of dust extinction.

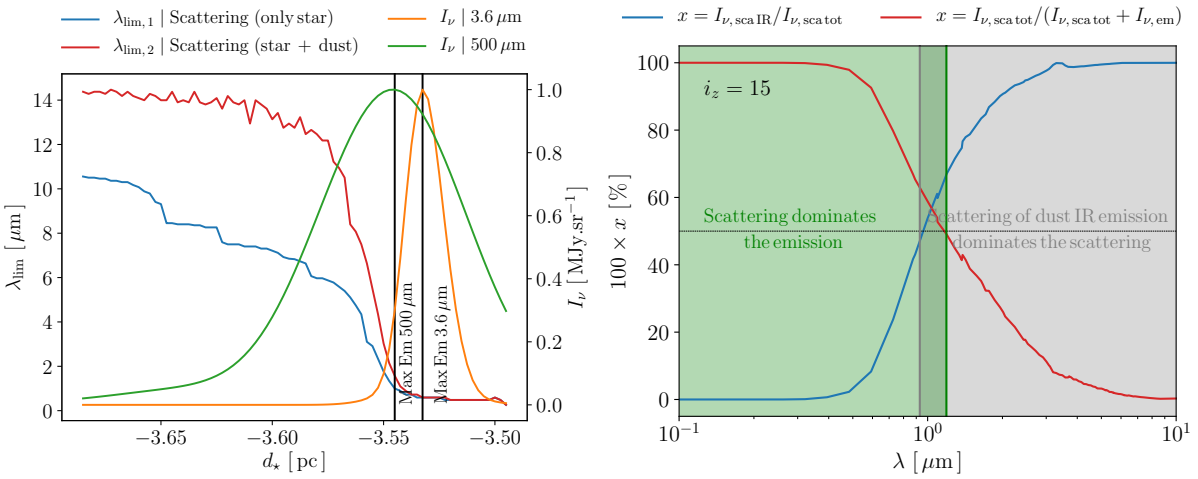

Figure 66: Left: Wavelength limit $\lambda_{\rm lim}$ as a function of the depth in the Horsehead. Below this limit, dust scattering is larger than dust emission. Blue line corresponds to this limit if only the dust scattering of the star radiation is considered. Red line corresponds to this limit if both the star radiation and the dust re-emission is considered in the scattering. Dust emission profiles are shown at 3.6 µm (orange line) and at 500 µm (green line). Right: Contribution of the dust scattering of photons that emerge from the heated dust, to the total dust scattering (red line) and contribution of the dust scattering to the total dust emission (scattering + emission) (blue line) at the position $i_z = 15$. The green part corresponds to wavelengths where scattering dominates the emission (that is, where $I_{\nu,\rm sca\,tot} > 0.5 \times I_{\nu,\rm em}$). The grey part corresponds to wavelengths where scattering of photons that emerge from the heated dust, dominates the scattering (that is, where $I_{\nu,\rm sca\,IR} > 0.5 \times I_{\nu,\rm sca\,tot}$). These results were obtained using diffuse ISM-like dust and the density profile used for the Horsehead.

At $i_z = 15$, the dust emission in the far-IR does not vary with M_{a-C}/M_H (see Fig. 68, top right panel), in contrast to what we show at $i_z = 23$ (top left panel). Because dust emission in the far-IR is unaffected by variations in M_{a-C}/M_H in the optically thin case (see Sect. 6.2.2.5), this is strictly a radiative transfer effect. The a-C grains exhibit a large fraction of the total dust cross-section and an increase in M_{a-C}/M_H therefore significantly increases the extinction. As M_{a-C}/M_H increases, the radiation field is therefore increasingly damped at $i_z = 15$, and fewer photons are available at $i_z = 23$ to heat the larger grains. The right panel in Fig. 68 shows that the wavelength associated with the highest emission shifts towards longer wavelengths with an increase in M_{a-C}/M_H. This means that dust emission in the far-IR varies with M_{a-C}/M_H, as a result of radiative transfer effects.

At $i_z = 15$, dust emission in the far-IR varies little with M_{a-C}/M_H (see Fig. 68, top right panel), in contrast to what we see at $i_z = 23$ (top left panel). Indeed, towards the cloud interior ($i_z = 23$), a decreasing M_{a-C}/M_H enhances the UV photon flux which then dominates the heating of large grains. Conversely, at the cloud border ($i_z = 15$) the unattenuated visible radiation field is more efficient at heating the large grains: this is why the far-IR peak is only weakly sensitive to UV extinction changes (which are controlled by M_{a-C}/M_H, see Fig. 65, upper panels).

The other changes in the spectra are not consequences of radiative transfer effects but are due to variations in dust properties. They are explained in Sect. 6.2.2.5.

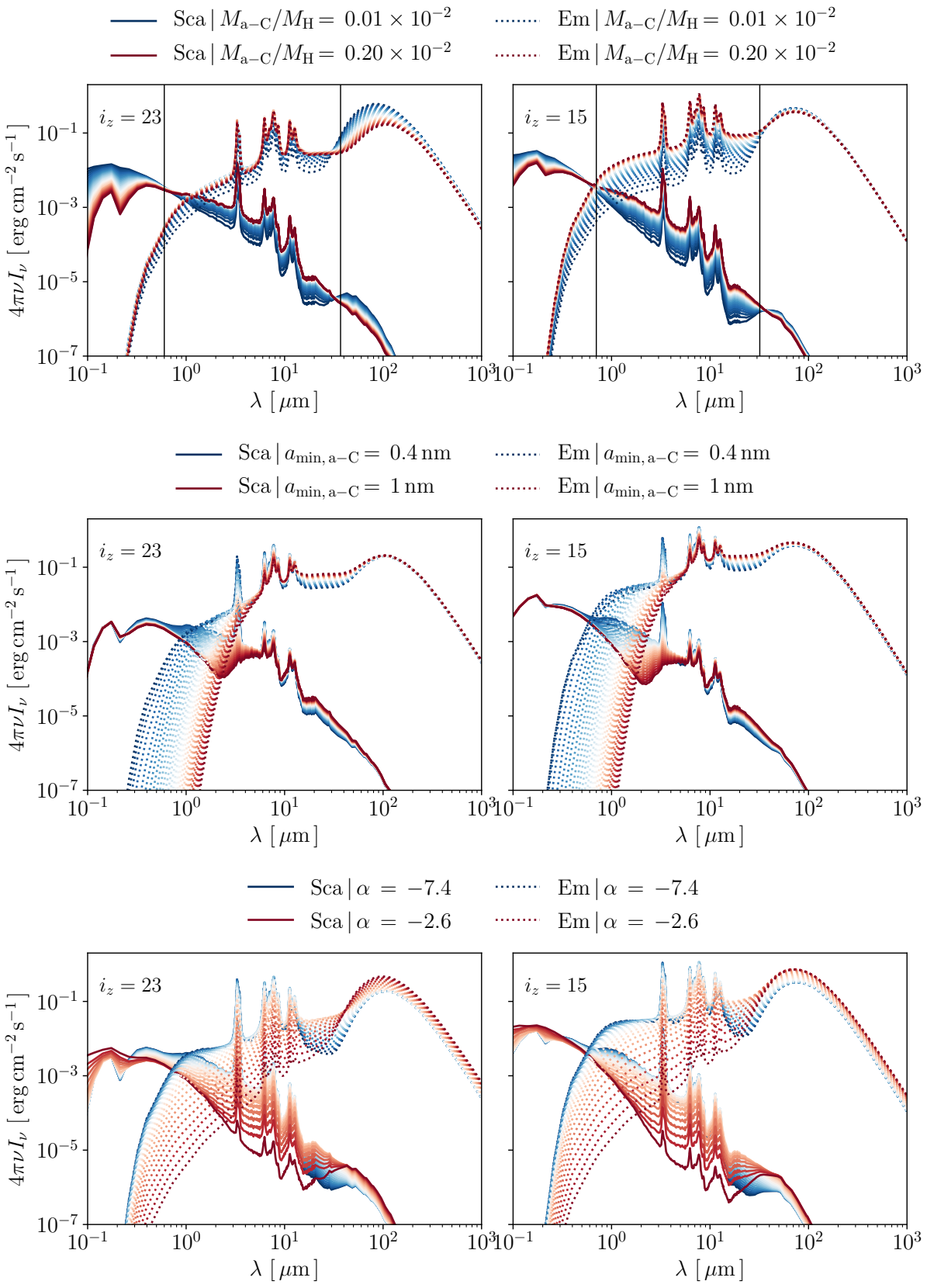

Figure 67: Top left: Scattering spectra at the position $i_z = 23$ for M_{a-C}/M_H that varies from 0.01×10^{-2} (blue line) to 0.20×10^{-2} (red line). In dotted lines, same for emission spectra. Top right: Same at $i_z = 15$. Middle left: Scattering spectra at the position $i_z = 23$ for $a_{min,a-C}$ that varies from 0.4 nm (blue line) to 1 nm (red line). In dotted lines, same for emission spectra. Middle right: Same at $i_z = 15$. Bottom left: Scattering spectra at the position $i_z = 23$ for α that varies from -7.4 (blue line) to -2.6 (red line). In dotted lines, same for emission spectra. Bottom right: Same at $i_z = 15$.

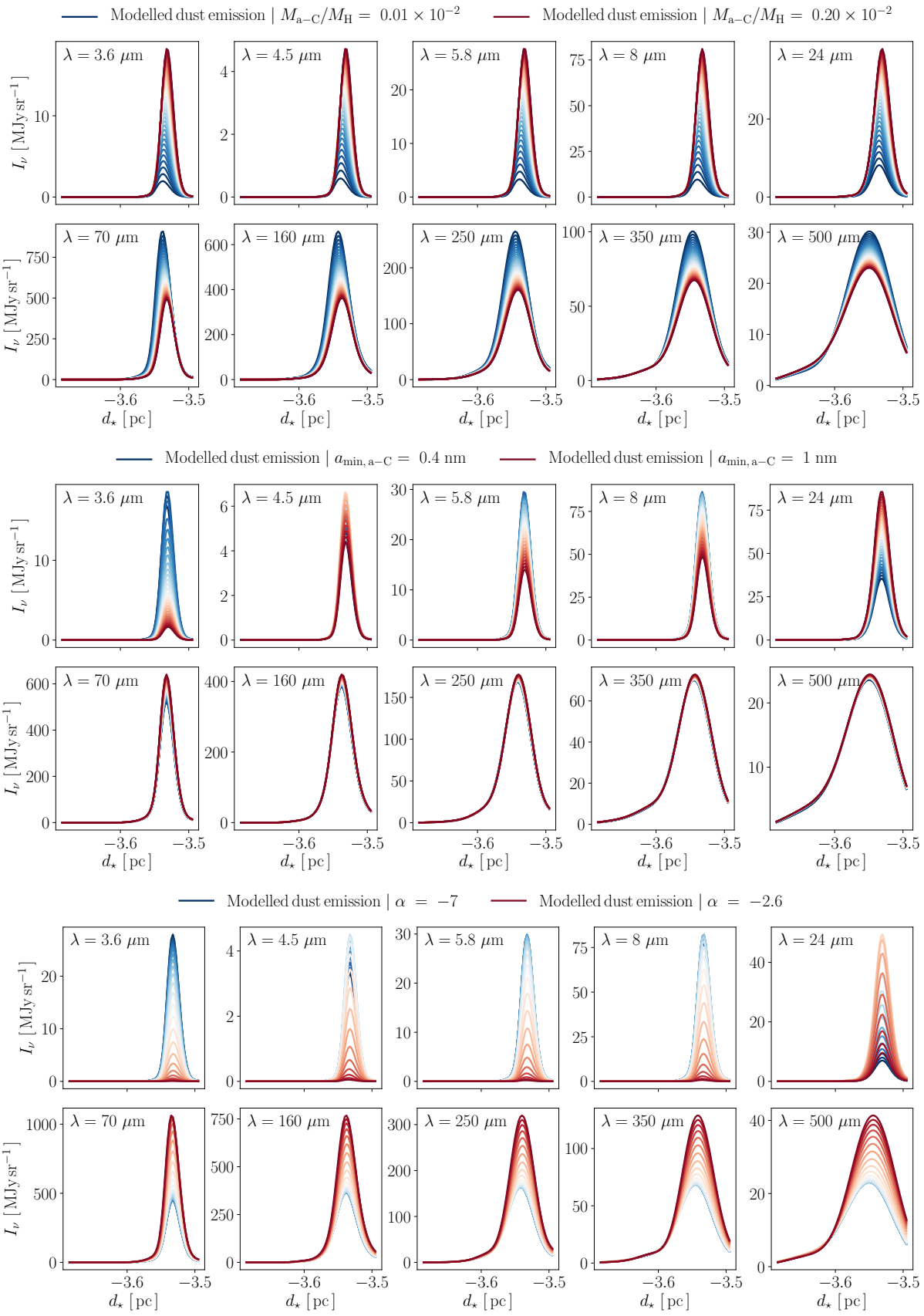

Figure 68: Top: Dust emission profiles across the Horsehead in the ten photometric bands (3.6, 4.5, 5.8, 8, 24, 70, 160, 250, 350, and 500 µm) for M_{a-C}/M_H that varies from 0.01×10^{-2} (blue line) to 0.20×10^{-2} (red line). Middle: Same for $a_{min,a-C}$ that varies from 0.4 nm (blue line) to 1 nm (red line). Bottom: Same for α that varies from -7 (blue line) to -2.6 (red line).

9.3.2 *Dust scattering*

In this section, we focus on dust scattering. We first present the scattering spectra using diffuse ISM-like dust and then describe the influence of variations in dust properties (M_{a-C}/M_H, $a_{min,a-C}$, and α) on dust scattering. Second, we study the contribution of the scattering of the photons that emerge from the heated dust in the PDR on the total scattering, which includes the scattering of the incident radiation and the scattering of the dust emission. Finally, we study the wavelength limit above which dust scattering is marginal compared to dust emission, both with diffuse-ISM like dust and dust with properties that vary.

9.3.2.1 *Dust scattering with diffuse ISM-like dust*

Fig. 69 shows scattering and emission spectra computed with SOC and using diffuse ISM-like dust (that is, CM grains with $M_{a-C}/M_H = 0.17 \times 10^{-2}$, $\alpha = -5$, and $a_{min,a-C} = 0.4$ nm).

Dust scattering has two contributions:

- dust scattering of photons that emerge from the illuminating star (essentially UV/visible photons);
- dust scattering of photons that emerge from the heated dust in the PDR (essentially IR photons).

It is therefore important to disentangle these two contributions in order to understand how dust scattering varies with the dust properties. It is usually understood that the scattering seen in PDRs is of photons from the illuminating source. Albeit mostly so, there is a range of wavelengths for which this is not the case. Fig. 66 (right panels) shows the contribution of the dust IR photons to the total scattering, as well as the contribution of the total scattering to the total emission.

We see that there is a narrow wavelength range around 1 μm where the total scattering is larger then the dust emission and, at the same time, that this total scattering is mostly due to the scattering of near-IR photons emitted by the dust.

Fig. 69 compares the dust emission spectrum (black line), the spectrum of the scattered photons which are coming from the illuminating star (blue line), and the spectrum of the scattered photons which are coming from both the illuminating star and heated dust (red line). We can see that the dust total scattering dominates the dust emission up to $\lambda \sim 1.2$ μm at $i_z = 23$ and $\lambda \sim 0.65$ μm at $i_z = 15$. Regardless of the position in the PDR, dust scattering dominates in the UV and part of the near-IR because it is efficient at these wavelengths (see Sect. 9.2 and especially Fig. 65, right panels). We also see that dust scattering in the visible decreases from $i_z = 15$ to $i_z = 23$ while it barely changes in the IR. This is due to dust extinction, which is more efficient in the UV/visible (see Sect. 9.2 and especially Fig. 65, left panel). This implies that there are less UV photons to be potentially scattered at $i_z = 23$ than at $i_z = 15$, although the number of IR photons barely decrease from $i_z = 15$ to $i_z = 23$.

Fig. 66 (left panel) shows dust emission profiles at 3.6 μm and 500 μm, as well as two wavelength limits as a function of depth in the Horsehead, defined as:

- the wavelength limit $\lambda_{lim,1}$ below which dust scattering of only photons that emerge from the star, dominates the total scattering (blue line);
- the wavelength limit $\lambda_{lim,2}$ below which dust scattering of both photons that emerge from the star and those that are emitted by dust grains, dominates dust emission (red line).

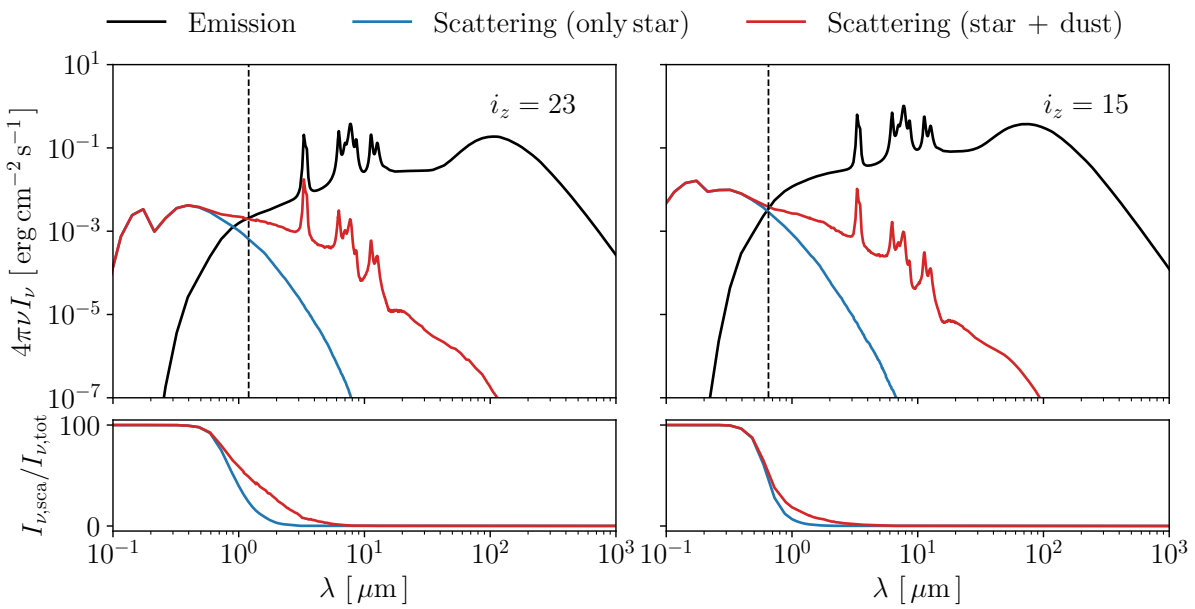

Figure 69: Top left: Dust emission (black line), dust scattering of both the stellar radiation and the dust emission (red line), and dust scattering of the stellar radiation only (blue line), for $i_z = 23$ (the position of the maximum dust emission in the far-IR). Top right: Same at $i_z = 15$ (the position of the maximum dust emission in the near-IR). Bottom left: contribution of the scattering to the total emission (scattering + emission) for dust scattering of both the star radiation and the dust re-emission (red line), and dust scattering of the stellar radiation only (blue line), for $i_z = 23$. Bottom right: Same at $i_z = 15$. The two vertical dashed lines correspond to the wavelength where dust emission is equal to dust total scattering.

Regardless of the depth, $\lambda_{\mathrm{lim},2} > \lambda_{\mathrm{lim},1}$. This is expected as the total scattering is higher than the scattering of photons that only emerge from the star (see Fig. 69). We also see that both $\lambda_{\mathrm{lim},1}$ and $\lambda_{\mathrm{lim},2}$ increase with depth into the Horsehead. As the UV/visible radiation field decreases with depth in the Horsehead because of dust extinction, there are two causes for this:

- the scattering in the visible-UV decreases with depth because it is proportional to the visible-UV field;
- less heated by the decreasing visible-UV field, the a-C grains emit less and the associated scattering in the near-to-mid IR falls off.

Finally, in the region where most dust emission occurs (that is, between the positions of the dust maximum emission at 3.6 µm and 500 µm), the wavelength limit $\lambda_{\mathrm{lim},2}$ is less than 1.5 µm. We can therefore conclude that in the Horsehead, and using diffuse ISM-like dust, dust scattering is marginal in the wavelengths covered by the ten photometric bands (3.6, 4.5, 5.8, 8, 24, 70, 160, 250, 350, and 500 µm) I used in my study. Nevertheless, I expect that the future JWST data between 0.6 and 2 µm should have a significant scattering contribution.

However, diffuse ISM-like dust are not representative of dust in PDRs (see Sect. 10). In the following section, I describe how scattering is influenced by variations in the dust properties.

9.3.2.2 *Influence of the dust properties on dust scattering*

Dust scattering is mainly due to scattering by large grains (that is, a-C:H/a-C and a-Sil/a-C grains). In the near- and mid-IR (between the two black vertical lines in Fig. 67, upper

panels), dust scattering is dominated by the scattering of IR photons emitted by heated a-C grains. Thus, as the dust IR radiation is only marginaly affected by dust extinction, near- and mid-IR scattering follows the same dependence on M_{a-C}/M_H (see Fig. 67, upper panels), $a_{min,a-C}$ (see Fig. 67, middle panels) , and α (see Fig. 67, bottom panels) as the IR dust emission.

However, opposite to the IR scattering, UV/visible scattering does depend on the dust properties, regardless of the position:

- it decreases with an increase in M_{a-C}/M_H (Fig. 67, upper panels). As dust extinction increases with M_{a-C}/M_H, the number of UV/visible photons therefore decreases with an increase in M_{a-C}/M_H, due to the high efficiency of dust extinction in the UV/visible. As a consequence, there are fewer UV/visible photons available for scattering as M_{a-C}/M_H increases;
- it barely varies with an increase of $a_{min,a-C}$ (Fig. 67, middle panels). As the total dust mass is fixed for variations in $a_{min,a-C}$ and α, an increase in $a_{min,a-C}$ implies a redistribution of the dust mass towards the larger a-C grains. Because dust extinction depends on both the dust mass and the opacity, the latter being almost unchanged in the UV/visible, dust extinction barely varies in the UV/visible. As a consequence, variation in $a_{min,a-C}$ have almost no effect on the number of UV/visible photons available to potentially be scattered;
- it increases with an increase in α (Fig. 67, bottom panels). An increase in α, as well as an increase in $a_{min,a-C}$, implies a redistribution of the dust mass from the smaller a-C grains to the larger a-C grains. However, such an increase in α leads to a significant increase in the number of larger a-C grains, that can efficiently scatter UV/visible photons. An increase in α will therefore increase dust scattering in the UV/visible.

We see that the dust properties have a strong influence on dust scattering hence, and especially on the wavelength limit below which dust scattering dominates dust emission.

9.3.2.3 *Dust emission vs. dust scattering*

As we will see in Sect. 10, the two a-C grain parameters that vary widely in the Horsehead, compared to the values of the diffuse ISM, are M_{a-C}/M_H and $a_{min,a-C}$. In this section, we study the wavelength limit λ_{lim}, below which dust scattering is larger than dust emission, in the 2D-space (M_{a-C}/M_H, $a_{min,a-C}$) defined by:

- M_{a-C}/M_H varying from 0.01×10^{-2} to 0.20×10^{-2} in steps of 0.01×10^{-2};
- $a_{min,a-C}$ varying from 0.4 nm to 1 nm in steps of 0.02 nm.

Fig. 70 shows this wavelength limit in the 2D-space (M_{a-C}/M_H, $a_{min,a-C}$) at two different positions in the Horsehead ($i_z = 15$ and $i_z = 23$).

First, we note that regardless of the position and M_{a-C}/M_H, the wavelength limit increases with an increase in $a_{min,a-C}$. As explained in Sect. 9.3.2.2, variations in $a_{min,a-C}$ barely affect the number of UV/Visible photons that can potentially be scattered hence dust scattering is almost unaffected by such variations in $a_{min,a-C}$. However, an increase in $a_{min,a-C}$ implies a large decrease of dust emission in the near-IR (see Fig. 67, middle panels). Consequently, as dust scattering is only weakly affected by variations in $a_{min,a-C}$ but that dust emission strongly decreases with an increase in $a_{min,a-C}$, the wavelength limit is shifted towards larger wavelengths when $a_{min,a-C}$ increases.

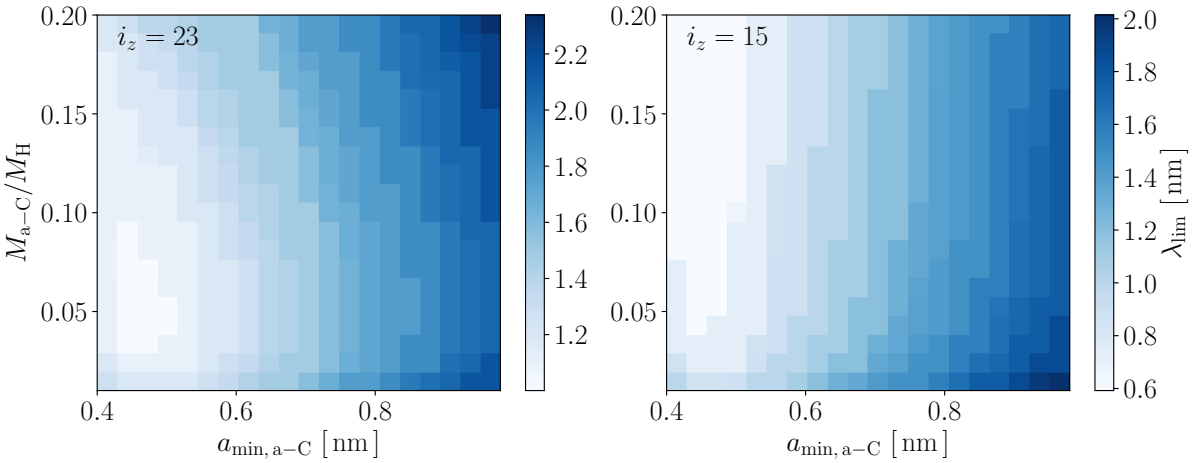

Figure 70: Left: Wavelength limit λ_{lim} at $i_z = 23$ in 2D-space (M_{a-C}/M_H, $a_{min,a-C}$) for M_{a-C}/M_H that varies from 0.01×10^{-2} to 0.20×10^{-2} and $a_{min,a-C}$ that varies from 0.4 to 1 nm. Below this limit, dust scattering is greater than dust emission. Right: Same at $i_z = 15$.

Second, we note that regardless of $a_{min,a-C}$, the evolution of the wavelength limit with M_{a-C}/M_H depends on the position:

- for $i_z = 23$, the wavelength limit slightly increases with an increase in M_{a-C}/M_H. As seen in Sect. 9.3.2.2, an increase in M_{a-C}/M_H implies an increase in dust scattering. At this position, despite the fact that dust emission increases with M_{a-C}/M_H (see Fig. 67, upper left panel), the overall dust emission is less than at $i_z = 15$ because the UV radiation field is lower than at $i_z = 15$ due to dust extinction. As a consequence, the position of the wavelength limit is dominated by dust scattering dynamics with M_{a-C}/M_H. The wavelength limit is therefore slightly shifted towards larger wavelengths when M_{a-C}/M_H increases;
- for $i_z = 15$, the wavelength limit slightly decreases with an increase in M_{a-C}/M_H. As seen in Sect. 9.3.2.2, an increase in M_{a-C}/M_H implies an increase in dust scattering. At this position, dust emission increases with M_{a-C}/M_H (see Fig. 67, upper right panel), the overall dust emission is greater than at $i_z = 15$. As a consequence, the position of the wavelength limit is dominated by dust emission variations with M_{a-C}/M_H. The wavelength limit is therefore slightly shifted towards lower wavelengths when M_{a-C}/M_H increases.

When we use diffuse ISM-like grains (that is, CM grains with $M_{a-C}/M_H = 0.17 \times 10^{-2}$, $a_{min,a-C} = 0.4$ nm, and $\alpha = -5$), the wavelength limit is $\lambda_{lim} \sim 1.2$ µm at $i_z = 23$ and $\lambda_{lim} \sim 0.65$ µm at $i_z = 15$ (see Fig. 69 or Fig. 70). In Sect. 10, we will see that in the Horsehead, the abundance of nano-grains is $6-10$ times lower than in the diffuse ISM (that is, $M_{a-C}/M_H \sim 0.01 \times 10^{-2}$) and that the minimum size of these grains is $2-25$ times higher than in the diffuse ISM (that is, $a_{min,a-C} \sim 0.85$ nm). These values corresponds to wavelengths limits of $\lambda_{lim} \sim 2$ µm at $i_z = 23$ and $\lambda_{lim} \sim 1.9$ µm at $i_z = 15$.

As a consequence, dust scattering is negligible in our study as our observations of the Horsehead cover a range of wavelengths from 3.6 to 500 µm. Nevertheless, this result is important for the future mission and especially for the JWST because a decrease in the nano-grain abundance together with an increase in the nano-grain minimum-size entails a more important contribution of dust scattering in the near-IR.

9.4 DUST SELF-ABSORPTION ALONG THE LINE-OF-SIGHT

In this section, it is necessary to define the column density along the line sight (that is, the x-axis, see Fig. 56):

$$N_H(y,z) = \int_0^{l_{PDR}} n_H(x,y,z)\,dx, \tag{100}$$

where x, y, and z are defined in Fig. 56, and as we assume here that $n_H(x,y,z) = n_H(z)$, the column density along the line of sight can be simplified and numerically be written:

$$N_H(y,z) = \sum_{i_x=1}^{N_x} n_H(z)\Delta = n_H(z)\,N_x\,\Delta, \tag{101}$$

where Δ is the bin size and N_x, the number of bins along the x-axis (that is the axis along which the line of sight is oriented). These quantities are also defined in Fig. 56. As explained in Sect. 9.1, we focus on $i_y = 3$ and therefore define, for the sake of simplicity, $N_H(i_y = 3, i_z) = N_H(i_z)$.

We also show in Fig. 72, the dust spectra from which these profiles were integrated, for different values of l_{PDR}, at the position $i_z = 23$ where dust emission is maximal in the far-IR (left panel) and at the position $i_z = 15$ where the dust emission is maximal in the near-IR (right panel). Along the line of sight, dust self-absorption depends on both the column density $N_H(i_z)$ and the dust opacity $\kappa_\nu(i_z)$.

9.4.1 *Dust self-absorption along the line of sight with diffuse ISM-like dust*

Here I study the influence of the dust self-absorption, which is sometimes neglected in the IR, albeit may be important in some cases. To this end, I performed radiative transfer across the Horsehead using diffuse ISM-like dust (CM grains with $M_{a-C}/M_H = 0.17 \times 10^{-2}$, $a_{min,a-C} = 0.4$ nm, and $\alpha = -5$) with l_{PDR} that varies from 0.005 pc to 0.5 pc in steps of 0.005 pc (that is, N_x that varies from 2 to 200 in steps of 2).

Fig. 71 shows the associated dust emission profiles in the ten photometric bands (3.6, 4.5, 5.8, 8, 24, 70, 160, 250, 350, and 500 µm), convolved with the PSFs. It is interesting to see that dust emission seems to increase linearly with l_{PDR} in all of the ten photometric bands and that the position of the maxima in each of these ten bands is unaffected by variations in l_{PDR}. We also show in Fig. 72, the dust spectra from which these profiles were integrated, for different values of l_{PDR}, at the position $i_z = 23$ where dust emission is maximal in the far-IR (left panel) and at the position $i_z = 15$ where the dust emission is maximal in the near-IR (right panel).

First, one can see that for a given l_{PDR}, the dust spectrum is slightly less intense for $i_z = 23$ than for $i_z = 15$. As there is dust extinction between $i_z = 15$ and $i_z = 23$, dust is therefore less heated further in the cloud. Moreover, another consequence of this dust extinction between those two positions is the shift towards higher wavelengths of the peak position associated with the maximum of emission of the larger grains, which implies that big grains are colder further into the cloud.

Second, regardless of the position in the cloud, we clearly see that these spectra evolve non-linearly with l_{PDR} in the near-IR, which is due to dust self-absorption. In the mid- and far-IR, the dust spectra seem to evolves linearly with l_{PDR}, which is expected since dust self-absorption is negligible at these wavelengths. We also see that this non linear increase in the

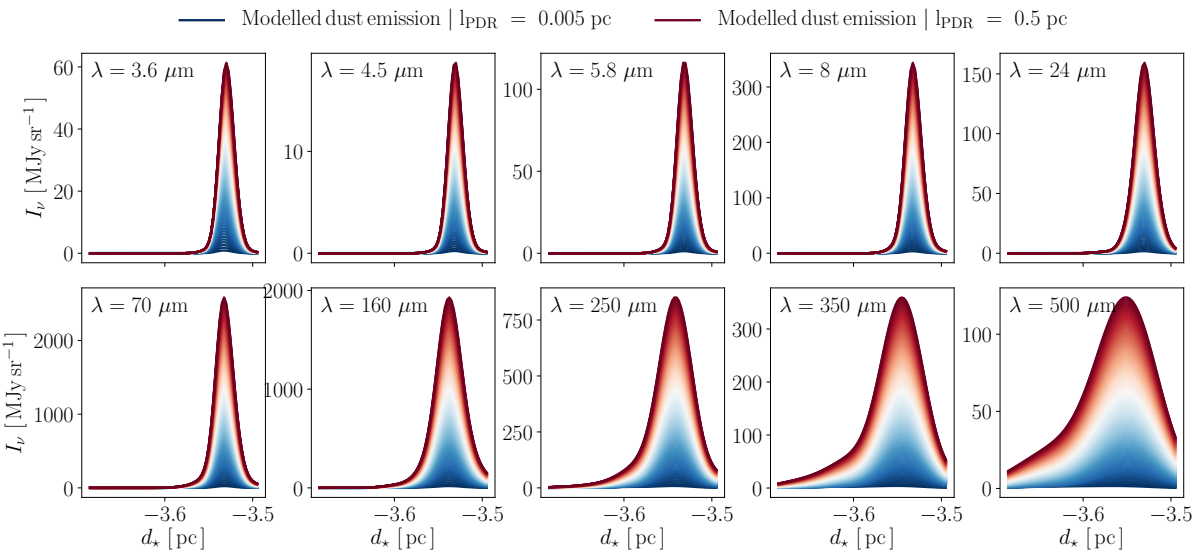

Figure 71: Dust emission profiles across the Horsehead in the ten photometric bands (3.6, 4.5, 5.8, 8, 24, 70, 160, 250, 350, and 500 µm) for l_{PDR} varying from 0.005 pc (blue line) to 0.5 pc (red line) in steps of 0.005 pc. This modelling was done with diffuse ISM-like dust (that is, $M_{a-C}/M_H = 0.17 \times 10^{-2}$, $a_{min,a-C}$ = 0.4 nm, and $\alpha = -5$). The radiation field that is illuminating the Horsehead on the right side (that is, $i_z = 0$) corresponds to a blackbody at 34 600 K with G_0 =100. All these dust emission profiles are convolved with the PSFs.

dust spectra with l_{PDR} in the near-IR is stronger at $i_z = 23$ than at $i_z = 15$ because the column density along the line of sight increases with depth inside the Horsehead and therefore, dust self-absorption increases too.

To go further, I performed linear regressions at $i_z = 15$ of $I_\lambda(i_z, l_{PDR})$ for each value of λ with l_{PDR} that varies from 0.005 pc to 0.5 pc. Fig. 73 shows the squared correlation coefficient of the linear regression of $I_\lambda(i_z = 15, l_{PDR})$ as a function of the wavelength. Two different cases are considered:

- $R^2 < 0.99$: $I_\lambda(i_z = 15, l_{PDR})$ does not evolve linearly with l_{PDR}, and dust self-absorption is therefore non-negligible along the line of sight in the l_{PDR} range we consider. This is the case for $\lambda < 4.8$ µm;
- $R^2 > 0.99$: $I_\lambda(i_z = 15, l_{PDR})$ does evolve linearly with l_{PDR}, and dust self-absorption is therefore negligible along the line of sight in the l_{PDR} range we consider. This is the case for $\lambda > 4.8$ µm.

As this study was done with diffuse ISM-like dust and because these grains are not representative of dust in PDRs (see Sect. 10), we study the influence of variations in dust properties on dust self-absorption in the following section.

9.4.2 *Dust self-absorption along the line of sight with varying dust properties*

In order to study the influence of variations in the dust properties on dust self-absorption, the following grid was explored:

- M_{a-C}/M_H varying from 0.01×10^{-2} to 0.20×10^{-2} in steps of 0.01×10^2. The squared correlation coefficients associated are shown in Fig. 74 (left panel) for $i_z = 15$;

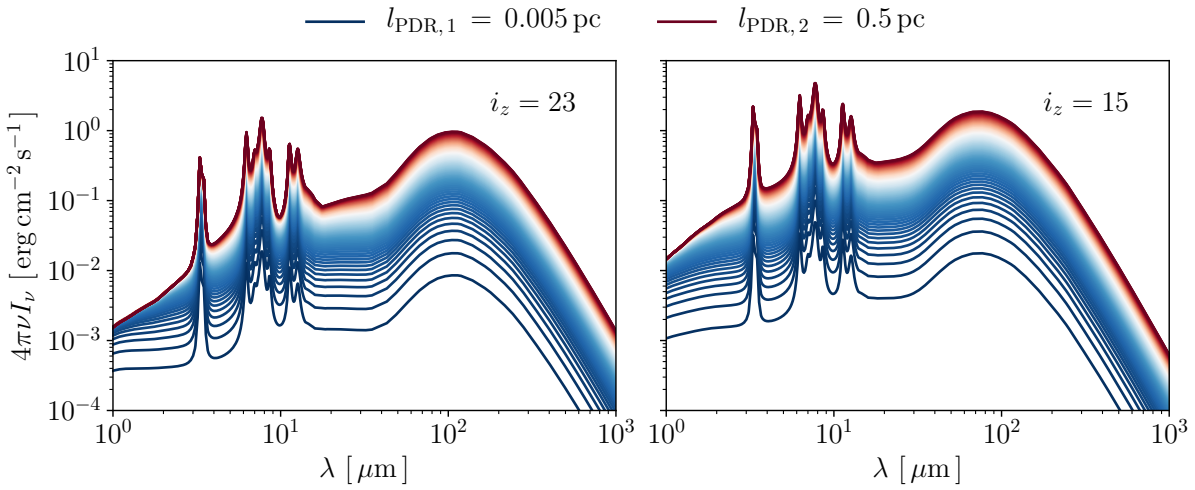

Figure 72: Left: Dust spectra for l_{PDR} varying from $l_{PDR,1} = 0.005$ pc (blue line) to $l_{PDR,2} = 0.5$ pc (red line) in steps of 0.005 pc, at the position $i_z = 23$ (that is, the position of the dust maximum emission in the far-IR, at 500 µm). Right: Same at the position $i_z = 15$ (that is, the position of the dust maximum emission in the near-IR, at 3.6 µm).

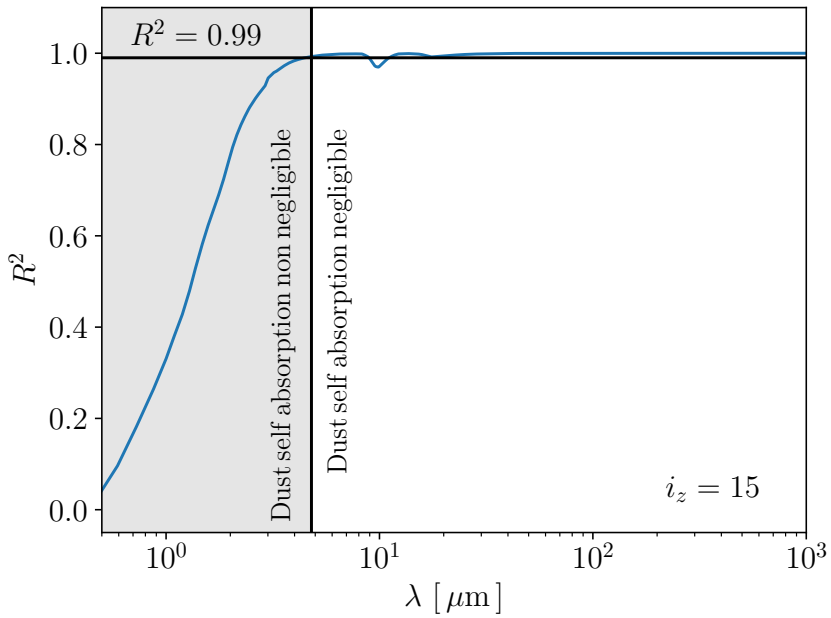

Figure 73: Squared correlation coefficient of the linear regression of $I_\lambda(i_z = 15, l_{PDR})$ as a function of the wavelength. The grey part corresponds to wavelengths where $R^2 < 0.99$ hence where dust self-absorption along the line of sight is not negligible.

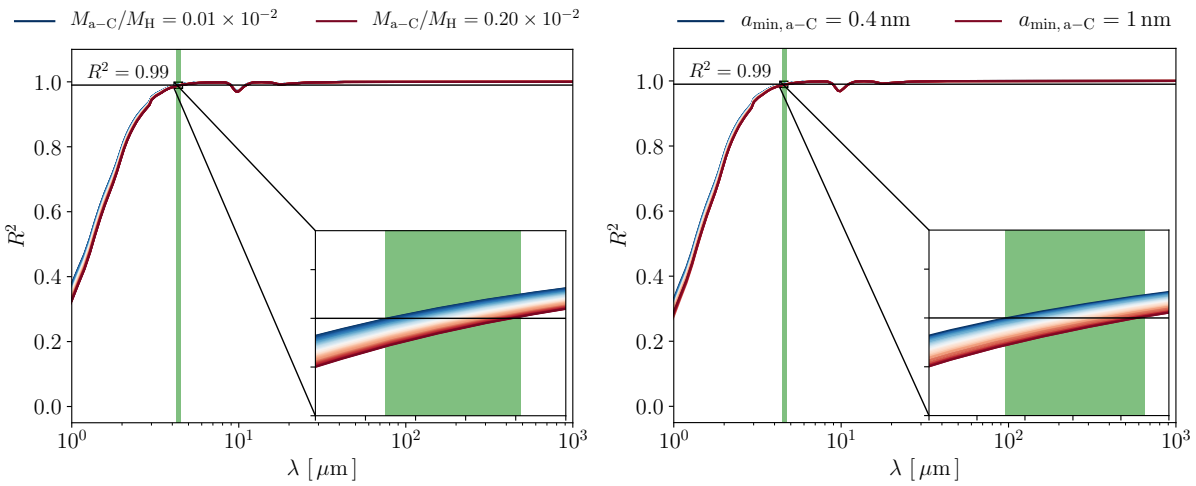

Figure 74: Left: Squared correlation coefficient of the linear regression of $I_\lambda(i_z = 15, I_{PDR})$ as a function of the wavelength, for M_{a-C}/M_H varying from 0.01×10^{-2} (blue line) to 0.20×10^{-2} (red line) in steps of 0.01×10^{-2}. Right: Same for $a_{min,a-C}$ varying from 0.4 nm (blue line) to 1 nm (red line).

- $a_{min,a-C}$ varying from 0.4 nm to 0.8 nm with steps of 0.02 nm. The squared correlation coefficients associated are shown in Fig. 74 (right panel) for $i_z = 15$.

We see that regardless of M_{a-C}/M_H and $a_{min,a-C}$, dust self-absorption is negligible longward of $\lambda \sim 4.8$ μm. This result is expected because dust extinction in the IR is mostly due to large grains (that is, a-C:H/a-C and a-Sil/a-C, see Fig. 64) and variations in M_{a-C}/M_H and $a_{min,a-C}$ barely affect a-C dust extinction (see Fig. 65, upper and middle panels). In our study, dust self-absorption is taken into account with SOC.

10 CONSTRAINING DUST PROPERTIES IN THE HORSEHEAD NEBULA

L'art est une démonstration dont la nature est la preuve.

George Sand - *Art & Nature*

Contents

10.1 INTRODUCTION

In this paper submitted to *Astronomy & Astrophysics* on 12 March 2020, accepted on 30 April 2020, and published in the volume 639 of *A&A*, we studied dust evolution in the Horsehead Nebula. The first two sections are dedicated to the introduction and the presentation of the Horsehead Nebula. In Sect. 3, we detail the dust model that we used, THEMIS, as well as the local dust emission tool, DustEM. We also present the effects of variations in the dust properties on its emission in the optically thin case with DustEM in order to distinguish variations in the dust spectrum that are due to changes in dust properties and those that are due to radiative transfer effects. In Sect. 4 we present SOC, the 3D radiative transfer code we used, as well as the effect of variations in the dust parameters on the dust emission in the optically thick case, in the case of the Horsehead. In Sect. 5 we compared our model with the observations and presented the best parameters we obtained. In Sect. 6 we discussed our results and proposed a scenario of dust evolution in the Horsehead. Finally, we presented our conclusions in Sect. 7.

10.2 PAPER

In the following paper, we show that only by including dust evolution, both in terms of the size distributions (in the outer part of the Horsehead) and compositions (in the inner part of the Horsehead), it is possible to get a good fit to the data.

A&A 639, A144 (2020)
https://doi.org/10.1051/0004-6361/202037937

Astronomy & Astrophysics

Dust evolution across the Horsehead nebula

T. Schirmer[1], A. Abergel[1], L. Verstraete[1], N. Ysard[1], M. Juvela[2], A. P. Jones[1], and E. Habart[1]

[1] Université Paris-Saclay, CNRS, Institut d'astrophysique spatiale, 91405 Orsay, France
e-mail: thiebaut.schirmer@ias.u-psud.fr
[2] Department of Physics, PO Box 64, University of Helsinki, 00014 Helsinki, Finland

Received 12 March 2020 / Accepted 30 April 2020

ABSTRACT

Context. Micro-physical processes on interstellar dust surfaces are tightly connected to dust properties (i.e. dust composition, size, and shape) and play a key role in numerous phenomena in the interstellar medium (ISM). The large disparity in physical conditions (i.e. density and gas temperature) in the ISM triggers an evolution of dust properties. The analysis of how dust evolves with the physical conditions is a stepping stone towards a more thorough understanding of interstellar dust.
Aims. We highlight dust evolution in the Horsehead nebula photon-dominated region.
Methods. We used *Spitzer*/IRAC (3.6, 4.5, 5.8 and 8 μm) and *Spitzer*/MIPS (24 μm) together with *Herschel*/PACS (70 and 160 μm) and *Herschel*/SPIRE (250, 350 and 500 μm) to map the spatial distribution of dust in the Horsehead nebula over the entire emission spectral range. We modelled dust emission and scattering using the THEMIS interstellar dust model together with the 3D radiative transfer code SOC.
Results. We find that the nano-grain dust-to-gas ratio in the irradiated outer part of the Horsehead is 6–10 times lower than in the diffuse ISM. The minimum size of these grains is 2–2.25 times larger than in the diffuse ISM, and the power-law exponent of their size distribution is 1.1–1.4 times lower than in the diffuse ISM. In the denser part of the Horsehead nebula, it is necessary to use evolved grains (i.e. aggregates, with or without an ice mantle).
Conclusions. It is not possible to explain the observations using grains from the diffuse medium. We therefore propose the following scenario to explain our results. In the outer part of the Horsehead nebula, all the nano-grain have not yet had time to re-form completely through photo-fragmentation of aggregates and the smallest of the nano-grain that are sensitive to the radiation field are photo-destroyed. In the inner part of the Horsehead nebula, grains most likely consist of multi-compositional mantled aggregates.

Key words. ISM: individual objects: Horsehead nebula – photon-dominated region – dust, extinction – evolution

1. Introduction

Interstellar dust plays an essential role within the interstellar medium (ISM) through different microphysical processes that occur on dust surfaces that can heat the gas, such as the photoelectric effect (e.g. Bakes & Tielens 1994; Weingartner & Draine 2001a), or cool the gas through gas-grain collisions (Burke & Hollenbach 1983). By acting as a catalyst, allowing atoms and molecules to react on its surface, dust is strongly involved in the chemistry of the ISM (e.g. Hollenbach & Salpeter 1971; Bron et al. 2014; Jones & Habart 2015; Wakelam et al. 2017). Dust also plays a role in the redistribution of UV-visible stellar radiation into IR-millimeter radiation, a process that depends on the dust mass and the volume of dust grains (e.g. Draine 2003; Compiègne et al. 2011). The efficiency of these processes strongly depends on dust properties such as the grain size, composition and shape. It is therefore important to constrain dust properties in order to understand the different phenomena that take place in the ISM. To this purpose, several dust models have been developed and are classified into three categories: dust composed of silicate and of graphite (e.g Mathis et al. 1977; Draine & Lee 1984; Kim et al. 1994), and an extension of these models that uses polycyclic aromatic hydrocarbons (PAHs; e.g. Siebenmorgen & Kruegel 1992; Li & Draine 2001; Weingartner & Draine 2001b). As a result of fragmentation and coagulation processes in the ISM, dust models with grains that have a core-mantle structure (e.g. Desert et al. 1990; Jones et al. 1990; Li & Greenberg 1997) and dust composite models composed of silicate and carbon grain aggregates (e.g. Mathis & Whiffen 1989; Zubko et al. 2004) have been proposed. In this paper, we use the THEMIS dust model (see Jones et al. 2013, 2014, 2017; Köhler et al. 2014, 2015; Ysard et al. 2015), which was developed in combination with the results of laboratory experiments and astronomical observations. The cornerstone of this model is its self-consistent view of the evolution of the dust constituents through the ISM. This view is required for understanding dust evolution in response to the local ISM conditions (i.e. density and radiation field).

Some of the first evidence of dust evolution was shown by Fitzpatrick & Massa (1986) through the variation in the 2175 Å interstellar bump from diffuse (R_V = 3.1) to denser regions (up to $R_V \sim 5.5$). Similarly, other studies (e.g. Cardelli et al. 1989; Cardelli & Clayton 1991; Campeggio et al. 2007) found the same variations, which were for the first time explained by Kim et al. (1994) by stating that these observations are consistent with a decrease in the carbonaceous nano-grain abundance (relative to the gas) together with an increase in larger grain abundance. It is also possible to follow dust evolution from its emission in the mid-IR (due to stochastically heated nano-grain) and in the far-IR (where large grains at thermal equilibrium emit). This has led to a wealth of studies (e.g. Boulanger et al. 1990; Laureijs et al. 1991; Abergel et al. 1994; Bernard et al. 1999; Stepnik et al. 2003; Flagey et al. 2009) revealing that nano-grain disappear in dense regions as they coagulate onto larger grains. Dust evolution is also highlighted by variation of its

far-IR opacity with the local environment (e.g. Juvela et al. 2011, 2015; Planck Collaboration XXIV 2011; Martin et al. 2012; Roy et al. 2013; Ysard et al. 2013; Köhler et al. 2015), which has been explained with dust coagulation and accretion of ice mantles. This scenario is supported by numerical simulations of dust evolution in dense regions (e.g. Ossenkopf & Henning 1994; Ormel et al. 2011; Köhler et al. 2015).

Photon-dominated regions (PDRs; Hollenbach & Tielens 1997, 1999) correspond to the interface between HII regions and molecular clouds that are irradiated by energetic stars that are located close by. In these regions, the physical conditions vary widely, and hence PDRs are a unique place to study how do dust, gas, and local physical conditions evolve with depth. Based on dust emission variations in the mid-IR observed with *Spitzer* in several PDRs (Ced 201, NGC 7023, and the western filament of ρ Ophiuchi), Berné et al. (2007) construed that such variations can be explained by the photo-processing of carbonaceous nano-grain, a scenario that was later reinforced in other PDRs (Abergel et al. 2010; Pilleri et al. 2012, 2015; Boersma et al. 2014). Using far-IR observations from *Herschel* together with the near- and mid-IR observations from *Spitzer*, Arab et al. (2012) found that the carbonaceous nano-grain abundance decreases together with an increase in the opacity of the large grains in the Orion bar. They claimed that these variations are likely due to coagulation processes in the denser part of this region. Evidence of dust evolution has also been shown in IC 63 based on extinction mapping (Van De Putte et al. 2019).

In this paper, we focus on a well-known PDR, the Horsehead nebula (Horsehead for short), which has previously been studied from the perspective of dust observations (e.g. Abergel et al. 2003; Teyssier et al. 2004; Compiègne et al. 2007, 2008; Pety et al. 2005; Arab 2012), gas observations (e.g. Habart et al. 2005; Goicoechea et al. 2006; Gerin et al. 2009; Guzmán et al. 2011; Pety et al. 2012; Le Gal et al. 2017) and laboratory experiments (Alata et al. 2015). The most important question we try to answer is the way in which the dust properties change with physical conditions. We investigate whether it is possible to understand these observations with grains from the diffuse ISM. Alternatively, there might be a viable dust evolution scenario that can explain the observations and is consistent with the physical conditions in the Horsehead.

The paper is organised as follows. In Sect. 2 we describe previous studies and the observations of the Horsehead. In Sect. 3 we detail the dust model we use, THEMIS, as well as the local dust emission tool, DustEM. We also present the effects of variations in dust properties on its emission in the optically thin case with DustEM in order to distinguish variations in the dust spectrum that are due to changes in dust properties and those that are due to radiative transfer effects. In Sect. 4 we present SOC, the 3D radiative transfer code we use, as well as the effect of variations in the dust parameters on dust emission in the optically thick case, in the case of the Horsehead. In Sect. 5 we compare our model with the observations and present the best parameters we obtain. In Sect. 6 we discuss our results and propose a scenario of dust evolution in the Horsehead. Finally, we present our conclusions in Sect. 7.

2. Prototypical PDR: the Horsehead nebula

As physical conditions vary widely and are spatially resolved in nearby PDRs, they are the ideal place to study dust evolution as a function of physical conditions. First, we introduce the different studies that have been made of the Horsehead; second, we present the observations of the Horsehead obtained with *Spitzer* and *Herschel*; and third, we describe the density profile that we used to perform radiative transfer across the Horsehead.

2.1. Well studied PDR

The Horsehead is an archetypal PDR situated at ∼400 pc (Anthony-Twarog 1982) that is illuminated by the binary star σ-Orionis which is an O9.5V binary system (Warren & Hesser 1977) with an effective temperature of $T_{\rm eff} \sim 34\,600$ K (Schaerer & de Koter 1997) located at a projected distance $d_{\rm edge} \sim 3.5$ pc from the Horsehead edge. Observations of the Horsehead have been made in the visible (e.g. de Boer 1983; Neckel & Sarcander 1985) and at millimeter wavelengths for ^{12}CO and ^{13}CO (e.g. Milman et al. 1975), CS (e.g. Lada et al. 1991), C^+ (e.g. Zhou et al. 1993) and ^{13}CO (e.g. Kramer et al. 1996).

Later, mid-IR observations (Abergel et al. 2003) with ISOCAM highlighted that the Horsehead is likely to be seen edge-on and therefore offers us a unique opportunity to study dust, gas and the evolution of local physical conditions with depth into the Horsehead. This has led to many studies at millimeter wavelengths for CO (Pound et al. 2003), $C^{18}O$ (Hily-Blant et al. 2005), CS, $C^{34}S$ and HCS^+ (Goicoechea et al. 2006), CI and CO (Philipp et al. 2006), DCO^+ (Pety et al. 2007), HCO and $H^{13}CO^+$ (Gerin et al. 2009), $H^{13}CO^+$, DCO^+, and HCO^+ (Goicoechea et al. 2009), H_2CO (Guzmán et al. 2011), CF^+ (Guzmán et al. 2012), l-C_3H^+ (Pety et al. 2012), CH_3CN, HC_3N, and C_3N (Gratier et al. 2013), H_2CO and CH_3OH (Guzmán et al. 2013), and HCOOH, CH_2CO, CH_3CHO and CH_3CCH (Le Gal et al. 2017).

Teyssier et al. (2004) found for the dust that although small hydrocarbons are expected to be photo-destroyed by the intense UV field at the edge of the Horsehead, they still exist. The authors suggest that the photo-erosion of carbonaceous nano-grain into small hydrocarbons is more efficient than the photo-destruction of small hydrocarbons at the Horsehead edge. This scenario is reinforced by observations in Pety et al. (2005), who found hydrocarbons such as CCH, c-C_3H_2, and C_4H in the UV-irradiated outer part of the Horsehead. It is also supported by laboratory experiments on thermal processed and UV-irradiated dust grains analogues (see Smith 1984; Zubko et al. 2004; Alata et al. 2014, 2015; Duley et al. 2015). Based on *Spitzer* observations, Compiègne et al. (2007) proposed a scenario where PAHs survive in HII regions, and Compiègne et al. (2008) reported that spectral variations in the mid-IR cannot be explained by radiative transfer effects alone and therefore are a consequence of the dust evolution across the Horsehead.

2.2. Observations with Spitzer and Herschel

We used *Spitzer* and *Herschel* observations (see Appendix B) of the Horsehead in ten photometric bands from 3.6 to 500 μm, which cover almost the entire dust spectrum. The processing of the *Spitzer* maps is detailed in Bowler et al. (2009). Data were processed in the HIPE environment, with standard *Herschel* corrections for instrumental effects and glitches. PACS 70 μm and 160 μm maps were obtained after the superposition of two observations with a scan speed of $20'' \, s^{-1}$, whose directions were perpendicular to one another. The overall duration of these observations is 4122 s, and they cover $8.8' \times 4.5'$ of the Horsehead. In SPIRE 250, 350 and 500 μm, they were obtained after the superposition of two observations with a scan speed of $30'' \, s^{-1}$, whose directions were perpendicular to one other. The overall duration of these observations is 1341 s, and they cover $8' \times 8'$ of

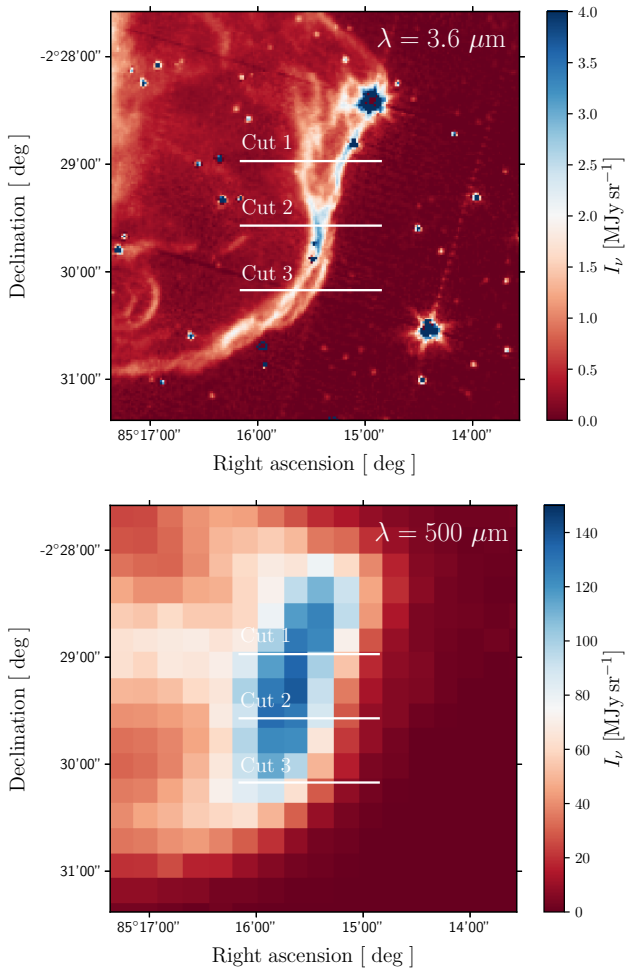

Fig. 1. *Top*: Horsehead seen with IRAC at 3.6 μm. The three white solid lines correspond to the three cuts we used in our study. *Bottom*: Horsehead seen with SPIRE at 500 μm.

the Horsehead. Striping induced by offsets in the flux calibration from one detector to another was removed using the Scan Map Destriper module included in the HIPE environment.

We studied the observed emission profiles through three different cuts across the Horsehead (see Fig. 1). The calibration uncertainty in the IRAC bands ($IRAC_{3.6}$, $IRAC_{4.5}$, $IRAC_{5.8}$, and $IRAC_{8.0}$) is 2% (Reach et al. 2005), 4% in $MIPS_{24}$ (Engelbracht et al. 2007), 5% in $PACS_{70}$ (Gordon et al. 2007), 12% in $PACS_{160}$ (Stansberry et al. 2007), and 15% in the three SPIRE bands (Swinyard et al. 2010). We considered all these errors to be independent of the wavelength to first order. We also considered that the emission in all of these ten bands comes from dust, which is not completely the case in $IRAC_{3.6}$ and $IRAC_{4.5}$. We estimated with a model of atomic and molecular gas in PDRs, the Meudon PDR Code (Le Petit et al. 2006), that gas can contribute less than 10% of the flux. However, this contribution does not affect the bulk of our results, therefore we consider that the observed emission is dust emission. Nevertheless, we must be careful in interpreting the observations because gas emission can be higher than dust emission in photometric bands that cover shorter wavelengths.

2.3. Density profile across the Horsehead

We performed radiative transfer calculations, which require information on the density profile across the Horsehead. We

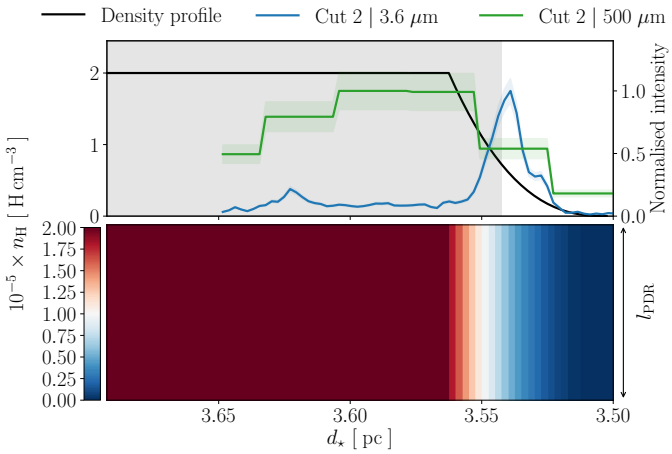

Fig. 2. *Top*: assumed density profile across the Horsehead (black line, see Sect. 2.3). Normalised dust-observed emission (blue line) in $IRAC_{3.6}$ (see Fig. 1). Normalised dust observed emission (green line) in $SPIRE_{500}$. The grey part corresponds to the inner part of the Horsehead, defined in Sect. 4.4. *Bottom*: density profile in 2D-space defined by the distance to the star, $d_\star$, and the length of the Horsehead along the line of sight, l_{PDR}.

used the profile described in Habart et al. (2005). Because the H_2 1–0 S(1) fluorescent emission is very sensitive to both the radiation field and the gas density, they observed this line with the SOFI instrument at the NTT. This observation was combined with previous observations of H_α and dust mid-IR emission in order to constrain the density profile at the edge of the Horsehead. Habart et al. (2005) also used CO millimeter observations from the IRAM 30 m telescope (Abergel et al. 2003; Teyssier et al. 2004) and the Plateau de Bure Interferometer (Pety et al. 2005), as well as 1.2 mm dust continuum emission obtained with MAMBO at the IRAM 30 m telescope (Teyssier et al. 2004) to constrain the density profile in the inner part. All these observations were interpreted with the Meudon PDR code. This density profile (see Fig. 2, upper panel) was also used in Compiègne et al. (2008) and Arab (2012) and is defined as follows:

$$n_{\rm H}(z) = \begin{cases} n_0 \times \left(\frac{z}{z_0}\right)^\gamma & \text{if } z < z_0 \\ n_0 & \text{if } z > z_0, \end{cases} \quad (1)$$

where

$$n_0 = 2 \times 10^5\,{\rm H\,cm^{-3}};\ z_0 = 0.06\,{\rm pc};\ \gamma = 2.5;\ z = d_\star - d_{\rm edge}, \quad (2)$$

with z the position from the edge of the Horsehead, γ the power-law exponent of the gas density profile and z_0 the depth beyond which constant density n_0 is reached.

The authors also estimated the length of the Horsehead along the line of sight, l_{PDR}. They found that this parameter is constrained to be between 0.1 and 0.5 pc. We assumed that the density profile is independent of the position along the line of sight (see Fig. 2, bottom panel).

3. Dust modelling

The interpretation of the multi-wavelength observations of the Horsehead depends on its structure, the incident radiation field, and the dust model. We therefore need a dust model and modelling tools to compute dust emission based on the local physical conditions. First, we describe our adopted dust model THEMIS;

second, we introduce DustEM, which we used to compute the local dust emission, and we describe the evolution of dust emission with its properties in the optically thin case using DustEM.

3.1. THEMIS

The Heterogeneous dust Evolution Model for Interstellar Solids, THEMIS[1] (e.g., Jones et al. 2013, 2017; Köhler et al. 2014) is based on observational constraints and laboratory measurements on interstellar dust analogues that are amorphous hydrocarbons, a-C(:H) (e.g., Jones 2012a,b,c), and amorphous silicates, a-Sil. This model includes dust evolution through processes such as photo-processing, fragmentation, and coagulation resulting from wide variations in the physical condition of the ISM.

THEMIS for the diffuse ISM (Jones et al. 2013; Köhler et al. 2014; Ysard et al. 2015) is composed of amorphous silicates (a-Sil/a-C) surrounded by a mantle of aromatic-rich carbon, and amorphous hydrocarbon solids that encompass a-C:H material that is H-rich and therefore aliphatic-rich, and a-C material that is H-poor and therefore aromatic-rich. When the typical penetration depth of a UV photon in an amorphous carbon grain is about 20 nm (see Fig. 15 in Jones 2012b), carbonaceous grains that are smaller than 20 nm are entirely photo-processed and therefore aromatic. Larger grains are composed of an aliphatic core and surrounded by an aromatic mantle that is 20 nm thick, which prevents photo-processing of the core and therefore allows the core to remain aliphatic. This view provides us with a continuous description of carbonaceous grains from the smallest that mostly contain aromatic cycles and are stochastically heated to the largest that are at thermal equilibrium. Details about the size distribution are listed in Table A.1. Because these grains are composed of either an a-C:H core or a silicate core surrounded in both cases by an aromatic carbonaceous mantle, they are called core-mantle grains (CM).

In the dust evolution framework assumed by THEMIS (Jones et al. 2014), large grains can form a second mantle either through accretion of C and H atoms, available in the gas phase or through coagulation of a-C nano-grains on the surfaces of larger grains. These grains are called core-mantle-mantle (CMM) grains. In denser regions, CMM grains coagulate together to form aggregates (Köhler et al. 2015) called aggregate-mantle-mantle (AMM) grains. Where the shielding from energetic photons is efficient enough, a mantle of water ice can form around AMM grains, leading to aggregated-mantle-mantle-ice (AMMI) grains.

In the following, we use several dust mixtures (see Fig. 1 in Jones et al. 2017). Parameters associated with the size distribution of these dust mixtures are listed in Table A.1 and the size distributions are shown in Fig. 3 (upper panel) with the associated spectra (see Fig. 3, bottom panel) computed with DustEM (see Sect. 3.2) using a radiation field corresponding to a star at 34 600 K with $G_0 = 100$, where

$$G_0 = \frac{1}{1.6 \times 10^{-3}\,(\mathrm{erg\,s^{-1}\,cm^{-2}})} \int_{6\,\mathrm{eV}}^{13.6\,\mathrm{eV}} I_\nu \,\mathrm{d}\nu. \quad (3)$$

In the near-IR (1–5 μm) and mid-IR (5–30 μm), dust emission comes mainly from the a-C grains. In the far-IR (from 50 to 500 μm), dust emission comes mainly from a-Sil/a-C and a-C:H/a-C grains.

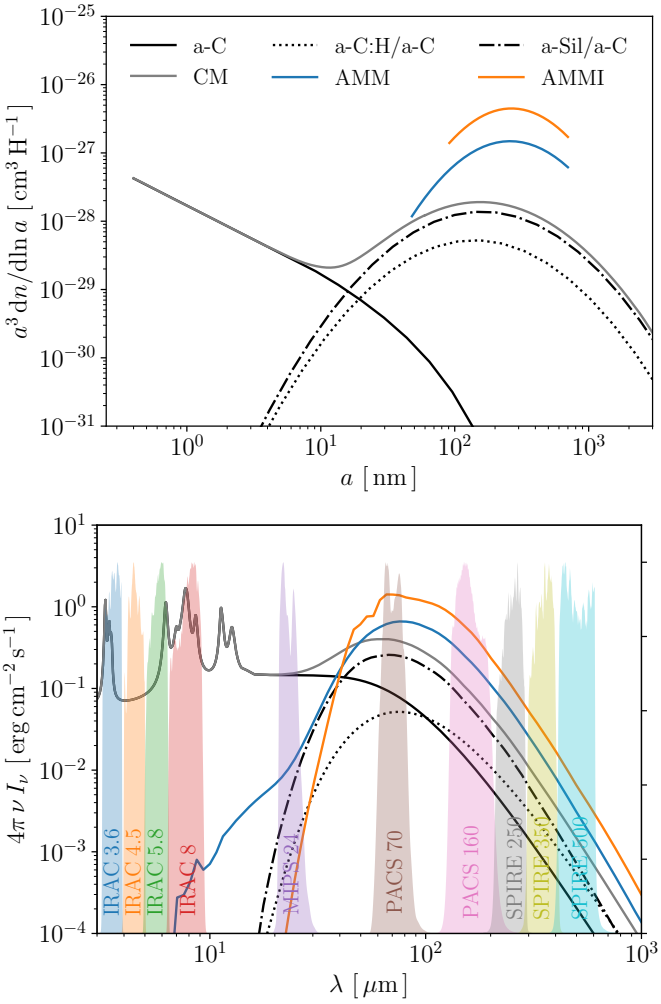

Fig. 3. *Top*: size distributions of the dust mixtures from THEMIS (parameters are listed in Table A.1) for CM-grains, i.e. diffuse ISM-like dust (grey line), AMM (blue line), and AMMI (orange line), i.e. grain aggregates typical of starless dense clouds. The black line, the dotted line, and the dash-dotted line correspond to a-C, a-C:H/a-C, and a-Sil/a-C respectively, which are the sub-components of the CM grains. *Bottom*: associated spectra, computed with DustEM with a radiation field corresponding to a star at 34 600 K with $G_0 = 100$.

3.2. Influence of dust properties on dust emission with DustEM

DustEM[2] (Compiègne et al. 2011) is a modelling tool that computes the extinction, the emission, and the polarisation of interstellar dust grains heated by photons in the optically thin case (i.e. no radiative transfer).

In order to distinguish the effects of radiative transfer from variations in the dust properties on emission, we studied the influence of such variations with DustEM. We modified the following parameters:

1. The a-C abundance, i.e. the a-C mass to gas ratio, $M_{\mathrm{a-C}}/M_{\mathrm{H}}$, which we varied from 0.01×10^{-2} to 0.20×10^{-2} in steps of 0.01×10^{-2}.
2. The a-C minimum size, $a_{\mathrm{min,\,a-C}}$, which we varied from 0.4 nm to 0.9 nm in steps of 0.02 nm.
3. The slope of the a-C power-law size distribution, α, which we varied from −6 to −4 in steps of 0.1.

[1] THEMIS is available here : https://www.ias.u-psud.fr/themis/

[2] DustEM is available here: http://www.ias.u-psud.fr/DUSTEM

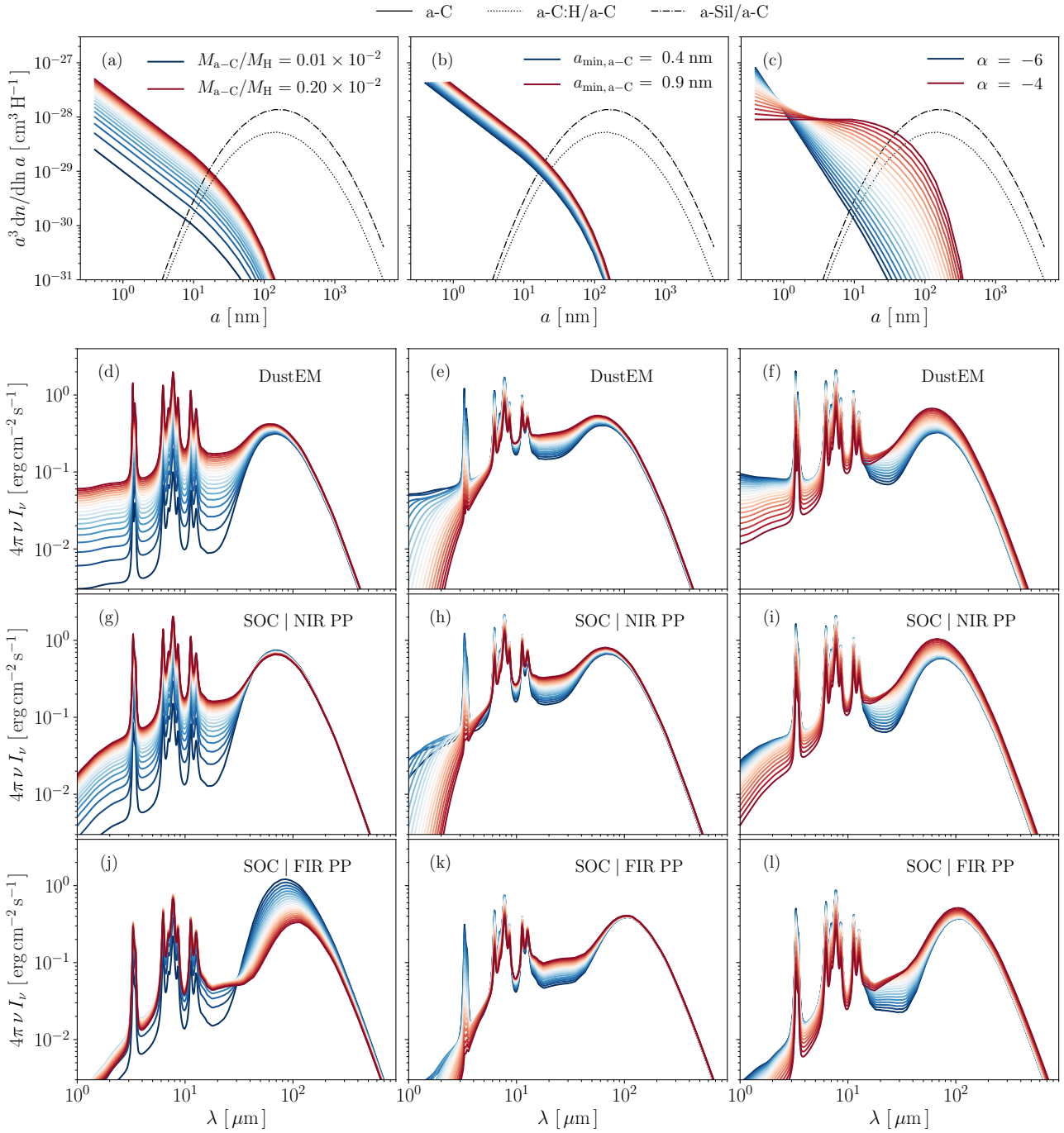

Fig. 4. Dust size distributions for different values of M_{a-C}/M_H (*panel a*), $a_{min,a-C}$ (*panel b*) and α (*panel c*). *Panels d–l*: dust spectra for the size distributions shown in the corresponding top-row panels. The spectra are computed with DustEM (*panels d–f*) and with radiative transfer for the near-IR (*panels g–i*) and the far-IR (*panels j–l*) peak positions.

The results are shown in Fig. 4, where the spectra in panels d, e, and f are associated with the size distributions in panels a, b, and c, respectively. All the spectra are obtained with a radiation field that corresponds to a blackbody at 34 600 K scaled so that $G_0 = 100$ (i.e. the radiation field illuminating the Horsehead).

A decrease in M_{a-C}/M_H or an increase in $a_{min,a-C}$ or α leads to a decrease in the smallest a-C grains and accordingly to a decrease in the near-IR emission. Because the total dust mass is fixed, an increase in $a_{min,a-C}$ or α leads to a redistribution of the dust mass from the smallest to the largest a-C grains and therefore to an increase in the mid-IR emission. In the far-IR, dust emission is unaffected by variations in M_{a-C}/M_H, $a_{min,a-C}$, and α because a-C grains are barely responsible for any dust emission at these long wavelengths. However, the dust emission in the far-IR slightly increases with an increase in α as the mass of the largest a-C increases significantly, unlike an increase in $a_{min,a-C}$.

4. Radiative transfer modelling within the Horsehead

The Horsehead is an optically thick region that requires radiative transfer modelling to properly interpret our multi-wavelength

observations. We present the 3D radiative transfer code SOC that we used here. Performing radiative transfer is time consuming, and we here therefore explore the influence of the Horsehead length along the line of sight $l_{\rm PDR}$, and dust properties (i.e. $M_{\rm a-C}/M_{\rm H}$, $a_{\rm min,\,a-C}$, α) on dust emission after radiative transfer calculations.

4.1. Radiative transfer code : SOC

SOC is a 3D Monte Carlo radiative transfer code, parallelised using OpenCL libraries (Juvela 2019). It computes dust emission and scattering. SOC has been benchmarked with other radiative transfer codes in Gordon et al. (2017) and used in Juvela et al. (2018a,b, 2019).

The radiation field corresponds to that of a blackbody at 34 600 K produced by a star to which a dilution factor has been applied to obtain $G_0 = 100$ at the Horsehead edge. This radiation field is estimated on a logarithmic grid of 334 frequencies that extends from 3×10^9 Hz to 3×10^{16} Hz. Because the Horsehead edge is located outside the HII region, there are no photons above 13.6 eV, hence we applied the Lyman cut to the radiation field that heats the Horsehead edge. Each frequency was simulated with 10^6 photons.

In SOC, clouds can be defined on regular Cartesian grids or octree grids. We modelled the Horsehead using a Cartesian grid that contains $N_X \times N_Y \times N_Z$ cubes that measure 0.0025 pc per side. N_X is equal to 77 and corresponds to the number of cubes along the Horsehead-star axis. N_Y is equal to 7 and corresponds to the number of cubes along the axis perpendicular to the Horsehead-star axis and the line-of-sight axis (i.e. the observer-Horsehead axis). N_Z corresponds to the number of cubes in the Horsehead along the line of sight and therefore depends on the value of $l_{\rm PDR}$: $N_Z = l_{\rm PDR}\,/\,0.0025$ pc. For each cube, we associated a value of the gas density as described in Sect. 2.3.

We computed only dust emission because regardless of the dust properties, dust scattering contributes less than 1% to the total dust brightness in the near-IR photometric bands. After the integration along the line of sight, dust emission profiles across the Horsehead were integrated into the different photometric bands and convolved with the PSFs.

4.2. Influence of l_{PDR} on dust emission

In the following, we study dust emission at two positions : the near-IR peak position (NIR PP) in the Horsehead, and the far-IR peak position (FIR PP). These positions corresponds to the peak of emission in $\rm IRAC_{3.6}$ and $\rm SPIRE_{500}$, respectively, shown in the Fig. 2. In order to facilitate reading the results we obtained, we also introduce $I_{\rm mod,\,max}(i) = \max(I_{{\rm mod},\,i}(z))$ where $I_{{\rm mod},\,i}(z)$ is the dust-modelled emission in the ith band at the position z along the cut.

Whether it is at the NIR PP or at the FIR PP, dust emission increases in all bands with $l_{\rm PDR}$ (see Fig. 5, top and middle panels) because the dust mass increases along the line of sight as the column density[3] increases with $l_{\rm PDR}$. Moreover, the dust emission increases linearly with $l_{\rm PDR}$ (see Fig. 5, bottom panel) revealing that dust self-absorption, which depends on both the column density and on the wavelength, is negligible at these wavelengths in the $l_{\rm PDR}$ range we considered. Consequently, we considered that the intensity increases linearly with $l_{\rm PDR}$ in the near-, mid-, and far-IR and does not affect the shape of the dust spectrum. In the following, we therefore consider $l_{\rm PDR}$ as a multiplying factor on the dust spectrum.

[3] $N_{\rm H}(z) = n_{\rm H}(z)\,l_{\rm PDR}$

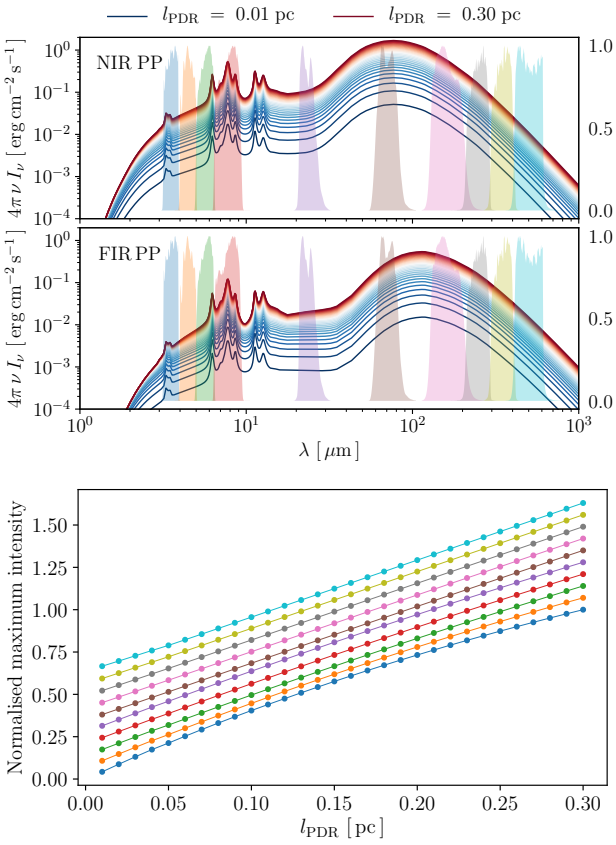

Fig. 5. *Top*: dust-modelled spectra with SOC and using CM grains, i.e. diffuse ISM-like dust, at the near-IR peak position (NIR PP) for $l_{\rm PDR}$ varying from 0.01 pc (blue line) to 0.30 pc (red line) with a step of 0.01 pc. The ten photometric bands are shown in colours behind the lines. *Middle*: same at the far-IR peak position (FIR PP). *Bottom*: normalised $I_{\rm mod,\,max}(i)$ for each band as a function of $l_{\rm PDR}$. Colours refer to the different photometric bands shown in the upper panels. Lines are shifted for clarification (from top to bottom in the order of decreasing wavelength).

4.3. Influence of dust properties on dust emission after radiative transfer

In contrast to Sect. 3.2, where we studied the influence of dust properties on dust emission in the optically thin case, we study here the influence of these properties in the optically thick case by performing a radiative transfer calculation. These results are shown in Fig. 4, where the spectra in panels g/j, h/k, and i/l are associated with the size distributions in panel a, b, and c, respectively. Spectra in panels g, h and i are located at the NIR PP, and those in panels j, k, and l are located at the FIR PP.

Dust grains are warmer at the NIR PP (see Fig. 4, panels g, h and i) than at the FIR PP (panels j, k and l) because the maximum intensity shifts towards longer wavelengths. This effect is due to the damping of the radiation field with increasing depth into the Horsehead.

At the NIR PP, dust emission in the far-IR does not vary with $M_{\rm a-C}/M_{\rm H}$ (see Fig. 4, panel g), in contrast to what we show in the inner part (panel j). Because dust emission in the far-IR is unaffected by variations in $M_{\rm a-C}/M_{\rm H}$ in the optically thin case (see Sect. 3.2), this is strictly a radiative transfer effect. Because the a-C grains bear a large fraction of the total dust cross-section,

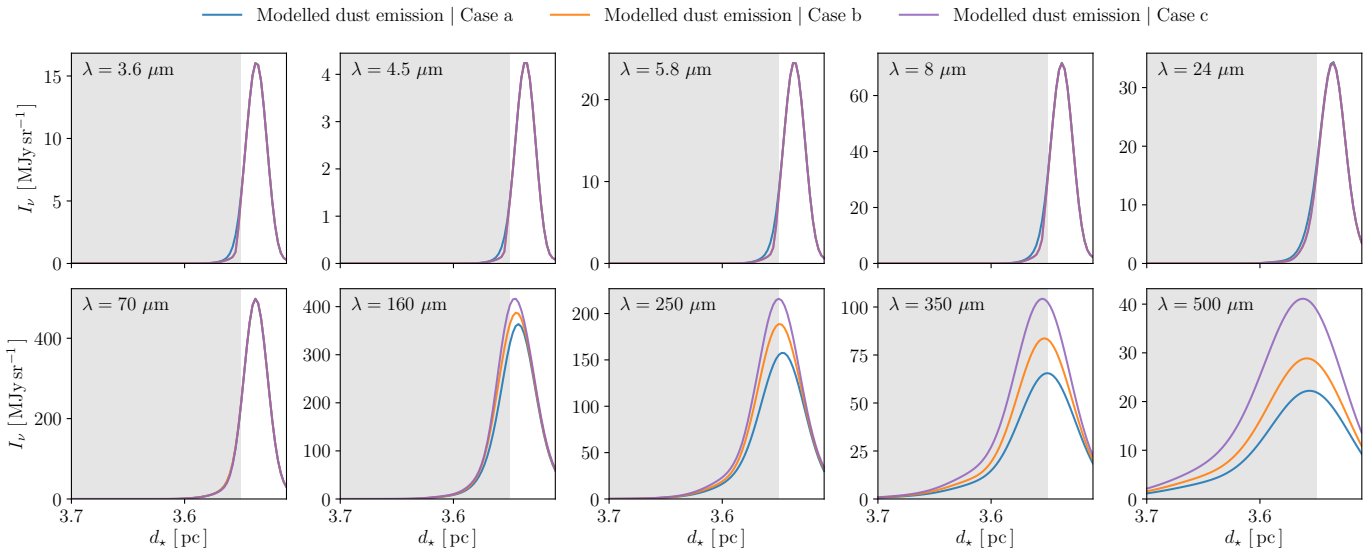

Fig. 6. Dust-modelled emission profiles in the ten photometric bands for case a (blue lines), case b (orange lines) and case c (purple lines). The darker grey parts correspond to the inner Horsehead where AMM and AMMI grains are used in cases b and c, respectively.

an increase in $M_{\mathrm{a-C}}/M_{\mathrm{H}}$ increases the extinction significantly. As $M_{\mathrm{a-C}}/M_{\mathrm{H}}$ increases, the radiation field is therefore increasingly damped at the NIR PP, and fewer photons are available at the FIR PP to heat the larger grains. Panel j shows that the wavelength associated with the highest emission shifts towards longer wavelengths with an increase in $M_{\mathrm{a-C}}/M_{\mathrm{H}}$. This means that dust emission in the far-IR varies with $M_{\mathrm{a-C}}/M_{\mathrm{H}}$, as a result of radiative transfer effects.

The other changes in the spectra are due to variations in dust properties and are explained in Sect. 3.2.

4.4. With evolved grains

Previously, we used only CM grains throughout the Horsehead. To study the influence of dust evolution on the emission across the Horsehead, we used CM grains with modified size distributions (i.e. CM grains with values of $M_{\mathrm{a-C}}/M_{\mathrm{H}}$, $a_{\mathrm{min,\,a-C}}$, and α that differ from the diffuse ISM) in the outer part of the Horsehead where the dust is likely to be more diffuse ISM-like, and aggregate grains (AMM, AMMI) above a density threshold of 7×10^4 H cm^{-3}, where dust grains are assumed to be coagulated. In order to simplify our study, we define three different cases depending on the dust we use:

- Case a: CM grains with modified size distributions throughout the Horsehead.
- Case b: CM grains with modified size distributions in the outer part of the Horsehead and AMM in the inner part of the Horsehead.
- Case c: CM grains with modified size distributions in the outer part of the Horsehead and AMMI in the inner part of the Horsehead.

The Dust-modelled emission profiles for the three cases are shown in Fig. 6.

Because the highest emission in the near- and mid-infrared is located in the outer part of the Horsehead, the dust emission at these wavelengths is not modified because we always use modified CM grains. The dust emission in the far-infrared increases when coagulated (AMM and AMMI) dust grains are used because they are more emissive. AMMI grains are more emissive than AMM grains because the dust mass in AMMI grains is higher than in AMM grains because of the ice mantle.

5. Comparison with observations

In this section we constrain our dust model with the observations. First, we present our results using diffuse ISM-like dust (i.e. CM grains); second, we introduce the method we use in the following parts; third, we constrain the four parameters $M_{\mathrm{a-C}}/M_{\mathrm{H}}$, $a_{\mathrm{min,\,a-C}}$, α, and l_{PDR} for the three cases of evolved grains as defined in Sect. 4.4 and across the three cuts (see Fig. 1).

5.1. Diffuse case

The results are shown in Fig. 7. The ten upper panels correspond to the modelled emission across the Horsehead using CM grains, with l_{PDR} varying from 0.1 to 0.5 pc, for the ten photometric bands. The observed emission is shown for cut 2. The bottom panels show the corresponding ratios of the highest observed and modelled intensities.

Regardless of the cut considered, it is not possible to simultaneously fit the observations in all the photometric bands (see Fig. 7, upper panel), independently of the l_{PDR} value. With l_{PDR} = 0.1 pc, we are able to roughly reproduce the observations in the near- and mid-infrared, but in the far-infrared, the modelled dust emission is too low by a factor ∼10 (see Fig. 7, bottom panels). With l_{PDR} = 0.5 pc, we are able to reproduce the observations in the far-infrared but in the near- and mid-infrared, the modelled dust emission is too high by a factor of at least ∼10.

If l_{PDR} is higher than 0.10 pc (see Sect. 2.3), near- and mid-infrared modelled dust emission will always be too high, which implies that reducing the dust abundance that is responsible for the emission at these wavelengths decreases the a-C dust-to-gas ratio, $M_{\mathrm{a-C}}/M_{\mathrm{H}}$ (see Sect. 4.3). On the other hand, the ratio between the modelled dust emission and the observations is not the same in the five near- and mid-IR bands. The shape of the spectrum therefore needs to be changed by varying $a_{\mathrm{min,\,a-C}}$ and α (see Sect. 4.3).

To summarise, it is not possible to reproduce the observations across any of the three cuts in the Horsehead for any value of l_{PDR} using diffuse ISM-like dust alone. We must therefore consider evolved dust.

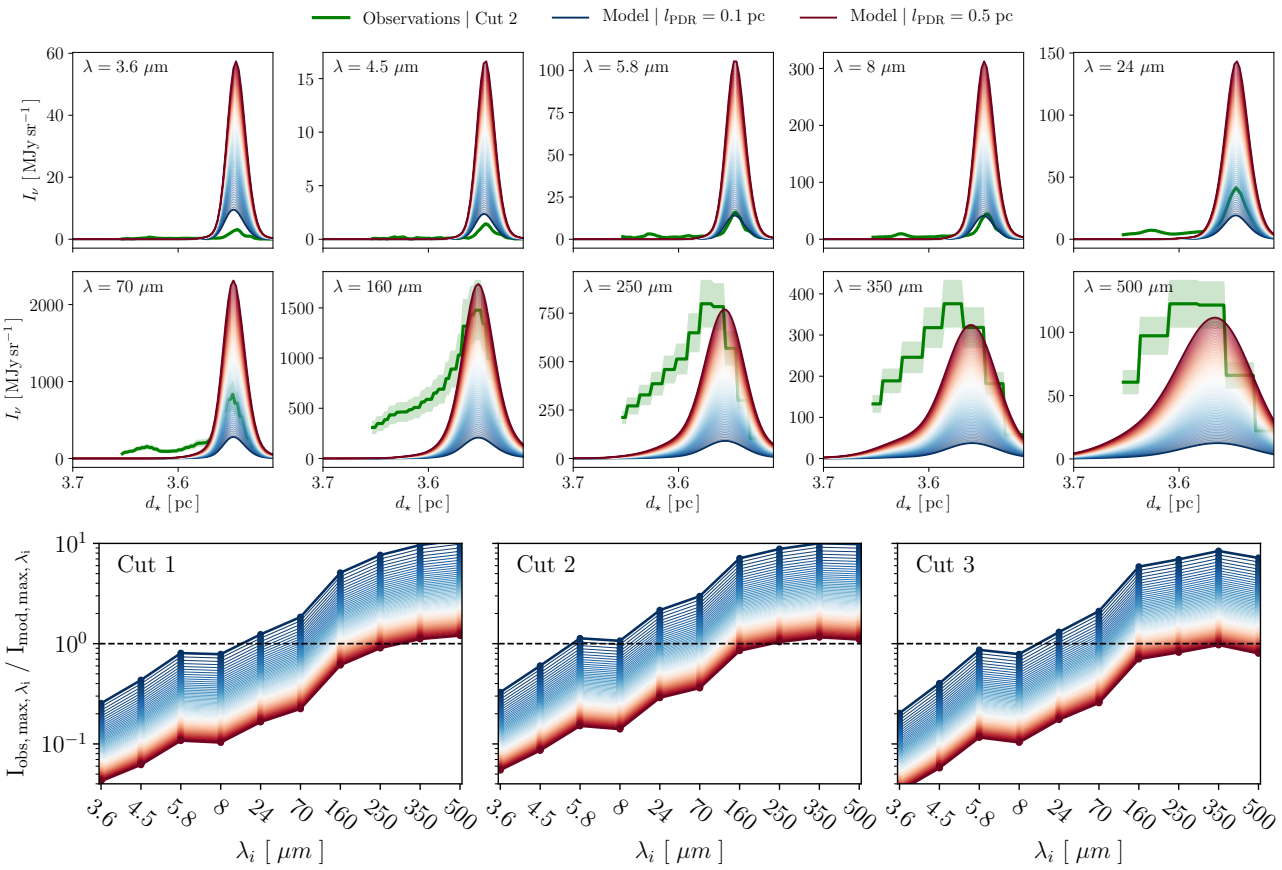

Fig. 7. *Top*: modelled dust emission for l_{PDR} varying from 0.1 pc (blue lines) to 0.5 pc (red lines) in steps of 0.01 pc for the ten photometric bands with diffuse ISM-like dust. The observed dust emission for cut 2 is shown by green lines. *Bottom*: ratio between the highest observed and modelled dust emissions in the ten photometric bands for the three cuts and l_{PDR} varying from 0.01 pc (blue lines) to 0.5 pc (red lines) in steps of 0.01 pc.

5.2. Method

To reduce computation time, instead of exploring the 4D space defined by M_{a-C}/M_H, $a_{min,a-C}$, α, and l_{PDR}, we explored the 3D space defined by M_{a-C}/M_H, $a_{min,a-C}$, and α as variation in l_{PDR} does not affect the shape of the dust spectrum (see Sect. 4.2), in contrast to variations in M_{a-C}/M_H, $a_{min,a-C}$, and α (see Sect. 4.3). Therefore, l_{PDR} can be adjusted after the fact.

Adjusting the shape of the modelled dust spectra to the observed dust spectra means that the ratio between $I_{obs,max}(i)$ and $I_{mod,max}(i)$ has to be roughly the same in every band. Therefore we minimised the following parameter:

$$\chi^2 = \sum_{i \in \text{filters}} \left(\frac{X_i - \mu}{\sigma_i} \right)^2 , \tag{4}$$

with

$$X_i = \frac{I_{obs,max}(i)}{I_{mod,max}(i)}; \quad \sigma_i = r_{obs}(i)\, X_i; \quad \mu = \langle X_i \rangle_{i \in \text{filters}} \tag{5}$$

where r_{obs} is the relative error for each filter and defined in Sect. 2.2 and $I_{obs,max}(i) = \max(I_{obs,i}(z))$ with $I_{obs,i}(z)$, the dust observed in the ith band at the position z along the cut.

The following procedure was thus applied. We constrained M_{a-C}/M_H, $a_{min,a-C}$ and α with a fixed l_{PDR} in order to adjust the shape of the modelled dust spectrum to the observed dust spectrum by minimising χ^2. We used the dust properties (M_{a-C}/M_H, $a_{min,a-C}$ and α) associated with χ^2_{min} (i.e. the minimum value of χ^2 in the 3D space defined by M_{a-C}/M_H, $a_{min,a-C}$, and α), and we adjusted the overall modelled dust spectrum to the observed dust spectrum by multiplying the flux in all bands by the same factor to obtain $\mu = 1$, which constrains l_{PDR}.

We chose to remove the IRAC$_{4.5}$ and PACS$_{70}$ bands because it is not possible to simultaneously fit the observations in the ten bands with these two included. We discuss this decision further in Sect. 6.1.

In contrast to cut 2, along which there is only one maximum in the near- and mid-IR, cuts 1 and 3 are composed of two maxima. The far-IR contains only one maximum because the spatial resolution is not sufficient to separate these two maxima. Cuts 1 and 3 contain two maxima and we chose to fit the brightest peak in each cut. We discuss this choice in Sect. 6.2.

5.3. Constrain l_{PDR} and dust properties M_{a-C}/M_H, $a_{min,a-C}$, and α

First, we studied the χ^2 distribution in the 3D space (M_{a-C}/M_H, $a_{min,a-C}$, and α) for each of the three cuts and the three cases in order to obtain the best set of parameters in these nine cases. The 3D space is defined as follows:

1. M_{a-C}/M_H varies from 0.001×10^{-2} to 0.041×10^{-2} in steps of 0.002×10^{-2}.
2. $a_{min,a-C}$ varies from 5 to 10 nm in steps of 0.25 nm.
3. α varies from -13 to -3 in steps of 0.5.

Second, we studied the χ^2 distribution in 2D space ($a_{min,a-C}$ and α), (M_{a-C}/M_H and $a_{min,a-C}$), and (M_{a-C}/M_H and α). Finally, we concluded with the comparison between the observed and

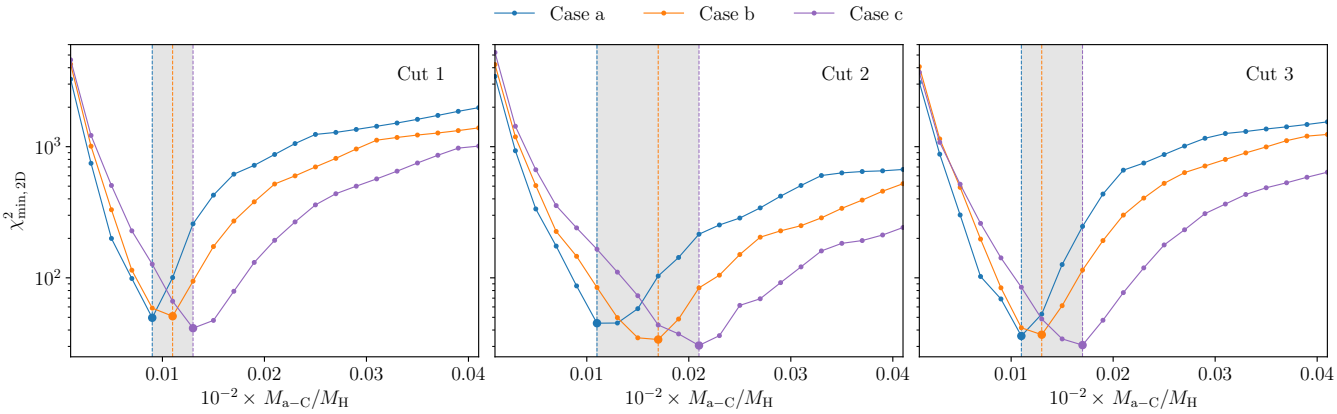

Fig. 8. $\chi^2_{\mathrm{min,\,2D}}\,(M_{\mathrm{a-C}}/M_{\mathrm{H}})$ as a function of $M_{\mathrm{a-C}}/M_{\mathrm{H}}$ for cut 1 (*left*), cut 2 (*middle*) and cut 3 (*right*). Blue lines refer to case a, orange lines to case b, and purple lines to case c. Vertical dashed lines correspond to the minima of $\chi^2_{\mathrm{min,\,2D}}$ (i.e. χ^2_{min}).

Table 1. Best set of parameters ($M_{\mathrm{a-C}}/M_{\mathrm{H}}$, $a_{\mathrm{min,\,a-C}}$, α, and l_{PDR}) and the χ^2_{min} associated with all cuts and cases.

	Case a			Case b			Case c		
	cut 1	cut 2	cut 3	cut 1	cut 2	cut 3	cut 1	cut 2	cut 3
$10^2 \times M_{\mathrm{a-C}}/M_{\mathrm{H}}$	0.009	0.011	0.011	0.011	0.017	0.013	0.013	0.021	0.017
$a_{\mathrm{min,\,a-C}}$ [nm]	0.825	0.825	0.925	0.825	0.8	0.925	0.825	0.8	0.9
α	−7.0	−6.0	−7.5	−6.5	−5.5	−7.5	−6.5	−5.5	−6.5
l_{PDR} [pc]	0.283	0.297	0.273	0.290	0.267	0.282	0.275	0.254	0.265
χ^2_{min}	49.6	45.1	36.0	51.0	33.9	36.9	41.3	30.5	30.7

modelled dust emission profiles for each of the three cuts and the three cases with the best sets of parameters.

For more clarity, we defined $\chi^2_{\mathrm{min,2D}}\,(M_{\mathrm{a-C}}/M_{\mathrm{H}})$, which is the minimum value of χ^2 in 2D space ($a_{\mathrm{min,\,a-C}}$ and α) for a given value of $M_{\mathrm{a-C}}/M_{\mathrm{H}}$. We also defined χ^2_{min}, which is the minimum value of χ^2 in 3D space ($M_{\mathrm{a-C}}/M_{\mathrm{H}}$, $a_{\mathrm{min,\,a-C}}$, and α), that is, the lowest value of $\chi^2_{\mathrm{min,\,2D}}\,(M_{\mathrm{a-C}}/M_{\mathrm{H}})$.

5.3.1. χ^2 distribution in 3D space ($M_{\mathrm{a-C}}/M_{\mathrm{H}}$, $a_{\mathrm{min,\,a-C}}$, and α)

Figure 8 shows $\chi^2_{\mathrm{min,2D}}\,(M_{\mathrm{a-C}}/M_{\mathrm{H}})$ and Table 1 summarises these results.

First and foremost, $M_{\mathrm{a-C}}/M_{\mathrm{H}}$ is between 0.01 $\times 10^{-2}$ and 0.03 $\times 10^{-2}$, that is, between 6 and 10 times lower than in the diffuse ISM (0.17 $\times 10^{-2}$) regardless of the cut or the case considered. Second, $a_{\mathrm{min,\,a-C}}$ is between 0.8 and 0.925 nm, that is between 2 and 2.25 times larger than in the diffuse ISM (0.4 nm). Third, α is between −7 and −5.5, that is, between 1.1 and 1.4 times lower than in the diffuse ISM (−5).

Regardless of the cut, $M_{\mathrm{a-C}}/M_{\mathrm{H}}$ increases from case a to case c (see Fig. 8). In case a, we only used modified CM grains (i.e. CM grains with values of $M_{\mathrm{a-C}}/M_{\mathrm{H}}$, $a_{\mathrm{min,\,a-C}}$, and α that differ from the diffuse ISM) in the outer part and in the inner part of the Horsehead, but we use modified CM grains in the outer part of the Horsehead and AMMI grains in the inner part in case *c*. Because AMMI grains are more emissive in the far-IR than CM grains, emission in this wavelength range must decrease to fit the observations, which can be achieved by reducing l_{PDR} (see Sect. 4.2), hence l_{PDR} decreases from case a to case *c*. This decrease in l_{PDR} implies a decrease in emission in the near- and mid-IR, which means that $M_{\mathrm{a-C}}/M_{\mathrm{H}}$ must increase to counterbalance this variation.

5.3.2. χ^2 distribution in 2D space ($a_{\mathrm{min,a-C}}$ and α), ($M_{\mathrm{a-C}}/M_{\mathrm{H}}$ and $a_{\mathrm{min,a-C}}$), and ($M_{\mathrm{a-C}}/M_{\mathrm{H}}$ and α)

We show in Fig. 9 the χ^2 distribution for cut 2 in 2D space ($a_{\mathrm{min,\,a-C}}$ and α), ($M_{\mathrm{a-C}}/M_{\mathrm{H}}$ and $a_{\mathrm{min,\,a-C}}$), and ($M_{\mathrm{a-C}}/M_{\mathrm{H}}$ and α). We chose to focus on only one cut because we are interested in the behaviour of the χ^2 distribution here, which is the same regardless of the cut.

The most important result is that regardless of the case, there is a unique minimum in all 2D spaces. Moreover, as explained in Sect. 3.2, a decrease in $M_{\mathrm{a-C}}/M_{\mathrm{H}}$, to first order, is similar to an increase in $a_{\mathrm{min,\,a-C}}$ and α, regarding dust emission in the near- and mid- IR. An increase in $a_{\mathrm{min,\,a-C}}$ is therefore counterbalanced by a decrease in α to keep low values of χ^2, and an increase in $M_{\mathrm{a-C}}/M_{\mathrm{H}}$ is counterbalanced by an increase in $a_{\mathrm{min,\,a-C}}$ and in α, which explains the banana-shape of the low χ^2 values in each of the 2D spaces.

Furthermore, from case a to case c, the position of χ^2 minimum value moves. From case a to case c, dust emission in the far-IR increases (see Fig. 6), which shows that this effect is counterbalanced by a decrease in l_{PDR} that also reduces dust emission in the near- and mid-IR. To compensate for this decrease in dust emission in the near- and mid-IR, the value of $M_{\mathrm{a-C}}/M_{\mathrm{H}}$ associated with the χ^2 minimum value increases from case a to case c in 2D spaces ($M_{\mathrm{a-C}}/M_{\mathrm{H}}$ and $a_{\mathrm{min,\,a-C}}$) and ($M_{\mathrm{a-C}}/M_{\mathrm{H}}$ and α). In 2D space ($a_{\mathrm{min,\,a-C}}$ and α), this effect is counterbalanced by a decrease in α and an increase in $a_{\mathrm{min,\,a-C}}$.

5.3.3. Comparison between dust-modelled emission and dust-observed emission profiles

Here, we use the best set of parameters ($M_{\mathrm{a-C}}/M_{\mathrm{H}}$, $a_{\mathrm{min,\,a-C}}$, α and l_{PDR}) that are listed in Table 1 and compare the modelled

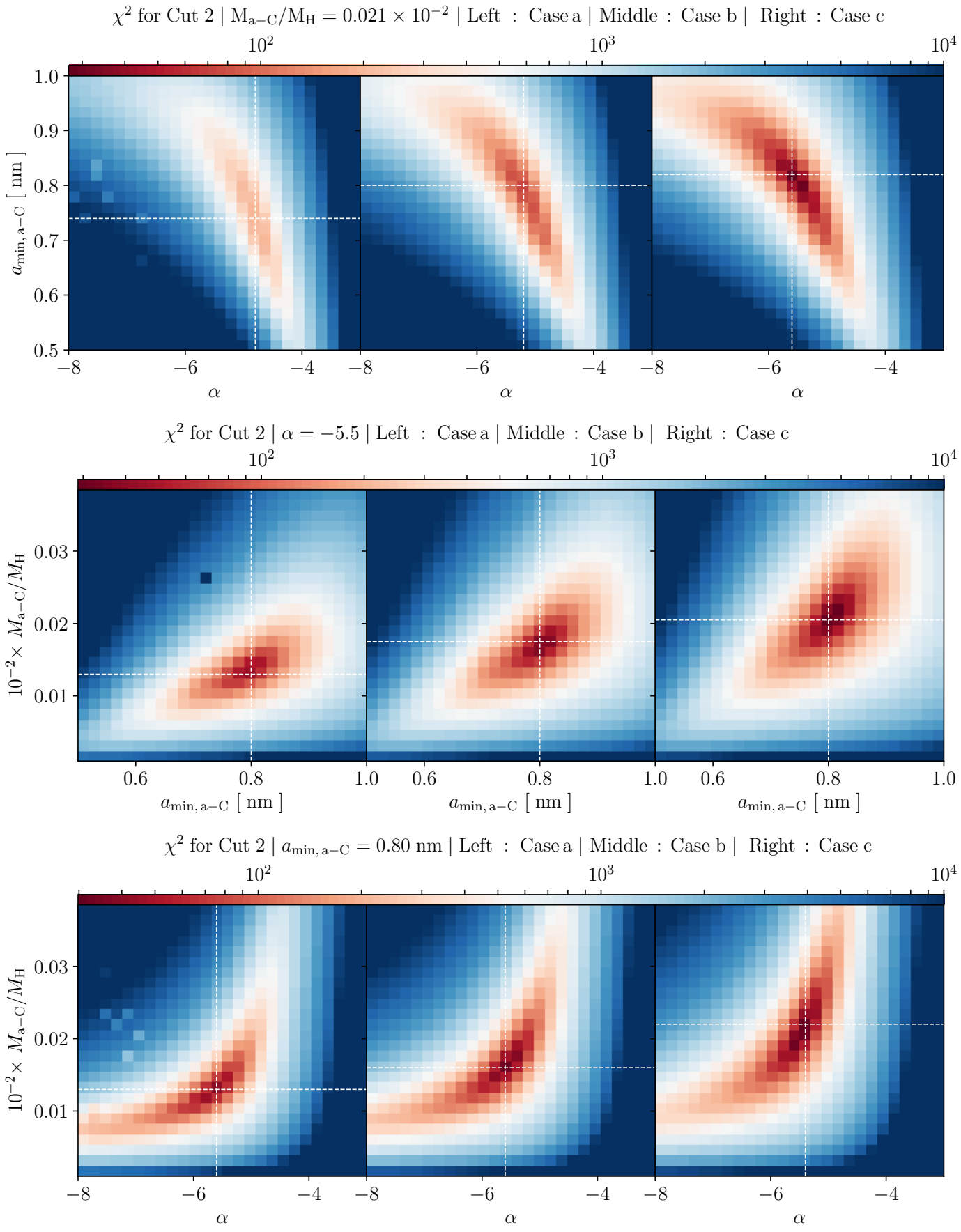

Fig. 9. *Top*: χ^2 in 2D space ($a_{\mathrm{min,a-C}}$ and α) for cut 2 with $M_{a-C}/M_H = 0.021 \times 10^{-2}$. *From left to right*: subplots correspond to case a (*left*), case b (*middle*), and case c (*right*). *Middle*: χ^2 in 2D space (M_{a-C}/M_H and $a_{\mathrm{min,a-C}}$) for cut 2 with $\alpha = -5.5$. *Bottom*: χ^2 in 2D space (M_{a-C}/M_H and α) for cut 2 with $a_{\mathrm{min,a-C}} = 0.80$ nm.

emission profiles in the ten photometric bands for the three cases with the observed emission profiles in the three cuts (see Fig. 10). We focus on three aspects: the highest intensity in each of the ten bands, the position of these maxima, and the width of these profiles.

In the near- and mid-IR, except in $IRAC_{4.5}$, the maximum emission is well reproduced, regardless the case or the cut. In $PACS_{70}$, although the maximum of emission is never reproduced, the discrepancy between the maximum modelled emission and the maximum observed emission decreases from case a to case c. From $SPIRE_{250}$ to $SPIRE_{500}$, the maximum emission is in the error bars, regardless of the case or the cut, and the discrepancy between the maximum modelled emission and the maximum observed emission decreases from case a to case c. In $PACS_{160}$, the maximum emission is within the error bars only for case c for cuts 2 and 3, but never for cut 1, regardless of the case.

The position of the maximum emission is well reproduced from $IRAC_{3.6}$ to $PACS_{70}$ regardless of the cut and the case. Cut 1 shows a small discrepancy between the position of the maximum emission and the position of the observed emission from $PACS_{70}$ to $SPIRE_{500}$. For cut 2, there is the same discrepancy in $SPIRE_{350}$ and $SPIRE_{500}$, regardless of the case. For cut 3, all the positions are well reproduced.

The width of the profiles are well reproduced from $IRAC_{3.6}$ to $PACS_{160}$, but slightly different from $SPIRE_{250}$ to $SPIRE_{500}$. This might be due to large structures in the Horsehead.

To summarise, the observed dust emission is well reproduced in the near- and mid-IR, except in $IRAC_{4.5}$, regardless of the case and the cut. In the far-IR, the discrepancy between observed dust emission and modelled dust emission decreases from case a to case c.

6. Discussion

First, we discuss the discrepancy between the dust-modelled emission and the dust-observed emission in $IRAC_{4.5}$ and in $PACS_{70}$; second, the results obtained are described; third, we propose a scenario of dust evolution in agreement with the results obtained. We conclude with a discussion of dust-processing timescales in support of this scenario.

6.1. Discrepancy in $IRAC_{4.5}$ and $PACS_{70}$

In $IRAC_{4.5}$, the modelled dust emission is always overestimated (see Fig. 10) by a factor 2–4. Because this filter covers the dust continuum and the wings of the IR bands from a-C:H nano-grain, this suggests that the wings of the IR bands in this region are different (i.e. weaker and/or narrower, see e.g. Boutéraon et al. 2019 for more details about the variability of the IR-band widths) from those in the diffuse ISM. We here study dust that evolves from dense cloud dust in response to interaction with UV photons.

Moreover, a-C:H nano-grain freshly produced may not yet have had time to be entirely photo-processed and therefore have a high band-to-continuum ratio because of their high fraction of aliphatic bonds, as opposed to aromatic bonds. As discussed in Jones et al. (2013), this requires a-C:H nano-grain with a band gap larger than 0.1 eV, the value adopted in the diffuse ISM.

However, because we lack dust spectroscopic information of the Horsehead in the near-IR, we are unable to answer to these previous questions. In the near future, JWST spectroscopic data should allow us to understand such changes in the structure of a-C:H nano-grains.

In $PACS_{70}$, models always overestimate the emission (see Fig. 10) by a factor 3-4. This suggests that large grains (a-Sil/a-C and a-C:H/a-C for case a, AMM grains for case b and AMMI grains for case c) are somewhat too warm and not emissive enough. This is supported by recent laboratory experiments in which the mass absorption coefficient of silicates in the far-IR is larger (up to an order of magnitude) than the coefficient that are currently used in THEMIS (see Fig. 5 in Demyk et al. 2017). As a consequence, the large grains we used here are probably not emissive enough. The incorporation of these new laboratory results in THEMIS will most likely reduce the discrepancy in $PACS_{70}$.

6.2. Main results

Using the 3D radiative transfer code SOC together with the dust model THEMIS, we can reproduce the Horsehead observations in eight of the ten photometric bands of *Spitzer* and *Herschel*.

The main results for the outer part of the Horsehead are the following:

1. The nano-grain (i.e. a-C grains) dust-to-gas mass ratio, $M_{\rm a-C}/M_{\rm H}$, is 6–10 times lower than in the diffuse ISM.
2. The minimum size of the nano-grain, $a_{\rm min,\,a-C}$, is 2 to 2.25 times larger than in the diffuse ISM.
3. The power-law exponent of the nano-grain size distribution, α, is 1.1–1.4 times lower than in the diffuse ISM, that is, the size distribution is steeper.

The best size distributions for the three cuts and case *c* are shown in Fig. 11. For the inner part of the Horsehead, we tested three different types of dust, diffuse ISM-like dust (CM) with modified size distributions in case a, aggregates of grains (AMM) in case b, and aggregates of grains with ice mantles (AMMI) in case c. At long wavelengths (from $PACS_{160}$ to $SPIRE_{500}$), the results are significantly better when we used AMMI instead of CM grains. For $PACS_{70}$, even though we are unable to reproduce the observed emission with our model, using aggregates (AMM or AMMI) instead of diffuse ISM-like dust (CM) with modified size distributions, significantly improved the fit in this band.

The length of the Horsehead along the line of sight, $l_{\rm PDR}$, is found to be within the range of 0.26 and 0.30 pc. This agrees with previous gas studies (Habart et al. 2005).

We note that $M_{\rm a-C}/M_{\rm H}$ is higher for cut 2 than cuts 1 and 3 (see Table 1). In these two cuts, the peak in the FIR is composed of two substructures that are spatially unresolved, in constrast to the near- and mid-IR. Consequently, $l_{\rm PDR}$ has to be larger for cuts 1 and 3, in contrast to what would have been expected if these two peaks had been resolved. Because an increase in $l_{\rm PDR}$ implies an increase in the near- and mid-infrared emission, it is therefore required to decrease $M_{\rm a-C}/M_{\rm H}$. We conclude that the different values of $M_{\rm a-C}/M_{\rm H}$ in Table 1 for the three cuts do not reveal any difference in dust properties.

6.3. Dust evolution scenario

Our results show significant variations of the dust size distribution, and in the following, we outline a possible scenario of dust evolution across the Horsehead interface. Because of the strong incident radiation field, we assume that the dominant process is the exposure of dust grains from the dense molecular cloud (the inner region) to the UV light of σ-Ori. This suggests two main photo-processing sequences: (i) the partial fragmentation

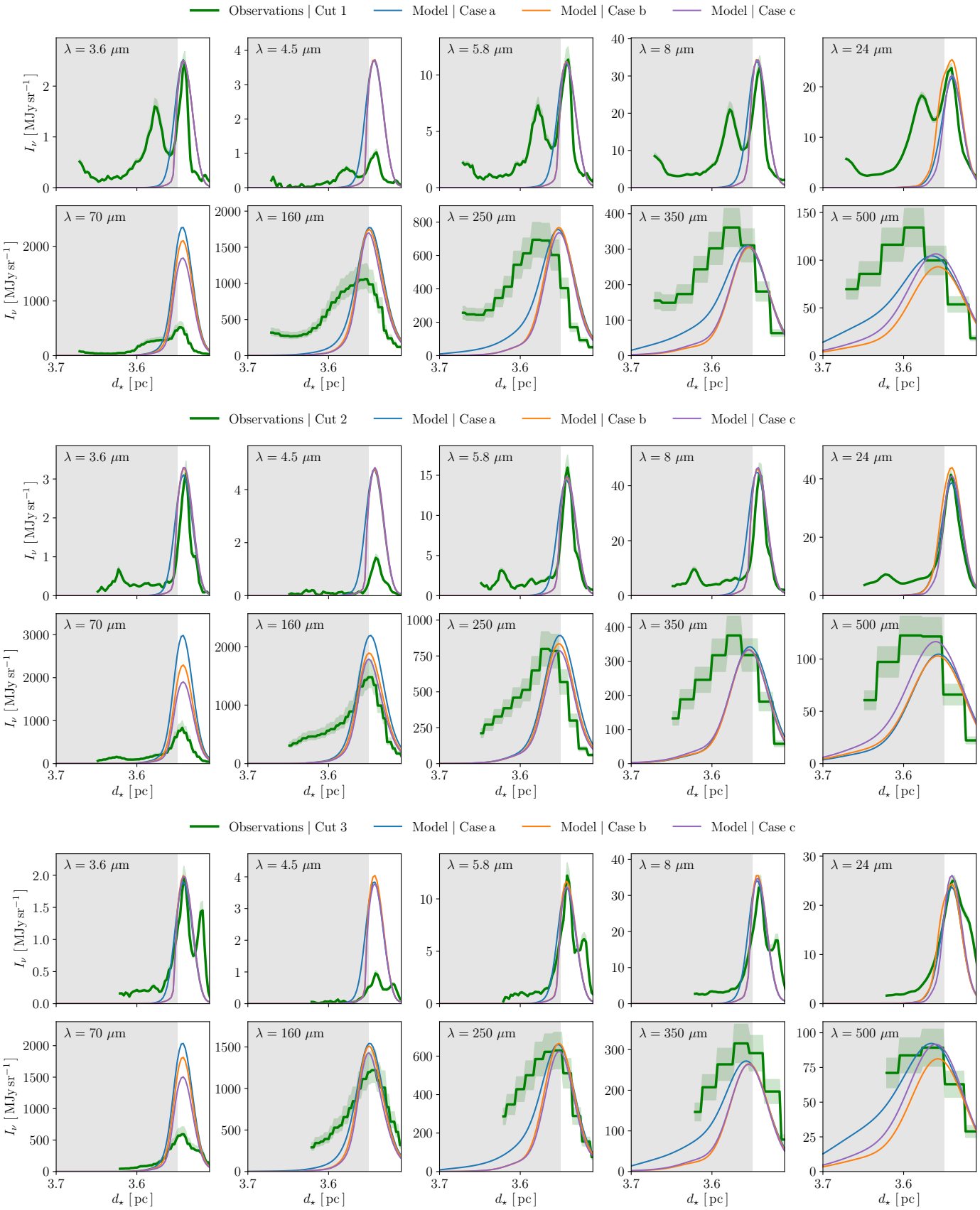

Fig. 10. *Top*: comparison between observed emission profiles for cut 1 (green line) with modelled emission profiles obtained with the best set of parameters (see Table 1) for case a (blue line), case b (orange line), and case c (purple line). *Middle*: same for cut 2. *Bottom:* same for cut 3. The grey parts correspond to the inner Horsehead, where AMM and AMMI grains are used in case b and case c, respectively.

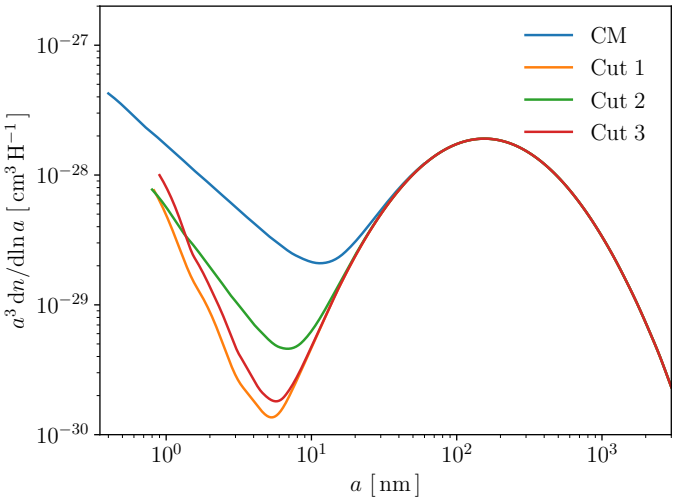

Fig. 11. Size distribution for diffuse ISM-like dust (CM) in blue. Modified size distributions using the best set of parameters (see Table 1) in case c for cut 1 (orange), cut 2 (green), and cut 3 (red).

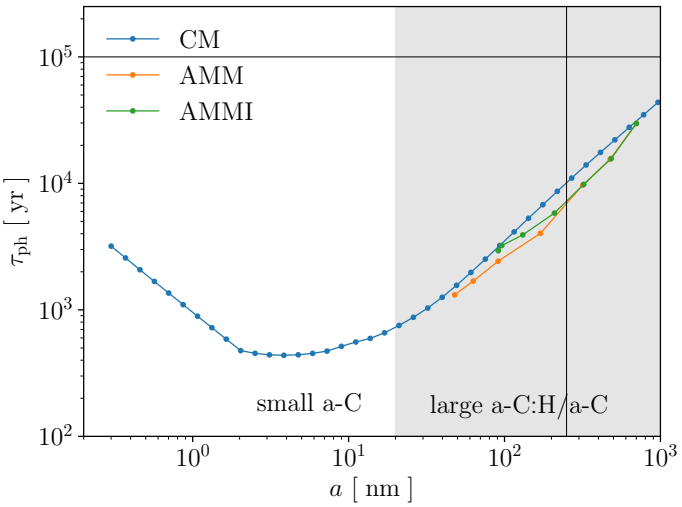

Fig. 12. Photo-fragmentation timescale at the Horsehead edge as a function of the grain radius, a. The blue line refers to CM grains, the orange line to AMM grains, and the green line to AMMI grains. The horizontal black line corresponds to the advection timescale $\tau_{\mathrm{a}} \sim 10^5$ yr in the outer part of the Horsehead. The vertical black line corresponds to the limit at 250 nm beyond which more than 50% of the AMM(I) dust mass is contained (Ysard et al. 2016). The darker grey part corresponds to sizes that cover large a-C:H/a-C grains.

of aggregate grains from the inner region and (ii) the destruction of the smallest a-C:H nano-grain. We discuss the significance of these sequences by comparing their timescales to the advection timescale τ_{a}, that is, the time that the incident UV light needs to heat up and dissociate the molecular gas at the cloud border.

The advection timescale is defined as $\tau_{\mathrm{a}} = L/v_{\mathrm{DF}}$ where $L \sim 0.05$ pc is the width of the outer part of the Horsehead, and $v_{\mathrm{DF}} \sim 0.5$ km s^{-1} is the velocity of the dissociation front (Hollenbach & Tielens 1999). With these values, we find $\tau_{\mathrm{a}} \sim 10^5$ yr.

Due to the lack of studies, we took the photo-darkening timescale as a lower limit to photo-fragmentation of aggregate grains and photo-destruction of a-C nano-grain, described by τ_{ph}. Photo-darkening involves the dissociation of CH-bonds, a process that is more likely faster than the breaking of CC-bonds that must occur in photo-fragmentation (Jones & Habart 2015). We therefore express τ_{ph} at the cloud edge in terms of the photo-darkening rate Λ_{pd} (Jones et al. 2014),

$$\tau_{\mathrm{ph}} \simeq \Lambda_{\mathrm{pd}}^{-1} = \frac{1}{\sigma_{\mathrm{CH}}\, F^0_{\mathrm{UV}}\, Q_{\mathrm{abs}}(a)\, \epsilon(a)}, \tag{6}$$

where $F^0_{\mathrm{UV}} \simeq 3.8 \times 10^9$ photons s^{-1} cm^{-2} is the unattenuated UV field, $\epsilon(a) = \min(1, \frac{2}{a[\mathrm{nm}]})$ is the size-dependent photo-darkening efficiency, $\sigma_{\mathrm{CH}} \simeq 10^{-19}$ cm^2 is the CH bond photo-dissociation cross-section, and $Q_{\mathrm{abs}}(a)$ is the dust absorption efficiency which depends almost solely on the radius in the UV range. In the case of AMMI, τ_{ph} is larger in reality because the ice mantle needs to be vaporised first, but we did not take this effect into account because the time τ_{ph} we estimate is already a lower limit.

We show $\tau_{\mathrm{ph}}(a)$ in Fig. 12 for CM, AMM, and AMMI grains. As discussed in Ysard et al. (2016), more than 50% of the AMM(I) dust mass is contained in grains larger than 250 nm. This figure shows that aggregate grains can be photo-fragmented because $\tau_{\mathrm{ph}} \sim \tau_{\mathrm{a}}$. Moreover, a-C nano-grain can be efficiently destroyed as $\tau_{\mathrm{ph}} < \tau_{\mathrm{a}}$ for a-C nano-grain. Similar results were found by Alata et al. (2014), from laboratory experiments on a-C:H grain analogues that were later applied to the Horsehead (Alata et al. 2015).

From this analysis emerges the following scenario. Within an advection timescale, the a-C nano-grain formed by fragmentation of aggregate grains are also partially destroyed by UV photons. This naturally explains the depletion of a-C:H grains around $a = 10$ nm seen in Fig. 11. We note that the size distribution of these freshly formed small grains is significanlty different from the diffuse ISM case (blue curve in Fig. 11). This evolved size distribution could reflect the photo-evaporated layer described by Bron et al. (2018).

7. Conclusion

With *Herschel* and *Spitzer* data, we studied the Horsehead using ten photometric bands from 3.6 to 500 μm, that cover the entire dust spectrum. We modelled the dust emission across the Horsehead using the THEMIS dust model together with the 3D radiative transfer code SOC.

We show that it is not possible to reproduce the observations in the Horsehead using dust grains from the diffuse ISM. It is therefore required to modify their size distributions and compositions. Dust therefore evolves across the Horsehead.

In the outer part of the Horsehead, the a-C nano-grain dust-to-gas ratio is 6–10 times lower and their minimum size is 2–2.25 times larger than in the diffuse ISM. The power law of the size distribution is steeper than in the diffuse ISM. In the inner part of the Horsehead, we showed that using aggregate grains with or without ice mantles significantly reduces the discrepancy between our model and the observations. The discrepancy between the observations and our model at 4.5 μm might be due to the shape of the aromatic band wings, whence the overestimation of the dust-modelled emission. We also find that large grains are too warm because our modelled dust emission at 70 μm is overestimated. However, laboratory studies show that large silicate grains are more emissive than those used in dust models and are therefore cooler. These new results will soon be implemented in THEMIS.

Based on a timescale analysis, we propose a scenario where the a-C nano-grain form by the partial photo-fragmentation of aggregate grains and are processed by the UV photons, leading to a size distribution depleted in grains of size from 5 to 10 nm.

In the denser regions of the Horsehead, the dust composition is typical of dense clouds.

Spectroscopic observations of the Horsehead are required to proceed on the structure and size distribution of a-C nanograin. Observations with the JWST will for the first time spatially resolve the individual IR dust signatures across the Horsehead, offering an unprecedented look at the evolution of the interstellar matter in photon-dominated regions.

Acknowledgements. We thank the anonymous referee for very helpful suggestions and comments. We also would like to thank the CNES and the P2IO LabeX for supporting Thiebaut Schirmer PhD work. This work was supported by the Programme National "Physique et Chimie du Milieu Interstellaire" (PCMI) of CNRS/INSU with INC/INP co-funded by CEA and CNES. HIPE is a joint development by the *Herschel* Science Ground Segment Consortium, consisting of ESA, the NASA *Herschel* Science Center, and the HIFI, PACS and SPIRE consortia. PACS has been developed by a consortium of institutes led by MPE (Germany) and including UVIE (Austria); KU Leuven, CSL, IMEC (Belgium); CEA, LAM (France); MPIA (Germany); INAF-IFSI/OAA/OAP/OAT, LENS, SISSA (Italy); IAC (Spain). This development has been supported by the funding agencies BMVIT (Austria), ESA-PRODEX (Belgium), CEA/CNES (France), DLR (Germany), ASI/INAF (Italy), and CICYT/MCYT (Spain). SPIRE has been developed by a consortium of institutes led by Cardiff Univ. (UK) and including Univ. Lethbridge (Canada); NAOC (China); CEA, LAM (France); IFSI, Univ. Padua (Italy); IAC (Spain); Stockholm Observatory (Sweden); Imperial College London, RAL, UCL-MSSL, UKATC, Univ. Sussex (UK); Caltech, JPL, NHSC, Univ. Colorado (USA). This development has been supported by national funding agencies: CSA (Canada); NAOC (China); CEA, CNES, CNRS (France); ASI (Italy); MCINN (Spain); SNSB (Sweden); STFC, UKSA (UK); and NASA (USA).

References

Abergel, A., Boulanger, F., Mizuno, A., & Fukui, Y. 1994, ApJ, 423, L59
Abergel, A., Teyssier, D., Bernard, J. P., et al. 2003, A&A, 410, 577
Abergel, A., Arab, H., Compiègne, M., et al. 2010, A&A, 518, L96
Alata, I., Cruz-Diaz, G. A., Muñoz Caro, G. M., & Dartois, E. 2014, A&A, 569, A119
Alata, I., Jallat, A., Gavilan, L., et al. 2015, A&A, 584, A123
Anthony-Twarog, B. J. 1982, AJ, 87, 1213
Arab, H. 2012, PhD thesis, Université Paris-Sud, Orsay
Arab, H., Abergel, A., Habart, E., et al. 2012, A&A, 541, A19
Bakes, E. L. O., & Tielens, A. G. G. M. 1994, ApJ, 427, 822
Bernard, J. P., Abergel, A., Ristorcelli, I., et al. 1999, A&A, 347, 640
Berné, O., Joblin, C., Deville, Y., et al. 2007, A&A, 469, 575
Boersma, C., Bregman, J., & Allamandola, L. J. 2014, ApJ, 795, 110
Boulanger, F., Falgarone, E., Puget, J. L., & Helou, G. 1990, ApJ, 364, 136
Boutéraon, T., Habart, E., Ysard, N., et al. 2019, A&A, 623, A135
Bowler, B. P., Waller, W. H., Megeath, S. T., Patten, B. M., & Tamura, M. 2009, AJ, 137, 3685
Bron, E., Le Bourlot, J., & Le Petit, F. 2014, A&A, 569, A100
Bron, E., Agúndez, M., Goicoechea, J. R., & Cernicharo, J. 2018, ArXiv e-prints, unpublished [arXiv:1801.01547]
Burke, J. R., & Hollenbach, D. J. 1983, ApJ, 265, 223
Campeggio, L., Strafella, F., Maiolo, B., Elia, D., & Aiello, S. 2007, ApJ, 668, 316
Cardelli, J. A., & Clayton, G. C. 1991, AJ, 101, 1021
Cardelli, J. A., Clayton, G. C., & Mathis, J. S. 1989, ApJ, 345, 245
Compiègne, M., Abergel, A., Verstraete, L., et al. 2007, A&A, 471, 205
Compiègne, M., Abergel, A., Verstraete, L., & Habart, E. 2008, A&A, 491, 797
Compiègne, M., Verstraete, L., Jones, A., et al. 2011, A&A, 525, A103
de Boer, K. S. 1983, A&A, 125, 258
Demyk, K., Meny, C., Lu, X.-H., et al. 2017, A&A, 600, A123
Desert, F.-X., Boulanger, F., & Puget, J. L. 1990, A&A, 237, 215
Draine, B. 2003, ARA&A, 41, 241
Draine, B. T., & Lee, H. M. 1984, ApJ, 285, 89
Duley, W. W., Zaidi, A., Wesolowski, M. J., & Kuzmin, S. 2015, MNRAS, 447, 1242
Engelbracht, C., Blaylock, M., Su, K., et al. 2007, PASP, 119, 994
Fitzpatrick, E. L., & Massa, D. 1986, ApJ, 307, 286
Flagey, N., Noriega-Crespo, A., Boulanger, F., et al. 2009, ApJ, 701, 1450
Gerin, M., Goicoechea, J. R., Pety, J., & Hily-Blant, P. 2009, A&A, 494, 977
Goicoechea, J. R., Pety, J., Gerin, M., et al. 2006, A&A, 456, 565
Goicoechea, J. R., Pety, J., Gerin, M., Hily-Blant, P., & Le Bourlot, J. 2009, A&A, 498, 771
Gordon, K., Engelbracht, C., Fadda, D., et al. 2007, PASP, 119, 1019
Gordon, K. D., Baes, M., Bianchi, S., et al. 2017, A&A, 603, A114
Gratier, P., Pety, J., Guzmán, V., et al. 2013, A&A, 557, A101
Guzmán, V., Pety, J., Goicoechea, J. R., Gerin, M., & Roueff, E. 2011, A&A, 534, A49
Guzmán, V., Pety, J., Gratier, P., et al. 2012, A&A, 543, L1
Guzmán, V. V., Goicoechea, J. R., Pety, J., et al. 2013, A&A, 560, A73
Habart, E., Abergel, A., Walmsley, C. M., Teyssier, D., & Pety, J. 2005, A&A, 437, 177
Hily-Blant, P., Teyssier, D., Philipp, S., & Güsten, R. 2005, A&A, 440, 909
Hollenbach, D., & Salpeter, E. E. 1971, ApJ, 163, 155
Hollenbach, D. J., & Tielens, A. G. G. M. 1997, ARA&A, 35, 179
Hollenbach, D. J., & Tielens, A. G. G. M. 1999, Rev. Mod. Phys., 71, 173
Jones, A. P. 2012a, A&A, 540, A1
Jones, A. P. 2012b, A&A, 540, A2
Jones, A. P. 2012c, A&A, 542, A98
Jones, A. P., & Habart, E. 2015, A&A, 581, A92
Jones, A. P., Duley, W. W., & Williams, D. A. 1990, QJRAS, 31, 567
Jones, A. P., Fanciullo, L., Köhler, M., et al. 2013, A&A, 558, A62
Jones, A. P., Ysard, N., Koehler, M., et al. 2014, Faraday Discuss., 168, 313
Jones, A. P., Köhler, M., Ysard, N., Bocchio, M., & Verstraete, L. 2017, A&A, 602, A46
Juvela, M. 2019, A&A, 622, A79
Juvela, M., Ristorcelli, I., Pelkonen, V.-M., et al. 2011, A&A, 527, A111
Juvela, M., Ristorcelli, I., Marshall, D. J., et al. 2015, A&A, 584, A93
Juvela, M., Guillet, V., Liu, T., et al. 2018a, A&A, 620, A26
Juvela, M., Malinen, J., Montillaud, J., et al. 2018b, A&A, 614, A83
Juvela, M., Padoan, P., Ristorcelli, I., & Pelkonen, V.-M. 2019, A&A, 629, A63
Kim, S.-H., Martin, P. G., & Hendry, P. D. 1994, ApJ, 422, 164
Köhler, M., Jones, A., & Ysard, N. 2014, A&A, 565, L9
Köhler, M., Ysard, N., & Jones, A. P. 2015, A&A, 579, A15
Kramer, C., Stutzki, J., & Winnewisser, G. 1996, A&A, 307, 915
Lada, E. A., Bally, J., & Stark, A. A. 1991, ApJ, 368, 432
Laureijs, R. J., Clark, F. O., & Prusti, T. 1991, ApJ, 372, 185
Le Gal, R., Herbst, E., Dufour, G., et al. 2017, A&A, 605, A88
Le Petit, F., Nehmé, C., Le Bourlot, J., & Roueff, E. 2006, ApJS, 164, 506
Li, A., & Draine, B. T. 2001, ApJ, 550, L213
Li, A., & Greenberg, J. M. 1997, A&A, 323, 566
Martin, P. G., Roy, A., Bontemps, S., et al. 2012, ApJ, 751, 28
Mathis, J. S., & Whiffen, G. 1989, ApJ, 341, 808
Mathis, J. S., Rumpl, W., & Nordsieck, K. H. 1977, ApJ, 217, 425
Milman, A. S., Knapp, G. R., Knapp, S. L., & Wilson, W. J. 1975, AJ, 80, 93
Neckel, T., & Sarcander, M. 1985, A&A, 147, L1
Ormel, C. W., Min, M., Tielens, A. G. G. M., Dominik, C., & Paszun, D. 2011, A&A, 532, A43
Ossenkopf, V., & Henning, T. 1994, A&A, 291, 943
Pety, J., Teyssier, D., Fossé, D., et al. 2005, A&A, 435, 885
Pety, J., Goicoechea, J. R., Hily-Blant, P., Gerin, M., & Teyssier, D. 2007, A&A, 464, L41
Pety, J., Gratier, P., Guzmán, V., et al. 2012, A&A, 548, A68
Philipp, S. D., Lis, D. C., Güsten, R., et al. 2006, A&A, 454, 213
Pilleri, P., Montillaud, J., Berné, O., & Joblin, C. 2012, A&A, 542, A69
Pilleri, P., Reisenfeld, D. B., Zurbuchen, T. H., et al. 2015, ApJ, 812, 1
Planck Collaboration XXIV. 2011, A&A, 536, A24
Pound, M. W., Reipurth, B., & Bally, J. 2003, AJ, 125, 2108
Reach, W., Megeath, S., Cohen, M., et al. 2005, PASP, 117, 978
Roy, A., Martin, P. G., Polychroni, D., et al. 2013, ApJ, 763, 55
Schaerer, D., & de Koter, A. 1997, A&A, 322, 598
Siebenmorgen, R., & Kruegel, E. 1992, A&A, 259, 614
Smith, F. W. 1984, J. Appl. Phys., 55, 764
Stansberry, J., Gordon, K., Bhattacharya, B., et al. 2007, PASP, 119, 1038
Stepnik, B., Abergel, A., Bernard, J.-P., et al. 2003, A&A, 398, 551
Swinyard, B. M., Ade, P., Baluteau, J.-P., et al. 2010, A&A, 518, L4
Teyssier, D., Fossé, D., Gerin, M., et al. 2004, A&A, 417, 135
Van De Putte, D., Gordon, K. D., Roman-Duval, J., et al. 2019, ApJ, 888, 22
Wakelam, V., Bron, E., Cazaux, S., et al. 2017, Mol. Astrophys., 9, 1
Warren, Jr., W. H., & Hesser, J. E. 1977, ApJS, 34, 115
Weingartner, J. C., & Draine, B. T. 2001a, ApJS, 134, 263
Weingartner, J. C., & Draine, B. T. 2001b, ApJ, 548, 296
Ysard, N., Abergel, A., Ristorcelli, I., et al. 2013, A&A, 559, A133
Ysard, N., Köhler, M., Jones, A., et al. 2015, A&A, 577, A110
Ysard, N., Köhler, M., Jones, A., et al. 2016, A&A, 588, A44
Zhou, S., Jaffe, D. T., Howe, J. E., et al. 1993, ApJ, 419, 190
Zubko, V., Dwek, E., & Arendt, R. G. 2004, ApJS, 152, 211

Appendix A: Size distribution

Size distributions of dust in THEMIS follow either a power law with an exponential cut-off, defined as

$$\frac{\mathrm{d}n}{\mathrm{d}a} \propto \begin{cases} a^{\alpha} & \text{if} \quad a < a_{\mathrm{t}} \\ a^{\alpha} \times \exp\left(-\left(\frac{a-a_{\mathrm{t}}}{a_{\mathrm{c}}}\right)^3\right) & \text{if} \quad a \geq a_{\mathrm{t}}, \end{cases} \tag{A.1}$$

or a log-normal law, defined as

$$\frac{\mathrm{d}n}{\mathrm{d}a} \propto \frac{1}{a} \times \exp\left(-\left(\frac{\log(a/a_0)}{\sigma}\right)^2\right) \tag{A.2}$$

where all the parameters for each dust distribution are listed in Table A.1.

Table A.1. Size distribution parameters for each dust population (see Appendix A for the equations).

Name	Size	α	a_{min}	a_{max}	a_{c}	a_{t}	a_0
			[nm]	[nm]	[nm]	[nm]	[nm]
Core Mantle grains (CM) – (Diffuse ISM-like dust)							
a-C	p-law	5	0.4	4900	10	50	–
a-C:H/a-C	log-n	–	0.5	4900	–	–	7
a-Sil/a-C	log-n	–	1	4900	–	–	8
Aggregated Mantle Mantle grains (AMM)							
AMM	log-n	–	47.9	700	–	–	479
Aggregated Mantle Mantle Ice grains (AMMI)							
AMMI	log-n	–	91.2	700	–	–	610

Notes. p-law is a power law with an exponential tail, and log-n is a log-normal distribution.

Appendix B: The Horsehead seen with *Spitzer* and *Herschel*

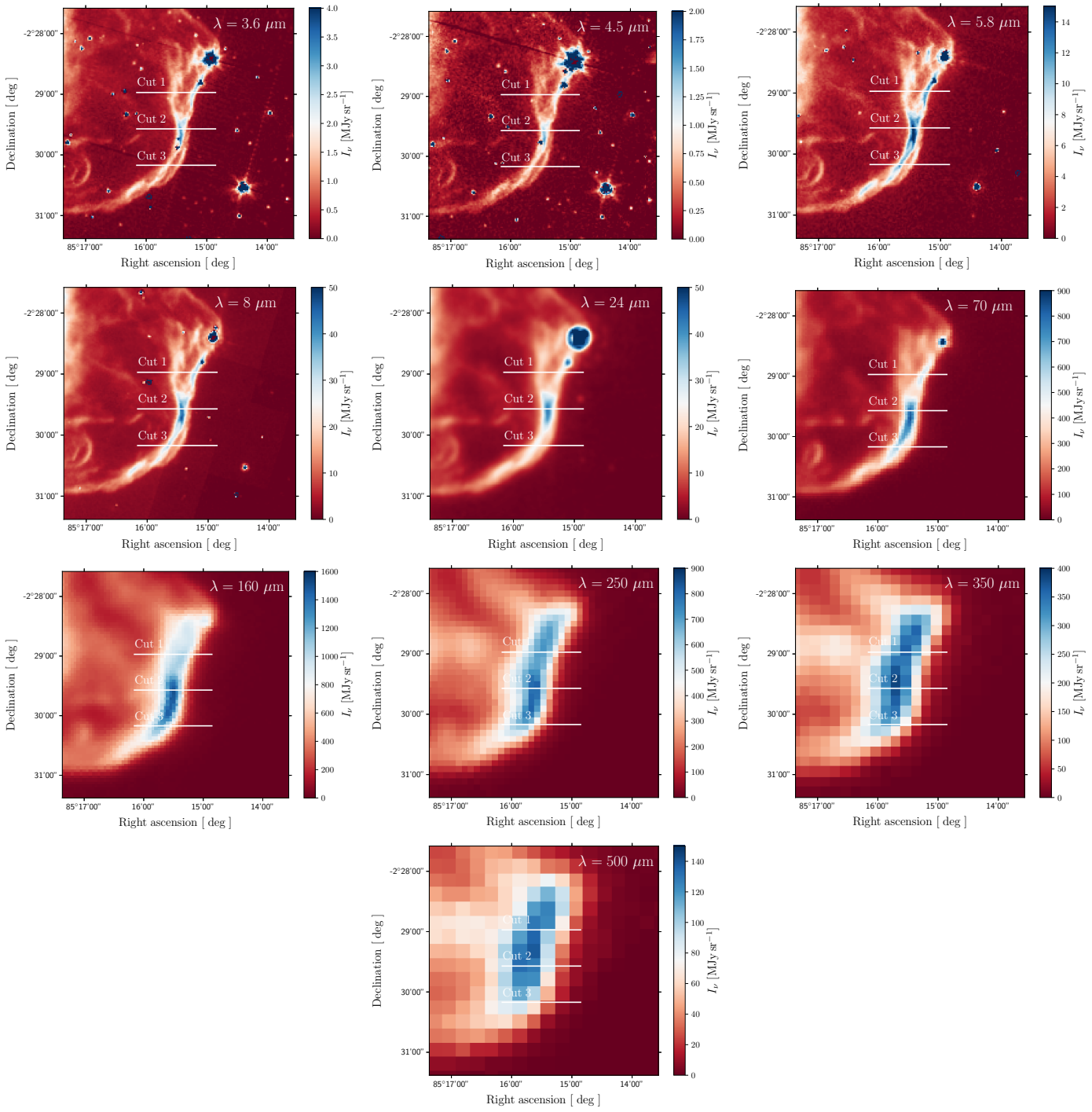

Fig. B.1. Horsehead seen in the ten photometric bands. The three solid white lines correspond to the three cuts we used.

10.3 SUMMARY AND CONSEQUENCES

Here I summarise here the main results of the paper presented above, as well as the consequences of these results for the physics and the chemistry of the dust and the gas, and their evolution, in the Horsehead.

10.3.1 *Summary*

Using *Herschel* and *Spitzer* data, we studied the Horsehead using ten photometric bands from 3.6 to 500 μm, which cover the entire dust spectrum. We modelled the dust emission across the Horsehead using the THEMIS dust model together with the 3D radiative transfer code SOC.

We show that it is not possible to reproduce the observations in the Horsehead using dust grains from the diffuse ISM. It is therefore necessary to modify their size distributions and compositions. Dust therefore evolves across the Horsehead. We therefore concluded that dust is not the same everywhere in the Horsehead and therefore that its properties must evolve across this region.

Indeed, in the outer part of the Horsehead, we found that:

- the nano-grain dust-to-gas ratio (that is, M_{a-C}/M_H) is $6-10$ times lower than in the diffuse ISM;
- the nano-grain minimum size (that is, $a_{min,a-C}$) is $2-2.25$ times larger than in the diffuse ISM;
- the power-law exponent of their size distribution (that is, α) is $1.1-1.4$ times lower than in the diffuse ISM.

In the inner part of the Horsehead, we found that it is necessary to use evolved grains (i.e. aggregates, with or without an ice mantle). Therefore, dust is in the form of aggregates (that is, AMM or AMMI, see Sect. 6) and neither nano-grains (that is, a-C grains) nor large grains (that is, a-C:H/a-C and a-Sil/a-C grains) are present but thaat they must both be incorporated into these AMM(I) aggregates.

We therefore proposed that in the outer part of the Horsehead nebula, all the nano-grains have not yet had time to completely re-form through photo-fragmentation of the aggregates and that the smallest of the nano-grains that are sensitive to photo-destruction in intense radiation fields. In the inner part of the Horsehead nebula, the grains most likely consist of multi-compositional mantled aggregates, as would be expected in dense regions (Köhler, Ysard, and Jones, 2015).

Using simple analytical models, we discussed here the consequences of the nano-grain depletion for the physics and chemistry in the Horsehead.

10.3.2 *Consequences*

Variations in the dust properties strongly affect the dust extinction (see Fig. 65, upper panels). In the outer part of the Horsehead, the variations in dust size distribution (see Fig. 75, left panel) entails a large decrease in the dust UV/visible extinction (see Fig. 76), by a factor of $2-5$. As a consequence, the UV radiation can penetrate deeper into the Horsehead.

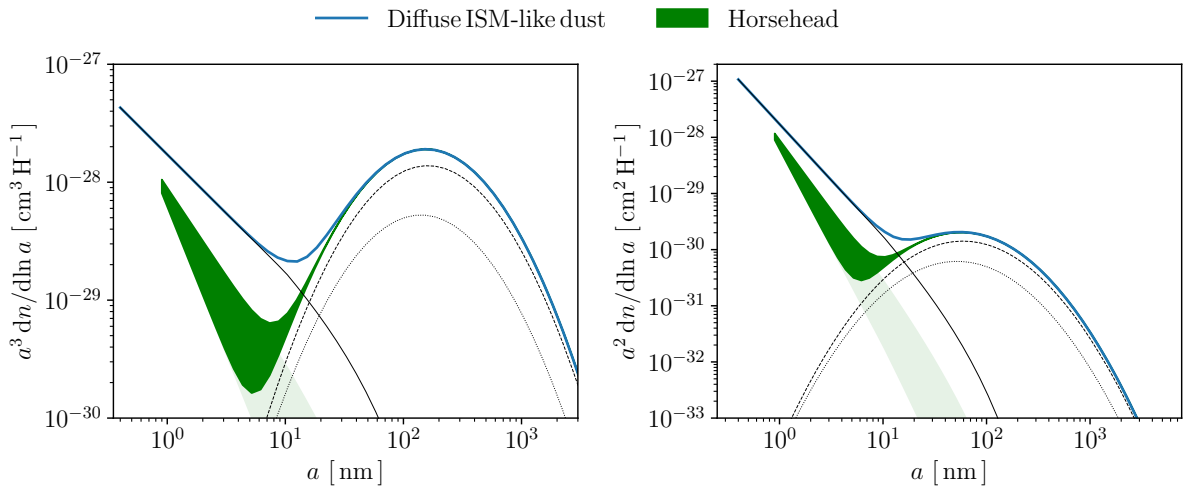

Figure 75: Left: Dust size distribution of diffuse ISM-like grains (blue line). The green band corresponds to the range of dust size distributions in the outer part of the Horsehead (see Sect. 10). Right: Same for dust surface area distribution. The black line shows the a-C dust distribution, black dashed line the a-Sil/a-C dust distribution, and black dotted line the a-C:H/a-C dust distribution.

Also, these variations in the dust size distribution imply large variations in the dust surface area distribution (see Fig. 75, right panel). In particular, the a-C dust surface area decreases by a factor $6-13$ from the diffuse ISM to the outer part of the Horsehead (see Table 3), which is due to the decrease in M_{a-C}/M_H. Regarding the increase in $a_{min,a-C}$, this implies the total removal of all a-C grains smaller than $a_{min,a-C} \sim 0.9$ nm (see Fig. 78) or that conditions are not favourable for their (re-)formation in such regions.

These variations, which imply a strong depletion of a-C grains, have a strong influence on the physics and chemistry in PDRs. In order to illustrate this, I now focus on two major consequences concerning the formation of H_2 (that is sensitive to the nano-grain total surface area) and the gas heating through the photoelectric effect (that is sensitive to the nano-grain dust-to-gas ratio).

	S_H(a-C) [cm^2 H^{-1}]	S_H(a-C:H/a-C) [cm^2 H^{-1}]	S_H(a-Sil/a-C) [cm^2 H^{-1}]	S_H(Tot) [cm^2 H^{-1}]
Diffuse ISM-like dust	4.3×10^{-21} (48 %)	1.3×10^{-21} (14 %)	3.5×10^{-21} (38 %)	9.1×10^{-21}
Horsehead (Max)	7.0×10^{-22} (12 %)	1.3×10^{-21} (24 %)	3.5×10^{-21} (64 %)	5.5×10^{-21}
Horsehead (Min)	3.3×10^{-22} (6 %)	1.3×10^{-21} (26 %)	3.5×10^{-21} (68 %)	5.1×10^{-21}

Table 3: Summary of the dust surface amount per proton for each dust population (a-C, a-C:H/a-C, and a-Sil/a-C), for both the diffuse ISM-like dust and inside the outer part of the Horsehead.

10.3.2.1 *H_2 formation and $H \rightarrow H_2$ transition*

I here investigate the consequences of variations in the dust properties for the H_2 formation. We first determine the influence of such variations on the H_2 formation rate, R_f, expressed in cm^3 s^{-1}. My analysis is based upon the assumption that H_2 formation occurs only on nano-grains (that is, a-C grains). As these grains are stochastically heated, they spend most of their time at low temperature (below 20 K, see Bron, Le Bourlot, and Le Petit, 2014) which allows

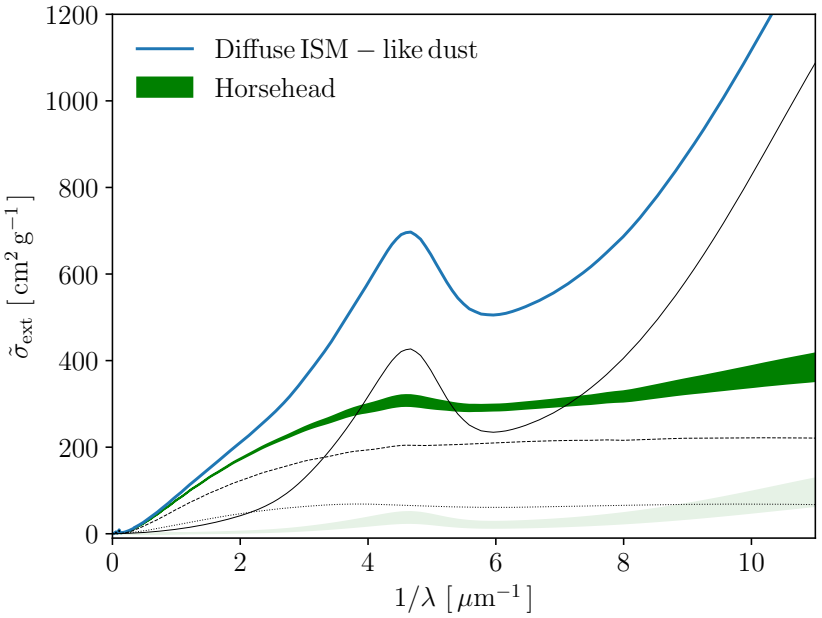

Figure 76: UV to near-IR extinction of diffuse ISM-like grains (blue line). The green band corresponds to the range of dust extinction in the outer part of the Horsehead, using the range of dust size distributions in Fig. 75 (left panel).

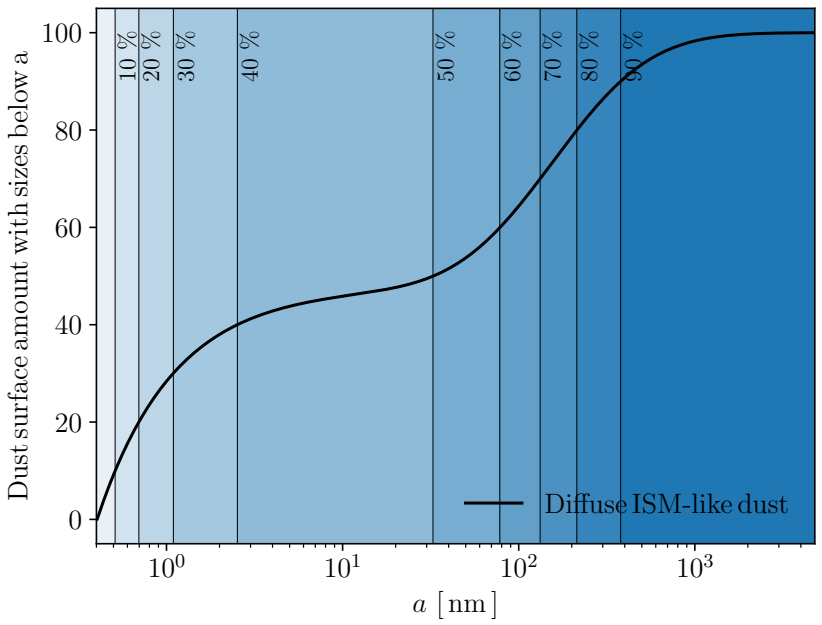

Figure 77: Cumulative surface area distribution for diffuse ISM-like dust.

H_2 formation to occur. Conversely, large grains (that is, a-C:H/a-C and a-Sil/a-C grains) are in thermal equilibrium and are too warm in the outer part part of the Horsehead, hence H_2 cannot form onto these grains. We therefore consider that variations in R_f are proportional to variations in the a-C total surface area. As the dust surface area per proton decreases by a factor $6-13$ from the diffuse ISM to the outer part of the Horsehead (see Table 3), the H_2 formation rate decreases by the same factor as well.

In the classical static, equilibrium picture widely used in PDR models, the H_2 number density n_2 is found from the balance between formation (left term in the following equation) and destruction (right term) rates:

$$n_1 n_H R_f = n_2 P_d G_0 \exp(-\tau_d)\,\beta, \tag{102}$$

where n_H is the number density of H atoms with $n_H = n_1 + 2n_2$, P_d the unattenuated photodissociation rate of H_2 in the ISRF of Mathis, Mezger, and Panagia, 1983, τ_d the dust opacity at $\lambda \sim 100$ nm and β the self-shielding factor of H_2.

At the $H \rightarrow H_2$ transition, $n_1 = 2\,n_2$ which corresponds to a H_2 fraction $2\,n_2/(n_1 + 2\,n_2)$ of 50 %. The position of the $H \rightarrow H_2$ transition is then set by the value of G_0/n_H (and therefore, A_V) which describes the competition between H_2 destruction (G_0) and formation (n_H) processes. In the Horsehead, Habart et al., 2005 find $G_0/n_H \sim 3 \times 10^{-3}$ cm^3. Using this value in Eq. 102 at the $H \rightarrow H_2$ transition (that is, $n_1 = 2\,n_2$), we find:

$$\exp(-\tau_d)\,\beta = \frac{2\,R_f}{P_d}\frac{n_H}{G_0} \approx 4 \times 10^{-4}. \tag{103}$$

As the H_2 formation rate decreases by a factor $6-13$ while $\tau_d \sim A_V$ (see Fig. 76, the extinction in the Horsehead is roughly flat from the visible to the UV) and assuming the UV attenuation to be dominated by the dust, this implies that:

$$\exp(-(A_{V,\,min} - 0.1)) \sim \frac{1}{6} \quad \text{and} \quad \exp(-(A_{V,\,max} - 0.1)) \sim \frac{1}{13}, \tag{104}$$

leading to:

$$A_{V,\,min} \sim 1.9 \quad \text{and} \quad A_{V,\,max} \sim 2.7, \tag{105}$$

where $A_{V,\,min}$ and $A_{V,\,max}$ are the minimum and maximum positions of the $H \rightarrow H_2$ transition in the Horsehead with the new evolved a-C grains.

The $H \rightarrow H_2$ transition would therefore occur deeper into the PDR ($A_V \sim 1.9-2.7$) with evolved grains than with diffuse ISM-like dust ($A_V \sim 0.1$). Note that these values were obtained with the assumption that H_2 can only form on a-C grains and hence the H_2 formation rates derived here are lower limit estimates. Therefore, the estimates of the positions of the H $\rightarrow H_2$ transition are the largest possible ($A_V \sim 1.9-2.7$).

Despite of the decreased UV extinction due to the a-C grain depletion, the UV flux ($\lambda =$ 100 nm) at $A_V = 2$ is around 5 times lower than if using diffuse ISM-like dust, leading to a significant reduction in the H_2 excitation, which occurs by direct UV pumping or by collisions with gas species. In particular, for the moderate densities of the Horsehead PDR edge ($n_H < 10^4$ H cm^{-3}), the rovibrational emission of H_2 is proportional to the UV flux at 100 nm (**sternberg_89**). Moreover as we show in the next section, the decrease in the a-C grain abundance leads to a strongly reduced gas temperature quenching the collisional excitation of H_2 rotational levels.

10.3.2.2 *Gas heating through the photoelectric effect*

The thermal balance and the gas temperature of PDRs are also strongly affected by variations in a-C grain properties. For instance, in the outer part of the Horsehead, the gas is mainly heated by the photoelectric effect due to a-C grains (see Fig. 24) and mainly cooled by O and C^+ emission (see Fig. 25). As the treatment of the cooling of the oxygen atom is more difficult than the one of C^+, we focus on this one. Even though this is a strong hypothesis to take only C^+ for the thermal equilibrium, it will provide us with an idea of the influence of the a-C depletion on the gas heating. The thermal equilibrium with only C^+ as a cooling species is therefore:

$$n_H \, G_0 \, H = n_e \, n_{C^+} \, C(T), \tag{106}$$

where H is the photoelectric heating rate per proton and $C(T)$ the cooling rate coefficient for the 158 µm line. In the outer part of the Horsehead, the excitation of the C^+ line is dominated by the contribution of electrons (**wolfire_95**). Assuming that $n(C^+) = 1.4 \times 10^{-4}$, we have:

$$n_e \, n_{C^+} \, C(T) = n_H^2 \frac{n_e}{n_H} \times 1.4 \times 10^{-23} \exp(-92/T) \, T^{-0.5} \quad \mathrm{erg\,cm^{-3}\,s^{-1}}. \tag{107}$$

Assuming $H \sim 3 \times 10^{-26}$ erg s^{-1} (see e.g. Weingartner and Draine, 2001b) and using Eq. (107) in Eq. (106), we have:

$$\frac{G_0 \, T^{1/2}}{n_H \, x} \approx 470 \exp(-92/T). \tag{108}$$

At the position of the $H \rightarrow H_2$ transition and for a constant pressure model at 4×10^6 K cm^{-3}, we estimate $G_0/n_H = 3 \times 10^{-3}$ (Habart et al., 2005). Assuming $x = n_e/n_H = 1.6 \times 10^{-4}$, Eq. gives $T \sim 100$ K.
As Bakes and Tielens, 1994 showed that the dust photoelectric effect is only efficient for nano-grains (that is, a-C grains) and because the a-C dust total surface decreases by a factor $6 - 13$, we can consider that the photoelectric heating rate per proton H decreases by the same factor as well, leading to:

$$T_{min} \sim 21\,\mathrm{K} \quad \text{and} \quad T_{max} \sim 27\,\mathrm{K}. \tag{109}$$

This simple calculation shows that the depletion of a-C grains we observe in the Horsehead has a strong impact on thermal balance of the gas.

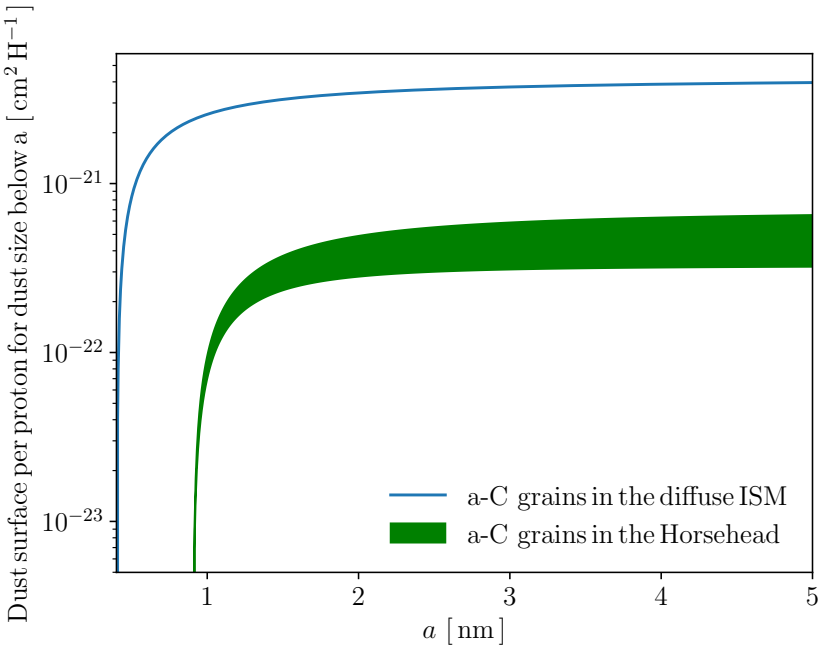

Figure 78: Cumulative surface area distribution per proton for a-C from diffuse ISM-like dust (blue line) and a-C grains inside the outer part of the Horsehead (green band).

Part VI

CONCLUSION

CONCLUSION

Dans l'abîme sans fond mon regard a plongé. De l'atome au soleil j'ai tout interrogé.
Alphonse de Lamartine - *Oeuvres de Lamartine de l'Académie Française*

All along the cycle of interstellar matter in galaxies throughout the Universe, gas and dust are constantly evolving, due to the wide disparity in physical and dynamical conditions encountered from diffuse clouds to regions where stars and planetary systems form. The microphysical processes that occur on interstellar dust surfaces are tightly connected to the dust properties (dust composition, size distribution, structure, and shape) and play a key role in numerous phenomena in the ISM. The analysis of how dust evolves with the physical conditions is a stepping stone towards a more thorough understanding of interstellar matter. During my PhD, I focused on understanding how dust evolves with physical conditions at the very beginning of the condensation processes of interstellar matter that can lead to star formation, i.e. at the edge of molecular clouds. To this end, I studied dust evolution in a nearby photon-dominated region, the Horsehead Nebula, where the physical conditions vary widely and can be spatially resolved.

In order to model the local dust emission, I have used DustEM. It allowed me to understand THEMIS, the interstellar dust model that I used throughout this work. As PDRs are optically thick, radiative transfer computation was essential. To this end, I first have used DustPDR, a 1D radiative transfer code, to model dust emission across the Horsehead. However, as this code is based upon a strong assumption (plane parallel geometry) and because it does not compute dust scattering, I needed a more rigorous 3D radiative transfer code, SOC. With the aim of understanding the difference between these two codes, I compared both codes for the same case and showed the necessity of using a 3D code (SOC) in order to properly describes how dust evolves in the Horsehead.

Radiative transfer is complex, and the results are rarely intuitive. Therefore I decided as a first step to study the influence of variations in the dust properties on the dust emission and dust scattering with radiative transfer, in order to disentangle radiative transfer effects from variations in the dust properties. Then I focused on the dust scattering, and showed that it can be neglected in the spectral range I used in my study ($3.6 - 500$ μm). I also showed that there is a narrow wavelength range around 1 μm where the scattering is mostly due to the scattering of the photons emitted by the dust, albeit it was usually understood that the scattering seen in PDRs is of photons from the illuminating source. I pointed out that variations in the nano-grain dust-to-gas ratio (M_{a-C}/M_H), minimum size ($a_{min,\,a-C}$), and the power-law exponent (α) of its size distribution, have a strong influence on the dust modelled emission.

Based on this preliminary study, I used *Spitzer*/IRAC (3.6, 4.5, 5.8 and 8 μm) and *Spitzer*/MIPS (24 μm) together with *Herschel*/PACS (70 and 160 μm) and *Herschel*/SPIRE (250, 350 and 500 μm) data to map the spatial distribution of dust in the Horsehead nebula over the entire emission spectral range of the dust emission. I found that it is not possible to explain the observations using diffuse ISM-like grains from THEMIS and in all probability those from any other diffuse ISM dust model. I therefore proposed the following scenario to explain these observed data. In the outer part of the Horsehead nebula, all the nano-grains have not yet had time to (re-)form completely through photo-fragmentation of the large aggregates and that the smallest of the nano-grains which are sensitive to the radiation field are photo-destroyed. In

the inner part of the Horsehead nebula, the grains most likely consist of multi-compositional mantled aggregates, as would be expected in high density regions.

Nano-grains contain only a small fraction of the total mass of interstellar dust grains, but most of the grain surface is in nano-grains. Therefore, our results have a strong impact on the H_2 formation which is directly sensitive to the nano-grain total surface, and on gas heating through the photoelectric effect which is sensitive to the nano-grain dust-to-gas ratio. Moreover, these two processes strongly influence other processes such as the H_2 excitation and emission in the $H \rightarrow H_2$ transition region.

In order to better understand the processes at the origin of dust evolution and with a view to modelling these, this work needs to be extended to other PDRs with different physical conditions, such as IC 63 or the Orion Bar. In particular, spectroscopic observations of the dust and the gas are needed to constrain the nature (composition, size distribution, structure, and shape) of a-C nano-grains but also to derive the physical conditions triggering their evolution. Besides, and in order to go further, spectroscopic observations of the Horsehead are required in order to proceed further with our understanding of the structure and size distribution of a-C nano-grain. Observations with the JWST will for the first time spatially resolve the individual IR dust signatures across the Horsehead, offering an unprecedented look at the evolution of the interstellar matter in photon-dominated regions.

Part VII

APPENDIX

BIBLIOGRAPHY

Barnard, E. E. (Dec. 1913). "Dark regions in the sky suggesting an obscuration of light." en. In: *The Astrophysical Journal* 38, p. 496. ISSN: 0004-637X, 1538-4357. DOI: 10.1086/142046. URL: http://adsabs.harvard.edu/doi/10.1086/142046.

Heger, Mary Lea (1922). "Further study of the sodium lines in class B stars ; The spectra of certain class B stars in the regions 5630A-6680A and 3280A-3380A ; Note on the spectrum of [gamma] Cassiopeiae between 5860A and 6600A." en. In: *Lick Observatory Bulletins* 10, pp. 141–148. ISSN: 0075-9317. DOI: 10.5479/ADS/bib/1922LicOB.10.141H. URL: http://adsabs.harvard.edu/abs/1922LicOB..10..141H.

Schalén, Carl (1929). "Zur Frage einer allgemeinen Absorption des Lichtes im Weltraum." de. In: *Astronomische Nachrichten* 236.16, pp. 249–258. ISSN: 00046337, 15213994. DOI: 10.1002/asna.19292361602. URL: http://doi.wiley.com/10.1002/asna.19292361602.

Trumpler, Robert J. (Aug. 1930). "Absorption of Light in the Galactic System." en. In: *Publications of the Astronomical Society of the Pacific* 42, p. 214. ISSN: 0004-6280, 1538-3873. DOI: 10.1086/124039. URL: http://iopscience.iop.org/article/10.1086/124039.

Merrill, P. W. (Aug. 1934). "Unidentified Interstellar Lines." en. In: *Publications of the Astronomical Society of the Pacific* 46, p. 206. ISSN: 0004-6280, 1538-3873. DOI: 10.1086/124460. URL: http://iopscience.iop.org/article/10.1086/124460.

Schoenberg, E. and B. Jung (1934). "Über die Lichtzerstreuung im interstellaren Raum durch Wolken metallischer Partikel." de. In: *Astronomische Nachrichten* 253.14, pp. 261–272. ISSN: 00046337, 15213994. DOI: 10.1002/asna.19342531402. URL: http://doi.wiley.com/10.1002/asna.19342531402.

Henyey, L. C. and J. L. Greenstein (Jan. 1941). "Diffuse radiation in the Galaxy." en. In: *The Astrophysical Journal* 93, p. 70. ISSN: 0004-637X, 1538-4357. DOI: 10.1086/144246. URL: http://adsabs.harvard.edu/doi/10.1086/144246.

Hulst, HC van de (1943). "De vorming van vaste deeltjes in het interstellaire gas. 6. De aangroeiing van de rookdeeltjes." In: *Ned. Tijdschr. v. Natuurkunde* 10, pp. 251–255.

Oort, J. H. and H. C. van de Hulst (Nov. 1946). "Gas and smoke in interstellar space." In: *bain* 10, p. 187.

Hall, J. S. (Feb. 1949). "Observations of the Polarized Light From Stars." en. In: *Science* 109.2825, pp. 166–167. ISSN: 0036-8075, 1095-9203. DOI: 10.1126/science.109.2825.166. URL: https://www.sciencemag.org/lookup/doi/10.1126/science.109.2825.166.

Hiltner, W. A. (Feb. 1949). "Polarization of Light From Distant Stars by Interstellar Medium." en. In: *Science* 109.2825, pp. 165–165. ISSN: 0036-8075, 1095-9203. DOI: 10.1126/science.109.2825.165. URL: https://www.sciencemag.org/lookup/doi/10.1126/science.109.2825.165.

Cayrel, R. and E. Schatzman (Jan. 1954). "Sur la polarisation interstellaire par des particules de graphite." In: *Annales d'Astrophysique* 17, p. 555. ISSN: 0365-0499. URL: http://adsabs.harvard.edu/abs/1954AnAp...17..555C.

Hoyle, F. and N. C. Wickramasinghe (May 1962). "On Graphite Particles as Interstellar Grains." en. In: *Monthly Notices of the Royal Astronomical Society* 124.5, pp. 417–433. ISSN: 0035-8711, 1365-2966. DOI: 10.1093/mnras/124.5.417. URL: https://academic.oup.com/mnras/article-lookup/doi/10.1093/mnras/124.5.417.

Gould, Robert J. and Edwin E. Salpeter (Aug. 1963). "The Interstellar Abundance of the Hydrogen Molecule. I. Basic Processes." en. In: *The Astrophysical Journal* 138, p. 393. ISSN:

0004-637X, 1538-4357. DOI: 10.1086/147654. URL: http://adsabs.harvard.edu/doi/10.1086/147654.

Kamijo, F. (Jan. 1963). "A Theoretical Study on the Long Period Variable Star, III. Formation of Solid or Liquid Particles in the Circumstellar Envelope." In: *pasj* 15, p. 440.

Wickramasinghe, N. C. (Feb. 1963). "On Graphite Particles as Interstellar Grains, II." en. In: *Monthly Notices of the Royal Astronomical Society* 126.1, pp. 99–114. ISSN: 0035-8711, 1365-2966. DOI: 10.1093/mnras/126.1.99. URL: https://academic.oup.com/mnras/article-lookup/doi/10.1093/mnras/126.1.99.

Danielson, R. E., N. J. Woolf, and J. E. Gaustad (Jan. 1965). "A Search for Interstellar Ice Absorption in the Infrared Spectrum of MU Cephei." en. In: *The Astrophysical Journal* 141, p. 116. ISSN: 0004-637X, 1538-4357. DOI: 10.1086/148093. URL: http://adsabs.harvard.edu/doi/10.1086/148093.

Stecher, T. P. and B. Donn (Nov. 1965). "On Graphite and Interstellar Extinction." In: *The Astrophysical Journal* 142, p. 1681. ISSN: 0004-637X. DOI: 10.1086/148461. URL: http://adsabs.harvard.edu/abs/1965ApJ...142.1681S.

Stecher, Theodore P. (Nov. 1965). "Interstellar Ectinction in the Ultraviolet." en. In: *The Astrophysical Journal* 142, p. 1683. ISSN: 0004-637X, 1538-4357. DOI: 10.1086/148462. URL: http://adsabs.harvard.edu/doi/10.1086/148462.

Habing, H. J. (Jan. 1968). "The interstellar radiation density between 912 A and 2400 A." In: *Bulletin of the Astronomical Institutes of the Netherlands* 19, p. 421. ISSN: 0365-8910. URL: http://adsabs.harvard.edu/abs/1968BAN....19..421H.

Gilman, Robert C. (Mar. 1969). "On the Composition of Circumstellar Grains." en. In: *The Astrophysical Journal* 155, p. L185. ISSN: 0004-637X, 1538-4357. DOI: 10.1086/180332. URL: http://adsabs.harvard.edu/doi/10.1086/180332.

Hoyle, F. and N. C. Wickramasinghe (Aug. 1969). "Interstellar Grains." en. In: *Nature* 223.5205, pp. 459–462. ISSN: 0028-0836, 1476-4687. DOI: 10.1038/223459a0. URL: http://www.nature.com/articles/223459a0.

Knacke, R. F., D. D. Cudaback, and J. E. Gaustad (Oct. 1969). "Infrared Spectra of Highly Reddened Stars: a Search for Interstellar Ice Grains." en. In: *The Astrophysical Journal* 158, p. 151. ISSN: 0004-637X, 1538-4357. DOI: 10.1086/150179. URL: http://adsabs.harvard.edu/doi/10.1086/150179.

Knacke, R. F., J. E. Gaustad, F. C. Gillett, and W. A. Stein (Mar. 1969). "A Possible Identification of Interstellar Silicate Absorption in the Infrared Spectrum of 119 Tauri." en. In: *The Astrophysical Journal* 155, p. L189. ISSN: 0004-637X, 1538-4357. DOI: 10.1086/180333. URL: http://adsabs.harvard.edu/doi/10.1086/180333.

Stein, Wayne A. and F. C. Gillett (Mar. 1969). "Spectral Distribution of Infrared Radiation from the Trapezium Region of the Orion Nebula." en. In: *The Astrophysical Journal* 155, p. L197. ISSN: 0004-637X, 1538-4357. DOI: 10.1086/180335. URL: http://adsabs.harvard.edu/doi/10.1086/180335.

Woolf, N. J. and E. P. Ney (Mar. 1969). "Circumstellar Infrared Emission from Cool Stars." en. In: *The Astrophysical Journal* 155, p. L181. ISSN: 0004-637X, 1538-4357. DOI: 10.1086/180331. URL: http://adsabs.harvard.edu/doi/10.1086/180331.

Hackwell, J. A., R. D. Gehrz, and N. J. Woolf (Aug. 1970). "Interstellar Silicate Absorption Bands." en. In: *Nature* 227.5260, pp. 822–823. ISSN: 0028-0836, 1476-4687. DOI: 10.1038/227822a0. URL: http://www.nature.com/articles/227822a0.

Maas, R. W., E. P. Ney, and N. J. Woolf (May 1970). "The 10-MICRON Emission Peak of Comet Bennett 1969i." en. In: *The Astrophysical Journal* 160, p. L101. ISSN: 0004-637X, 1538-4357. DOI: 10.1086/180537. URL: http://adsabs.harvard.edu/doi/10.1086/180537.

Hollenbach, David and E. E. Salpeter (Jan. 1971). "Surface Recombination of Hydrogen Molecules." en. In: *The Astrophysical Journal* 163, p. 155. ISSN: 0004-637X, 1538-4357. DOI: 10.1086/150754. URL: http://adsabs.harvard.edu/doi/10.1086/150754.

Carrasco, L., S. E. Strom, and K. M. Strom (May 1973). "Interstellar dust in the Rho Ophiuchi dark cloud." In: *The Astrophysical Journal* 182, pp. 95–109. ISSN: 0004-637X. DOI: 10.1086/152121. URL: http://adsabs.harvard.edu/abs/1973ApJ...182...95C.

Dyck, H. M., R. W. Capps, W. J. Forrest, and F. C. Gillett (Aug. 1973). "Discovery of Large 10-MICRON Linear Polarization of the Becklinneugebauer Source in the Orion Nebula." en. In: *The Astrophysical Journal* 183, p. L99. ISSN: 0004-637X, 1538-4357. DOI: 10.1086/181262. URL: http://adsabs.harvard.edu/doi/10.1086/181262.

Gillett, F. C. and W. J. Forrest (Jan. 1973). "Spectra of the Becklin-Neugebauer point source and the Kleinmann-low nebula from 2.8 to 13.5 microns." en. In: *The Astrophysical Journal* 179, p. 483. ISSN: 0004-637X, 1538-4357. DOI: 10.1086/151888. URL: http://adsabs.harvard.edu/doi/10.1086/151888.

Gillett, F. C., W. J. Forrest, and K. M. Merrill (July 1973). "8-13 micron spectra of NGC 7027, BD +30 3639 and NGC 6572." en. In: *The Astrophysical Journal* 183, p. 87. ISSN: 0004-637X, 1538-4357. DOI: 10.1086/152211. URL: http://adsabs.harvard.edu/doi/10.1086/152211.

Greenberg, J. Mayo (Jan. 1973). "Chemical and Physical Properties of Interstellar Dust." In: *Molecules in the Galactic Environment*. Ed. by M. A. Gordon and Lewis E. Snyder, p. 93.

Milman, A. S., G. R. Knapp, S. L. Knapp, and W. J. Wilson (June 1973). "CO Observations of the Horsehead Nebula." In: vol. 5, p. 332. URL: http://adsabs.harvard.edu/abs/1973BAAS....5..332M.

Martin, P. G. and J. R. P. Angel (Mar. 1974). "A study of interstellar polarization at the lambda 4430 and 5780 features in HD 183143." en. In: *The Astrophysical Journal* 188, p. 517. ISSN: 0004-637X, 1538-4357. DOI: 10.1086/152741. URL: http://adsabs.harvard.edu/doi/10.1086/152741.

— (Jan. 1975). "The diffuse interstellar features studied in HD 21389 by polarimetry and spectrophotometry." en. In: *The Astrophysical Journal* 195, p. 379. ISSN: 0004-637X, 1538-4357. DOI: 10.1086/153335. URL: http://adsabs.harvard.edu/doi/10.1086/153335.

Danks, A. C. and D. L. Lambert (Mar. 1976). "Line Profiles of the Diffuse Interstellar Lines at 5780 A, 5797 A." en. In: *Monthly Notices of the Royal Astronomical Society* 174.3, pp. 571–586. ISSN: 0035-8711, 1365-2966. DOI: 10.1093/mnras/174.3.571. URL: https://academic.oup.com/mnras/article-lookup/doi/10.1093/mnras/174.3.571.

Mathis, J. S., W. Rumpl, and K. H. Nordsieck (Oct. 1977). "The size distribution of interstellar grains." In: *The Astrophysical Journal* 217, pp. 425–433. ISSN: 0004-637X. DOI: 10.1086/155591. URL: http://adsabs.harvard.edu/abs/1977ApJ...217..425M.

McKee, C. F. and J. P. Ostriker (Nov. 1977). "A theory of the interstellar medium - Three components regulated by supernova explosions in an inhomogeneous substrate." en. In: *The Astrophysical Journal* 218, p. 148. ISSN: 0004-637X, 1538-4357. DOI: 10.1086/155667. URL: http://adsabs.harvard.edu/doi/10.1086/155667.

Smith, W. H., T. P. Snow Jr., and D. G. York (Nov. 1977). "Comments on the origins of the diffuse interstellar bands." en. In: *The Astrophysical Journal* 218, p. 124. ISSN: 0004-637X, 1538-4357. DOI: 10.1086/155664. URL: http://adsabs.harvard.edu/doi/10.1086/155664.

Warren Jr., W. H. and J. E. Hesser (June 1977). "A photometric study of the Orion OB 1 association. I - Observational data." In: *The Astrophysical Journal Supplement Series* 34, pp. 115–206. ISSN: 0067-0049. DOI: 10.1086/190446. URL: http://adsabs.harvard.edu/abs/1977ApJS..34..115W.

Phillips, J. C. (Apr. 1979). "Structure of Amorphous (G e , S i) 1 x Y x Alloys." en. In: *Physical Review Letters* 42.17, pp. 1151–1154. ISSN: 0031-9007. DOI: 10.1103/PhysRevLett.42.1151. URL: https://link.aps.org/doi/10.1103/PhysRevLett.42.1151.

Willner, S. P., R. C. Puetter, R. W. Russell, and B. T. Soifer (Sept. 1979). "Unidentified infrared spectral features." en. In: *Astrophysics and Space Science* 65.1, pp. 95–101. ISSN: 0004-640X, 1572-946X. DOI: 10.1007/BF00643492. URL: http://link.springer.com/10.1007/BF00643492.

Döhler, G.H., R. Dandoloff, and H. Bilz (Oct. 1980). "A topological-dynamical model of amorphycity." en. In: *Journal of Non-Crystalline Solids* 42.1-3, pp. 87–95. ISSN: 00223093. DOI: 10.1016/0022-3093(80)90010-1. URL: https://linkinghub.elsevier.com/retrieve/pii/0022309380900101.

Jura, M. (Jan. 1980). "Origin of large interstellar grains toward Rho Ophiuchi." In: *The Astrophysical Journal* 235, pp. 63–65. ISSN: 0004-637X. DOI: 10.1086/157610. URL: http://adsabs.harvard.edu/abs/1980ApJ...235...63J.

Schmidt, G. D., M. Cohen, and B. Margon (Aug. 1980). "Discovery of optical molecular emission from the bipolar nebula surrounding HD 44179." en. In: *The Astrophysical Journal* 239, p. L133. ISSN: 0004-637X, 1538-4357. DOI: 10.1086/183309. URL: http://adsabs.harvard.edu/doi/10.1086/183309.

Wickramasinghe, D. T. and D. A. Allen (Oct. 1980). "The 3.4-μm interstellar absorption feature." en. In: *Nature* 287.5782, pp. 518–519. ISSN: 0028-0836, 1476-4687. DOI: 10.1038/287518a0. URL: http://www.nature.com/articles/287518a0.

Duley, W. W. and D. A. Williams (Sept. 1981). "The infrared spectrum of interstellar dust: Surface functional groups on carbon." en. In: *Monthly Notices of the Royal Astronomical Society* 196.2, pp. 269–274. ISSN: 0035-8711, 1365-2966. DOI: 10.1093/mnras/196.2.269. URL: https://academic.oup.com/mnras/article-lookup/doi/10.1093/mnras/196.2.269.

Anthony-Twarog, B. J. (Aug. 1982). "The H-beta distance scale for B stars - The Orion association." In: *The Astronomical Journal* 87, pp. 1213–1222. ISSN: 0004-6256. DOI: 10.1086/113204. URL: http://adsabs.harvard.edu/abs/1982AJ.....87.1213A.

Greenberg, J. M. (Jan. 1982). "What are comets made of - A model based on interstellar dust." In: *IAU Colloq. 61: Comet Discoveries, Statistics, and Observational Selection*. Ed. by L. L. Wilkening, pp. 131–163.

Stark, A. A. and J. Bally (1982). "CO in the horsehead nebula." In: vol. 93, pp. 329–333. DOI: 10.1007/978-94-009-7778-5_43. URL: http://adsabs.harvard.edu/abs/1982ASSL...93..329S.

Boer, K. S. de (Sept. 1983). "Diffuse light near Zeta Orionis and the Horsehead nebula, and anomalous extinction of HD 37903, as measured with the ANS." In: *Astronomy and Astrophysics* 125, pp. 258–264. ISSN: 0004-6361. URL: http://adsabs.harvard.edu/abs/1983A%26A...125..258D.

Duley, W. W. and D. A. Williams (Nov. 1983). "A 3.4 m absorption band in amorphous carbon: implications for interstellar dust." en. In: *Monthly Notices of the Royal Astronomical Society* 205.1, 67P–70P. ISSN: 0035-8711, 1365-2966. DOI: 10.1093/mnras/205.1.67P. URL: https://academic.oup.com/mnras/article-lookup/doi/10.1093/mnras/205.1.67P.

Mathis, J. S., P. G. Mezger, and N. Panagia (Nov. 1983). "Interstellar radiation field and dust temperatures in the diffuse interstellar matter and in giant molecular clouds." In: *aap* 500, pp. 259–276.

Thorpe, M.F. (Sept. 1983). "Continuous deformations in random networks." en. In: *Journal of Non-Crystalline Solids* 57.3, pp. 355–370. ISSN: 00223093. DOI: 10.1016/0022-3093(83)90424-6. URL: https://linkinghub.elsevier.com/retrieve/pii/0022309383904246.

Draine, B. T. and H. M. Lee (Oct. 1984). "Optical properties of interstellar graphite and silicate grains." In: *The Astrophysical Journal* 285, pp. 89–108. ISSN: 0004-637X. DOI: 10.1086/162480. URL: http://adsabs.harvard.edu/abs/1984ApJ...285...89D.

Leger, A. and J. L. Puget (Aug. 1984). "Identification of the "unidentified" IR emission features of interstellar dust ?" In: *aap* 500, pp. 279–282.

Smith, F. W. (Feb. 1984). "Optical constants of a hydrogenated amorphous carbon film." en. In: *Journal of Applied Physics* 55.3, pp. 764–771. ISSN: 0021-8979, 1089-7550. DOI: 10.1063/1.333135. URL: http://aip.scitation.org/doi/10.1063/1.333135.

Allamandola, L. J., A. G. G. M. Tielens, and J. R. Barker (Mar. 1985). "Polycyclic aromatic hydrocarbons and the unidentified infrared emission bands - Auto exhaust along the Milky Way." en. In: *The Astrophysical Journal* 290, p. L25. ISSN: 0004-637X, 1538-4357. DOI: 10.1086/184435. URL: http://adsabs.harvard.edu/doi/10.1086/184435.

Draine, B. T. and N. Anderson (May 1985). "Temperature fluctuations and infrared emission from interstellar grains." In: *The Astrophysical Journal* 292, pp. 494–499. ISSN: 0004-637X. DOI: 10.1086/163181. URL: http://adsabs.harvard.edu/abs/1985ApJ...292..494D.

Duley, W. W. (July 1985). "Evidence for hydrogenated amorphous carbon in the Red Rectangle." en. In: *Monthly Notices of the Royal Astronomical Society* 215.2, pp. 259–263. ISSN: 0035-8711, 1365-2966. DOI: 10.1093/mnras/215.2.259. URL: https://academic.oup.com/mnras/article-lookup/doi/10.1093/mnras/215.2.259.

Neckel, T. and M. Sarcander (June 1985). "Spectroscopic observations of the Horsehead Nebula." In: *Astronomy and Astrophysics* 147, p. L1. ISSN: 0004-6361. URL: http://adsabs.harvard.edu/abs/1985A%26A...147L...1N.

Butchart, I., A. D. McFadzean, D. C. B. Whittet, T. R. Geballe, and J. M. Greenberg (Jan. 1986). "Three micron spectroscopy of the galactic centre source IRS 7." In: *aap* 154, pp. L5–L7.

D'Hendecourt, L. B., A. Leger, G. Olofsson, and W. Schmidt (Dec. 1986). "The Red Rectangle : a possible case of visible luminescence from polycyclic aromatic hydrocarbons." In: *aap* 170, pp. 91–96.

Desert, F. X., F. Boulanger, and S. N. Shore (May 1986). "Grain temperature fluctuations - A key to infrared spectra." In: *Astronomy and Astrophysics* 160, pp. 295–300. ISSN: 0004-6361. URL: http://adsabs.harvard.edu/abs/1986A%26A...160..295D.

Fitzpatrick, E. L. and D. Massa (Aug. 1986). "An analysis on the shapes of ultraviolet extinction curves. I - The 2175 A bump." In: *The Astrophysical Journal* 307, pp. 286–294. ISSN: 0004-637X. DOI: 10.1086/164415. URL: http://adsabs.harvard.edu/abs/1986ApJ...307..286F.

Hecht, J. H. (June 1986). "A physical model for the 2175 A interstellar extinction feature." en. In: *The Astrophysical Journal* 305, p. 817. ISSN: 0004-637X, 1538-4357. DOI: 10.1086/164295. URL: http://adsabs.harvard.edu/doi/10.1086/164295.

Sandell, G., B. Reipurth, C. Menten, M. Walmsley, and H. Ungerechts (1986). "Young Stars and High Density Condensations in the Horsehead Region." In: vol. 124, p. 295. DOI: 10.1007/978-94-009-4672-9_63. URL: http://adsabs.harvard.edu/abs/1986ASSL..124..295S.

Jones, A. P., W. W. Duley, and D. A. Williams (Nov. 1987). "Interstellar extinction correlations." en. In: *Monthly Notices of the Royal Astronomical Society* 229.2, pp. 213–221. ISSN: 0035-8711, 1365-2966. DOI: 10.1093/mnras/229.2.213. URL: https://academic.oup.com/mnras/article-lookup/doi/10.1093/mnras/229.2.213.

Steel, T. M. and W. W. Duley (Apr. 1987). "A 217.5 nanometer absorption feature in the spectrum of small silicate particles." en. In: *The Astrophysical Journal* 315, p. 337. ISSN: 0004-637X, 1538-4357. DOI: 10.1086/165138. URL: http://adsabs.harvard.edu/doi/10.1086/165138.

Draine, B. T. (Oct. 1988). "The discrete-dipole approximation and its application to interstellar graphite grains." en. In: *The Astrophysical Journal* 333, p. 848. ISSN: 0004-637X, 1538-4357. DOI: 10.1086/166795. URL: http://adsabs.harvard.edu/doi/10.1086/166795.

Nagata, Tetsuya, Alan T. Tokunaga, K. Sellgren, Robert G. Smith, Takashi Onaka, Yoshikazu Nakada, and Akira Sakata (Mar. 1988). "High-resolution spectroscopy of the 3 micron emission features in NGC 7027 and IRAS 21282+5050." en. In: *The Astrophysical Journal* 326, p. 157. ISSN: 0004-637X, 1538-4357. DOI: 10.1086/166076. URL: http://adsabs.harvard.edu/doi/10.1086/166076.

Witt, Adolf N. and Rudolph E. Schild (Feb. 1988). "Hydrogenated amorphous carbon grains in reflection nebulae." en. In: *The Astrophysical Journal* 325, p. 837. ISSN: 0004-637X, 1538-4357. DOI: 10.1086/166054. URL: http://adsabs.harvard.edu/doi/10.1086/166054.

Allamandola, L. J., G. G. M. Tielens, and J. R. Barker (Dec. 1989). "Interstellar polycyclic aromatic hydrocarbons - The infrared emission bands, the excitation/emission mechanism, and the astrophysical implications." en. In: *The Astrophysical Journal Supplement Series* 71, p. 733. ISSN: 0067-0049, 1538-4365. DOI: 10.1086/191396. URL: http://adsabs.harvard.edu/doi/10.1086/191396.

Cardelli, Jason A., Geoffrey C. Clayton, and John S. Mathis (Oct. 1989). "The relationship between infrared, optical, and ultraviolet extinction." In: *The Astrophysical Journal* 345, pp. 245–256. ISSN: 0004-637X. DOI: 10.1086/167900. URL: http://adsabs.harvard.edu/abs/1989ApJ...345..245C.

Draine, B. (Jan. 1989). "On the Interpretation of the \ensuremath\lambda 2175 Å Feature." In: *Interstellar Dust*. Ed. by Louis J. Allamandola and A. G. G. M. Tielens. Vol. 135. IAU Symposium, p. 313.

Duley, W. W., A. P. Jones, and D. A. Williams (Feb. 1989). "Hydrogenated amorphous carbon-coated silicate particles as a source of interstellar extinction." In: *Monthly Notices of the Royal Astronomical Society* 236, pp. 709–725. ISSN: 0035-8711. DOI: 10.1093/mnras/236.4.709. URL: http://adsabs.harvard.edu/abs/1989MNRAS.236..709D.

Mathis, John S. and G. Whiffen (June 1989). "Composite interstellar grains." In: *The Astrophysical Journal* 341, pp. 808–822. ISSN: 0004-637X. DOI: 10.1086/167538. URL: http://adsabs.harvard.edu/abs/1989ApJ...341..808M.

Adamson, A. J., D. C. B. Whittet, and W. W. Duley (Apr. 1990). "The 3.4-mu.m interstellar absorption feature in CYG OB2 No 12." In: *mnras* 243, pp. 400–404.

Boulanger, F., E. Falgarone, J. L. Puget, and G. Helou (Nov. 1990). "Variations in the abundance of transiently heated particles within nearby molecular clouds." In: *The Astrophysical Journal* 364, pp. 136–145. ISSN: 0004-637X. DOI: 10.1086/169394. URL: http://adsabs.harvard.edu/abs/1990ApJ...364..136B.

Desert, F.-X., F. Boulanger, and J. L. Puget (Oct. 1990). "Interstellar dust models for extinction and emission." In: *Astronomy and Astrophysics* 237, pp. 215–236. ISSN: 0004-6361. URL: http://adsabs.harvard.edu/abs/1990A%26A...237..215D.

Draine, Bruce T. (Jan. 1990). "Evolution of interstellar dust." In: *The Evolution of the Interstellar Medium*. Ed. by Leo Blitz. Vol. 12. Astronomical Society of the Pacific Conference Series, pp. 193–205.

Furton, D. G. and A. N. Witt (Dec. 1990). "The spatial distribution of extended red emission in the planetary nebula NGC 7027." en. In: *The Astrophysical Journal* 364, p. L45. ISSN: 0004-637X, 1538-4357. DOI: 10.1086/185871. URL: http://adsabs.harvard.edu/doi/10.1086/185871.

Jones, A. P. (Nov. 1990). "Carbon atom clusters in random covalent networks: PAHs as an integral component of interstellar HAC." In: *Monthly Notices of the Royal Astronomical Society*

247, pp. 305–310. ISSN: 0035-8711. URL: http://adsabs.harvard.edu/abs/1990MNRAS.247..305J.

Muizon, M. Jourdain de, L. B. D'Hendecourt, and T. R. Geballe (Aug. 1990). "Three micron spectroscopy of IRAS sources : observed and laboratory signatures of PAHs." In: *aap* 235, p. 367.

Sorrell, Wilfred H. (Apr. 1990). "The lambda 2175-A feature from irradiated graphitic particles." In: *mnras* 243, pp. 570–587.

Tamor, M. A. and C. H. Wu (Jan. 1990). "Graphitic network models of "diamondlike" carbon." en. In: *Journal of Applied Physics* 67.2, pp. 1007–1012. ISSN: 0021-8979, 1089-7550. DOI: 10.1063/1.345808. URL: http://aip.scitation.org/doi/10.1063/1.345808.

Witt, Adolf N. and Todd A. Boroson (May 1990). "Spectroscopy of extended red emission in reflection nebulae." en. In: *The Astrophysical Journal* 355, p. 182. ISSN: 0004-637X, 1538-4357. DOI: 10.1086/168752. URL: http://adsabs.harvard.edu/doi/10.1086/168752.

Cardelli, Jason A. and Geoffrey C. Clayton (Mar. 1991). "Absolute extinction and the influence of environment - Dark cloud sight lines toward VCT 10, 30, and Walker 67." In: *The Astronomical Journal* 101, pp. 1021–1032. ISSN: 0004-6256. DOI: 10.1086/115744. URL: http://adsabs.harvard.edu/abs/1991AJ....101.1021C.

Lada, Elizabeth A., John Bally, and Antony A. Stark (Feb. 1991). "An unbiased survey for dense cores in the LYNDS 1630 molecular cloud." In: *The Astrophysical Journal* 368, pp. 432–444. ISSN: 0004-637X. DOI: 10.1086/169708. URL: http://adsabs.harvard.edu/abs/1991ApJ...368..432L.

Laureijs, R. J., F. O. Clark, and T. Prusti (May 1991). "IRAS detection of very cold dust in the LYNDS 134 cloud complex." In: *The Astrophysical Journal* 372, pp. 185–193. ISSN: 0004-637X. DOI: 10.1086/169963. URL: http://adsabs.harvard.edu/abs/1991ApJ...372..185L.

Sandford, S. A., L. J. Allamandola, A. G. G. M. Tielens, K. Sellgren, M. Tapia, and Y. Pendleton (Apr. 1991). "The interstellar C-H stretching band near 3.4 microns - Constraints on the composition of organic material in the diffuse interstellar medium." en. In: *The Astrophysical Journal* 371, p. 607. ISSN: 0004-637X, 1538-4357. DOI: 10.1086/169925. URL: http://adsabs.harvard.edu/doi/10.1086/169925.

Adamson, A. J. and D. C. B. Whittet (Oct. 1992). "Spectropolarimetry of the 5797 A diffuse interstellar band." en. In: *The Astrophysical Journal* 398, p. L69. ISSN: 0004-637X, 1538-4357. DOI: 10.1086/186579. URL: http://adsabs.harvard.edu/doi/10.1086/186579.

Geballe, T. R., A. G. G. M. Tielens, S. Kwok, and B. J. Hrivnak (Mar. 1992). "Unusual 3 micron emission features in three proto-planetary nebulae." en. In: *The Astrophysical Journal* 387, p. L89. ISSN: 0004-637X, 1538-4357. DOI: 10.1086/186312. URL: http://adsabs.harvard.edu/doi/10.1086/186312.

Joblin, C., A. Leger, and P. Martin (July 1992). "Contribution of polycyclic aromatic hydrocarbon molecules to the interstellar extinction curve." en. In: *The Astrophysical Journal* 393, p. L79. ISSN: 0004-637X, 1538-4357. DOI: 10.1086/186456. URL: http://adsabs.harvard.edu/doi/10.1086/186456.

Perrin, J. M. and J. P. Sivan (Feb. 1992). "Discovery of a red luminescence band in the spectrum of the Orion Nebula." In: *aap* 255, pp. 271–280.

Rowan-Robinson, Michael (Oct. 1992). "Interstellar dust in galaxies." en. In: *Monthly Notices of the Royal Astronomical Society* 258.4, pp. 787–799. ISSN: 0035-8711, 1365-2966. DOI: 10.1093/mnras/258.4.787. URL: https://academic.oup.com/mnras/article-lookup/doi/10.1093/mnras/258.4.787.

Sakata, Akira, Setsuko Wada, Takatoshi Narisawa, Yoichi Asano, Yutaka Iijima, Takashi Onaka, and Alan T. Tokunaga (July 1992). "Quenched carbonaceous composite - Fluorescence spectrum compared to the extended red emission observed in reflection nebulae."

en. In: *The Astrophysical Journal* 393, p. L83. ISSN: 0004-637X, 1538-4357. DOI: 10.1086/186457. URL: http://adsabs.harvard.edu/doi/10.1086/186457.

Salama, F. and L. J. Allamandola (Aug. 1992). "The ultraviolet and visible spectrum of the polycyclic aromatic hydrocarbon C10H8(+) - Possible contributions to the diffuse interstellar bands and to the ultraviolet-visible extinction." en. In: *The Astrophysical Journal* 395, p. 301. ISSN: 0004-637X, 1538-4357. DOI: 10.1086/171652. URL: http://adsabs.harvard.edu/doi/10.1086/171652.

Siebenmorgen, R. and E. Kruegel (June 1992). "Dust model containing polycyclic aromatic hydrocarbons in various environments." In: *Astronomy and Astrophysics* 259, pp. 614–626. ISSN: 0004-6361. URL: http://adsabs.harvard.edu/abs/1992A%26A...259..614S.

Brooke, T. Y., A. T. Tokunaga, and S. E. Strom (Aug. 1993). "Dust emission features in 3-micron spectra of Herbig Ae/Be stars." In: *The Astronomical Journal* 106, p. 656. ISSN: 00046256. DOI: 10.1086/116672. URL: http://adsabs.harvard.edu/cgi-bin/bib_query?1993AJ....106..656B.

Sivan, Jean-Pierre and Jean-Marie Perrin (Feb. 1993). "Scattering and luminescence in the Bubble Nebula." en. In: *The Astrophysical Journal* 404, p. 258. ISSN: 0004-637X, 1538-4357. DOI: 10.1086/172273. URL: http://adsabs.harvard.edu/doi/10.1086/172273.

Webster, A. (Sept. 1993). "The extended red emission and the fluorescence of C60." en. In: *Monthly Notices of the Royal Astronomical Society* 264.1, pp. L1–L2. ISSN: 0035-8711, 1365-2966. DOI: 10.1093/mnras/264.1.L1. URL: https://academic.oup.com/mnras/article-lookup/doi/10.1093/mnras/264.1.L1.

Zhou, S., D. T. Jaffe, J. E. Howe, N. Geis, F. Herrmann, S. C. Madden, A. Poglitsch, and G. J. Stacey (Dec. 1993). "The [C ii] 158 Micron Emission from the Horsehead Nebula." In: *The Astrophysical Journal* 419, p. 190. ISSN: 0004-637X. DOI: 10.1086/173473. URL: http://adsabs.harvard.edu/abs/1993ApJ...419..190Z.

Abergel, Alain, Francois Boulanger, Akira Mizuno, and Yasuo Fukui (Mar. 1994). "Comparative analysis of the far-infrared and (13)CO (J = 0-1) emissions of the Taurus complex." In: *The Astrophysical Journal Letters* 423, pp. L59–L62. ISSN: 0004-637X. DOI: 10.1086/187235. URL: http://adsabs.harvard.edu/abs/1994ApJ...423L..59A.

Bakes, E. L. O. and A. G. G. M. Tielens (June 1994). "The photoelectric heating mechanism for very small graphitic grains and polycyclic aromatic hydrocarbons." en. In: *The Astrophysical Journal* 427, p. 822. ISSN: 0004-637X, 1538-4357. DOI: 10.1086/174188. URL: http://adsabs.harvard.edu/doi/10.1086/174188.

Draine, Bruce T. and Piotr J. Flatau (Apr. 1994). "Discrete-Dipole Approximation For Scattering Calculations." en. In: *Journal of the Optical Society of America A* 11.4, p. 1491. ISSN: 1084-7529, 1520-8532. DOI: 10.1364/JOSAA.11.001491. URL: https://www.osapublishing.org/abstract.cfm?URI=josaa-11-4-1491.

Foing, B. H. and P. Ehrenfreund (May 1994). "Detection of two interstellar absorption bands coincident with spectral features of C60+." en. In: *Nature* 369.6478, pp. 296–298. ISSN: 0028-0836, 1476-4687. DOI: 10.1038/369296a0. URL: http://www.nature.com/articles/369296a0.

Jenniskens, P. and F. X. Desert (July 1994). "A survey of diffuse interstellar bands (3800-8680 A)." In: *aaps* 106, pp. 39–78.

Kim, Sang-Hee, P. G. Martin, and Paul D. Hendry (Feb. 1994). "The size distribution of interstellar dust particles as determined from extinction." In: *The Astrophysical Journal* 422, pp. 164–175. ISSN: 0004-637X. DOI: 10.1086/173714. URL: http://adsabs.harvard.edu/abs/1994ApJ...422..164K.

Ossenkopf, V. and Th. Henning (Nov. 1994). "Dust opacities for protostellar cores." In: *Astronomy and Astrophysics* 291, pp. 943–959. ISSN: 0004-6361. URL: http://adsabs.harvard.edu/abs/1994A%26A...291..943O.

Pendleton, Y. J., S. A. Sandford, L. J. Allamandola, A. G. G. M. Tielens, and K. Sellgren (Dec. 1994). "Near-infrared absorption spectroscopy of interstellar hydrocarbon grains." en. In: *The Astrophysical Journal* 437, p. 683. ISSN: 0004-637X, 1538-4357. DOI: 10.1086/175031. URL: http://adsabs.harvard.edu/doi/10.1086/175031.

Adamson, A. J. and D. C. B. Whittet (July 1995). "A Search for Polarization in Diffuse Interstellar Bands toward HD 197770." In: *The Astrophysical Journal* 448.1. ISSN: 0004637X. DOI: 10.1086/309592. URL: https://iopscience.iop.org/article/10.1086/309592.

Greenberg, J. Mayo, Aigen Li, Celia X. Mendoza-Gomez, Willem A. Schutte, Perry A. Gerakines, and Menno de Groot (Dec. 1995). "Approaching the Interstellar Grain Organic Refractory Component." In: *The Astrophysical Journal Letters* 455, p. L177. ISSN: 0004-637X. DOI: 10.1086/309834. URL: http://adsabs.harvard.edu/abs/1995ApJ...455L.177G.

Papoular, R., O. Guillois, I. Nenner, J.-M. Perrin, C. Reynaud, and J.-P. Sivan (Oct. 1995). "On the nature of interstellar carbonaceous dust." en. In: *Planetary and Space Science* 43.10-11, pp. 1287–1291. ISSN: 00320633. DOI: 10.1016/0032-0633(95)00056-B. URL: https://linkinghub.elsevier.com/retrieve/pii/003206339500056B.

Sakata, Akira, Setsuko Wada, Alan T. Tokunaga, and Takatoshi Narisawa (Oct. 1995). "Comparison of the absorption curves of soots, pitch samples and QCCs to the interstellar extinction curve." en. In: *Planetary and Space Science* 43.10-11, pp. 1223–1226. ISSN: 00320633. DOI: 10.1016/0032-0633(95)00034-3. URL: https://linkinghub.elsevier.com/retrieve/pii/0032063395000343.

Sellgren, K., T. Y. Brooke, R. G. Smith, and T. R. Geballe (Aug. 1995). "A New 3.25 Micron Absorption Feature toward Monoceros R2/IRS 3." In: *The Astrophysical Journal* 449.1. ISSN: 0004637X. DOI: 10.1086/309627. URL: https://iopscience.iop.org/article/10.1086/309627.

Aitken, David, Craig Smith, Toby Moore, and Patrick Roche (Jan. 1996). "10pm Imaging Polarimetry." In: *The Galactic Center*. Ed. by Roland Gredel. Vol. 102. Astronomical Society of the Pacific Conference Series, p. 179.

Kramer, C., J. Stutzki, and G. Winnewisser (Mar. 1996). "Structure and excitation conditions of the southern part of the Orion B molecular cloud: a CO multiline study." In: *Astronomy and Astrophysics* 307, pp. 915–935. ISSN: 0004-6361. URL: http://adsabs.harvard.edu/abs/1996A%26A...307..915K.

Mathis, John S. (Dec. 1996). "Dust Models with Tight Abundance Constraints." en. In: *The Astrophysical Journal* 472.2, pp. 643–655. ISSN: 0004-637X, 1538-4357. DOI: 10.1086/178094. URL: https://iopscience.iop.org/article/10.1086/178094.

Mennella, V., L. Colangeli, P. Palumbo, A. Rotundi, W. Schutte, and E. Bussoletti (June 1996). "Activation of an Ultraviolet Resonance in Hydrogenated Amorphous Carbon Grains by Exposure to Ultraviolet Radiation." In: *The Astrophysical Journal* 464.2, pp. L191–L194. ISSN: 0004637X. DOI: 10.1086/310116. URL: https://iopscience.iop.org/article/10.1086/310116.

Papoular, R., J. Conard, O. Guillois, I. Nenner, C. Reynaud, and J. N. Rouzaud (Nov. 1996). "A comparison of solid-state carbonaceous models of cosmic dust." In: *aap* 315, pp. 222–236.

Somerville, W. B. (Jan. 1996). "Spectropolarimetry of Optical and Ultraviolet Extinction Features." In: *Polarimetry of the Interstellar Medium*. Ed. by Wayne G. Roberge and Doug C. B. Whittet. Vol. 97. Astronomical Society of the Pacific Conference Series, p. 143.

Verstraete, L., J. L. Puget, E. Falgarone, S. Drapatz, C. M. Wright, and R. Timmermann (Nov. 1996). "SWS spectroscopy of small grain features across the M17-Southwest photodissociation front." In: *aap* 315, pp. L337–L340.

Waters, L. B. F. M. et al. (Nov. 1996). "Mineralogy of oxygen-rich dust shells." In: *aap* 315, pp. L361–L364.

Dwek, Eli (July 1997). "Can Composite Fluffy Dust Particles Solve the Interstellar Carbon Crisis?" In: *The Astrophysical Journal* 484, pp. 779–784. ISSN: 0004-637X. DOI: 10.1086/304370. URL: http://adsabs.harvard.edu/abs/1997ApJ...484..779D.

Hollenbach, D. J. and A. G. G. M. Tielens (Sept. 1997). "DENSE PHOTODISSOCIATION REGIONS (PDRs)." en. In: *Annual Review of Astronomy and Astrophysics* 35.1, pp. 179–215. ISSN: 0066-4146, 1545-4282. DOI: 10.1146/annurev.astro.35.1.179. URL: http://www.annualreviews.org/doi/10.1146/annurev.astro.35.1.179.

Li, A. and J. M. Greenberg (July 1997). "A unified model of interstellar dust." In: *Astronomy and Astrophysics* 323, pp. 566–584. ISSN: 0004-6361. URL: http://adsabs.harvard.edu/abs/1997A%26A...323..566L.

Schaerer, D. and A. de Koter (June 1997). "Combined stellar structure and atmosphere models for massive stars. III. Spectral evolution and revised ionizing fluxes of O3-Bo stars." In: *Astronomy and Astrophysics* 322, pp. 598–614. ISSN: 0004-6361. URL: http://adsabs.harvard.edu/abs/1997A%26A...322..598S.

Whittet, D. C. B., A. C. A. Boogert, P. A. Gerakines, W. Schutte, A. G. G. M. Tielens, Th. de Graauw, T. Prusti, E. F. van Dishoeck, P. R. Wesselius, and C. M. Wright (Dec. 1997). "Infrared Spectroscopy of Dust in the Diffuse Interstellar Medium toward Cygnus OB2 No. 12." en. In: *The Astrophysical Journal* 490.2, pp. 729–734. ISSN: 0004-637X, 1538-4357. DOI: 10.1086/304914. URL: https://iopscience.iop.org/article/10.1086/304914.

Witt, Adolf N., Brian C. Friedmann, and Timothy P. Sasseen (June 1997). "Radiative Transfer Analysis of Far-Ultraviolet Background Observations Obtained with the Far Ultraviolet Space Telescope." en. In: *The Astrophysical Journal* 481.2, pp. 809–820. ISSN: 0004-637X, 1538-4357. DOI: 10.1086/304093. URL: https://iopscience.iop.org/article/10.1086/304093.

Duley, W. W. and S. Seahra (Nov. 1998). "Graphite, Polycyclic Aromatic Hydrocarbons, and the 2175 A Extinction Feature." en. In: *The Astrophysical Journal* 507.2, pp. 874–888. ISSN: 0004-637X, 1538-4357. DOI: 10.1086/306344. URL: https://iopscience.iop.org/article/10.1086/306344.

Genzel, R. et al. (May 1998). "What Powers Ultraluminous *IRAS* Galaxies?" en. In: *The Astrophysical Journal* 498.2, pp. 579–605. ISSN: 0004-637X, 1538-4357. DOI: 10.1086/305576. URL: https://iopscience.iop.org/article/10.1086/305576.

Ledoux, G. et al. (May 1998). "Silicon as a candidate carrier for ERE." In: *aap* 333, pp. L39–L42.

Schutte, W. A. et al. (Sept. 1998). "ISO-SWS observations of infrared absorption bands of the diffuse interstellar medium: The 6.2 MU M feature of aromatic compounds." In: *aap* 337, pp. 261–274.

Tulej, M., D. A. Kirkwood, M. Pachkov, and J. P. Maier (Oct. 1998). "Gas-Phase Electronic Transitions of Carbon Chain Anions Coinciding with Diffuse Interstellar Bands." In: *The Astrophysical Journal* 506.1, pp. L69–L73. ISSN: 0004637X. DOI: 10.1086/311637. URL: https://iopscience.iop.org/article/10.1086/311637.

Witt, Adolf N., Karl D. Gordon, and Douglas G. Furton (July 1998). "Silicon Nanoparticles: Source of Extended Red Emission?" In: *The Astrophysical Journal* 501.1, pp. L111–L115. ISSN: 0004637X. DOI: 10.1086/311453. URL: https://iopscience.iop.org/article/10.1086/311453.

Adamson, A. J., D. C. B. Whittet, A. Chrysostomou, J. H. Hough, D. K. Aitken, G. S. Wright, and P. F. Roche (Feb. 1999). "Spectropolarimetric Constraints on the Nature of the 3.4 Micron Absorber in the Interstellar Medium." In: *The Astrophysical Journal* 512, pp. 224–229. ISSN: 0004-637X. DOI: 10.1086/306766. URL: http://adsabs.harvard.edu/abs/1999ApJ...512..224A.

Bernard, J. P. et al. (July 1999). "PRONAOS observations of MCLD 123.5 + 24.9: cold dust in the Polaris cirrus cloud." In: *Astronomy and Astrophysics* 347, pp. 640–649. ISSN: 0004-6361. URL: http://adsabs.harvard.edu/abs/1999A%26A...347..640B.

Brooke, T. Y., K. Sellgren, and T. R. Geballe (June 1999). "New 3 Micron Spectra of Young Stellar Objects with H $_2$ O Ice Bands." en. In: *The Astrophysical Journal* 517.2, pp. 883–900. ISSN: 0004-637X, 1538-4357. DOI: 10.1086/307237. URL: https://iopscience.iop.org/article/10.1086/307237.

Greenberg, J. Mayo and Aigen Li (1999). "[No title found]." In: *Space Science Reviews* 90.1/2, pp. 149–161. ISSN: 00386308. DOI: 10.1023/A:1005298014670. URL: http://link.springer.com/10.1023/A:1005298014670.

Hollenbach, D. J. and A. G. G. M. Tielens (Jan. 1999). "Photodissociation regions in the interstellar medium of galaxies." en. In: *Reviews of Modern Physics* 71.1, pp. 173–230. ISSN: 0034-6861, 1539-0756. DOI: 10.1103/RevModPhys.71.173. URL: https://link.aps.org/doi/10.1103/RevModPhys.71.173.

Kerr, T. H., M. E. Hurst, J. R. Miles, and P. J. Sarre (Mar. 1999). "Observations of the 3.3- m UIR band in the Red Rectangle: relation to unidentified optical emission." en. In: *Monthly Notices of the Royal Astronomical Society* 303.3, pp. 446–454. ISSN: 0035-8711, 1365-2966. DOI: 10.1046/j.1365-8711.1999.02157.x. URL: https://academic.oup.com/mnras/article-lookup/doi/10.1046/j.1365-8711.1999.02157.x.

Kwok, Sun, Kevin Volk, and Bruce J. Hrivnak (Oct. 1999). "Chemical evolution of carbonaceous materials in the last stages of stellar evolution." In: *aap* 350, pp. L35–L38.

Le Bourlot, J., G. Pineau des Forêts, and D. R. Flower (May 1999). "The cooling of astrophysical media by H2." en. In: *Monthly Notices of the Royal Astronomical Society* 305.4, pp. 802–810. ISSN: 0035-8711, 1365-2966. DOI: 10.1046/j.1365-8711.1999.02497.x. URL: https://academic.oup.com/mnras/article-lookup/doi/10.1046/j.1365-8711.1999.02497.x.

Moutou, C., L. Verstraete, K. Sellgren, and A. Leger (Mar. 1999). "The rich spectroscopy of reflection nebulae." In: *The Universe as Seen by ISO*. Ed. by P. Cox and Martin Kessler. Vol. 427. ESA Special Publication, p. 727.

Seahra, S. S. and W. W. Duley (Aug. 1999). "Extended Red Emission from Carbon Clusters in Interstellar Clouds." en. In: *The Astrophysical Journal* 520.2, pp. 719–723. ISSN: 0004-637X, 1538-4357. DOI: 10.1086/307470. URL: https://iopscience.iop.org/article/10.1086/307470.

Burton, M. G. et al. (Oct. 2000). "High-Resolution Imaging of Photodissociation Regions in NGC 6334." en. In: *The Astrophysical Journal* 542.1, pp. 359–366. ISSN: 0004-637X, 1538-4357. DOI: 10.1086/309510. URL: https://iopscience.iop.org/article/10.1086/309510.

Chiar, J. E., A. G. G. M. Tielens, D. C. B. Whittet, W. A. Schutte, A. C. A. Boogert, D. Lutz, E. F. van Dishoeck, and M. P. Bernstein (July 2000). "The Composition and Distribution of Dust along the Line of Sight toward the Galactic Center." en. In: *The Astrophysical Journal* 537.2, pp. 749–762. ISSN: 0004-637X, 1538-4357. DOI: 10.1086/309047. URL: https://iopscience.iop.org/article/10.1086/309047.

Darbon, S., A. Zavagno, J. M. Perrin, C. Savine, V. Ducci, and J. P. Sivan (Dec. 2000). "Extended red emission and unidentified infrared bands in the galactic compact H II region Sh 152." In: *aap* 364, pp. 723–731.

Ehrenfreund, Pascale and Steven B. Charnley (Sept. 2000). "Organic Molecules in the Interstellar Medium, Comets, and Meteorites: A Voyage from Dark Clouds to the Early Earth." en. In: *Annual Review of Astronomy and Astrophysics* 38.1, pp. 427–483. ISSN: 0066-4146, 1545-4282. DOI: 10.1146/annurev.astro.38.1.427. URL: http://www.annualreviews.org/doi/10.1146/annurev.astro.38.1.427.

Imanishi, Masatoshi and C. C. Dudley (Dec. 2000). "Energy Diagnoses of Nine Infrared Luminous Galaxies Based on 3–4 Micron Spectra." en. In: *The Astrophysical Journal* 545.2, pp. 701–711. ISSN: 0004-637X, 1538-4357. DOI: 10.1086/317863. URL: https://iopscience.iop.org/article/10.1086/317863.

Smith, C. H., C. M. Wright, D. K. Aitken, P. F. Roche, and J. H. Hough (Feb. 2000). "Studies in mid-infrared spectropolarimetry – II. An atlas of spectra." en. In: *Monthly Notices of the Royal Astronomical Society* 312.2, pp. 327–361. ISSN: 0035-8711, 1365-2966. DOI: 10.1046/j.1365-8711.2000.03158.x. URL: https://academic.oup.com/mnras/article-lookup/doi/10.1046/j.1365-8711.2000.03158.x.

Demyk, K., Ph. Carrez, H. Leroux, P. Cordier, A. P. Jones, J. Borg, E. Quirico, P. I. Raynal, and L. d'Hendecourt (Mar. 2001). "Structural and chemical alteration of crystalline olivine under low energy He $^{+}$ irradiation." In: *Astronomy & Astrophysics* 368.3, pp. L38–L41. ISSN: 0004-6361, 1432-0746. DOI: 10.1051/0004-6361:20010208. URL: http://www.aanda.org/10.1051/0004-6361:20010208.

Draine, B. T. and Aigen Li (Apr. 2001). "Infrared Emission from Interstellar Dust. I. Stochastic Heating of Small Grains." In: *The Astrophysical Journal* 551, pp. 807–824. ISSN: 0004-637X. DOI: 10.1086/320227. URL: http://adsabs.harvard.edu/abs/2001ApJ...551..807D.

Ferrière, Katia M. (Dec. 2001). "The interstellar environment of our galaxy." en. In: *Reviews of Modern Physics* 73.4, pp. 1031–1066. ISSN: 0034-6861, 1539-0756. DOI: 10.1103/RevModPhys.73.1031. URL: https://link.aps.org/doi/10.1103/RevModPhys.73.1031.

Habart, E., L. Verstraete, F. Boulanger, G. Pineau des Forêts, F. Le Peintre, and J. P. Bernard (July 2001). "Photoelectric effect on dust grains across the L1721 cloud in the Ophiuchi molecular complex." In: *Astronomy & Astrophysics* 373.2, pp. 702–713. ISSN: 0004-6361, 1432-0746. DOI: 10.1051/0004-6361:20010342. URL: http://www.aanda.org/10.1051/0004-6361:20010342.

Hony, S., C. Van Kerckhoven, E. Peeters, A. G. G. M. Tielens, D. M. Hudgins, and L. J. Allamandola (May 2001). "The CH out-of-plane bending modes of PAH molecules in astrophysical environments." In: *Astronomy & Astrophysics* 370.3, pp. 1030–1043. ISSN: 0004-6361, 1432-0746. DOI: 10.1051/0004-6361:20010242. URL: http://www.aanda.org/10.1051/0004-6361:20010242.

Li, Aigen and B. T. Draine (June 2001a). "Infrared Emission from Interstellar Dust. II. The Diffuse Interstellar Medium." In: *The Astrophysical Journal* 554, pp. 778–802. ISSN: 0004-637X. DOI: 10.1086/323147. URL: http://adsabs.harvard.edu/abs/2001ApJ...554..778L.

— (Apr. 2001b). "On Ultrasmall Silicate Grains in the Diffuse Interstellar Medium." In: *The Astrophysical Journal Letters* 550, pp. L213–L217. ISSN: 0004-637X. DOI: 10.1086/319640. URL: http://adsabs.harvard.edu/abs/2001ApJ...550L.213L.

Meeus, G., L. B. F. M. Waters, J. Bouwman, M. E. van den Ancker, C. Waelkens, and K. Malfait (Jan. 2001). "ISO spectroscopy of circumstellar dust in 14 Herbig Ae/Be systems: Towards an understanding of dust processing." In: *Astronomy & Astrophysics* 365.3, pp. 476–490. ISSN: 0004-6361, 1432-0746. DOI: 10.1051/0004-6361:20000144. URL: http://www.aanda.org/10.1051/0004-6361:20000144.

Schiminovich, D., P. G. Friedman, C. Martin, and P. F. Morrissey (Dec. 2001). "The Narrowband Ultraviolet Imaging Experiment for Wide-Field Surveys. I. Dust-scattered Contin-

uum." In: *The Astrophysical Journal* 563.2, pp. L161–L164. ISSN: 0004637X. DOI: 10.1086/338656. URL: https://iopscience.iop.org/article/10.1086/338656.

Verstraete, L., C. Pech, C. Moutou, K. Sellgren, C. M. Wright, M. Giard, A. Léger, R. Timmermann, and S. Drapatz (June 2001). "The Aromatic Infrared Bands as seen by ISO-SWS: Probing the PAH model." In: *Astronomy & Astrophysics* 372.3, pp. 981–997. ISSN: 0004-6361, 1432-0746. DOI: 10.1051/0004-6361:20010515. URL: http://www.aanda.org/10.1051/0004-6361:20010515.

Weingartner, Joseph C. and B. T. Draine (Feb. 2001a). "Dust Grain-Size Distributions and Extinction in the Milky Way, Large Magellanic Cloud, and Small Magellanic Cloud." In: *The Astrophysical Journal* 548, pp. 296–309. ISSN: 0004-637X. DOI: 10.1086/318651. URL: http://adsabs.harvard.edu/abs/2001ApJ...548..296W.

— (June 2001b). "Photoelectric Emission from Interstellar Dust: Grain Charging and Gas Heating." In: *The Astrophysical Journal Supplement Series* 134, pp. 263–281. ISSN: 0067-0049. DOI: 10.1086/320852. URL: http://adsabs.harvard.edu/abs/2001ApJS..134..263W.

Abergel, A. et al. (July 2002). "Evolution of very small particles in the southern part of Orion B observed by ISOCAM." In: *Astronomy and Astrophysics* 389, pp. 239–251. ISSN: 0004-6361. DOI: 10.1051/0004-6361:20020324. URL: http://adsabs.harvard.edu/abs/2002A%26A...389..239A.

Li, Aigen and J. Mayo Greenberg (Apr. 2002a). "In Dust We Trust: An Overview of Observations and Theories of Interstellar Dust." In: *arXiv:astro-ph/0204392*. arXiv: astro-ph/0204392. URL: http://arxiv.org/abs/astro-ph/0204392.

— (Oct. 2002b). "Mid-Infrared Spectropolarimetric Constraints on the Core-Mantle Interstellar Dust Model." In: *The Astrophysical Journal* 577, pp. 789–794. ISSN: 0004-637X. DOI: 10.1086/342222. URL: http://adsabs.harvard.edu/abs/2002ApJ...577..789L.

Peeters, E., S. Hony, C. Van Kerckhoven, A. G. G. M. Tielens, L. J. Allamandola, D. M. Hudgins, and C. W. Bauschlicher (Aug. 2002). "The rich 6 to 9 vec mu m spectrum of interstellar PAHs." In: *Astronomy and Astrophysics* 390, pp. 1089–1113. ISSN: 0004-6361. DOI: 10.1051/0004-6361:20020773. URL: http://adsabs.harvard.edu/abs/2002A%26A...390.1089P.

Abergel, A. et al. (Nov. 2003). "ISOCAM and molecular observations of the edge of the Horsehead nebula." In: *Astronomy and Astrophysics* 410, pp. 577–585. ISSN: 0004-6361. DOI: 10.1051/0004-6361:20030878. URL: http://adsabs.harvard.edu/abs/2003A%26A...410..577A.

Pound, Marc W., Bo Reipurth, and John Bally (Apr. 2003). "Looking into the Horsehead." In: *The Astronomical Journal* 125, pp. 2108–2122. ISSN: 0004-6256. DOI: 10.1086/368138. URL: http://adsabs.harvard.edu/abs/2003AJ....125.2108P.

Stepnik, B. et al. (Feb. 2003). "Evolution of dust properties in an interstellar filament." In: *Astronomy and Astrophysics* 398, pp. 551–563. ISSN: 0004-6361. DOI: 10.1051/0004-6361:20021309. URL: http://adsabs.harvard.edu/abs/2003A%26A...398..551S.

Acke, B. and M. E. van den Ancker (Oct. 2004). "ISO spectroscopy of disks around Herbig Ae/Be stars." In: *Astronomy & Astrophysics* 426.1, pp. 151–170. ISSN: 0004-6361, 1432-0746. DOI: 10.1051/0004-6361:20040400. URL: http://www.aanda.org/10.1051/0004-6361:20040400.

Bohren, Craig F. and Donald R. Huffman (2004). *Absorption and scattering of light by small particles*. eng. OCLC: 254937169. Weinheim: Wiley-VCH. ISBN: 978-0-471-29340-8 978-0-471-05772-7 978-3-527-61815-6.

Cazaux, S. and A. G. G. M. Tielens (Mar. 2004). "H $_2$ Formation on Grain Surfaces." en. In: *The Astrophysical Journal* 604.1, pp. 222–237. ISSN: 0004-637X, 1538-4357. DOI: 10.1086/381775. URL: https://iopscience.iop.org/article/10.1086/381775.

Gibb, E. L., D. C. B. Whittet, A. C. A. Boogert, and A. G. G. M. Tielens (Mar. 2004). "Interstellar Ice: The *Infrared Space Observatory* Legacy." en. In: *The Astrophysical Journal Supplement Series* 151.1, pp. 35–73. ISSN: 0067-0049, 1538-4365. DOI: 10.1086/381182. URL: https://iopscience.iop.org/article/10.1086/381182.

Habart, E., A. Natta, and E. Krügel (Nov. 2004). "PAHs in circumstellar disks around Herbig Ae/Be stars." In: *Astronomy & Astrophysics* 427.1, pp. 179–192. ISSN: 0004-6361, 1432-0746. DOI: 10.1051/0004-6361:20035916. URL: http://www.aanda.org/10.1051/0004-6361:20035916.

Habart, E., F. Boulanger, L. Verstraete, C. M. Walmsley, and G. Pineau des Forêts (Feb. 2004). "Some empirical estimates of the H2 formation rate in photon-dominated regions." In: *Astronomy and Astrophysics* 414, pp. 531–544. ISSN: 0004-6361. DOI: 10.1051/0004-6361:20031659. URL: http://adsabs.harvard.edu/abs/2004A%26A...414..531H.

Kemper, F., W. J. Vriend, and A. G. G. M. Tielens (July 2004). "The Absence of Crystalline Silicates in the Diffuse Interstellar Medium." In: *The Astrophysical Journal* 609, pp. 826–837. ISSN: 0004-637X. DOI: 10.1086/421339. URL: http://adsabs.harvard.edu/abs/2004ApJ...609..826K.

Peeters, E., A. L. Mattioda, D. M. Hudgins, and L. J. Allamandola (Dec. 2004). "Polycyclic Aromatic Hydrocarbon Emission in the 15-21 Micron Region." In: *The Astrophysical Journal Letters* 617, pp. L65–L68. ISSN: 0004-637X. DOI: 10.1086/427186. URL: http://adsabs.harvard.edu/abs/2004ApJ...617L..65P.

Regan, Michael W. et al. (Sept. 2004). "*Spitzer* Infrared Nearby Galaxies Survey (SINGS) Imaging of NGC 7331: A Panchromatic View of a Ringed Galaxy." en. In: *The Astrophysical Journal Supplement Series* 154.1, pp. 204–210. ISSN: 0067-0049, 1538-4365. DOI: 10.1086/423204. URL: https://iopscience.iop.org/article/10.1086/423204.

Teyssier, D., D. Fossé, M. Gerin, J. Pety, A. Abergel, and E. Roueff (Apr. 2004). "Carbon budget and carbon chemistry in Photon Dominated Regions." In: *Astronomy and Astrophysics* 417, pp. 135–149. ISSN: 0004-6361. DOI: 10.1051/0004-6361:20034534. URL: http://adsabs.harvard.edu/abs/2004A%26A...417..135T.

Werner, M. W. et al. (Sept. 2004). "The *Spitzer Space Telescope* Mission." en. In: *The Astrophysical Journal Supplement Series* 154.1, pp. 1–9. ISSN: 0067-0049, 1538-4365. DOI: 10.1086/422992. URL: https://iopscience.iop.org/article/10.1086/422992.

Zubko, Viktor, Eli Dwek, and Richard G. Arendt (June 2004). "Interstellar Dust Models Consistent with Extinction, Emission, and Abundance Constraints." In: *The Astrophysical Journal Supplement Series* 152, pp. 211–249. ISSN: 0067-0049. DOI: 10.1086/382351. URL: http://adsabs.harvard.edu/abs/2004ApJS..152..211Z.

Habart, E., A. Abergel, C. M. Walmsley, D. Teyssier, and J. Pety (July 2005). "Density structure of the Horsehead nebula photo-dissociation region." In: *Astronomy and Astrophysics* 437, pp. 177–188. ISSN: 0004-6361. DOI: 10.1051/0004-6361:20041546. URL: http://adsabs.harvard.edu/abs/2005A%26A...437..177H.

Hily-Blant, P., D. Teyssier, S. Philipp, and R. Güsten (Sept. 2005). "Velocity field and star formation in the Horsehead nebula." In: *Astronomy and Astrophysics* 440, pp. 909–919. ISSN: 0004-6361. DOI: 10.1051/0004-6361:20041733. URL: http://adsabs.harvard.edu/abs/2005A%26A...440..909H.

Miville-Deschênes, M.-A., F. Boulanger, W. T. Reach, and A. Noriega-Crespo (Sept. 2005). "The First Detection of Dust Emission in a High-Velocity Cloud." en. In: *The Astrophysical Journal* 631.1, pp. L57–L60. ISSN: 0004-637X, 1538-4357. DOI: 10.1086/496961. URL: https://iopscience.iop.org/article/10.1086/496961.

Molster, Frank and Ciska Kemper (Aug. 2005). "Crystalline Silicates." en. In: *Space Science Reviews* 119.1-4, pp. 3–28. ISSN: 0038-6308, 1572-9672. DOI: 10.1007/s11214-005-8066-x. URL: http://link.springer.com/10.1007/s11214-005-8066-x.

Pety, J., D. Teyssier, D. Fossé, M. Gerin, E. Roueff, A. Abergel, E. Habart, and J. Cernicharo (June 2005). "Are PAHs precursors of small hydrocarbons in photo-dissociation regions? The Horsehead case." In: *Astronomy and Astrophysics* 435, pp. 885–899. ISSN: 0004-6361. DOI: 10.1051/0004-6361:20041170. URL: http://adsabs.harvard.edu/abs/2005A%26A...435..885P.

Rapacioli, M., C. Joblin, and P. Boissel (Jan. 2005). "Spectroscopy of polycyclic aromatic hydrocarbons and very small grains in photodissociation regions." In: *Astronomy and Astrophysics* 429, pp. 193–204. ISSN: 0004-6361. DOI: 10.1051/0004-6361:20041247. URL: http://adsabs.harvard.edu/abs/2005A%26A...429..193R.

Reach, William T. et al. (Sept. 2005). "Absolute Calibration of the Infrared Array Camera on the *Spitzer Space Telescope*." en. In: *Publications of the Astronomical Society of the Pacific* 117.835, pp. 978–990. ISSN: 0004-6280, 1538-3873. DOI: 10.1086/432670. URL: http://iopscience.iop.org/article/10.1086/432670.

Vijh, Uma P., Adolf N. Witt, and Karl D. Gordon (Nov. 2005). "Blue Luminescence and the Presence of Small Polycyclic Aromatic Hydrocarbons in the Interstellar Medium." en. In: *The Astrophysical Journal* 633.1, pp. 262–271. ISSN: 0004-637X, 1538-4357. DOI: 10.1086/447763. URL: https://iopscience.iop.org/article/10.1086/447763.

Brandl, B. R. et al. (Dec. 2006). "The Mid-Infrared Properties of Starburst Galaxies from *Spitzer* -IRS Spectroscopy." en. In: *The Astrophysical Journal* 653.2, pp. 1129–1144. ISSN: 0004-637X, 1538-4357. DOI: 10.1086/508849. URL: https://iopscience.iop.org/article/10.1086/508849.

Chang, Q., H. M. Cuppen, and E. Herbst (Nov. 2006). "Effective rate coefficients for molecular hydrogen formation in diffuse interstellar clouds." In: *Astronomy & Astrophysics* 458.2, pp. 497–505. ISSN: 0004-6361, 1432-0746. DOI: 10.1051/0004-6361:20065913. URL: http://www.aanda.org/10.1051/0004-6361:20065913.

Chiar, J. E. and A. G. G. M. Tielens (Feb. 2006). "Pixie Dust: The Silicate Features in the Diffuse Interstellar Medium." In: *The Astrophysical Journal* 637, pp. 774–785. ISSN: 0004-637X. DOI: 10.1086/498406. URL: http://adsabs.harvard.edu/abs/2006ApJ...637..774C.

Chiar, J. E., A. J. Adamson, D. C. B. Whittet, A. Chrysostomou, J. H. Hough, T. H. Kerr, R. E. Mason, P. F. Roche, and G. Wright (Nov. 2006). "Spectropolarimetry of the 3.4 μm Feature in the Diffuse ISM toward the Galactic Center Quintuplet Cluster." In: *The Astrophysical Journal* 651, pp. 268–271. ISSN: 0004-637X. DOI: 10.1086/507462. URL: http://adsabs.harvard.edu/abs/2006ApJ...651..268C.

Foster, Jonathan B. and Alyssa A. Goodman (Jan. 2006). "Cloudshine: New Light on Dark Clouds." In: *The Astrophysical Journal Letters* 636, pp. L105–L108. ISSN: 0004-637X. DOI: 10.1086/500131. URL: http://adsabs.harvard.edu/abs/2006ApJ...636L.105F.

Geers, V. C. et al. (Nov. 2006). "C2D Spitzer-IRS spectra of disks around T Tauri stars: II. PAH emission features." In: *Astronomy & Astrophysics* 459.2, pp. 545–556. ISSN: 0004-6361, 1432-0746. DOI: 10.1051/0004-6361:20064830. URL: http://www.aanda.org/10.1051/0004-6361:20064830.

Goicoechea, J. R., J. Pety, M. Gerin, D. Teyssier, E. Roueff, P. Hily-Blant, and S. Baek (Sept. 2006). "Low sulfur depletion in the Horsehead PDR." In: *Astronomy and Astrophysics* 456, pp. 565–580. ISSN: 0004-6361. DOI: 10.1051/0004-6361:20065260. URL: http://adsabs.harvard.edu/abs/2006A%26A...456..565G.

Le Petit, Franck, Cyrine Nehmé, Jacques Le Bourlot, and Evelyne Roueff (June 2006). "A Model for Atomic and Molecular Interstellar Gas: The Meudon PDR Code." In: *The Astro-*

physical Journal Supplement Series 164, pp. 506–529. ISSN: 0067-0049. DOI: 10.1086/503252. URL: http://adsabs.harvard.edu/abs/2006ApJS..164..506L.

Martín-Hernández, N. L., D. Schaerer, E. Peeters, A. G. G. M. Tielens, and M. Sauvage (Sept. 2006). "High spatial resolution mid-infrared spectroscopy of the starburst galaxies NGC 3256, II Zw 40 and Henize 2-10." In: *Astronomy and Astrophysics* 455, pp. 853–870. ISSN: 0004-6361. DOI: 10.1051/0004-6361:20054302. URL: http://adsabs.harvard.edu/abs/2006A%26A...455..853M.

Philipp, S. D., D. C. Lis, R. Güsten, C. Kasemann, T. Klein, and T. G. Phillips (July 2006). "Submillimeter imaging spectroscopy of the Horsehead nebula." In: *Astronomy and Astrophysics* 454, pp. 213–219. ISSN: 0004-6361. DOI: 10.1051/0004-6361:20053533. URL: http://adsabs.harvard.edu/abs/2006A%26A...454..213P.

Rapacioli, M., F. Calvo, C. Joblin, P. Parneix, D. Toublanc, and F. Spiegelman (Dec. 2006). "Formation and destruction of polycyclic aromatic hydrocarbon clusters in the interstellar medium." In: *Astronomy and Astrophysics* 460, pp. 519–531. ISSN: 0004-6361. DOI: 10.1051/0004-6361:20065412. URL: http://adsabs.harvard.edu/abs/2006A%26A...460..519R.

Snow, Theodore P. and Benjamin J. McCall (Sept. 2006). "Diffuse Atomic and Molecular Clouds." en. In: *Annual Review of Astronomy and Astrophysics* 44.1, pp. 367–414. ISSN: 0066-4146, 1545-4282. DOI: 10.1146/annurev.astro.43.072103.150624. URL: http://www.annualreviews.org/doi/10.1146/annurev.astro.43.072103.150624.

Witt, Adolf N., Karl D. Gordon, Uma P. Vijh, Paul H. Sell, Tracy L. Smith, and Rui-Hua Xie (Jan. 2006). "The Excitation of Extended Red Emission: New Constraints on Its Carrier from *Hubble Space Telescope* Observations of NGC 7023." en. In: *The Astrophysical Journal* 636.1, pp. 303–315. ISSN: 0004-637X, 1538-4357. DOI: 10.1086/498052. URL: https://iopscience.iop.org/article/10.1086/498052.

Armus, L. et al. (Feb. 2007). "Observations of Ultraluminous Infrared Galaxies with the Infrared Spectrograph on the *Spitzer Space Telescope* . II. The *IRAS* Bright Galaxy Sample." en. In: *The Astrophysical Journal* 656.1, pp. 148–167. ISSN: 0004-637X, 1538-4357. DOI: 10.1086/510107. URL: https://iopscience.iop.org/article/10.1086/510107.

Berné, O., C. Joblin, Y. Deville, J. D. Smith, M. Rapacioli, J. P. Bernard, J. Thomas, W. Reach, and A. Abergel (July 2007). "Analysis of the emission of very small dust particles from Spitzer spectro-imagery data using blind signal separation methods." In: *Astronomy and Astrophysics* 469, pp. 575–586. ISSN: 0004-6361. DOI: 10.1051/0004-6361:20066282. URL: http://adsabs.harvard.edu/abs/2007A%26A...469..575B.

Campeggio, L., F. Strafella, B. Maiolo, D. Elia, and S. Aiello (Oct. 2007). "Total to Selective Extinction in the Dark Globule CB 107." In: *The Astrophysical Journal* 668, pp. 316–330. ISSN: 0004-637X. DOI: 10.1086/520950. URL: http://adsabs.harvard.edu/abs/2007ApJ...668..316C.

Compiègne, M., A. Abergel, L. Verstraete, W. T. Reach, E. Habart, J. D. Smith, F. Boulanger, and C. Joblin (Aug. 2007). "Aromatic emission from the ionised mane of the Horsehead nebula." In: *Astronomy and Astrophysics* 471, pp. 205–212. ISSN: 0004-6361. DOI: 10.1051/0004-6361:20066172. URL: http://adsabs.harvard.edu/abs/2007A%26A...471..205C.

Draine, B. T. and Aigen Li (Mar. 2007). "Infrared Emission from Interstellar Dust. IV. The Silicate-Graphite-PAH Model in the Post-Spitzer Era." In: *The Astrophysical Journal* 657, pp. 810–837. ISSN: 0004-637X. DOI: 10.1086/511055. URL: http://adsabs.harvard.edu/abs/2007ApJ...657..810D.

Engelbracht, C. W. et al. (Sept. 2007). "Absolute Calibration and Characterization of the Multiband Imaging Photometer for *Spitzer* . I. The Stellar Calibrator Sample and the 24 m Calibration." en. In: *Publications of the Astronomical Society of the Pacific* 119.859, pp. 994–1018.

ISSN: 0004-6280, 1538-3873. DOI: 10.1086/521881. URL: http://iopscience.iop.org/article/10.1086/521881.

Fitzpatrick, E. L. and D. Massa (July 2007). "An Analysis of the Shapes of Interstellar Extinction Curves. V. The IR-through-UV Curve Morphology." In: *The Astrophysical Journal* 663, pp. 320–341. ISSN: 0004-637X. DOI: 10.1086/518158. URL: http://adsabs.harvard.edu/abs/2007ApJ...663..320F.

Flaherty, K. M., J. L. Pipher, S. T. Megeath, E. M. Winston, R. A. Gutermuth, J. Muzerolle, L. E. Allen, and G. G. Fazio (July 2007). "Infrared Extinction toward Nearby Star-forming Regions." en. In: *The Astrophysical Journal* 663.2, pp. 1069–1082. ISSN: 0004-637X, 1538-4357. DOI: 10.1086/518411. URL: https://iopscience.iop.org/article/10.1086/518411.

Gordon, Karl D. et al. (Sept. 2007). "Absolute Calibration and Characterization of the Multiband Imaging Photometer for *Spitzer* . II. 70 m Imaging." en. In: *Publications of the Astronomical Society of the Pacific* 119.859, pp. 1019–1037. ISSN: 0004-6280, 1538-3873. DOI: 10.1086/522675. URL: http://iopscience.iop.org/article/10.1086/522675.

Hrivnak, Bruce J., T. R. Geballe, and Sun Kwok (June 2007). "A Study of the 3.3 and 3.4 m Emission Features in Proto–Planetary Nebulae." en. In: *The Astrophysical Journal* 662.2, pp. 1059–1066. ISSN: 0004-637X, 1538-4357. DOI: 10.1086/518109. URL: https://iopscience.iop.org/article/10.1086/518109.

Pety, J., J. R. Goicoechea, P. Hily-Blant, M. Gerin, and D. Teyssier (Mar. 2007). "Deuterium fractionation in the Horsehead edge." In: *Astronomy and Astrophysics* 464, pp. L41–L44. ISSN: 0004-6361. DOI: 10.1051/0004-6361:20067009. URL: http://adsabs.harvard.edu/abs/2007A%26A...464L..41P.

Smith, J. D. T. et al. (Feb. 2007). "The Mid-Infrared Spectrum of Star-forming Galaxies: Global Properties of Polycyclic Aromatic Hydrocarbon Emission." en. In: *The Astrophysical Journal* 656.2, pp. 770–791. ISSN: 0004-637X, 1538-4357. DOI: 10.1086/510549. URL: https://iopscience.iop.org/article/10.1086/510549.

Stansberry, J. A. et al. (Sept. 2007). "Absolute Calibration and Characterization of the Multiband Imaging Photometer for *Spitzer* . III. An Asteroid-based Calibration of MIPS at 160 m." en. In: *Publications of the Astronomical Society of the Pacific* 119.859, pp. 1038–1051. ISSN: 0004-6280, 1538-3873. DOI: 10.1086/521880. URL: http://iopscience.iop.org/article/10.1086/521880.

Bernard, Jean-Philippe et al. (Sept. 2008). "*SPITZER* SURVEY OF THE LARGE MAGELLANIC CLOUD, SURVEYING THE AGENTS OF A GALAXY'S EVOLUTION (SAGE). IV. DUST PROPERTIES IN THE INTERSTELLAR MEDIUM." In: *The Astronomical Journal* 136.3, pp. 919–945. ISSN: 0004-6256, 1538-3881. DOI: 10.1088/0004-6256/136/3/919. URL: https://iopscience.iop.org/article/10.1088/0004-6256/136/3/919.

Berné, O., C. Joblin, M. Rapacioli, J. Thomas, J.-C. Cuillandre, and Y. Deville (Mar. 2008). "Extended Red Emission and the evolution of carbonaceous nanograins in NGC 7023." In: *Astronomy and Astrophysics* 479, pp. L41–L44. ISSN: 0004-6361. DOI: 10.1051/0004-6361:20079158. URL: http://adsabs.harvard.edu/abs/2008A%26A...479L..41B.

Compiègne, M., A. Abergel, L. Verstraete, and E. Habart (Dec. 2008). "Dust processing in photodissociation regions. Mid-IR emission modelling." In: *Astronomy and Astrophysics* 491, pp. 797–807. ISSN: 0004-6361. DOI: 10.1051/0004-6361:200809850. URL: http://adsabs.harvard.edu/abs/2008A%26A...491..797C.

Galliano, Frédéric, Suzanne C. Madden, Alexander G. G. M. Tielens, Els Peeters, and Anthony P. Jones (May 2008). "Variations of the Mid-IR Aromatic Features inside and among Galaxies." In: *The Astrophysical Journal* 679, pp. 310–345. ISSN: 0004-637X. DOI: 10.1086/587051. URL: http://adsabs.harvard.edu/abs/2008ApJ...679..310G.

Tielens, A.G.G.M. (Sept. 2008). "Interstellar Polycyclic Aromatic Hydrocarbon Molecules." en. In: *Annual Review of Astronomy and Astrophysics* 46.1, pp. 289–337. ISSN: 0066-4146, 1545-4282. DOI: 10.1146/annurev.astro.46.060407.145211. URL: http://www.annualreviews.org/doi/10.1146/annurev.astro.46.060407.145211.

Witt, Adolf N., Steve Mandel, Paul H. Sell, Thomas Dixon, and Uma P. Vijh (May 2008). "Extended Red Emission in High Galactic Latitude Interstellar Clouds." en. In: *The Astrophysical Journal* 679.1, pp. 497–511. ISSN: 0004-637X, 1538-4357. DOI: 10.1086/587131. URL: https://iopscience.iop.org/article/10.1086/587131.

Chapman, Nicholas L., Lee G. Mundy, Shih-Ping Lai, and Neal J. Evans (Jan. 2009). "THE MID-INFRARED EXTINCTION LAW IN THE OPHIUCHUS, PERSEUS, AND SERPENS MOLECULAR CLOUDS." In: *The Astrophysical Journal* 690.1, pp. 496–511. ISSN: 0004-637X, 1538-4357. DOI: 10.1088/0004-637X/690/1/496. URL: https://iopscience.iop.org/article/10.1088/0004-637X/690/1/496.

Duley, W. W. (Nov. 2009). "EXCITATION OF EXTENDED RED EMISSION AND NEAR-INFRARED CONTINUUM RADIATION IN THE INTERSTELLAR MEDIUM." In: *The Astrophysical Journal* 705.1, pp. 446–453. ISSN: 0004-637X, 1538-4357. DOI: 10.1088/0004-637X/705/1/446. URL: https://iopscience.iop.org/article/10.1088/0004-637X/705/1/446.

Flagey, N. et al. (Aug. 2009). "Evidence for Dust Evolution Within the Taurus Complex from Spitzer Images." In: *The Astrophysical Journal* 701, pp. 1450–1463. ISSN: 0004-637X. DOI: 10.1088/0004-637X/701/2/1450. URL: http://adsabs.harvard.edu/abs/2009ApJ...701.1450F.

Gerin, M., J. R. Goicoechea, J. Pety, and P. Hily-Blant (Feb. 2009). "HCO mapping of the Horsehead: tracing the illuminated dense molecular cloud surfaces." In: *Astronomy and Astrophysics* 494, pp. 977–985. ISSN: 0004-6361. DOI: 10.1051/0004-6361:200810933. URL: http://adsabs.harvard.edu/abs/2009A%26A...494..977G.

Goicoechea, J. R., J. Pety, M. Gerin, P. Hily-Blant, and J. Le Bourlot (May 2009). "The ionization fraction gradient across the Horsehead edge: an archetype for molecular clouds." In: *Astronomy and Astrophysics* 498, pp. 771–783. ISSN: 0004-6361. DOI: 10.1051/0004-6361/200811496. URL: http://adsabs.harvard.edu/abs/2009A%26A...498..771G.

Haffner, L. M., R.-J. Dettmar, J. E. Beckman, K. Wood, J. D. Slavin, C. Giammanco, G. J. Madsen, A. Zurita, and R. J. Reynolds (July 2009). "The warm ionized medium in spiral galaxies." en. In: *Reviews of Modern Physics* 81.3, pp. 969–997. ISSN: 0034-6861, 1539-0756. DOI: 10.1103/RevModPhys.81.969. URL: https://link.aps.org/doi/10.1103/RevModPhys.81.969.

Hobbs, L. M. et al. (Nov. 2009). "STUDIES OF THE DIFFUSE INTERSTELLAR BANDS. III. HD 183143." In: *The Astrophysical Journal* 705.1, pp. 32–45. ISSN: 0004-637X, 1538-4357. DOI: 10.1088/0004-637X/705/1/32. URL: https://iopscience.iop.org/article/10.1088/0004-637X/705/1/32.

McClure, M. (Mar. 2009). "Observational 5-20 m Interstellar Extinction Curves Toward Star-Forming Regions Derived From Spitzer IRS Spectra." In: *The Astrophysical Journal Letters* 693, pp. L81–L85. ISSN: 0004-637X. DOI: 10.1088/0004-637X/693/2/L81. URL: http://adsabs.harvard.edu/abs/2009ApJ...693L..81M.

Abergel, A. et al. (July 2010). "Evolution of interstellar dust with Herschel. First results in the photodissociation regions of NGC 7023." In: *Astronomy and Astrophysics* 518, p. L96. ISSN: 0004-6361. DOI: 10.1051/0004-6361/201014643. URL: http://adsabs.harvard.edu/abs/2010A%26A...518L..96A.

Acke, B., J. Bouwman, A. Juhász, Th. Henning, M. E. van den Ancker, G. Meeus, A. G. G. M. Tielens, and L. B. F. M. Waters (July 2010). "*SPITZER* 'S VIEW ON AROMATIC AND

ALIPHATIC HYDROCARBON EMISSION IN HERBIG Ae STARS." In: *The Astrophysical Journal* 718.1, pp. 558–574. ISSN: 0004-637X, 1538-4357. DOI: 10.1088/0004-637X/718/1/558. URL: http://stacks.iop.org/0004-637X/718/i=1/a=558?key=crossref.8432e8c0fb0aedfd1feb21efb9425891.

Arendt, Richard G., Eli Dwek, William P. Blair, Parviz Ghavamian, Una Hwang, Knox S. Long, Robert Petre, Jeonghee Rho, and P. Frank Winkler (Dec. 2010). "*SPITZER* OBSERVATIONS OF DUST DESTRUCTION IN THE PUPPIS A SUPERNOVA REMNANT." In: *The Astrophysical Journal* 725.1, pp. 585–597. ISSN: 0004-637X, 1538-4357. DOI: 10.1088/0004-637X/725/1/585. URL: https://iopscience.iop.org/article/10.1088/0004-637X/725/1/585.

Cecchi-Pestellini, C., A. Cacciola, M. A. Iatì, R. Saija, F. Borghese, P. Denti, A. Giusto, and D. A. Williams (July 2010). "Stratified dust grains in the interstellar medium - II. Time-dependent interstellar extinction: Time-dependent interstellar extinction." en. In: *Monthly Notices of the Royal Astronomical Society* 408.1, pp. 535–541. ISSN: 00358711. DOI: 10.1111/j.1365-2966.2010.17138.x. URL: https://academic.oup.com/mnras/article-lookup/doi/10.1111/j.1365-2966.2010.17138.x.

Pagani, Laurent, Jürgen Steinacker, Aurore Bacmann, Amelia Stutz, and Thomas Henning (Sept. 2010). "The Ubiquity of Micrometer-Sized Dust Grains in the Dense Interstellar Medium." In: *Science* 329, p. 1622. ISSN: 0036-8075. DOI: 10.1126/science.1193211. URL: http://adsabs.harvard.edu/abs/2010Sci...329.1622P.

Swinyard, B. M. et al. (July 2010). "In-flight calibration of the *Herschel* -SPIRE instrument." In: *Astronomy and Astrophysics* 518, p. L4. ISSN: 0004-6361, 1432-0746. DOI: 10.1051/0004-6361/201014605. URL: http://www.aanda.org/10.1051/0004-6361/201014605.

Zonca, A., C. Cecchi-Pestellini, G. Mulas, and G. Malloci (Oct. 2010). "Modelling peculiar extinction curves: Peculiar extinction curves." en. In: *Monthly Notices of the Royal Astronomical Society*, no–no. ISSN: 00358711. DOI: 10.1111/j.1365-2966.2010.17571.x. URL: https://academic.oup.com/mnras/article-lookup/doi/10.1111/j.1365-2966.2010.17571.x.

Breemen, J. M. van et al. (Feb. 2011). "The 9.7 and 18 m silicate absorption profiles towards diffuse and molecular cloud lines-of-sight." In: *Astronomy & Astrophysics* 526, A152. ISSN: 0004-6361, 1432-0746. DOI: 10.1051/0004-6361/200811142. URL: http://www.aanda.org/10.1051/0004-6361/200811142.

Compiègne, M., L. Verstraete, A. Jones, J.-P. Bernard, F. Boulanger, N. Flagey, J. Le Bourlot, D. Paradis, and N. Ysard (Jan. 2011). "The global dust SED: tracing the nature and evolution of dust with DustEM." In: *Astronomy and Astrophysics* 525, A103. ISSN: 0004-6361. DOI: 10.1051/0004-6361/201015292. URL: http://adsabs.harvard.edu/abs/2011A%26A...525A.103C.

Draine, Bruce T. (2011). *Physics of the interstellar and intergalactic medium*. Princeton series in astrophysics. OCLC: ocn649926225. Princeton, N.J: Princeton University Press. ISBN: 978-0-691-12213-7 978-0-691-12214-4.

Galliano, F. et al. (Dec. 2011). "Non-standard grain properties, dark gas reservoir, and extended submillimeter excess, probed by *Herschel* in the Large Magellanic Cloud." In: *Astronomy & Astrophysics* 536, A88. ISSN: 0004-6361, 1432-0746. DOI: 10.1051/0004-6361/201117952. URL: http://www.aanda.org/10.1051/0004-6361/201117952.

Guzmán, V., J. Pety, J. R. Goicoechea, M. Gerin, and E. Roueff (Oct. 2011). "H2CO in the Horsehead PDR: photo-desorption of dust grain ice mantles." In: *Astronomy and Astrophysics* 534, A49. ISSN: 0004-6361. DOI: 10.1051/0004-6361/201117257. URL: http://adsabs.harvard.edu/abs/2011A%26A...534A..49G.

Habart, E., A. Abergel, F. Boulanger, C. Joblin, L. Verstraete, M. Compiègne, G. Pineau Des Forêts, and J. Le Bourlot (Mar. 2011). "Excitation of H2 in photodissociation regions as

seen by Spitzer." In: *Astronomy and Astrophysics* 527, A122. ISSN: 0004-6361. DOI: 10.1051/0004-6361/20077327. URL: http://adsabs.harvard.edu/abs/2011A%26A...527A.122H.

Juvela, M. et al. (Mar. 2011). "Galactic cold cores: II. *Herschel* study of the extended dust emission around the first *Planck* detections." In: *Astronomy & Astrophysics* 527, A111. ISSN: 0004-6361, 1432-0746. DOI: 10.1051/0004-6361/201015916. URL: http://www.aanda.org/10.1051/0004-6361/201015916.

Ormel, C. W., M. Min, A. G. G. M. Tielens, C. Dominik, and D. Paszun (Aug. 2011). "Dust coagulation and fragmentation in molecular clouds. II. The opacity of the dust aggregate size distribution." In: *Astronomy and Astrophysics* 532, A43. ISSN: 0004-6361. DOI: 10.1051/0004-6361/201117058. URL: http://adsabs.harvard.edu/abs/2011A%26A...532A..43O.

Planck Collaboration et al. (Dec. 2011a). "Planck early results. XXIV. Dust in the diffuse interstellar medium and the Galactic halo." In: *Astronomy and Astrophysics* 536, A24. ISSN: 0004-6361. DOI: 10.1051/0004-6361/201116485. URL: http://adsabs.harvard.edu/abs/2011A%26A...536A..24P.

Planck Collaboration et al. (Dec. 2011b). "Planck early results. XXV. Thermal dust in nearby molecular clouds." In: *Astronomy and Astrophysics* 536, A25. ISSN: 0004-6361. DOI: 10.1051/0004-6361/201116483. URL: http://adsabs.harvard.edu/abs/2011A%26A...536A..25P.

Snow, T.P. and J.D. Destree (2011). "The Diffuse Interstellar Bands in History and in the UV." In: *EAS Publications Series* 46, pp. 341–347. ISSN: 1633-4760, 1638-1963. DOI: 10.1051/eas/1146035. URL: http://www.eas-journal.org/10.1051/eas/1146035.

Steglich, M., J. Bouwman, F. Huisken, and Th. Henning (Nov. 2011). "CAN NEUTRAL AND IONIZED POLYCYCLIC AROMATIC HYDROCARBONS BE CARRIERS OF THE ULTRAVIOLET EXTINCTION BUMP AND THE DIFFUSE INTERSTELLAR BANDS?" In: *The Astrophysical Journal* 742.1, p. 2. ISSN: 0004-637X, 1538-4357. DOI: 10.1088/0004-637X/742/1/2. URL: https://iopscience.iop.org/article/10.1088/0004-637X/742/1/2.

Arab, H., A. Abergel, E. Habart, J. Bernard-Salas, H. Ayasso, K. Dassas, P. G. Martin, and G. J. White (May 2012). "Evolution of dust in the Orion Bar with Herschel. I. Radiative transfer modelling." In: *Astronomy and Astrophysics* 541, A19. ISSN: 0004-6361. DOI: 10.1051/0004-6361/201118537. URL: http://adsabs.harvard.edu/abs/2012A%26A...541A..19A.

Bocchio, M., E. R. Micelotta, A.-L. Gautier, and A. P. Jones (Sept. 2012). "Small hydrocarbon particle erosion in a hot gas: A comparative study." In: *Astronomy & Astrophysics* 545, A124. ISSN: 0004-6361, 1432-0746. DOI: 10.1051/0004-6361/201219705. URL: http://www.aanda.org/10.1051/0004-6361/201219705.

Guzmán, V., J. Pety, P. Gratier, J. R. Goicoechea, M. Gerin, E. Roueff, and D. Teyssier (July 2012). "The IRAM-30m line survey of the Horsehead PDR. I. CF+ as a tracer of C+ and as a measure of the fluorine abundance." In: *Astronomy and Astrophysics* 543, p. L1. ISSN: 0004-6361. DOI: 10.1051/0004-6361/201219449. URL: http://adsabs.harvard.edu/abs/2012A%26A...543L...1G.

Jones, A. P. (Apr. 2012a). "Variations on a theme - the evolution of hydrocarbon solids. I. Compositional and spectral modelling - the eRCN and DG models." In: *Astronomy and Astrophysics* 540, A1. ISSN: 0004-6361. DOI: 10.1051/0004-6361/201117623. URL: http://adsabs.harvard.edu/abs/2012A%26A...540A...1J.

— (Apr. 2012b). "Variations on a theme - the evolution of hydrocarbon solids. II. Optical property modelling - the optEC(s) model." In: *Astronomy and Astrophysics* 540, A2. ISSN: 0004-6361. DOI: 10.1051/0004-6361/201117624. URL: http://adsabs.harvard.edu/abs/2012A%26A...540A...2J.

— (June 2012c). "Variations on a theme - the evolution of hydrocarbon solids. III. Size-dependent properties - the optEC(s)(a) model." In: *Astronomy and Astrophysics* 542, A98.

ISSN: 0004-6361. DOI: 10.1051/0004-6361/201118483. URL: http://adsabs.harvard.edu/abs/2012A%26A...542A..98J.

Köhler, M., B. Stepnik, A. P. Jones, V. Guillet, A. Abergel, I. Ristorcelli, and J.-P. Bernard (Dec. 2012). "Dust coagulation processes as constrained by far-infrared observations." In: *Astronomy and Astrophysics* 548, A61. ISSN: 0004-6361. DOI: 10.1051/0004-6361/201218975. URL: http://adsabs.harvard.edu/abs/2012A%26A...548A..61K.

Le Bourlot, J., F. Le Petit, C. Pinto, E. Roueff, and F. Roy (May 2012). "Surface chemistry in the interstellar medium: I. H $_2$ formation by Langmuir-Hinshelwood and Eley-Rideal mechanisms." In: *Astronomy & Astrophysics* 541, A76. ISSN: 0004-6361, 1432-0746. DOI: 10.1051/0004-6361/201118126. URL: http://www.aanda.org/10.1051/0004-6361/201118126.

Martin, Peter G. et al. (May 2012). "EVIDENCE FOR ENVIRONMENTAL CHANGES IN THE SUBMILLIMETER DUST OPACITY." In: *The Astrophysical Journal* 751.1, p. 28. ISSN: 0004-637X, 1538-4357. DOI: 10.1088/0004-637X/751/1/28. URL: http://stacks.iop.org/0004-637X/751/i=1/a=28?key=crossref.94816bf60df3db12071a76eb3bbb0365.

Pety, J. et al. (Dec. 2012). "The IRAM-30 m line survey of the Horsehead PDR. II. First detection of the l-C3H+ hydrocarbon cation." In: *Astronomy and Astrophysics* 548, A68. ISSN: 0004-6361. DOI: 10.1051/0004-6361/201220062. URL: http://adsabs.harvard.edu/abs/2012A%26A...548A..68P.

Pilleri, P., J. Montillaud, O. Berné, and C. Joblin (June 2012). "Evaporating very small grains as tracers of the UV radiation field in photo-dissociation regions." In: *Astronomy and Astrophysics* 542, A69. ISSN: 0004-6361. DOI: 10.1051/0004-6361/201015915. URL: http://adsabs.harvard.edu/abs/2012A%26A...542A..69P.

Yamagishi, M., H. Kaneda, D. Ishihara, T. Kondo, T. Onaka, T. Suzuki, and Y. C. Minh (May 2012). "AKARI near-infrared spectroscopy of the aromatic and aliphatic hydrocarbon emission features in the galactic superwind of M 82." In: *Astronomy & Astrophysics* 541, A10. ISSN: 0004-6361, 1432-0746. DOI: 10.1051/0004-6361/201218904. URL: http://www.aanda.org/10.1051/0004-6361/201218904.

Bocchio, M., A. P. Jones, L. Verstraete, E. M. Xilouris, E. R. Micelotta, and S. Bianchi (Aug. 2013). "Dust heating. Photon absorption versus electron collisions." In: *Astronomy and Astrophysics* 556, A6. ISSN: 0004-6361. DOI: 10.1051/0004-6361/201321054. URL: http://adsabs.harvard.edu/abs/2013A%26A...556A...6B.

Chiar, J. E., A. G. G. M. Tielens, A. J. Adamson, and A. Ricca (June 2013). "The Structure, Origin, and Evolution of Interstellar Hydrocarbon Grains." In: *The Astrophysical Journal* 770, p. 78. ISSN: 0004-637X. DOI: 10.1088/0004-637X/770/1/78. URL: http://adsabs.harvard.edu/abs/2013ApJ...770...78C.

Gratier, P., J. Pety, V. Guzmán, M. Gerin, J. R. Goicoechea, E. Roueff, and A. Faure (Sept. 2013). "The IRAM-30 m line survey of the Horsehead PDR. III. High abundance of complex (iso-)nitrile molecules in UV-illuminated gas." In: *Astronomy and Astrophysics* 557, A101. ISSN: 0004-6361. DOI: 10.1051/0004-6361/201321031. URL: http://adsabs.harvard.edu/abs/2013A%26A...557A.101G.

Guzmán, V. V., J. R. Goicoechea, J. Pety, P. Gratier, M. Gerin, E. Roueff, F. Le Petit, J. Le Bourlot, and A. Faure (Dec. 2013). "The IRAM-30 m line survey of the Horsehead PDR. IV. Comparative chemistry of H2CO and CH3OH." In: *Astronomy and Astrophysics* 560, A73. ISSN: 0004-6361. DOI: 10.1051/0004-6361/201322460. URL: http://adsabs.harvard.edu/abs/2013A%26A...560A..73G.

Jones, A. P., L. Fanciullo, M. Köhler, L. Verstraete, V. Guillet, M. Bocchio, and N. Ysard (Oct. 2013). "The evolution of amorphous hydrocarbons in the ISM: dust modelling from a new vantage point." In: *Astronomy and Astrophysics* 558, A62. ISSN: 0004-6361. DOI: 10.1051/0004-6361/201321686. URL: http://adsabs.harvard.edu/abs/2013A%26A...558A..62J.

Ohashi, S., Y. Kitamura, and T. Akashi (Oct. 2013). "Mapping Observations of the Horsehead Nebula and the NGC 2023 Region in the NH3 (1,1),(2,2) and (3,3) Lines with the Nobeyama 45 m Telescope." In: vol. 476, p. 345. URL: http://adsabs.harvard.edu/abs/2013ASPC..476..345O.

Roy, Arabindo et al. (Jan. 2013). "Changes of Dust Opacity with Density in the Orion A Molecular Cloud." In: *The Astrophysical Journal* 763, p. 55. ISSN: 0004-637X. DOI: 10.1088/0004-637X/763/1/55. URL: http://adsabs.harvard.edu/abs/2013ApJ...763...55R.

Wang, Shu, Jian Gao, B. W. Jiang, Aigen Li, and Yang Chen (July 2013). "THE MID-INFRARED EXTINCTION LAW AND ITS VARIATION IN THE COALSACK NEBULA." In: *The Astrophysical Journal* 773.1, p. 30. ISSN: 0004-637X, 1538-4357. DOI: 10.1088/0004-637X/773/1/30. URL: https://iopscience.iop.org/article/10.1088/0004-637X/773/1/30.

Winkler, P. Frank, Brian J. Williams, William P. Blair, Kazimierz J. Borkowski, Parviz Ghavamian, Knox S. Long, John C. Raymond, and Stephen P. Reynolds (Feb. 2013). "THE FIRST REPORTED INFRARED EMISSION FROM THE SN 1006 REMNANT." In: *The Astrophysical Journal* 764.2, p. 156. ISSN: 0004-637X, 1538-4357. DOI: 10.1088/0004-637X/764/2/156. URL: https://iopscience.iop.org/article/10.1088/0004-637X/764/2/156.

Ysard, N., A. Abergel, I. Ristorcelli, M. Juvela, L. Pagani, V. Könyves, L. Spencer, G. White, and A. Zavagno (Nov. 2013). "Variation in dust properties in a dense filament of the Taurus molecular complex (L1506)." In: *Astronomy and Astrophysics* 559, A133. ISSN: 0004-6361. DOI: 10.1051/0004-6361/201322066. URL: http://adsabs.harvard.edu/abs/2013A%26A...559A.133Y.

Alata, I., G. A. Cruz-Diaz, G. M. Muñoz Caro, and E. Dartois (Sept. 2014). "Vacuum ultraviolet photolysis of hydrogenated amorphous carbons . I. Interstellar H2 and CH4 formation rates." In: *Astronomy and Astrophysics* 569, A119. ISSN: 0004-6361. DOI: 10.1051/0004-6361/201323118. URL: http://adsabs.harvard.edu/abs/2014A%26A...569A.119A.

Bocchio, Marco, Anthony P. Jones, and Jonathan D. Slavin (Oct. 2014). "A re-evaluation of dust processing in supernova shock waves." In: *Astronomy & Astrophysics* 570, A32. ISSN: 0004-6361, 1432-0746. DOI: 10.1051/0004-6361/201424368. URL: http://www.aanda.org/10.1051/0004-6361/201424368.

Bron, Emeric (2014). "Stochastic processes in the interstellar medium." PhD Thesis. URL: http://www.theses.fr/2014PA077169.

Bron, Emeric, Jacques Le Bourlot, and Franck Le Petit (Sept. 2014). "Surface chemistry in the interstellar medium. II. H2 formation on dust with random temperature fluctuations." In: *Astronomy and Astrophysics* 569, A100. ISSN: 0004-6361. DOI: 10.1051/0004-6361/201322101. URL: http://adsabs.harvard.edu/abs/2014A%26A...569A.100B.

Cecchi-Pestellini, Cesare, Serena Viti, and David A. Williams (May 2014). "EXTRAGALACTIC INTERSTELLAR EXTINCTION CURVES: INDICATORS OF LOCAL PHYSICAL CONDITIONS." In: *The Astrophysical Journal* 788.2, p. 100. ISSN: 0004-637X, 1538-4357. DOI: 10.1088/0004-637X/788/2/100. URL: https://iopscience.iop.org/article/10.1088/0004-637X/788/2/100.

Cecchi-Pestellini, Cesare, Silvia Casu, Giacomo Mulas, and Alberto Zonca (Mar. 2014). "OBSERVATIONAL EVIDENCE OF DUST EVOLUTION IN GALACTIC EXTINCTION CURVES." In: *The Astrophysical Journal* 785.1, p. 41. ISSN: 0004-637X, 1538-4357. DOI: 10.1088/0004-637X/785/1/41. URL: https://iopscience.iop.org/article/10.1088/0004-637X/785/1/41.

Jones, Anthony P., Nathalie Ysard, Melanie Koehler, Lapo Fanciullo, Marco Bocchio, Elisabetta Micelotta, Laurent Verstraete, and Vincent Guillet (2014). "The cycling of carbon into and out of dust." In: *Faraday Discuss.* 168. arXiv: 1411.5877, pp. 313–326. ISSN: 1359-6640, 1364-5498. DOI: 10.1039/C3FD00128H. URL: http://arxiv.org/abs/1411.5877.

Köhler, M., A. Jones, and N. Ysard (May 2014). "A hidden reservoir of Fe/FeS in interstellar silicates?" In: *Astronomy and Astrophysics* 565, p. L9. ISSN: 0004-6361. DOI: 10.1051/0004-6361/201423985. URL: http://adsabs.harvard.edu/abs/2014A%26A...565L...9K.

Lefèvre, C. et al. (Dec. 2014). "Dust properties inside molecular clouds from coreshine modeling and observations." In: *Astronomy and Astrophysics* 572, A20. ISSN: 0004-6361. DOI: 10.1051/0004-6361/201424081. URL: http://adsabs.harvard.edu/abs/2014A%26A...572A..20L.

Maaskant, K. M., M. Min, L. B. F. M. Waters, and A. G. G. M. Tielens (Mar. 2014). "Polycyclic aromatic hydrocarbon ionization as a tracer of gas flows through protoplanetary disk gaps." In: *Astronomy & Astrophysics* 563, A78. ISSN: 0004-6361, 1432-0746. DOI: 10.1051/0004-6361/201323137. URL: http://www.aanda.org/10.1051/0004-6361/201323137.

Planck Collaboration et al. (Nov. 2014). "Planck 2013 results. XI. All-sky model of thermal dust emission." In: *Astronomy and Astrophysics* 571, A11. ISSN: 0004-6361. DOI: 10.1051/0004-6361/201323195. URL: http://adsabs.harvard.edu/abs/2014A%26A...571A..11P.

Roman-Duval, Julia et al. (Dec. 2014). "DUST AND GAS IN THE MAGELLANIC CLOUDS FROM THE HERITAGE HERSCHEL KEY PROJECT. II. GAS-TO-DUST RATIO VARIATIONS ACROSS INTERSTELLAR MEDIUM PHASES." In: *The Astrophysical Journal* 797.2, p. 86. ISSN: 1538-4357. DOI: 10.1088/0004-637X/797/2/86. URL: https://iopscience.iop.org/article/10.1088/0004-637X/797/2/86.

Siebenmorgen, R., N. V. Voshchinnikov, and S. Bagnulo (Jan. 2014). "Dust in the diffuse interstellar medium: Extinction, emission, linear and circular polarisation." In: *Astronomy & Astrophysics* 561, A82. ISSN: 0004-6361, 1432-0746. DOI: 10.1051/0004-6361/201321716. URL: http://www.aanda.org/10.1051/0004-6361/201321716.

Alata, I., A. Jallat, L. Gavilan, M. Chabot, G. A. Cruz-Diaz, G. M. Munoz Caro, K. Béroff, and E. Dartois (Dec. 2015). "Vacuum ultraviolet of hydrogenated amorphous carbons. II. Small hydrocarbons production in Photon Dominated Regions." In: *Astronomy and Astrophysics* 584, A123. ISSN: 0004-6361. DOI: 10.1051/0004-6361/201526368. URL: http://adsabs.harvard.edu/abs/2015A%26A...584A.123A.

Andrews, H., C. Boersma, M. W. Werner, J. Livingston, L. J. Allamandola, and A. G. G. M. Tielens (July 2015). "PAH EMISSION AT THE BRIGHT LOCATIONS OF PDRs: THE grandPAH HYPOTHESIS." In: *The Astrophysical Journal* 807.1, p. 99. ISSN: 1538-4357. DOI: 10.1088/0004-637X/807/1/99. URL: https://iopscience.iop.org/article/10.1088/0004-637X/807/1/99.

Boogert, A. C. Adwin, Perry A. Gerakines, and Douglas C. B. Whittet (Aug. 2015). "Observations of the icy universe." In: *Annual Review of Astronomy and Astrophysics* 53, pp. 541–581. ISSN: 0066-4146. DOI: 10.1146/annurev-astro-082214-122348. URL: http://adsabs.harvard.edu/abs/2015ARA%26A..53..541B.

Campbell, E. K., M. Holz, D. Gerlich, and J. P. Maier (July 2015). "Laboratory confirmation of C60+ as the carrier of two diffuse interstellar bands." en. In: *Nature* 523.7560, pp. 322–323. ISSN: 0028-0836, 1476-4687. DOI: 10.1038/nature14566. URL: http://www.nature.com/articles/nature14566.

Duley, W. W., A. Zaidi, M. J. Wesolowski, and S. Kuzmin (Feb. 2015). "Small molecules from the decomposition of interstellar carbons." In: *Monthly Notices of the Royal Astronomical Society* 447, pp. 1242–1246. ISSN: 0035-8711. DOI: 10.1093/mnras/stu2508. URL: http://adsabs.harvard.edu/abs/2015MNRAS.447.1242D.

Jones, A. P. and E. Habart (Sept. 2015). "H_2 formation via the UV photo-processing of a-C:H nano-particles." In: *Astronomy & Astrophysics* 581, A92. ISSN: 0004-6361, 1432-0746. DOI: 10.1051/0004-6361/201526487. URL: http://www.aanda.org/10.1051/0004-6361/201526487.

Juvela, M. et al. (Dec. 2015). "Galactic cold cores. V. Dust opacity." In: *Astronomy and Astrophysics* 584, A93. ISSN: 0004-6361. DOI: 10.1051/0004-6361/201423788. URL: http://adsabs.harvard.edu/abs/2015A%26A...584A..93J.

Köhler, M., N. Ysard, and A. P. Jones (July 2015). "Dust evolution in the transition towards the denser ISM: impact on dust temperature, opacity, and spectral index." In: *Astronomy and Astrophysics* 579, A15. ISSN: 0004-6361. DOI: 10.1051/0004-6361/201525646. URL: http://adsabs.harvard.edu/abs/2015A%26A...579A..15K.

Lim, Wanggi, Sean J. Carey, and Jonathan C. Tan (Nov. 2015). "SPECTROSCOPIC INFRARED EXTINCTION MAPPING AS A PROBE OF GRAIN GROWTH IN IRDCs." In: *The Astrophysical Journal* 814.1, p. 28. ISSN: 1538-4357. DOI: 10.1088/0004-637X/814/1/28. URL: https://iopscience.iop.org/article/10.1088/0004-637X/814/1/28.

Ochsendorf, B. B. and A. G. G. M. Tielens (Apr. 2015). "A bimodal dust grain distribution in the IC 434 H ii region." In: *Astronomy and Astrophysics* 576, A2. ISSN: 0004-6361. DOI: 10.1051/0004-6361/201424799. URL: http://adsabs.harvard.edu/abs/2015A%26A...576A...20.

Ysard, N., M. Köhler, A. Jones, M.-A. Miville-Deschênes, A. Abergel, and L. Fanciullo (May 2015). "Dust variations in the diffuse interstellar medium: constraints on Milky Way dust from Planck-HFI observations." In: *Astronomy and Astrophysics* 577, A110. ISSN: 0004-6361. DOI: 10.1051/0004-6361/201425523. URL: http://adsabs.harvard.edu/abs/2015A%26A..577A.110Y.

Bocchio, M., S. Bianchi, L. K. Hunt, and R. Schneider (Feb. 2016). "Halo dust detection around NGC 891." In: *Astronomy and Astrophysics* 586, A8. ISSN: 0004-6361. DOI: 10.1051/0004-6361/201526950. URL: http://adsabs.harvard.edu/abs/2016A%26A...586A...8B.

Fogerty, S., W. Forrest, D. M. Watson, B. A. Sargent, and I. Koch (Oct. 2016). "SILICATE COMPOSITION OF THE INTERSTELLAR MEDIUM." In: *The Astrophysical Journal* 830.2, p. 71. ISSN: 1538-4357. DOI: 10.3847/0004-637X/830/2/71. URL: https://iopscience.iop.org/article/10.3847/0004-637X/830/2/71.

Jones, A. P. (Dec. 2016). "Dust evolution, a global view: II. Top-down branching, nanoparticle fragmentation and the mystery of the diffuse interstellar band carriers." en. In: *Royal Society Open Science* 3.12, p. 160223. ISSN: 2054-5703, 2054-5703. DOI: 10.1098/rsos.160223. URL: https://royalsocietypublishing.org/doi/10.1098/rsos.160223.

Jones, A. P., M. Köhler, N. Ysard, E. Dartois, M. Godard, and L. Gavilan (Apr. 2016). "Mantle formation, coagulation, and the origin of cloud/core shine: I. Modelling dust scattering and absorption in the infrared." In: *Astronomy & Astrophysics* 588, A43. ISSN: 0004-6361, 1432-0746. DOI: 10.1051/0004-6361/201527488. URL: http://www.aanda.org/10.1051/0004-6361/201527488.

Salgado, F., O. Berné, J. D. Adams, T. L. Herter, L. D. Keller, and A. G. G. M. Tielens (Oct. 2016). "The Orion HII Region and the Orion Bar in the Mid-infrared." In: *The Astrophysical Journal* 830, p. 118. ISSN: 0004-637X. DOI: 10.3847/0004-637X/830/2/118. URL: http://adsabs.harvard.edu/abs/2016ApJ...830..118S.

Wright, Christopher M., Tho Do Duy, and Warrick Lawson (Apr. 2016). "Absorption at 11 m in the interstellar medium and embedded sources: evidence for crystalline silicates." en. In: *Monthly Notices of the Royal Astronomical Society* 457.2, pp. 1593–1625. ISSN: 0035-8711, 1365-2966. DOI: 10.1093/mnras/stw041. URL: https://academic.oup.com/mnras/article-lookup/doi/10.1093/mnras/stw041.

Ysard, N., M. Köhler, A. Jones, E. Dartois, M. Godard, and L. Gavilan (Apr. 2016). "Mantle formation, coagulation, and the origin of cloud/core shine. II. Comparison with observations." In: *Astronomy and Astrophysics* 588, A44. ISSN: 0004-6361. DOI: 10.1051/0004-6361/201527487. URL: http://adsabs.harvard.edu/abs/2016A%26A...588A..44Y.

Fan, Haoyu et al. (Dec. 2017). "The Behavior of Selected Diffuse Interstellar Bands with Molecular Fraction in Diffuse Atomic and Molecular Clouds." In: *The Astrophysical Journal* 850.2, p. 194. ISSN: 1538-4357. DOI: 10.3847/1538-4357/aa9480. URL: https://iopscience.iop.org/article/10.3847/1538-4357/aa9480.

Gavilan, L., K. C. Le, T. Pino, I. Alata, A. Giuliani, and E. Dartois (Nov. 2017). "Polyaromatic disordered carbon grains as carriers of the UV bump: Far-UV to mid-IR spectroscopy of laboratory analogs." In: *Astronomy & Astrophysics* 607, A73. ISSN: 0004-6361, 1432-0746. DOI: 10.1051/0004-6361/201730712. URL: http://www.aanda.org/10.1051/0004-6361/201730712.

Gordon, K. D. et al. (July 2017). "TRUST. I. A 3D externally illuminated slab benchmark for dust radiative transfer." In: *Astronomy and Astrophysics* 603, A114. ISSN: 0004-6361. DOI: 10.1051/0004-6361/201629976. URL: http://adsabs.harvard.edu/abs/2017A%26A...603A.114G.

Jones, A. P., M. Köhler, N. Ysard, M. Bocchio, and L. Verstraete (June 2017). "The global dust modelling framework THEMIS." In: *Astronomy and Astrophysics* 602, A46. ISSN: 0004-6361. DOI: 10.1051/0004-6361/201630225. URL: http://adsabs.harvard.edu/abs/2017A%26A..602A..46J.

Le Gal, R., E. Herbst, G. Dufour, P. Gratier, M. Ruaud, T. H. G. Vidal, and V. Wakelam (Sept. 2017). "A new study of the chemical structure of the Horsehead nebula: the influence of grain-surface chemistry." In: *Astronomy and Astrophysics* 605, A88. ISSN: 0004-6361. DOI: 10.1051/0004-6361/201730980. URL: http://adsabs.harvard.edu/abs/2017A%26A...605A..88L.

Seok, Ji Yeon and Aigen Li (Feb. 2017). "Polycyclic Aromatic Hydrocarbons in Protoplanetary Disks around Herbig Ae/Be and T Tauri Stars." In: *The Astrophysical Journal* 835.2, p. 291. ISSN: 1538-4357. DOI: 10.3847/1538-4357/835/2/291. URL: https://iopscience.iop.org/article/10.3847/1538-4357/835/2/291.

Juvela, M., J. Malinen, J. Montillaud, V.-M. Pelkonen, I. Ristorcelli, and L. V. Tóth (June 2018a). "Galactic cold cores. IX. Column density structures and radiative-transfer modelling." In: *Astronomy and Astrophysics* 614, A83. ISSN: 0004-6361. DOI: 10.1051/0004-6361/201630304. URL: http://adsabs.harvard.edu/abs/2018A%26A...614A..83J.

Juvela, Mika et al. (Nov. 2018b). "Dust spectrum and polarisation at 850 m in the massive IRDC G035.39-00.33." In: *Astronomy and Astrophysics* 620, A26. ISSN: 0004-6361. DOI: 10.1051/0004-6361/201833245. URL: http://adsabs.harvard.edu/abs/2018A%26A...620A..26J.

Relaño, M. et al. (May 2018). "Spatially resolving the dust properties and submillimetre excess in M 33." In: *Astronomy & Astrophysics* 613, A43. ISSN: 0004-6361, 1432-0746. DOI: 10.1051/0004-6361/201732347. URL: https://www.aanda.org/10.1051/0004-6361/201732347.

Ysard, N., A. P. Jones, K. Demyk, T. Boutéraon, and M. Koehler (Sept. 2018). "The optical properties of dust: the effects of composition, size, and structure." In: *Astronomy & Astrophysics* 617, A124. ISSN: 0004-6361, 1432-0746. DOI: 10.1051/0004-6361/201833386. URL: https://www.aanda.org/10.1051/0004-6361/201833386.

Boutéraon, T., E. Habart, N. Ysard, A. P. Jones, E. Dartois, and T. Pino (Mar. 2019). "Carbonaceous nano-dust emission in proto-planetary discs: the aliphatic-aromatic components." In: *Astronomy & Astrophysics* 623, A135. ISSN: 0004-6361, 1432-0746. DOI: 10.1051/0004-6361/201834016. URL: https://www.aanda.org/10.1051/0004-6361/201834016.

Chastenet, Jérémy et al. (May 2019). "The Polycyclic Aromatic Hydrocarbon Mass Fraction on a 10 pc Scale in the Magellanic Clouds." In: *The Astrophysical Journal* 876.1, p. 62. ISSN: 1538-4357. DOI: 10.3847/1538-4357/ab16cf. URL: https://iopscience.iop.org/article/10.3847/1538-4357/ab16cf.

Elyajouri, M. and R. Lallement (Aug. 2019). "Updated extraction of the APOGEE 1.5273 m diffuse interstellar band: a *Planck* view on the carrier depletion in dense cores." In: *Astronomy & Astrophysics* 628, A67. ISSN: 0004-6361, 1432-0746. DOI: 10.1051/0004-6361/201834452. URL: https://www.aanda.org/10.1051/0004-6361/201834452.

Juvela, Mika (Feb. 2019). "SOC program for dust continuum radiative transfer." In: *Astronomy and Astrophysics* 622, A79. ISSN: 0004-6361. DOI: 10.1051/0004-6361/201834354. URL: http://adsabs.harvard.edu/abs/2019A%26A...622A..79J.

Juvela, Mika, Paolo Padoan, Isabelle Ristorcelli, and Veli-Matti Pelkonen (Sept. 2019). "Synthetic observations of dust emission and polarisation of Galactic cold clumps." In: *Astronomy & Astrophysics* 629, A63. ISSN: 0004-6361, 1432-0746. DOI: 10.1051/0004-6361/201935882. URL: https://www.aanda.org/10.1051/0004-6361/201935882.

Marchal, Antoine, Marc-Antoine Miville-Deschênes, François Orieux, Nicolas Gac, Charles Soussen, Marie-Jeanne Lesot, Adrien Revault d'Allonnes, and Quentin Salomé (June 2019). "ROHSA: Regularized Optimization for Hyper-Spectral Analysis: Application to phase separation of 21 cm data." In: *Astronomy & Astrophysics* 626, A101. ISSN: 0004-6361, 1432-0746. DOI: 10.1051/0004-6361/201935335. URL: https://www.aanda.org/10.1051/0004-6361/201935335.

Van De Putte, Dries, Karl D. Gordon, Julia Roman-Duval, Benjamin F. Williams, Maarten Baes, Kirill Tchernyshyov, Brandon L. Lawton, and Heddy Arab (Dec. 2019). "Evidence of Dust Grain Evolution from Extinction Mapping in the IC 63 Photodissociation Region." In: *The Astrophysical Journal* 888.1, p. 22. ISSN: 1538-4357. DOI: 10.3847/1538-4357/ab557f. URL: https://iopscience.iop.org/article/10.3847/1538-4357/ab557f.

Schirmer, T., A. Abergel, L. Verstraete, N. Ysard, M. Juvela, A. P. Jones, and E. Habart (Mar. 2020). "Dust evolution across the Horsehead Nebula." In: *arXiv e-prints*. _eprint: 2003.05902, arXiv:2003.05902.

université PARIS-SACLAY
ÉCOLE DOCTORALE
Astronomie
et Astrophysique
d'Île-de-France (AAIF)

Titre: Evolution des poussières interstellaires dans les régions photon-dominées

Mots clés: nano-poussière carbonées, régions photon-dominées, observations IR, modélisation

Résumé: Les processus microphysiques à la surface des poussières interstellaires sont étroitement liés à leurs propriétés (i.e. la taille et la forme des poussières) et jouent un rôle clé dans de nombreux phénomènes du milieu interstellaire (MIS). La grande disparité des conditions physiques (i.e. la densité et la température du gaz) dans le MIS déclenche une évolution des propriétés des poussières. L'analyse de l'évolution de la poussière en fonction des conditions physiques est un tremplin vers une compréhension plus approfondie de la poussière interstellaire. Étant donné que les conditions physiques varient considérablement et sont spatialement résolues dans les régions photon-dominées (PDRs) proches, elles constituent le lieu idéal pour étudier l'évolution de la poussière en fonction des conditions physiques. Dans cette thèse, je me concentre sur la façon dont la poussière interstellaire évolue en fonction des conditions physiques dans les PDRs proches. À cette fin, j'ai modélisé l'émission et la diffusion de la poussière en utilisant le modèle de poussière interstellaire THEMIS ainsi que le code de transfert radiatif 3D SOC. J'ai utilisé les observations Spitzer et Herschel pour confronter les résultats de ma modélisation afin de contraindre les propriétés de la poussière. J'ai constaté que les nano-grains sont fortement déplétés dans la partie irradiée de la tête de cheval et que les grains coagulent pour former des agrégats dans la partie dense de la tête de cheval. J'ai proposé un scénario dans lequel, dans la partie irradiée de la nébuleuse de la tête de cheval, tous les nano-grains n'ont pas encore eu le temps de se reformer par la photofragmentation des agrégats et les plus petits des nano-grains sensibles au champ de rayonnement sont détruits par le rayonnement. Dans la partie intérieure de la nébuleuse de la Tête de cheval, les grains sont constitués d'agrégats, comme attendu dans les régions à haute densité.

Title: Dust evolution in photon-dominated regions

Keywords: Carbonaceous nano-dust, photon-dominated regions, IR observations, modelling

Abstract: Micro-physical processes on interstellar dust surfaces are tightly connected to dust properties (i.e. dust composition, size, and shape) and play a key role in numerous phenomena in the interstellar medium (ISM). The large disparity in physical conditions (i.e. density and gas temperature) in the ISM triggers an evolution of dust properties. The analysis of how dust evolves with the physical conditions is a stepping stone towards a more thorough understanding of interstellar dust. As physical conditions vary widely and are spatially resolved in nearby photon-dominated regions (PDRs), they are the ideal place to study dust evolution as a function of physical conditions. In this thesis, I focus on how does interstellar dust evolves with physical conditions in nearby PDRs. To this end, I modelled dust emission and scattering using the THEMIS interstellar dust model together with the 3D radiative transfer code SOC. I used Spitzer and Herschel observations to confront the results of my modelling in order to constrain the dust properties. I found that nano-grains are strongly depleted in the outer irradiated part of the Horsehead and that grains coagulate together to form aggregates in the inner dense part of the Horsehead. I proposed a scenario where in the outer part of the Horsehead nebula, all the nano-grain have not yet had time to re-form completely through photo-fragmentation of aggregates and the smallest of the nano-grain that are sensitive to the radiation field are photo-destroyed. In the inner part of the Horsehead nebula, grains most likely consist of multi-compositional mantled aggregates, as would expected in high density regions.

Université Paris-Saclay
Espace Technologique / Immeuble Discovery
Route de l'Orme aux Merisiers RD 128 / 91190 Saint-Aubin, France